

**Scuola Internazionale Superiore  
di Studi Avanzati**

*New generation of nanostructured sensors  
and electrodes to bypass CNS lesions*



**SISSA**  
====

*Thesis for Philosophiae Doctor Degree*

*Candidate: Ivo Calaresu*

*Supervisor: Prof. Laura Ballerini*





# *Table of Contents*

ABSTRACT.....	1
INTRODUCTION.....	2
1. Nanomaterials for biomedical interfaces .....	2
1.1 Overview.....	2
1.2 Targeting the CNS.....	9
1.3 Topographical cues of implantable devices .....	15
2. Electrical recording and stimulation of excitable tissues .....	21
2.1 Advances in electrode design .....	21
2.2 Potential of electrical stimulation in biomedicine: electroceuticals ....	29
3. In vitro approaches to nanomaterials and device testing.....	34
3.1 Dissociated cultures.....	34
3.2 Organotypic cultures .....	39
4. Spinal cord: a yarned target.....	45
4.1 Spinal cord anatomy .....	45
4.2 Spinal cord injury .....	50
4.3 Implantable devices for spinal cord restoration .....	55

AIMS OF THE STUDY.....	59
RESULTS.....	62
APPENDIX.....	150
1. Longitudinal hemi-spinal organotypic culture from mouse embryo.....	164
2. Spinal fibers elongation over polymeric micropatterned substrates .....	167
3. External Collaborations.....	171
PATENTS INVOLVEMENT.....	205
CONCLUSIVE REMARKS .....	206
BIBLIOGRAPHY .....	210

## ABSTRACT

Since the dawn of neurobiology research, neural activity recording and stimulation have experienced a dramatic evolution. Such a process encouraged not only the conception of new technologies to improve our ability to study neurophysiology at the laboratory level, but also the formulation of new solutions to defeat neurological disorder. Among these, neuroprosthetics and neuroelectronic interfaces represent an intriguing panacea to resolve pathological states where conventional methods failed. This arduous challenge requires the collaboration of various subfields in neurobiology research to produce more efficient and highly physiological central nervous system interfacing. In this context, nanotechnologies seem to date eligible candidates to fulfill the needs for the design of next generation implantable neural prosthesis. Size-dependent chemical, topographical or electrical cues can be exploited to mimic biological environments and to faithfully reproduce physiological cells behavior. To safely improve our scientific knowledge about nanotechnologies applicability in biomedicine and more specifically in the context of neuroprosthetics design, a multidisciplinary approach is compulsory. The mutual support between neurobiology and nanoscience has resulted in a large amount of novel neurotechnologies, whose pertinence must be validated by conventional investigation methods in neurobiology to prove their safety and applicability. In particular, *in vitro* cells and tissue cultures and *ex vivo* preparations are interrogated by electrophysiology, live imaging, as well as various microscopy and nanoscopy methods, enabling neuroscientists to dissect cell physiology, mechanics and biophysics as a consequence of the interaction with the nanoworld. The purpose of my thesis is to explore the perspective of nanomaterials in the context of neuroprosthetics formulation.

# INTRODUCTION

## 1. Nanomaterials for biomedical interfaces

### 1.1 Overview

Nanomaterials science and more in general nanotechnology are novel fields of science and engineering, developed upon the precious intuitions of brilliant scientists such as Richard Feynman (with the illuminating lecture, “*There’s Plenty of Room at the Bottom*”, 1959) [1], Mohamed Atalla and Dawon Kahng (fabrication of the first MOSFET with nanosized component, 1960) [2,3], and Norio Taniguchi (coining the word “*Nanotechnology*”, 1974) [4]. The major merit of these and others scientists has been that of raising the interest of our society towards innovative nanotechnology tools enabling to manipulate or manufacture materials at the nanoscale in controlled manner [5]. In a provocative approach, the use of nanomaterials may be dated back to the 4<sup>th</sup> century (A.D.) when Romans craftsmen demonstrated a unique ability in designing ravishing artefacts, such as the Lycurgus Cup (**Figure 1A**), with metal-glass nanocomposites (**Figure 1B**) [6,7]. Obviously, in ancient and even more recent times, people were not aware of dealing with matter at the nanoscale, but they surely knew which new properties they could achieve with their skills. In the same epoch, until the 17<sup>th</sup> century (A.D.), Persians blacksmiths were forging sabers, which outstanding physical properties gave rise to many legends. Damascus steel swords (**Figure 1C**), as they were known in the entire world, were fabricated with wootz steel, a particular alloy which fabrication methods remains thus far unknown. A research from University of Dresden in 2006, demonstrated the presence of cementite nanowires and carbon nanotubes (CNTs, **Figure 1D**) in the blade of ancient Damascus sabers [8,9]. Another research few years later tried to explain the presence of such nanostructures in these

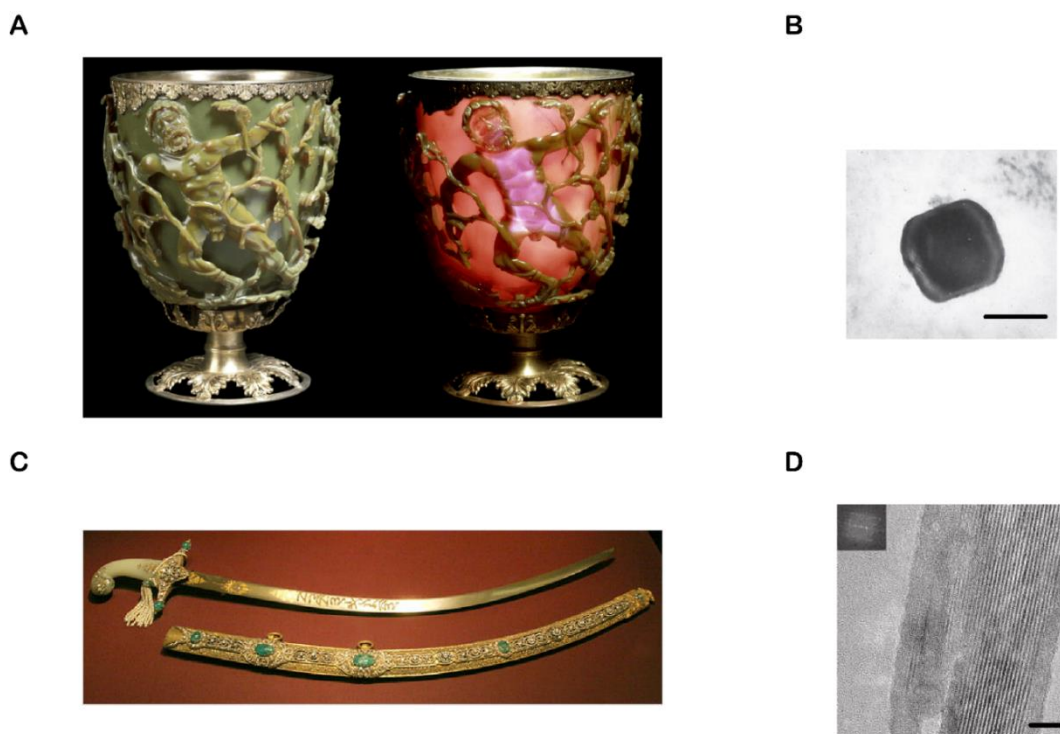


**Figure 1.** Ancient artifacts revealing nanomaterials presence. **A.** The Roman Lycurgus Cup (© *The Trustees of the British Museum*) made with a dichroic glass including colloidal silver-gold alloy nanoparticles, resulting in a green coloration when light reflects to its external surface (left) or red when light is transmitted from the inside of the cup (right). **B.** Transmission Electron Microscopy (TEM) image of a silver-gold nanoparticle found in a fragment of the Lycurgus Cup (scale bar = 50 nm) [6,7]. **C.** A Damascus steel saber with its scabbard (*photo by Tina Fineberg for the New York Times*). **D.** High-Resolution Transmission Electron Microscopy (HRTEM) image of carbon nanotubes-encapsulated cementite nanowires found in an ancient Damascus saber (scale bar = 5 nm). On the image top left the Fourier transform of cementite lattice planes is also shown [8,9].

antique artifacts, suggesting that Persians craftsmen probably added woody biomasses as carburizing agents during smelting processes to achieve outstanding materials' features [10]. To date, we assume that these manufactures were the result of a trial-by-trial selection of innovative fabrication methods with the only purpose of favoring stunning physical properties that nowadays can be explained. For example, light radiation, reflecting to or transmitting through the Lycurgus Cup, behaves in two different ways thanks to the presence of a plasmon layer on the colloidal gold-silver nanoparticles surface acting as an anisotropic medium that results in its dichroic behavior [11,12]. On the other hand, the surprising mechanical properties of Damascus steel blades, such as the high tensile strength, toughness, stiffness and sharpness, can

be reconducted to nanowires and nanotubes presence within the alloy, and relates to size-dependence and behavior of material properties at the nanoscale [13]. In fact, several properties are closer to those of the bulk material for objects with a very large *characteristic length*, while for a nanostructured object several physical properties are closer to those of the material surface [14,15]. For this reason nanostructures are often defined as *all surface*, indeed showing a higher surface-to-volume ratio as feature size decreases [16]. The possibility to control interfacial physical properties by surface modifications and structural size scaling of the materials, boosted technological development in the last century [17] together with advances in microscopy, which from the beginning of the 20<sup>th</sup> century provided a way to “view” nanostructures. Abbe, in 1873, clarified that the diffraction limit of light microscopy would have never allowed the observation of structures with a size being half the wavelength of the imaging light [18]. In a couple of decades, such an awareness brought to development of the first *transmission electron microscope* (TEM) in 1931 before and the *scanning electron microscope* (SEM) few years later, in 1938 [19–22]. This trend reached then its climax in the second half of the century when further inventions such as the *scanning tunneling microscope* (STM) and the *atomic force microscope* (AFM) emerged allowing not only the imaging and the study of nanoscale objects [23,24], but enabled controlled nanostructures’ engineering [25]. The increasing expertise in nanomaterials synthesis on one hand and the availability of these (and further) new tools for their characterization on the other, indicated a straightforward way to the design of novel technologies with striking implications in several fields, including biomedicine.

The reason why nanotechnology can efficiently meet biomedical needs resides in the size of biological structures (from cells to molecules). Vessels, nerves and more in

general cells show micrometric dimension, with their building blocks being instead nanometric structures [26]. Nanotechnology engineers nanostructures that interact with the cells-surrounding nanoworld (**Figure 2**). Intra ed extracellular macromolecules such as enzymes and proteins can reach 5 nm in diameter (such as hemoglobin or antibodies), the thickness of a lipid bilayer is about 6 nm, the size of a synaptic cleft (mammals central nervous system, CNS) is around 12 nm and collagen fibers show a 65 nm patterning [27–30]. This means that, for example, a 20 nm nanoparticle easily transits through blood vessels [31,32], crosses the blood-brain barrier [33–35] and traverses fenestrated capillaries or liver sinusoids [36–38]. By virtue of these features and thanks to the biocompatibility that can be achieved through specific functionalization, several nanoparticles have been approved by the *Food and Drug Administration* (FDA) for cancer therapy, drug delivery and contrast imaging [39–42]. Given this size paradigm, regenerative medicine and tissue engineering are also taking extensive advantage of nanomaterial science by controlling prosthetic implants physicochemical cues through nanotechnologies and nanofabrication methods [43].

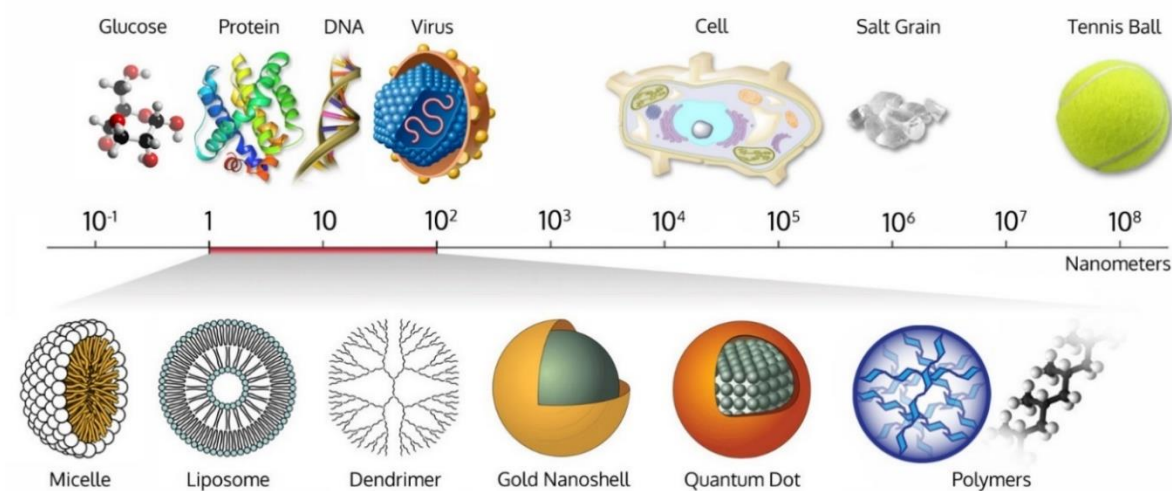


**Figure 2.** Nanostructures size comparison with familiar structures size expressed in nanometers. *Sketch from Peter R. Wich Laboratory web page (<https://www.wichlab.com/research/>).*

Remarkable achievements in the field have been earned by controlling surface energy, surface charge, chemical composition and topography at the nanoscale level to overcome common issues related to biomaterial implantation such as surface fouling and contamination, material oxidation and degradation, undesirable fibrosis around the implant or poor specific cell-type adhesion, among others [44–50]. To replace or regenerate an injured organ is probably the most challenging goal in biomedicine, where various constraints must be taken into account; for example, cell fate is determined, which impedes some cell type to revert to a proliferative state once they are differentiated or the lack of tissue inside a lesion hampers the cavity repopulation and affects structural and mechanical stability if the void inside is too prominent, or still, organ allografts often suffer from *non-self* immune responses lessening transplantations outcome [51–53]. Tissue engineering synergistically with stem cell-based technologies attempts to overwhelm these and other issues through 3D organoids, 3D scaffolds and bioartificial organs development [54–58]. In such scenarios, nanomaterial science has been dealing with various medical areas including orthopedics, dentistry, cardiology, endocrinology and neuroscience. The big challenges in so variegated biomedical fields are multiple, to mention one, the mechanical properties of target tissues: material engineers are seeking to reproduce, with artificial or bio-hybrid constructs, specific organs Young's modulus, which might range from the 0.5–1 kPa of the soft brain tissue to the 20 GPa of the cortical bone [59,60]. When soft materials design is required to better approach tissues mechanical properties or to reduce the invasiveness other problems emerge; for example, energy storage and power supply together with the size reduction and the flexibility of electronics within a wearable or an implantable device are among the major challenges in bio-nanomaterial science and electronic engineering [61,62]. Along with the mechanical features,



implantable 3D scaffolds might be either permanent or degradable, they can be filled with cells to compensate loss of function in the injured tissue or texturized with topographical or biochemical cues to mimic extracellular signaling or to elude immunogenic responses [63–69].

In last decades, the overall knowledge acquired in these areas has been favoring the development of biomedical devices capable of actively interacting with biological micro and nano worlds to manage various pathological conditions. To give some example, along the NANOCI European project (ID: 281056) cochlear implants (**Figure 3A**) were implemented with a 3D gel-nanomatrix functionalized with neurotrophins to promote neural outgrowth of nerve fibers through the *scala tympani* onto the surface of the cochlear implant electrode pad implanted in a guinea pig [70]. Lee and colleagues in 2016 developed a graphene-based skin patch for sensing homeostatic parameters such as temperature, humidity, glucose and pH. The sensor was also provided with polymeric microneedles that could be thermally activated to deliver drugs transcutaneously; this was indeed proven by automatic metformin release upon hyperglycemia sensing in diabetic mice, thus restoring blood glucose levels (**Figure 3B**) [71]. Nanomaterial-based wireless implants for intraocular pressure monitoring and treatment were proposed to prevent gradual loss of vision in patients with glaucoma (**Figure 3C**) [72–74]. Even more surprisingly, an implantable soft optoelectronic device was recently developed to work as an artificial eye able to detect optical signals and to consequently trigger programmed electrical stimulation to optic nerves (**Figure 3D**) [75].

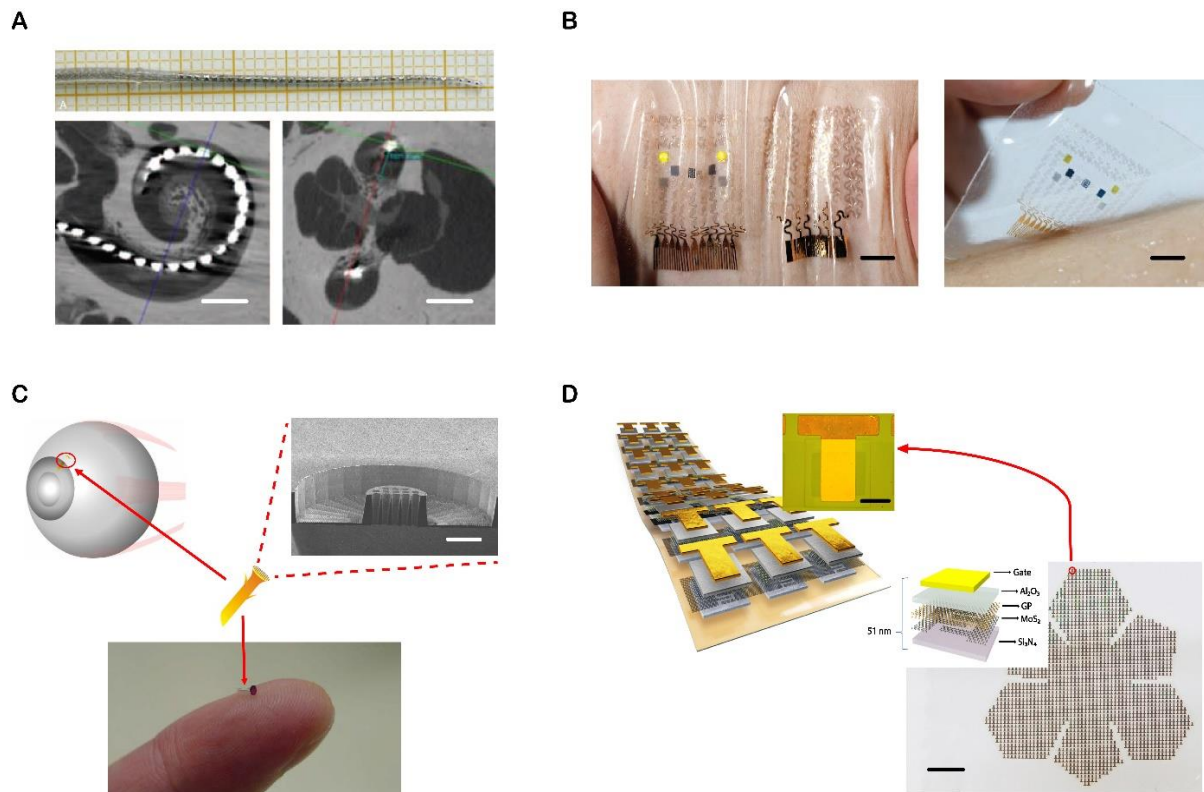


**Figure 3.** Novel nanotechnology-based devices. **A.** Top image shows a prototype of the NANOCI electrode array. Below, two distinct sections obtained through cone-beam computed tomography (CBCT) of human temporal bones scala tympani implanted with cochlear implant electrode arrays (scale bars = 3 mm) [72]. **B.** Graphene-based electrochemical wearable device for sweat-based diabetes monitoring and therapy, under stretch condition (left; scale bar = 1 cm) and during application (right; scale bar = 5 mm) [73]. **C.** Sketch and photo of the artificial nano-drainage implant (ANDI) for glaucoma, top right scanning electron micrograph (SEM) shows a backside cross-sectional view of the implant (scale bar = 400  $\mu\text{m}$ ) [76]. **D.** Top left illustrates device design, while the arrowed inset shows a single phototransistor at the optical microscope (scale bar = 100  $\mu\text{m}$ ). Below, another optical image of the whole phototransistor lens array (scale bar = 3 mm) is presented together with a schematic of phototransistor nanometric layering [77].

## 1.2 Targeting the CNS

A recent report from the World Health Organization (WHO) showed that neurological disorders, ranging from epilepsy to Alzheimer disease, from stroke to headache, including brain injuries, neuroinfections, multiple sclerosis and Parkinson disease, affect almost 1/6 of world's population, thus implying a public annual cost that in Europe reached €139 billion in 2004 [76]. So far, therapeutic solutions have been investigated through drug screening, with tremendous impact on public expenditure. According to a study of the *Tufts Center for the Study of Drug Development*, the estimated post-approval R&D cost per new drug is around \$2870 million (in 2013 dollars) [77]. Unfortunately, drug discovery in neurology presents the lowest success rate along the pharmacovigilance process when compared to other medical areas [78]. Besides the socioeconomic burden, ethics also comes into play since several neuropathological disorders associate not only with acute or chronic pain sensation, but also dissociative symptoms, some degree of paralysis or even vegetative states, thus compromising patients self-awareness, their life quality and that of their relatives [79]. An action is required, and nano-based therapeutic interventions integrating physiological monitoring and real-time automated treatment may represent a successful alternative [69,80]. Allowing to work at a smaller spatiotemporal scale, novel nanotechnologies demonstrated their relevance also in basic research where the pathophysiology of neurological disease can be addressed with improved resolution [81]. CNS therapeutic targeting has long been a challenging issue in medicine, mainly cause the existence of physical barriers such as the blood-brain barrier (BBB), bones and meninges (**Figure 4**) [82]. Nanomedicine for the CNS is trying to contribute solving this problem providing *ad hoc* carriers that could deliver and topically release drugs, antibiotics or other molecules. These can be eventually loaded into or bound onto

nanocarriers such as liposomes, micelles, nanoparticles, dendrimers, hydrogels and mesoporous materials, but fancier vehicles like nanorobots have also been proposed [83–86].

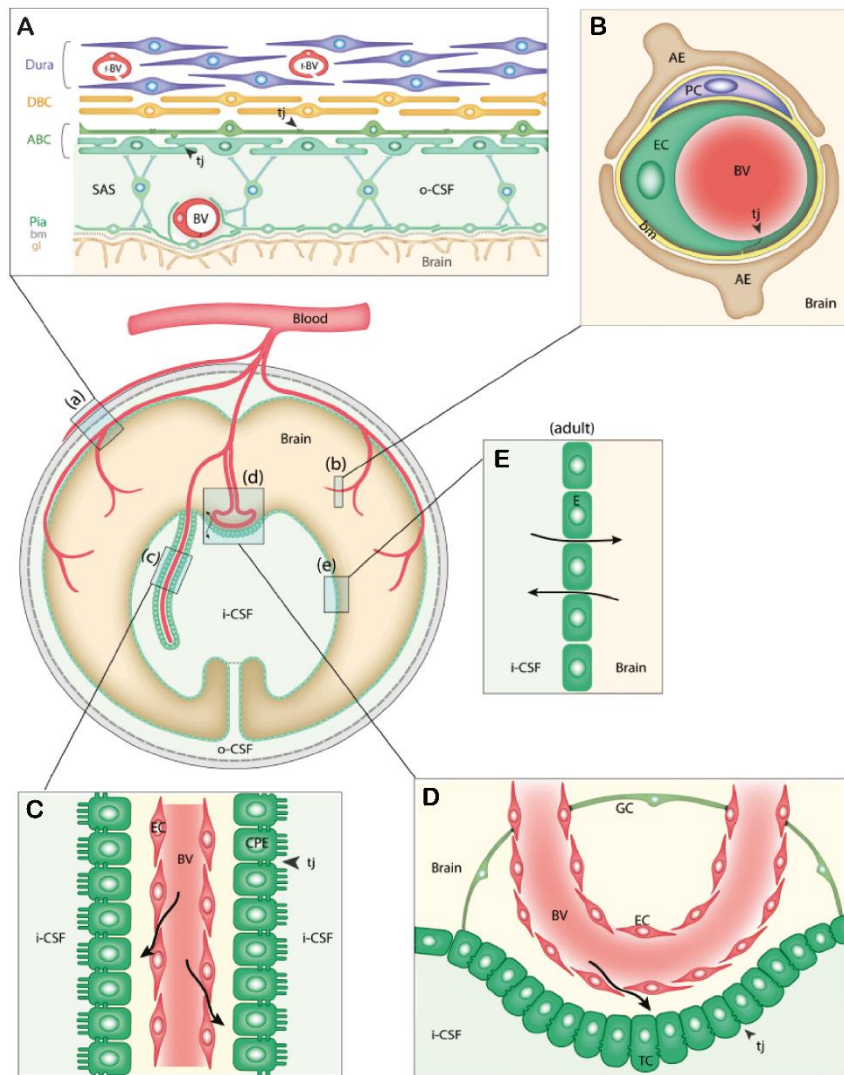


**Figure 4.** Schematic diagram (center left) of the five main barrier interfaces in the brain from Saunders et al [83]. The cellular layers forming the barrier at each interface are colored green. **A.** Cell layers in the meningeal barrier are shown; the more superficial layers are represented by dura mater and dural border cells (DBC). Note that blood vessels within the dura mater are fenestrated (f-BV). Just below, the arachnoid barrier cells (ABC) in the outer layer of the arachnoid membrane have tight junctions (tj, arrowheads) resulting in a barrier between the outer cerebrospinal fluid (o-CSF) in the subarachnoid space (SAS). Blood vessels (BV) in the SAS have also tj; bm = basement membrane, gl = glia limitans. **B.** The blood-brain barrier (BBB) is situated at the level of cerebral BV. Endothelial cells (EC) and BV are in contact through tj (arrowhead) to minimize the paracellular space; bm = basement membrane, PC = pericytes, AE = end feet from astroglial cells. **C.** Within each brain ventricle, the choroid plexus epithelium (CPE) forms the cell layer acting as BBB; CPE apical microvilli increase exchange surface of the epithelium toward internal CSF (i-CSF). CPE barrier is supported by tj among cells (arrowhead), while BV are fenestrated and do not form a barrier (arrows). **D.** Blood vessels reaching circumventricular organs (including median eminence, pineal gland, area postrema, subfornical organ), have comparable permeability features to other areas of the body in order to allow feedback penetration of peptide hormones related to the hypothalamic-pituitary axis. CSF entering of these molecules is prevented by tanycytes (TC), ependymal cells connected by tj between their apices (arrowhead); tj between astroglial cells (GC) further block the access to CNS. **E.** Ependymal cells (E) between the i-CSF and brain interstitial space are linked by gap junctions that do not restrict exchange of even large molecules (solid arrows).

In some instances, such as traumatic brain, spine or nerve injury, pharmacological treatment might not be sufficient to restore physiological parameters due to the lack, across the lesion, of functional neural tissue as a result of trauma. Remarkably, three-dimensional nano-scaffolds, electrospun nanofibers and injectable hydrogel have been used to provide ease of regeneration across and within a lesion [87,88]. In 2006, Gerald E. Schneider group grafted self-assembling peptide nanofiber (SAPNS) hydrogels onto transected visual P2 and superior colliculus areas, demonstrating visually oriented behavior recovery in living hamsters [89]. In last years other reports followed reporting the high potential of SAPNS technology in peripheral and central nerves injury repair [90–92]. In alternative studies nanofibers electrospinning has been preferred to approach severed nerve regeneration [88,93]. This technique provides a cost-effective and up-scalable solution for neural tissue engineering [94,95]. Electrospun polycaprolactone (PCL) and poly-L-lactic acid (PLA) fibers have been largely used to achieve axonal guidance and *in vivo* reports showed their ability to promote nerve fibers regrowth over either peripheral or spinal lesions [96–98]. Noteworthy in this field is the work by Nguyen and colleagues, which combined these technologies to design 3D nanofibers hydrogels, bio-functionalized with miRNAs and trophic factors, to provide both topic gene/drug delivery, contact guidance and mechanical support thus favoring injured nerves regrowth [99]. The success of 3D scaffold in neural tissue engineering evolved in parallel to several 3D bioprinting techniques allowing to work at increasingly higher resolution to fine control scaffold architectures and better mimic extracellular matrix (ECM) chemical and topographical composition [100,101]. For instance, laser-based two photon polymerization (TPP) bioprinting can achieve around 100 nm lateral resolution, while microscale digital light processing (DLP)-based bioprinting offers a faster and precise alternative [102,103]. Moreover, the availability of

3D imaging techniques such as magnetic resonance imaging (MRI) and computed tomography (CT) have helped computer-aided design (CAD) to create more precise 3D reproductions of lesion cavities [104]. Koffler et al. in 2019, used magnetic resonance images of spinal injury to reconstruct in CAD and 3D print a biomimetic hydrogel scaffold. The resulting prosthesis, loaded with neural progenitor cells (NPCs), was implanted in the severed spinal cord of a rodent to restore synaptic transmission and locomotion [55].

Together with the geometrical parameters, implantable scaffolds to approach neurological disorders are commonly required to be electrically conductive for obvious reasons. Nanostructured materials have been broadly used to implantable electrodes design for either neural activity recording or stimulation. Carbon-based nanomaterials are one of the most promising in the field thanks to their high surface area, electrical conductivity and toughness [105]. Moreover, the outstanding physical properties of carbon nanotubes (CNTs) and graphene are combined with an intimate coupling between neuronal networks and these materials [106–110]. A particular attention has also been devoted to conductive polymers (CPs) which usually show very low tissue reactivity and appropriate mechanical properties in relation to nervous tissue [111]. Intrinsically CPs, such as poly(3,4-ethylenedioxythiophene) (PEDOT) and polypyrrole (PPy), tissue response and neural activity recording have been studied *in vivo* [112–115]. These polymers are often doped to tune their electrical conductivity along with their surface and mechanical properties [116]. Biomimetic molecules such as specific ECM components, can be included during the polymerization process either covalently, resulting in copolymers formation, or non-covalently, providing the implant with molecules of interest that can be subsequently released in the biological milieu [111]. The

doping paradigm has been further extended to achieve a next generation of biodegradable electrically conductive polymers (BECP) through either the inclusion of ester linkers within the electroactive oligomers or by electroactive macromonomers assembly, to create block copolymers and graft copolymers [117,118]. Overall, the synergistic collaboration among electronic engineering, material science and nervous system physiology is supporting the world of neuro-nanotechnology towards the development of various tools with astounding fallouts to basic research, diagnostics and therapeutics. The future aim of all these developments is to integrate all these features with an unprecedented level of targeting, developing patient-specific solutions for several CNS disorders.



### 1.3 Topographical cues of implantable devices

As summarized above, physical and chemical properties of materials composing an implantable device play a pivotal role in determining tissue integration, device durability and its functioning. In the last three decades, a particular attention has been also devoted to relatively recent observations indicating that certain cell behavior might be elicited by topographical modification of surfaces contacting biological tissues.

The very first report of “*paths of predilection*” during nerve cells development dates back to the early nineteenth hundreds in the comparative anatomy essay of Prof. Ross G. Harrison on tissue morphogenesis [119]. The observed response of an organism upon a physical contact stimulus was therefore classified under the definitions of thigmotaxis or stereotropism and eventually further studies confirmed this behavior growing neuronal cells onto various patterned materials [120]. Studies on stereotropism soon extended to several biomedical fields showing this process to be relevant not only during tissue development, but also during tissue repair and regeneration, either in physiological or pathological conditions [121–123]. Within the CNS, glial cells as well as the ECM were shown to provide geometrical support for neuronal guidance, both *in vivo* and *in vitro* [124,125]. These evidences resulted in the emergence of mechanobiology, a novel field studying the conversion of mechanical forces into biochemical signals. In last years, the molecular machinery responsible for cellular mechanotransduction has been studied and major players have been identified. Cadherins/catenins-dependent adherent junctions (aj) and integrin/focal adhesion kinase (FAK)-based focal adhesions (fa) stabilize respectively, cell-cell and cell-ECM interactions, anchoring to the cytoskeletal f-actin (**Figure 5**) [126]. Both cadherins/catenins and integrins/FAK

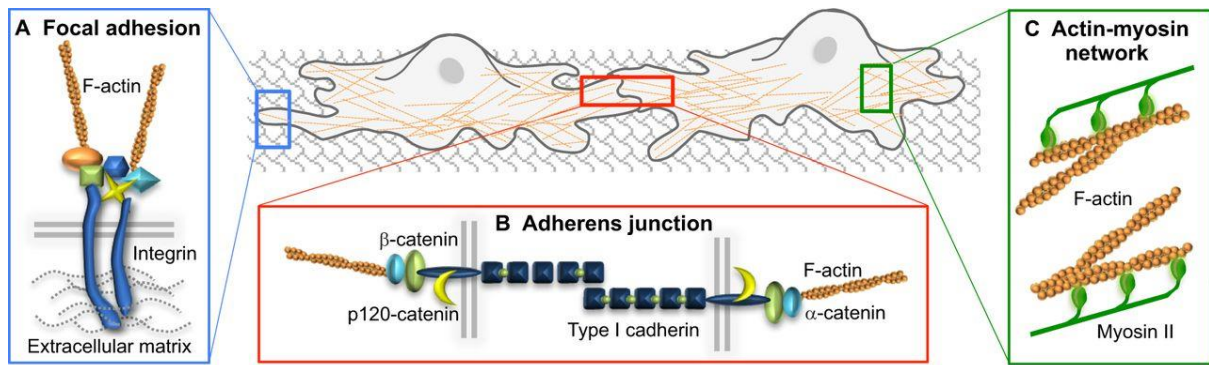


**Figure 5.** Representation of the front line mechano-sensing pathways of the cell [126]. **A.** Cells tethering to ECM is ensured by focal adhesions, relying on integrins-actin complexes. **B.** Mechanical information between adjacent cells is relayed by adherens junctions involving cadherins signaling to cytoskeletal actin. **C.** Contractile actin–myosin network traduces integrins and cadherins cues in tensional changes, thereby interlinking the two pathways.

signaling cascades can activate upon appropriate stimuli the Rho family of GTPases (Rho, Rac and Cdc42) to regulate stress fiber formation and cell contraction (Rho) and the formation of lamellipodia and filopodia (Rac and Cdc42, respectively) or promote protrusive behavior [127]. Rho GTPases subsequently activate an intracellular cascade through Rho-associated kinases (ROCK) to phosphorylate, for instance, the myosin light chain (MLC) and allow actin binding to myosin II, thus increasing contractility. Further protein phosphorylation by other kinases (such as Src, PAK and LIMK) create docking site for additional structural proteins such as vinculin, paxillin, cofilin and talin, thereby regulating cytoskeleton strengthening/softening and actin assembly/disassembly [127–129]. Moreover, these downstream signaling result in the crosstalk with Wnt/ $\beta$ -catenin and YAP/TAZ pathways, which impact cell fate, proliferation, tissue regeneration and tissue morphogenesis [123,130]. Interestingly, cell adhesion molecules (CAMs) including cadherin/catenin and FAK/integrins but also nectins, neurexin-neuroligin and ephrins are fundamental for synaptic stabilization as they have been shown to play important role in memory, learning and plasticity [131–134]. Evidences were also provided for CAMs direct binding to  $\alpha$ -amino-3-hydroxy-5-

methyl-4-isoxazolepropionic acid (AMPA) and  $\gamma$ -aminobutyric acid (GABA<sub>A</sub>) receptors and the control of their expression/trafficking at the synapses, supporting the idea that topographical information can modulate neuronal activity [135–138]. In addition, transcriptomic profiling of neurons interfacing nanopatterns has revealed higher expressions of synaptic regulation- and synaptogenesis-related genes compared to isolated neurons with no topographic bias; surprisingly such up-regulated expression profile matched that of interconnected neuronal network [139].

All these knowledges converged to the intuition that, surfaces micro- and nano-patterning might be exploited not only to promote morphological and developmental responses at the nervous tissue interface, but also to target network physiology and functioning. Nowadays topography is recognized as a potential tool to ameliorate implant integration within the nervous tissue and several studies are trying to classify shape, size and stiffness signals according to the elicited cell behavior [140–143]. Indeed, micro and nanostructures are primarily distinguished for their topographical anisotropy (e.g. grooves, fibers) or isotropy (e.g. pillars, holes) which lead to different neuronal responses [122,141]. For instance, grooved substrata have been reported to promote either parallel or perpendicular contact guidance depending on pattern size and neuronal type. Primary spinal neurons polarize preferably parallel to grooves as wide as 1-4  $\mu$ m in a range of grooves depth, while primary hippocampal neurons on the same patterns showed a more variable response, but seemed to favor perpendicular guidance and smallest grooves [144]. Other studies focused on pillars highlighted the importance of these structures in determining primary hippocampal neurons polarization and their ability to enhance neurite length and axonal collateral branches formation compared to flat surfaces [145,146]. Focal adhesion signaling was recognized

as a fundamental character in pillars-mediated neuronal polarization, tyrosine phosphorylation was enhanced at the pillar contact point and it colocalized with F-actin patches and paxillin to recruit N-cadherins clustering, thereby initiating axonal sprouting onto pillar tips [147]. By studying competition between topographic and chemorepulsive cues, the same group shown that optimal pillars spacing signals are sufficient to overcome Semaphorin3A (Sema3A)-mediated repulsion of neurite outgrowth [148]. In the last decade a particular attention has been devoted also to carbon nanotubes (CNTs) and carbon nanofibers (CNFs), thanks to their reported ability to enhance neurite outgrowth and functional reconnection after lesion in CNS organ slice cultures (**Figure 6**) [106,149–151]. Carbon nanomaterials-based substrates usually result in a dense and intricate mesh of nanometric structures able to electrically and mechanically couple neuronal tissues. By consequence several groups have been addressing patterned surfaces decoration with CNTs and CNFs to integrate material electrical properties and nanometric feature size with microtopographical guidance [152–154]. As expected, among CNS cells, neurons are not the sole cell type responding to geometrical cues. Evidences of astroglial cells morphological changes and reduced adhesion in response to surface micro-patterning have been provided [155,156]. Interestingly, cultures of cortical astrocytes onto grooved polymethylmethacrylate (PMMA) were found to develop into radial glia-like cells with a pro-regenerative phenotype [157]. Erkin Seker's group extensively studied cortical primary cultures adhesion onto nanoporous (np-Au) *versus* planar gold (pl-Au) showing that focal adhesion formation can be controlled in a feature size-dependent manner. They reported a significant reduction in astrocytes surface coverage onto np-Au with no effect on neuronal adhesion, suggesting that underlying mechanisms are cell-type specific [158]. Adhesion strength lowering correlated with reduced area, but increased

number, of astrocytic focal adhesions onto nanostructured gold [159,160]. Similar findings were reported after PEDOT:PTS micropatterning and in addition to increase neuron-to-glia ratios, attenuated gliotic response was observed by proinflammatory cytokines and chemokine factor profiling *in vitro* [161]. Indeed, microglia too can respond to topographical stimuli by morphological adaptation and specific cytokines secretion [162,163]. Surprisingly, microglia-dependent multinucleated giant cells (MGCs) formation and myelin phagocytosis were hampered onto PCL-based electrospun fibers compared to solvent casted planar films [163]. It is pertinent to mention oligodendrocytes and their precursors (OPCs). Topography and stiffness of the extracellular environment can impact OPCs and oligodendrocytes differentiation and guidance through mechanotransduction signaling pathways [164,165]. Moreover, micro- and nanofibers have been used to study myelination process in neuron-free cultures, highlighting oligodendrocytes ability to enwrap artificial fibers even in the absence of chemical cues just by defined size threshold recognition [166].

To stress the concept of topographical cues relevance in implant manufacturing for neurology, it suffice to think about the frequent requirement of electrode insertion within the nervous tissue. Such procedure implicates tissue damage and results in a series of tissue reactions leading to glial cells activation [50,167]. A potential consequence is represented by the formation of a fibrotic glial scar wrapped around the implanted electrode, increasing the impedance and progressively reducing the signal-to-noise ratio (SNR), thus worsening neural stimulation and recording [168,169]. As described before, topographical modification can be exploited to reduced undesired glial reactions and overcome such drawbacks.

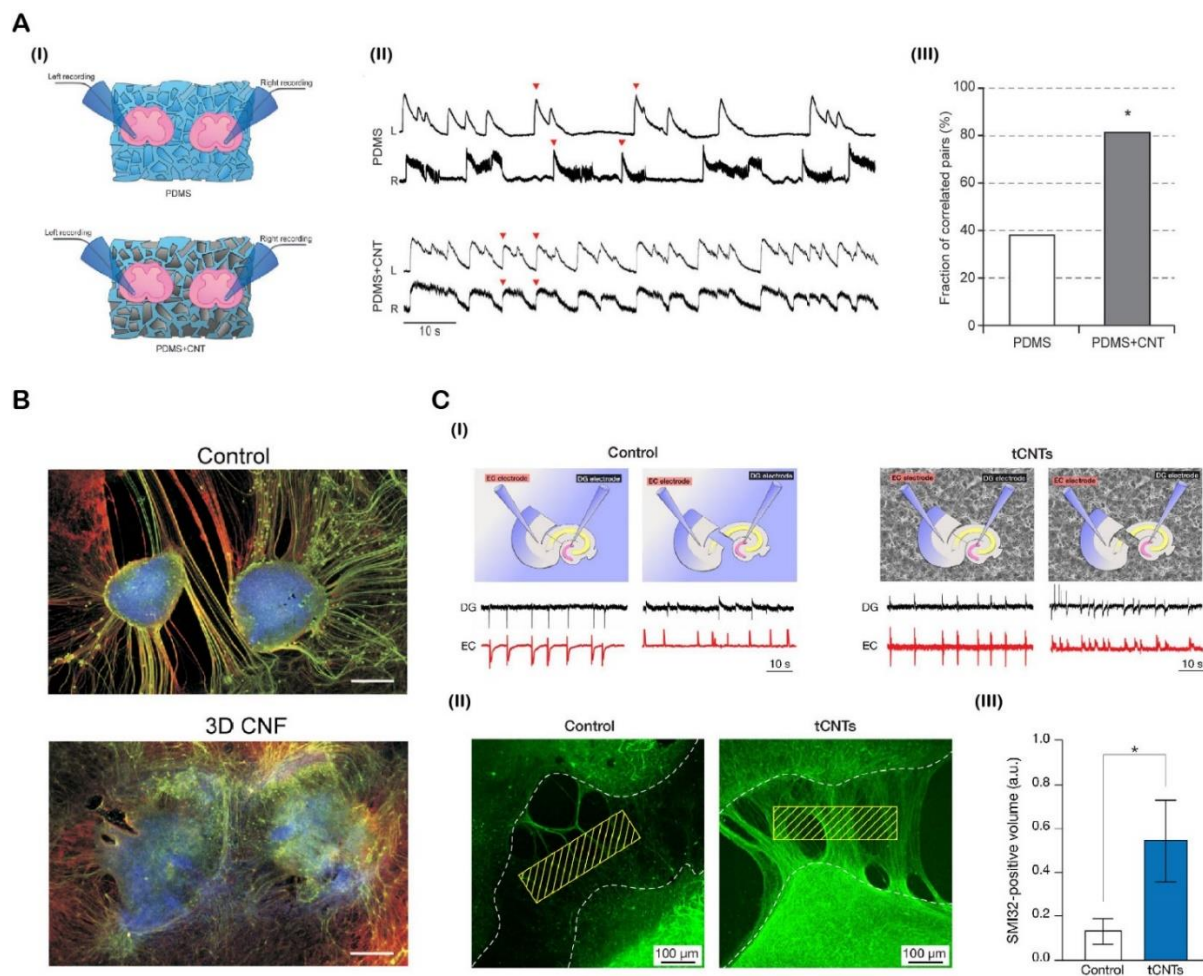


**Figure 6.** Carbon nanomaterials -interfaced CNS organotypic slice cultures. **A.** (I) Two spinal cord/DRG organotypic slices were co-cultured onto PDMS and PDMS-CNTs 3D scaffolds. Extracellular field potential paired recording from the premotor region in the ventral zone was used to study functional reconnection between tissues. (II) Representative voltage traces of each condition highlighted a greater electrophysiological signal synchronization (red arrows) and increased communication between slice pairs developed on PDMS-CNTs. (III) The extent of synchronization was estimated through cross-correlation analysis and plotted as percentage of correlated pairs of slices [150]. **B.** Spinal cord/DRG paired slice cultures were plated onto control glass coverslips (top) and 3D CNFs (bottom). After 14 days *in vitro* (DIV) immunolabeling of neuronal microtubules ( $\beta$ -tubulin III; red), motoneuronal neurofilament H (SMI-32; green), and total nuclei [4',6-diamidino-2-phenylindole (DAPI); blue], revealed diffuse fibers sprouting towards the neighboring slice on 3D CNFs (scale bars = 500  $\mu\text{m}$ ) [149]. **C.** (I) An organotypic culture model of lesion where the main excitatory entorhinal input to hippocampal dentate gyrus (DG) can be studied was interfaced to flat glass coverslips (control, top left sketch) and transparent CNTs carpets (tCNTs, top right sketch). Local field potential co-recording from entorhinal cortex (EC, red traces) and DG (black traces) served to monitor electrophysiological entorhino-hippocampal communication through the performant pathway (PP). Maximal signals synchronization between EC and DG electrodes was always observed before PP transection either in control or tCNTs groups. Synchronization dropped dramatically in lesioned slices grown for 8 DIV onto control glass, whereas it was totally recovered in lesioned slices developed in contact with tCNTs (see representative traces). (II) Immunolabeling of neurofilament H (SMI-32; green) displayed a tremendous fiber regrowth across the transected area onto tCNTs compared to glass control [151]. (III) The volume of SMI-32-positive projections was estimated by confocal reconstruction at the lesion site confirming electrophysiological recording data [151].



## 2. Electrical recording and stimulation of excitable tissues

### 2.1 Advances in electrode design

Neural recording and stimulation have been representing two crucial tools for the study and the comprehension of neurophysiological processes [170]. The firsts evidence of bioelectricity controlling body functions dates back to the second half of the 18<sup>th</sup> century (A.D.) thanks to the electrophysiological studies of Luigi Galvani and his wife Lucia Galeazzi on *ex vivo* frog neuromuscular preparations. Their observations were directly linked to the possibility of stimulating the frog sciatic nerve, resulting in muscle contraction and leg motion, using electrical charge stored in a *Leyden jar* (the oldest electrostatic capacitor) [171]. At that epoch instrumentations and skepticism represented the major limits, but between 1830 - 1844 Carlo Matteucci provided further evidences of the biological origin of electric nervous signals measuring physiological currents in various experimental configurations with the astatic galvanometer developed about a decade earlier by Leopoldo Nobili (which also performed the first electrophysiological recording although misinterpreting it) [172-174]. Hermann von Helmholtz first tried to measure the speed of nerve impulse, but for a more precise estimate his assistant Julius Bernstein invented the “differential rheotome”, a device enabling to sample signals at 10 - 20 kHz rate [175]. In such a way, they provided for the first time an accurate measurement of the nerve resting potential, action potential kinetics and conduction velocity [176]. In the same years, Richard Caton recorded the first electroencephalogram (EEG) from mammal scalps using a Thomson’s mirror galvanometer, also discovering that cerebral potentials could be evoked by sensory stimulation [177]. This factual framework definitely laid the foundations for electrophysiology research take-off. Along with the advances in instrumentation development, at the beginning of the XX century electrodes design

innovation played a pivotal role in the progression of this discipline. Great improvements were initially made possible by the introduction of heat-pulled glass microelectrodes, which were first reported in 1919 for extracellular focal stimulation and subsequently applied to intracellular and extracellular recordings by the half of the century [178–180]. Glass micropipettes filled with proper electrolyte and connected to the amplifier input *via* platinum or Ag/AgCl wires soon became the gold standard for *in vitro* electrophysiology research. Some explanations for their extensive application are of course their ease of preparation and their versatility in terms of electrical resistance, allowing to record extracellularly single-units, population spikes and field potentials, to probe intracellularly single-neurons activity and later to investigate single-channels properties by patch-clamp methods [181–183]. In accordance with the aims of this thesis, focused on implantable neuroprosthetic devices, I will address exclusively extracellular approaches. Indeed, glass micropipettes have represented an important tool to monitor either single-units or the collective behavior of multiple neurons from the extracellular milieu in animal models *in vivo*, but the improvements in metal electrodes manufacturing from the second half of the XX century led back to a material-based approach [184–186]. Simple protocols for the insulation/coating of various metals (e.g. tungsten, platinum, stainless steel, iridium, Elgiloy™), resulted in manufacturing sharp, low-noise microelectrodes (particularly in the 1 - 2 kHz frequency range) with appropriate stiffness/rigidity for meningeal barriers and neural tissue penetration [187–191]. More importantly, the mechanical properties of metal electrodes favored also the early introduction of microwires for chronic recordings in freely moving animals [192]. As semiconductor microfabrication strategies rapidly evolved from 1980s, also silicon-based multielectrode arrays (MEAs) such as Utah and Michigan probes came into play [193–195] (**Figure 7A, B**). Soon, these designs were



implemented with integrated active electronics prompted by advancements in complementary metal-oxide semiconductor (CMOS), printed-circuit technologies and microelectromechanical systems (MEMS), allowing a dramatic size reduction of neural probes or inspiring the further development of sophisticated multifunctional microelectrodes <sup>[196–198]</sup> (**Figure 7C**). The use of transistors was fundamental in this process, providing the tools to increase the density of MEAs by multiplexing read out lines, to amplify signals at the electrode-tissue interface and to minimize power-consumption required for logic operations, without impacting device size <sup>[199–202]</sup>. Even though, the need for non-penetrating probes to reduce invasiveness and improve the chronic performance of implanted device became relevant. On one hand, cortical, epidural and subdural arrays for the CNS were made possible with the introduction of polymeric coatings of electronics and all-polymer electrodes <sup>[203]</sup> (**Figure 7D**). On the other hand, PNS probes evolved from invasive intrafascicular nerve electrodes to non-penetrating cuff electrodes <sup>[204–207]</sup> (**Figure 7E**). Anyway, these solutions often represent a compromise in terms of reduced specificity towards target neurons. Despite the stunning progresses in implantable electrodes technology in the last decades, issues still remain; of major concern are the foreign body response (FBR) together with the mismatch between material and neural tissue.

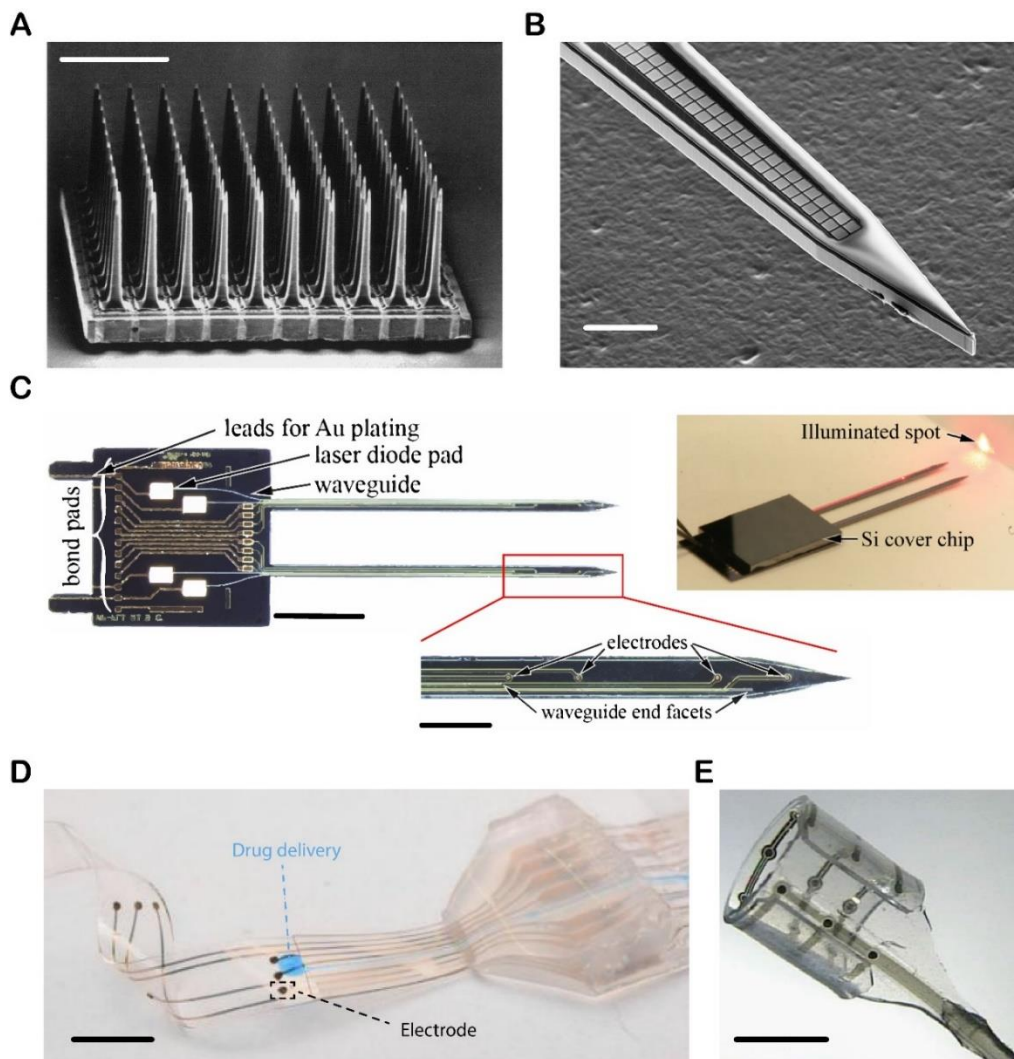


**Figure 7.** Novel electrodes for recording and stimulation. **A.** SEM image of the 100 microelectrodes Utah electrode array (UEA) developed by Normann *et al.* 1999 for cortical vision prosthesis (scale bar = 1 mm). **B.** Michigan-type probe composed by 200 channels of close-packed silicon microelectrodes designed by Scholvin *et al.* 2016 (scale bar = 50  $\mu\text{m}$ ). **C.** Optical micrographs of two-shank silicon optrode fabricated by Schwaerzle *et al.* 2013 including laser diode chips and waveguides for optogenetic stimulation and platinum electrodes for neural activity recording (from left to right, scale bars = 2 mm, 500  $\mu\text{m}$ ). **D.** Optical image of the electronic dura mater (e-dura) designed by Minev *et al.* 2015 for spinal cord injury non-invasive application. It combines silicone-embedded electrodes, chemotrodes and microfluidics to perform both electrical and chemical stimulations (scale bar = 3 mm). **E.** Illustration of the multipolar cuff electrode conceived by Prof. Hoffmann group at the Fraunhofer IBMT. Ramachandran *et al.* 2005 integrated the technology with pre-amplifier and filter at the electrode site (scale bar = 500  $\mu\text{m}$ ).

The two phenomena are strictly interconnected and can be overall reconducted to (1) chemical, (2) biological and (3) mechanical origins [208]. (1) When an electrode is placed in the nervous tissue is by consequence submerged in an electrolyte, i.e. the cerebrospinal fluid (CSF) or more in general the extracellular *milieu*. This event enhances redox reactions potentially leading to corrosion, delamination, or progressive deterioration of coatings [196] (**Figure 8A**). Importantly, electrode insertion inevitably leads to BBB impairment, provoking vascular disruption with prominent release of iron, which in turns promotes Fenton's reactions known to increase oxidative damage [209,210]. Moreover, events such as biofouling, resulting from the absorption of biological material can further compromise electrode stability [211,212]. (2) The lasts two scenarios can be somehow reconducted to a biological origin even if the consequent electrode impairment is actually driven by chemical reactions. Along with the afore-described effects, tissue penetration by a foreign body severs the tissue integrity. Tissue reactivity activate microglia and astrocytes, with increased proliferation and changes in their morphologies, ultimately resulting in electrode encapsulation by a fibrotic/gliotic scar [50,168,208] (**Figure 8B**). (3) The mechanical mismatch caused by elasticity differences between most materials (Young's modulus in the GPa range) and the soft brain tissue (Young's modulus kPa), is chronically

observed during micromotions of implanted electrodes [186,213,214] (**Figure 8C**). This persistent tissue stress enhances neuroglial activation and foreign body reaction [208].

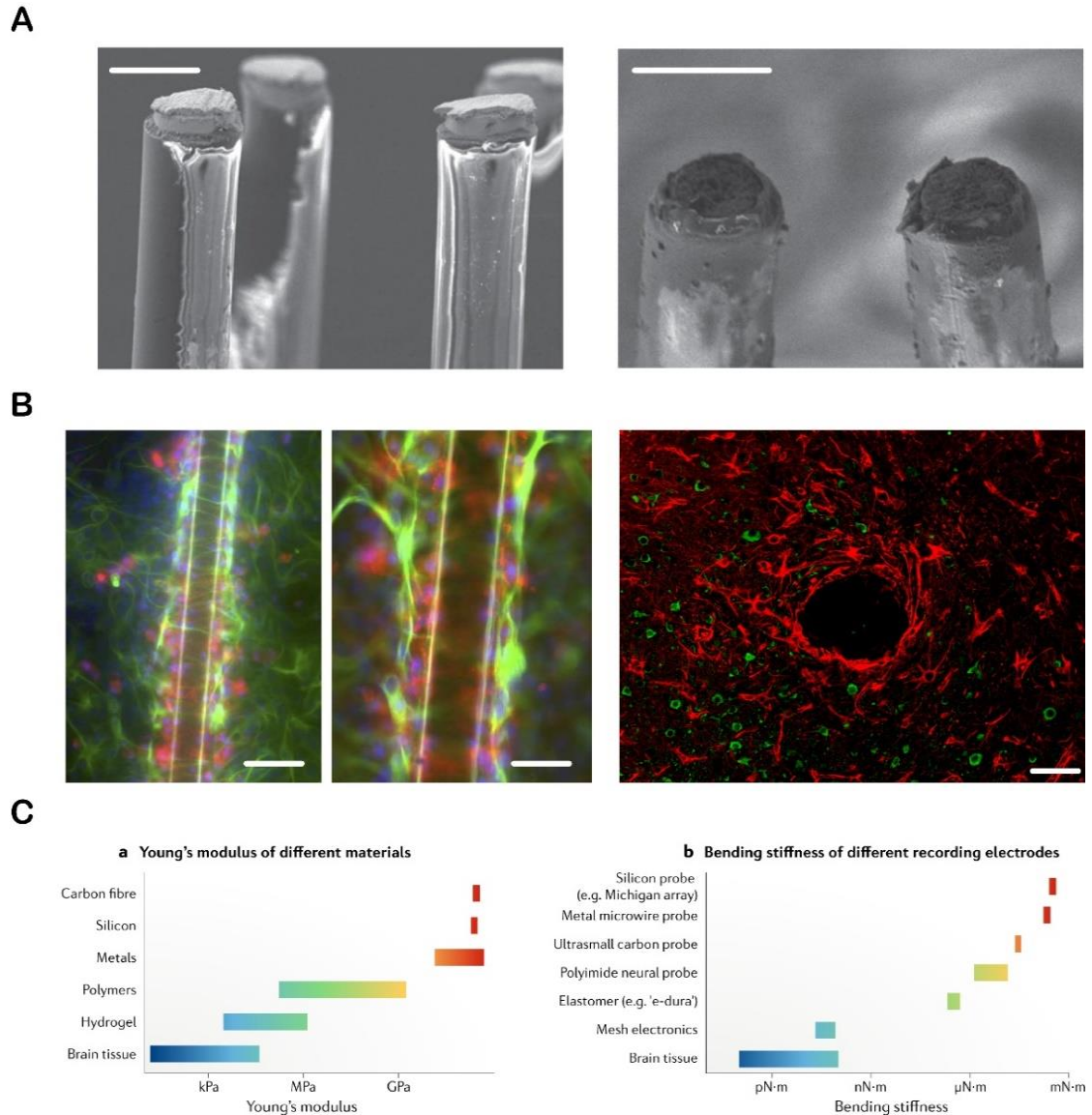


**Figure 8.** The material mismatch issue. **A.** SEM of polyimide-coated tungsten microelectrodes pre-implantation (left) and post-implantation (7 days, right). Tip darkening and reduced volume represent signs of corrosion (scale bars = 50  $\mu\text{m}$ ). Idil and Donaldson 2018 reviewed the oxidizing effects of human physiological environment against tungsten. **B.** Polikov *et al.* 2006, proposed an *in vitro* model to study glial scarring of neural electrodes (left and middle). Their fluorescent micrographs display astrocytic (green) and microglial (red) cells wrapping up microwire electrodes after 10 DIV (scale bars = 100 and 50  $\mu\text{m}$  respectively). On the right, a similar result after chronic MEA implantation in the rabbit cortex is reported by Marin and Fernandez 2010. Astrocytes (red) are densely packed around electrode track while neuronal nuclei (green) remain apart (scale bar = 50  $\mu\text{m}$ ). **C.** Two intuitive charts, reproduced from Hong and Lieber 2019, show the tremendous differences of elastic moduli and bending stiffness among most materials and brain tissue, highlighting the potential of hydrogels, polymers and mesh electronics for novel neural technology development.

All together, these events seriously compromise chronic recording and stimulating capabilities, usually by increasing electrode impedance thus reducing the charge transfer at the electrode-electrolyte interface (EEI) [215]. Chemical and biological responses against implanted devices can be fairly contained by surface functionalization through bioactive/biomimetic molecules, drugs or inert materials, used as protective coatings [208,210,216,217]. The introduction of highly corrosion resistant materials, such as amorphous silicon carbide, represented an alternative and valid strategy [218–220]. Comparably, surface topographical and geometrical modifications, together with electrodes size reduction, also are extensively adopted methods to limit protein absorption and biofouling [221,222]. As mentioned in the section 1.3 “*Topographical cues of implantable devices*”, micro- and nano-topography have been used to reduce glial adhesion and reactivity, and a size range of the probes exists to elude FBR [161,208]. To face the mechanical mismatch instead, the bending stiffness is often addressed through shank probes thinning, to reduce rigidity during micromotion and ameliorate compatibility [196,197]. The choice of new materials mechanically compliant with the nervous tissue is also important, liquid crystal polymers (LCP), conductive polymers and polymers composite became a trend for implant design [203,223–225]. Either flexible or rigid organic field-effect transistors (OFET) for high SNR ( $\geq 20$  dB) recordings and stimulation were developed for both *in vitro* and *in vivo* applications [201,226,227]. Conductive hydrogels electrodes have also been explored with successful results [228,229]. Other promising achievements have been reached by Charles Lieber’s group, which proposed in the last years syringe-injectable mesh electronics for chronic implant design [230–232]. To conclude, interesting overviews of new technologies recently provided by Polina Anikeeva and collaborators, included microfluidic- , optogenetic- and ultrasound-based probes to address neural behavior [196,198]; a

particular mention is reserved to the research made towards magnetic sensors for completely non-invasive recording of neurophysiological activity, which might represent an unprecedented breakthrough in neuroprosthetic [233–235].



## 2.2 Potential of electrical stimulation in biomedicine: electroceuticals

The presence of CNS physical barriers complicates the delivery of several chemical compounds for therapeutic purposes and at the same time, it limits to a certain extent the use of body fluids-based diagnostic tests to enquire into CNS health state (nevertheless important advancements have been done also in this field) [236,237]. Thus, provided that diagnosis and treatment of several neurological disorders can be tackled from an electronic perspective, neurobiology may benefit from nanomaterials and nanotechnologies to design new approaches [81,238]. Importantly, not only the CNS, but essentially all organs and body functions are regulated through neuronal circuitry, namely by the autonomic nervous system (ANS), divided in sympathetic and parasympathetic nervous systems (thoracolumbar and craniosacral outflows respectively; **Figure 9**) [239]. Therefore, intercepting these axes at the nerve fibers level could be exploited also for therapeutic intervention of homeostatic, metabolic, and

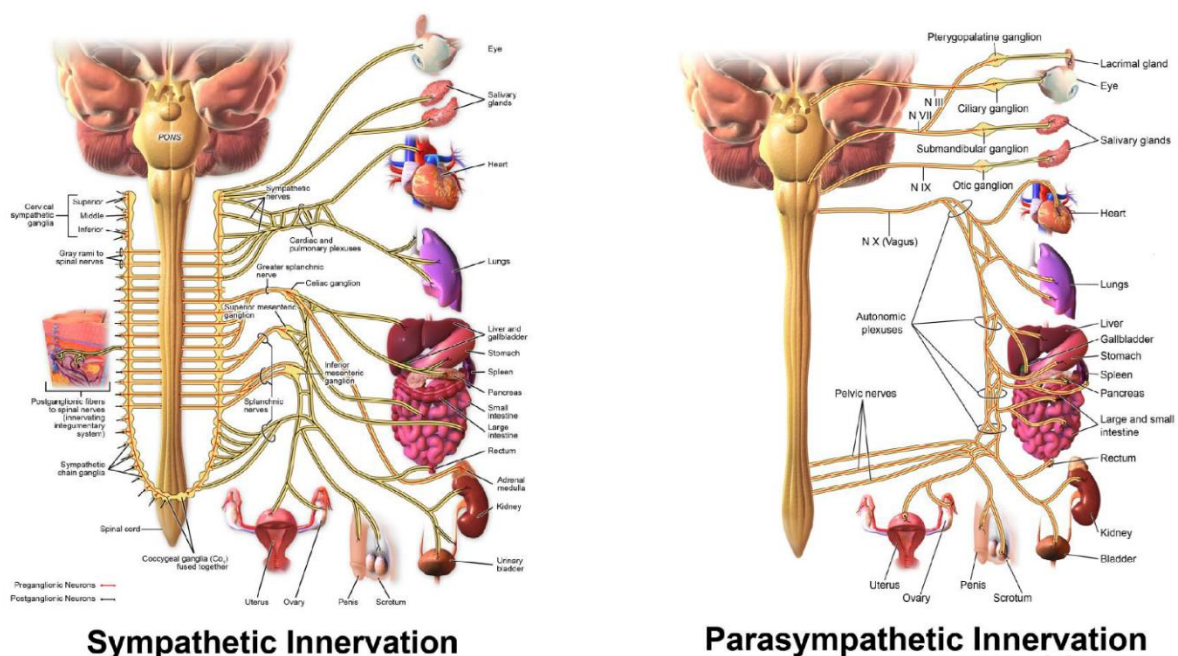


**Figure 9.** Organs innervation by the autonomic nervous system (ANS). Not only the CNS, but also the PNS is increasingly considered as a potential target for neurological and non-neurological diseases. *Sketch by Phillip Low, MD* (<https://www.merckmanuals.com>).

endocrine disorders. Moreover, pharmacodynamics and pharmacokinetics of existing drugs display a dramatic interpersonal variability due to genetic polymorphisms among populations, complicating the design of treatments [240,241]. This drawback might be overcome, in some cases, by electrical stimulating approaches acting on nerves or excitable targets, where responses are mediated by patterns of action potentials that can be reshaped to elicit healing effects.

As a matter of fact, electrical stimulation has long been identified as a precious tool for several conditions. Historically, Scribonius Largus (1 - 50 A.D.) was likely the first physician proposing, in his *Compositiones medicamentorum*, the electrotherapy to relieve headache and gout pain by using the shock of a torpedo ray; eventually such healing effects were further investigated and extended to other conditions [242]. To date, the most familiar electrical stimulators are probably the artificial cardiac pacemakers, introduced as early as 1932 and having since then experienced a continuous evolution with a tremendous impact in patients' life expectancy [243]. Likewise, also non-fatal conditions such as deafness and blindness took advantage of the technological progress in sensory deficits restoration through cochlear implants and visual prosthesis [244-246]. By the end of the XX century, deep brain stimulation (DBS) was approved for Parkinson's disease cognitive and motor symptoms relief, and subsequently it went to trial for other neurological and neuropsychiatric disorders, including epilepsy [247,248]. Interestingly, closed-loop electrical modulation/recording approaches have recently provided a relevant contribution to spinal cord injury (SCI) neurorehabilitation [249,250]. Epidural electrical stimulation was proven to induce rhythmic hindlimb movements in animals, leading to partial recovery of locomotion [251,252] and strong evidences support spinal cord stimulation efficacy in chronic pain treatment [253,254]. Indeed, in the last



decade, governments, academia and industries increasingly invested in the development of therapies exploiting electrical stimuli delivery to excitable tissues [255,256]. A number of electroceutical products were recently developed, entered clinical trials, and reached the market after governmental approval (**Table 1**). Among the different stimulation targets, vagus nerve has been successfully addressed and thus far represents the most successful in several conditions. Hence, a rationale is required to construct appropriate solutions [257]. Since the very end of the XX century, vagus nerve stimulation (VNS) was shown to be an effective treatment for epilepsy, but researches on the exact mechanisms are still ongoing [258–260]. A remarkable role in the field of vagal axis physiology has been fulfilled by Kevin J. Tracey and collaborators which showed how VNS attenuates tumor necrosis factor  $\alpha$  (TNF $\alpha$ ), interleukin 6 (IL-6) and others pro-inflammatory cytokines release from macrophages acting on  $\alpha 7$  nicotinic receptor, thus preventing a wide range of inflammatory diseases [261,262]. The so called “cholinergic anti-inflammatory pathway” can be recruited by electroceutical stimulators for therapeutic purposes in the case of rheumatoid arthritis and Chron’s disease, and further solutions will be available also for acute inflammatory conditions (*e.g.* septic shocks) [263–265]. Comparably, studies have described that ANS neuromodulation could be an effective solution for gastrointestinal and eating disorders [266]. In a recent work of Guyot *et al.* targeted with micro-cuff electrodes the proximal sympathetic efferent to the pancreatic draining lymph nodes to prevent T cells-mediated autoimmune diabetes progression in mice, paving the way for new therapeutic solutions for type 1 diabetes [267]. Ascending sympathetic pathways to the pineal gland were also modulated by electrical stimulation of ascending superior cervical ganglia to foster N-acetyl serotonin and melatonin levels, for neuroprotection in circadian rhythm disorders [268]. A number of *in vitro* studies are contributing to

Device	Company	Target	Condition
aura6000™	ImThera (LivaNova)	hypoglossal nerve	obstructive sleep apnea
Axonics®	Axonics	sacral nerve	bladder and bowel disfunctions
gammaCore™	electroCore	vagus nerve	cluster headache
IB-Stim™	IB-Stim	cranial/occipital nerves	abdominal pain, irritable bowel syndrome
L300™/H200™	Bioness	limbs/hand	rehabilitation and regain of motor functions
Monarch eTNS®	NeuroSigma	trigeminal nerve	attention deficit hyperactivity disorder
Omnia™	NEVRO	spinal cord	chronic back pain
SenTiva®	LivaNova	vagus nerve	drug-resistant epilepsy
StimRouter™	Bioness	peripheral nerves	chronic pain, bladder and bowel disfunctions
Symmetry™	LivaNova	vagus nerve	drug-resistant depression

**Table 1.** List of some electroceutical devices present in the market. To date the Food and Drug Administration (FDA) approved several electrical protocols for the treatment of mild and severe disturbs and the European Medicines Agency (EMA) is aligning to this trend.

characterize electrophysiological and molecular responses to various electrical stimulation protocols, to address nerve remyelination, tissues regeneration, cell differentiation and immunomodulation [269–271]. Therapeutics is looking forward to new strategies that would adapt to impairing conditions where surgical or pharmaceutical approaches failed, and electronic medicine seems to be an optimal candidate to tackle this challenge.

In the digital era, electroceuticals will also result in multifaceted devices enabling continuous monitoring of physiological parameters that could be directly accessed by the specialized physician to provide patient surveillance on a daily basis; remote device control will be feasible and closed-loop neuromodulation systems could be tuned *ad-hoc* in real-time [272]. Limitations of course exist also for electroceuticals: CNS mapping

remains a challenge that deals with the ability to individually address bunch of neurons within specific regions in a durable and reliable way and with minimal invasiveness; to avoid cross-talks with nearby regulatory loops, several physiopathological mechanisms still need to be fully dissected.

### 3. In vitro approaches to nanomaterials and device testing

#### 3.1 Dissociated cultures

Throughout the 19<sup>th</sup> century it was widely agreed that all organisms with their organs and tissues were composed by cells [273]. Nevertheless, according to the *reticular theory* supported also by Camillo Golgi the brain was thought as an exception and it was described as a single continuous network. Santiago Ramón y Cajal, who refined the histological techniques of the epoch developed right by Golgi, suggested that individual neurons form a contiguous network (at the synapse level), arising the so-called *neuron doctrine* [274]. In such a disputed scenario, Prof. Ross G. Harrison attempting to support the *neuron doctrine*, produced the first (“hanging drop”) neural cultures where he observed neurites outgrowth from neuronal somata [275]. The comprehension that neuronal cells and network can be developed and studied in culture prompt the design of new tools to grow cells and tissues *in vitro* [276,277].

Since their earliest years, long-term culture preparation from dissociated tissues were recognized as a crucial tool to dissect at the cellular level basic mechanisms inherent to various physiological and biomedical issues [278]. A large amount of work was made to optimize growth conditions and maintenance, providing standardized protocols to favor reproducibility and comparability [279–282]. Remarkably, neurospheres introduced by Reynolds and Weiss in 1992 allowed cells passaging by continuous and symmetrical division of a stable niche of multipotent cells. The resulting neural progenitor cells which can be stored after freezing and expanded in culture, provided a valuable tool to abate animal use in neurobiology research [283–285]. A comparable impact was produced by the introduction of novel immortalization protocols, such as telomerase gene overexpression and induced pluripotent stem cells (iPSC) technology,

which permitted also human biopsied cells to be studied long-term after *in vitro* development [286–288]. Nonetheless, genetic and epigenetic stability can be seriously compromised in the aforementioned models and therefore primary cultures with defined genetic background are often preferred [289,290]. Dissociated cultures from various rodent CNS regions of late embryonic or newborn pups have been extensively studied and embody to date the benchmark to compare physiological and biophysical properties of single neurons and networks during development [291,292]. Certainly, neurodegeneration and neural tissue regeneration represent two major topics in neurobiology, which features can be faithfully reproduced *in vitro* (**Figure 10A**) [269,293,294]. Events such as synaptogenesis and plasticity are easily and reliably observed through electrophysiological means or fluorescence microscopy in developing neuronal cultures (**Figure 10B**) [295–298].

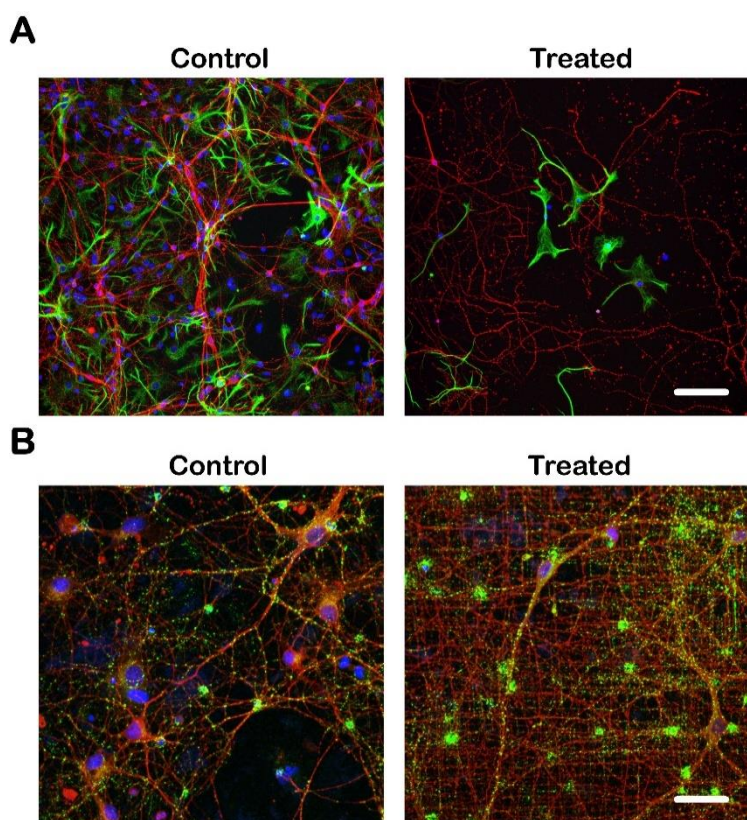


**Figure 10.** Immunofluorescence on primary hippocampal cultures. **A.** Neuronal damage upon non-biocompatible metallic nanostructures exposure (right) can be easily observed *in vitro*. Primary dissociated cultures represent the first line screening for safe biomaterial identification (scale bar = 60  $\mu\text{m}$ ). **B.** Nanopatterned electrodes surfaces (right) are able to promote neurite elongation and synapse formation compared to flat surfaces (left) as shown by the greater neuronal processes (red) and synaptic protein clusters (green) densities (scale bar = 25  $\mu\text{m}$ ).

Noticeably, also the design of safe and targeted neurostimulation protocols has benefited of fundamental observations in primary dissociated cultures [299,300]. Stern and colleagues for example studied the chronaxie of cultured hippocampal neurons grown in oriented patterns; network pharmacology and rotating electric field application were used to derive the strength-duration curves and led to the observation that, given their lower rheobase with a slightly higher chronaxie, dendrites could be a more suitable target for action potential stimulation compared to axons which require higher currents [301]. Also, exogenous electric fields are known to be effective, under certain circumstances, in promoting fiber regrowth and remyelination of impaired peripheral and central nerves, and co-cultures of primary dorsal root ganglia (DRG) and oligodendrocytes / Schwann cells were essential to elucidate the molecular mechanisms underlying such processes [269,270,302,303]. Ishibashi and co-workers shed light on the phenomenon demonstrating that as a result of electrical stimulation, the ATP released from the axons of an excited neuron activates purinergic (P2) receptors on astrocytes thereby promoting the release of the cytokine LIF (leukemia inhibitory factor) which in turn, acting on mature oligodendrocytes, promote dorsal root fibers remyelination [304]. As in the latter case, the combination of different primary cells in co-culture has been exploited to gain insight on the contribution of the various cell-types to physiological and pathophysiological processes within the neural tissue. From such studies emerged that support cells are crucial characters in regenerative processes for examples: in adult rat with spinal cord lesion, Schwann cells or microglial cells grafted at the injury site are known to promote partial axon regrowth, but with co-cultures of Schwann cells and DRG neurons it was demonstrated that microglia co-

grafting or microglia conditioned medium enhance DRG fiber regeneration *in vitro* (**Figure 11**) [305–307]. In an electrophysiological study the impact of cell replacement therapy was further addressed in co-cultures of NPCs and postnatal hippocampal neurons where, functional NPCs maturation was speeded up by the presence of spiking hippocampal neurons [308]. On the other hand, co-cultures and tri-cultures of neuronal, astrocytic, and microglial cells are nowadays considered a reliable model to observe neuroinflammatory processes at the molecular level [309,310]. Importantly, *in vitro* single cell electrophysiology methods have long been, and still are, considered a fundamental step for pharmacological screening process. On a par with that, nanotechnologies are considered xenobiotics and by consequence, their testing also requires meticulous electrophysiological validations [311,312].

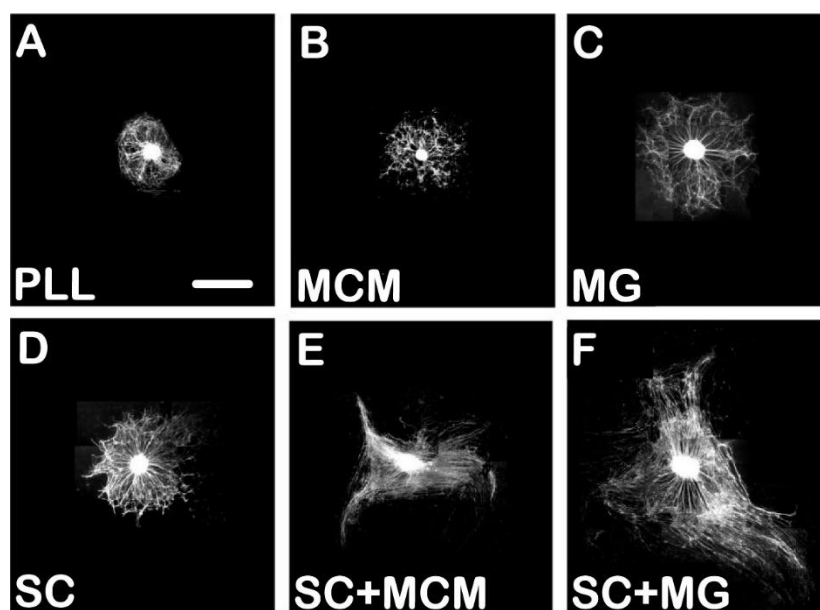


**Figure 11.** DRG explant outgrowth (scale bar = 1 mm) [307]. **A.** DRG grown onto poly-L-lysine (PLL) coating. **B.** DRG grown with microglia conditioned medium (MCM). **C.** DRGs grown in the presence of microglia. **D.** Similarly, DRGs in culture exposed to Schwann cells (SC) showed a comparable fiber outgrowth. **E.** The combination of Schwann cells and microglia conditioned medium increased explanted fibers length. **F.** Co-cultured Schwann cells and microglia added to DRG explants elicited the greatest fibers outspreading.



Indeed, the hike in nanomaterials supply to neural technologies development, has created a demand for first-line screening tools to assess toxicity of nanostructures and to monitor cell behavior over mesoscopic systems [313]. The advent of outperforming materials showing particular physical properties (*e.g.* piezoelectricity, bolometric response, hygroscopicity, magnetoresistivity, superconductivity *etc.*) encouraged the characterization of their interaction with neuronal networks for neural engineering approaches. For instance, carbon-based materials such as graphene and carbon nanotubes, demonstrated to intimately interact with developing neurons *in vitro*, influencing synapse formation, plasticity and neurotransmission [107,110,314–318]. Indeed, high-SNR recordings and efficient stimulation have been succeeded using these and others nanostructured materials [319–322]. By consequence, the combination of such nanotools resulted in CMOS and FET technologies which already demonstrated their efficacy *in vitro*, and that will be soon available for the design of new biomedical devices capable of an unprecedented resolution [323–327].

### 3.2 Organotypic cultures

Studies on dispersed CNS cells in culture undoubtedly lays the groundwork for whatever study that would attempt to reach the *in vivo* application, but, unfortunately, much more is needed to reproduce some whole-organism feature such as three-dimensionality, including cells embedding into ECM, cyto- and histo-architectures, vascularization, metabolic zonation and others [328–331]. Brain slices prepared with an appropriate anatomical rationale are considered for this reason the best tool to bridge the gap between *in vitro* and *in vivo* models [332,333]. Two main types of tissue slice preparations consist in short-term survival acute slices (usually from postnatal/juvenile animals) and long-term organotypic slices cultures (usually prenatal or early postnatal animals). It was around 1920s that the expression “organotypic” first appeared in the scientific literature and it refers to the possibility to maintain *ex vivo* morphological and cytoarchitectural aspects representative of the organ tissue *in vivo* [334]. Most of complications in the setup of a reproducible methodology for organotypic slice cultures from the nervous tissue, emerged from their high metabolic demand, which *in vitro* is poorly supplied due to the absence of blood flow.

The earliest attempts to obtain nervous tissue cultures are attributed to R. G. Harrison with his “hanging drop” methods allowing explants survival just for a couple of days [275]. Subsequently, in 1925 A. Maximow, who coined the term “organotypic”, developed the “double coverslip” (a.k.a. “lying drop”) method, with extended explant survival during culture [334]. As such, this latter approach remained for decades the most suitable for neurobiology research and it resulted in the pioneering works of M. B. Bornstein, E. R. Peterson, S. M. Crain and M. R. Murray on myelination and

bioelectrical activity in developing CNS organotypic cultures [335–337]. By second half of the century further refinements of the method, allowing long-term culturing, were proposed as the: *in oculo* method, roller-tube method (dynamic) and the interface method (static) [338–340]. The latter two are currently the most used, allowing a greater tissue flattening which is convenient for microscopy and electrophysiological studies [339,340]. As a consequence of the flattening better oxygenation and nutrient supply are guaranteed, thus allowing explants perpetuation for months in vitro (**Figure 12**) [341].

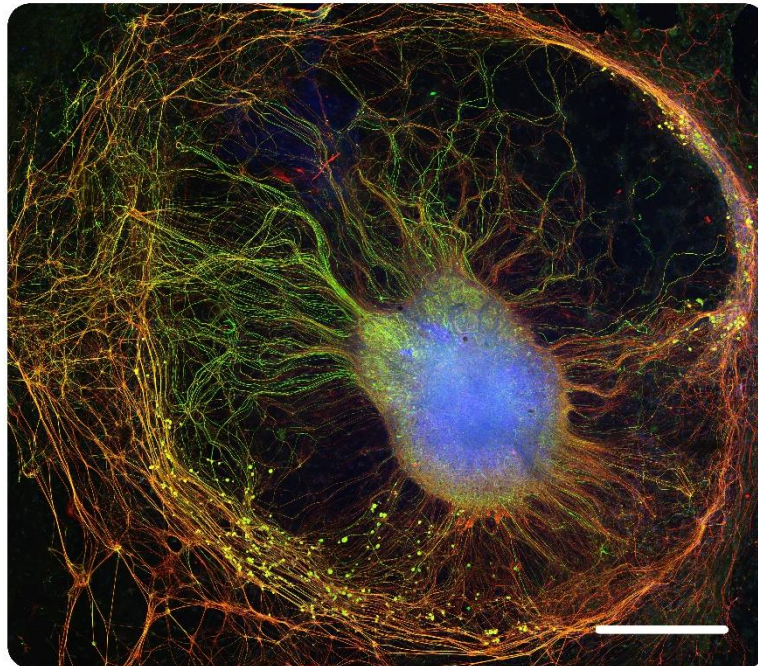


**Figure 12.** Transversal section of an embryonic spinal cord grown as organotypic slice culture for two months with the roller-tube method. The slice was immunolabeled for neuron-specific cytoskeletal components ( $\beta$ -tubulin III, red), motoneuron-specific neurofilaments (SMI – 32, green) and nuclei (DAPI, blue; scale bar = 600  $\mu$ m).

Overall, these features make organotypic slice cultures a perfect candidate to model CNS development or disease, study neurodegeneration and neuroinflammation, evaluate xenobiotics and nanomaterials biocompatibility and more [342–345]. Long-term cultures of nervous tissue have been prepared from various CNS regions including

cortex, cerebellum, hypothalamus and substantia nigra, but hippocampal and spinal cord slices certainly remain the most common models [339,346–349]. Slice co-cultures from neighboring and anatomically-related structures, are fairly used as well, and served to investigate axonal sprouting, target-dependent fiber regrowth, de- and re-myelination processes and developmental changes in neuronal networks [350–356]. In all cases, the recognition of defined anatomical structures is the starting point to isolate specific circuitry and therefore, different cuts can lead to the preservation of different networks to be studied in culture. Good examples are found in the hippocampal or entorhino-hippocampal slices where cutting angle choice is crucial to maintain intact portions of the main pathways in the hippocampal formation (e.g. perforant path, mossy fibers and Schaffer collaterals) [357–359]. Comparably, spinal cord slices obtained by transversal or longitudinal sectioning result in two different models, being the former more suitable for sensory inputs and interneuronal circuits investigation, while the latter more appropriate for spinal lesion modeling and/or to study propriospinal fibers involved in locomotion [354,360–362]. Organotypic explants retaining tissue-resident and specialized cell populations are crucial to gain insight on the interplay between neurons and supporting cells in both physiological and pathological conditions [363]. For example, astrocytes active role in sustaining neuronal activity and synchronization through  $\text{Ca}^{2+}$  signaling have been observed in organotypic cultures [364,365]. Also, microglial and astrocytic cells reactivity can be easily induced in such models in a way that neuroinflammation can be studied long-term, as shown for cerebellar, hippocampal and spinal cord slice cultures (**Figure 13A**) [366–368]. Similar reports highlighted the presence of oligodendrocytes and observed myelin sheet formation in several organotypic models *in vitro* (**Figure 13B-D**) [367,369,370].

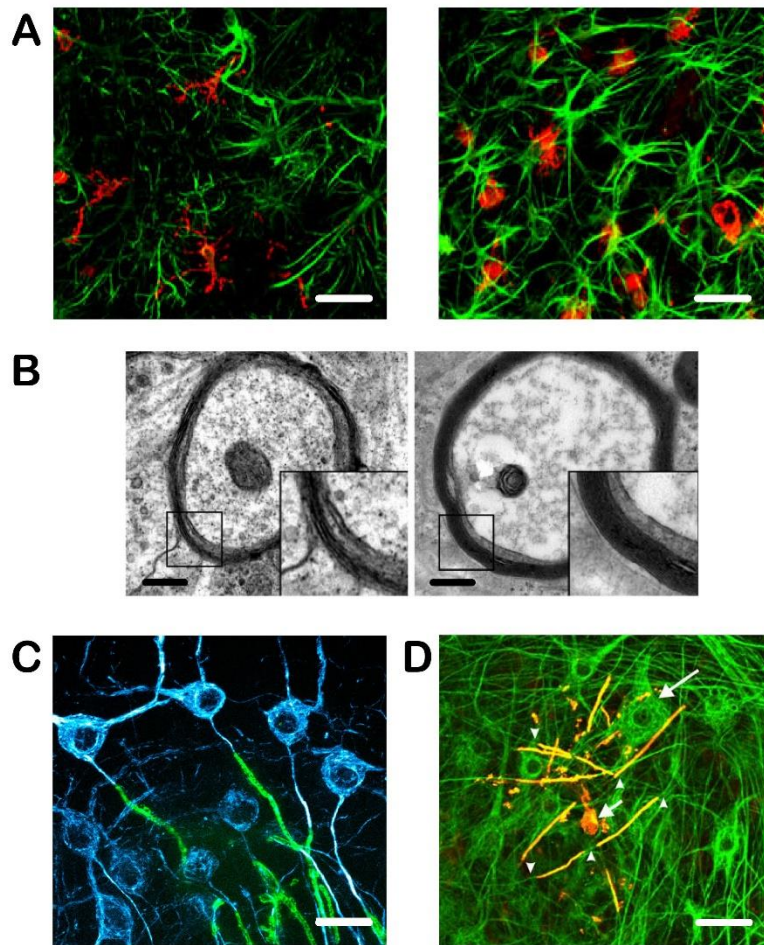


**Figure 13.** Micrographs demonstrating supporting cells activity within organotypic slice cultures. **A.** Confocal Z-projection of two organotypic spinal cord slices before (left) and after (right) 6 hours exposure to a proinflammatory cytokine cocktail; microglial cells activation can be observed by Iba1 labeling (in red), while reactive astrocytes are shown by GFAP (in green; scale bar = 50  $\mu\text{m}$ ) [368]. **B.** Electron micrograph cross-sections of myelinated fibers in two organotypic hippocampal slice culture after 7 DIV (left) and 21 DIV (right); circular electron-dense structure corresponds to the compact myelin sheath (scale bar = 1  $\mu\text{m}$ ) [369]. **C.** Calbindin-positive Purkinje neurons (cyan) found in a cerebellar slice is co-labeled with anti-MBP (myelin basic protein, green) to visualize myelinated axons (scale bar = 25  $\mu\text{m}$ ) [370]. **D.** Confocal reconstruction of SMI-32-positive motoneurons (green) in an organotypic spinal cord slice culture; anti-MBP (red) co-labeling of myelinated motoneuronal axons is visible (yellow; scale bar = 50  $\mu\text{m}$ ) [355].

In this scenario, neuro and nanotechnologies are finding an appropriate milieu where their properties can be elucidated in models with an increased complexity, reminiscent to some extent of what is observed *in vivo*. For example, potential nanoparticles cytotoxicity must be finely assessed before their applications for drug delivery or as contrast agents. In hippocampal slice cultures it has been shown how microglial uptake of superparamagnetic iron oxide nanoparticles is fundamental to prevent cell deaths



of hippocampal neurons [371]. Similarly, in an *in vitro* model of traumatic spinal cord injury (SCI) using organotypic spinal cords, it has been shown that gold nanoparticles injected within injury foci are rapidly sequestered by reactive microglia, thus reducing nanoparticles availability as potential vector for therapeutic approaches [372]. Another study on lipopolysaccharide (LPS)-treated hippocampal slice cultures, showed that microglial fate was reverted to an anti-inflammatory (M2 polarized) phenotype by administration of retinoic acid-loaded polymeric nanoparticles, resulting in the substantial recovery of neuronal survival [373]. In our lab similar topic has been tackled for many years and research using organotypic models unraveled the unique properties of nanocarbon materials and textured substrates at the interface with the neural tissue. In organotypic spinal slices, Musto *et al.* observed that upon exposure to small-graphene oxide (s-GO), ventral interneurons activity is downregulated conversely to what usually observed during neuroinflammation, paving the way for new therapeutics [368,374]. Moreover, microglial cells were shown to scavenge s-GO with time in culture; this occurred in the absence of proinflammatory markers such as astrocytes reactivity and neuronal damage [375]. Importantly, we previously, showed that tissue explants accept and integrate other carbon-based nanostructures with no cytotoxic effects: multi-walled carbon nanotubes (MWCNT) meshwork provided an anisotropic environment able to enhance nerve fibers elongation out of a spinal cord explant *in vitro*, the same behavior in segregated double-slice co-cultures onto 3D-carbon nanofibers (CNF) led to the functional reconnection of spinal slices, as shown by increased field potentials synchronization [106,149]. A comparable study using 3D-PDMS vs. 3D-PDMS-CNT scaffolds resulted in the same observations, thus motivating the use of such nanostructures for 3D neural-interfaces engineering [150]. The CNT potential of promoting fiber regrowth and tissue reconnection across a gap have been further

explored in our lab in a lesion model of the entorhino-hippocampal complex in slice cultures [151]. Interestingly, Yu and colleagues fabricated a CNF-based MEA that they used for electrophysiological recording and stimulation in organotypic hippocampal slices [376]. The great advantage of using long-term organotypic cultures for neural device testing has been proven by Stoppini and colleagues since the beginning of the century, and it led to the design of multi-site platforms with an unexpectedly high spatiotemporal resolution [377–379]. Constant monitoring of cultured CNS explants electrophysiological activity has been achieved with transistors arrays manufactured with microfabrication technologies and CMOS-based high density MEA, chronically interfaced to organotypic hippocampal slices, were used to reliably produce multiple single-unit recordings for months *in vitro* [380,381]. Thanks to these and other advancements neurotechnologies are increasingly drawing industries attention and gaining public consent, with a potential economic impact to the sector, that will hopefully lead advanced device to clinical testing and eventually to enter the market.



## 4. Spinal cord: a yarned target

### 4.1 Spinal cord anatomy

First testimonies of physicians showing particular consideration to spinal cord functions date back to XX century B.C. with the *Edwin Smith Papyrus* [382]. After that, Galen of Pergamum (II A.D.) provided the first description of its gross anatomy, and studies advanced thanks to the contribution of several scientists that elucidated various tracts in the mammalian spinal cord [383,384]. This keen interest translated after some time to the meticulous works of Flatau, which first recognized laminar patterns in thick, transverse sections of spinal cord, but also of Rexed and Scheibel who produced a detailed description of laminae subdivision and their fine cyto- and dendro-architecture [385-389]. According to these and subsequent studies, spinal cord architecture can be to date illustrated across two main axes: (i) longitudinal and (ii) transversal.

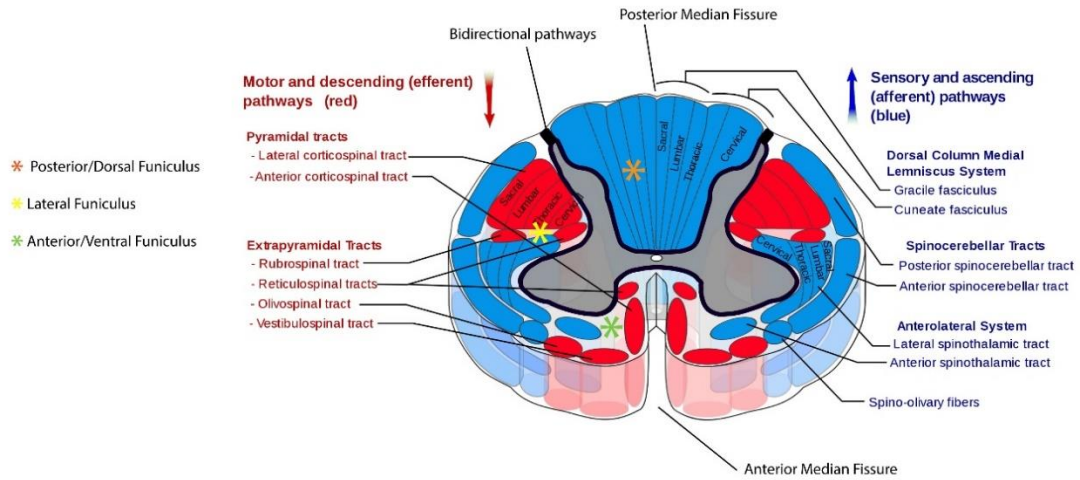
Spinal cord is the caudal extension of the CNS responsible for conveying sensorimotor information between the body and the brain, in either controlled or autonomic fashion. Conversely from the brain, the white matter in the spinal cord is found in the outermost part of the tissue surrounding the grey matter throughout its length [390]. In vertebrates, it is encased inside a number of vertebrae, which intercalate with the intravertebral fibrocartilage to provide mechanical protection and flexibility. According to its longitudinal axis, it is rostrocaudally subdivided in four major regions: cervical, thoracic, lumbar, and sacrococcygeal. Cervical and lumbar portions are characterized by two enlargements that are justified by denser motoneuronal populations in the grey matter, controlling upper (cervical) and lower (lumbar) limbs motor outputs [391]. Sensory signals from the periphery enter instead at each of the aforementioned

rostrocaudal segments through the intervertebral foramen, where DRG have formed. These primary afferent fibers are divided into three main categories: A $\alpha$ / $\beta$ , A $\delta$  and C fibers. Still along the longitudinal axis, ascending and descending (or bidirectional) pathways enable the communication with the brainstem and the brain, while propriospinal pathways mediate information transfer within the spinal cord at various levels. These pathways run in the white matter entering or exiting the spinal cord at various levels, resulting in a decrease density of the white matter in the rostrocaudal direction. Indicatively, ascending pathways transmit sensory cues and visceral information to supraspinal centers, while descending pathways convey motor commands and tune spinal reflex mechanisms (propriospinal pathways integrate and modulate all these functions) [392,393]. Anyway, for a proper understanding of ascending and descending tracts circuitry, the observation of the spinal cord in its transversal axis is mandatory (**Figure 14A**). In this regard, the spinal cord can be subdivided in two symmetrical halves along the median-sagittal plane, coincident with the anterior and posterior median fissures; the two hemispheres are connected by a pair of transverse commissures (anterior and posterior). On the lateral sides of the spinal cord ventral and dorsal roots emerge from anterolateral and posterolateral sulci to form spinal nerves [391]. Still, considering the spinal cord cross section, the white matter can be partitioned into dorsal, dorsolateral, lateral, ventrolateral and ventral funiculi, where myelinated ascending and descending fibers are located (**Figure 14A**). On the other hand, the grey matter is conventionally subdivided into a dorsal horn, intermediate grey and ventral horn, plus a centromedial area embracing the central canal (central grey; **Figure 14B**). Within these areas, appropriate stainings permit laminar pattern observation (**Figure 14B**); as first proposed by Rexed, lamina I is the most dorsal and it is considered a major source for supraspinal projections. In the dorsoventral

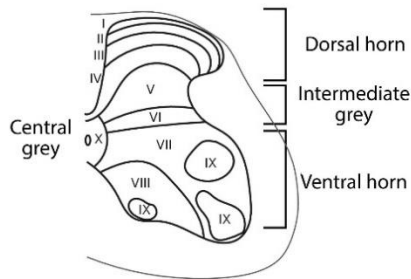
direction, it is followed by lamina II (divided in outer and inner portions) and lamina III, all receiving primary afferent inputs that are then redirected to ascending pathways to process sensory and visceral information. Lamina IV is still part of the dorsal horn, from here dendrites extend to laminae I – III, but also provide input to ascending spinal pathways; two interruptions exist in this lamina at the T1 – L3 and C1 – C6 levels, corresponding respectively to the *dorsal nucleus* (Clarke's column) and the *internal basilar nucleus*. Laminae V and VI are found at the boundaries with the intermediate zone and are both divided in two (lateral and medial) portions. Lamina V neurons possess dendrites extending to both dorsal and ventral locations (laminae II, III and VII). Lamina VI instead, is only observable in cervical and lumbar enlargements, propriospinal neurons here mainly receive afferents from group Ia muscle spindles, but also from interneuronal networks involved in reflex pathways. Lamina VII corresponds to the intermediate/ventral zone, where most of premotor interneurons are located. These latter project to motoneurons in lamina IX and by consequence they are modulated by descending pathways from the brain controlling motor functions. From lamina VII, projections to supraspinal centers were also observed. Importantly, in this lamina, several spinal nuclei were identified at different rostrocaudal extents: *central cervical nucleus* (C1 – C4 segments), *sacral parasympathetic nucleus* (S1 – S2), *intermediolateral nucleus* (T2 – L2), *sacral dorsal commissural nucleus* (L6 – S4) and *sacral precerebellar nucleus* (S1 – Co3). Lamina VIII neurons are heterogeneously represented in the rostrocaudal direction, they project dorsoventrally in the grey matter, but also in the white matters at the very boundary with the grey. These ascending and descending projections represent propriospinal fibers, that, together with commissural fibers to the contralateral ventral horn and to supraspinal centers, play a crucial role in motor activity coordination.

Lamina IX is the most ventral and it is mainly populated by somatic, larger  $\alpha$ - and smaller  $\gamma$ -, motoneurons; nevertheless, a number of  $\beta$ -motoneurons and small interneurons can be identified as well at this location [394–396]. Spinal motoneurons are usually referred as lower motoneurons and are cholinergic (in contrast with upper glutamatergic motoneurons), their distribution within this lamina varies according to the rostrocaudal axis and by consequence their segmented organization has led to the definition of distinct motor columns (**Figure 14C**): medial motor column (MMC), lateral motor column (LMC), hypaxial motor column (HMC), preganglionic column (PGC), spinal accessory column (SAC) and phrenic motor column (PMC) [397]. It is worth to note, as recent studies showed, that also the different interneuronal subtypes are distributed in a similar segmental organization along the longitudinal axis, motivating further investigations on these cell types within spinal circuitries [398]. Finally, lamina X is located around the central canal, with its neurons showing two main kind of dendroarchitectures (dorsoventral and rostrocaudal). In this region, somatic and visceral afferents convey nociceptive sensations and projections to supraspinal centers are present together with propriospinal fibers at all levels. Lamina X is in fact the seat of the *intermediomedial nucleus* and a part of the *intercalated nucleus*, both involved in gathering autonomic information from visceral organs [394,395].

**A**



**B**



**C**

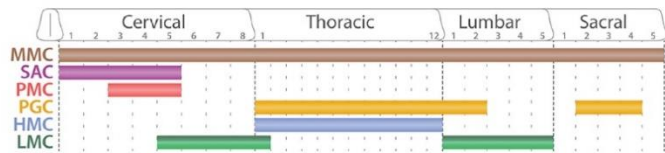


**Figure 14.** Schematic representations of spinal cord architectures. **A.** A Sketched cross-section of the spinal cord white matter illustrating the localization of some descending (red) and ascending (blue) tracts at different funiculi; bidirectional pathways (black) are instead found at the boundary between white and grey matters (*adapted from Wikipedia*). **B.** Drawing of a spinal cord hemisphere depicts the grey matter laminar subdivision [398]. **C.** Scheme of the longitudinal organization of motor columns within the grey matter in the ventral horn [397].

Although a general overview of spinal cord anatomy can be easily provided, inter- and intra-species differences exists at the fine cytoarchitectural levels, and therefore they must be considered for any experimental design.

## 4.2 Spinal cord injury

According to WHO statistics, worldwide up to half a million people suffer each year from spinal cord injury (SCI). These include both traumatic and non-traumatic injuries, with the first group representing the majority of the cases [399]. Spinal lesions are anyhow heterogenous in nature depending on the localization (**Figure 15A**), but also on the type and size of the lesion. The American Spinal Injury Association (ASIA) published in 1982 the first “*International Standards for Neurological Classification of Spinal Cord Injury*” to assess lesion severity based on four criteria: (1) sensory and motor levels, (2) ASIA impairment scale, (3) completeness of the lesion and (4) zone of partial preservation for complete lesions; importantly, these guidelines have been continuously revised and updated until today [400,401]. As reported in an MRI study by Bunge and colleagues, the type of SCI can be also classified in at least four pathological correlates: contusion cyst, cord maceration, cord laceration and solid cord injury [402,403]; contusion lesions (**Figure 15B**) are the most commons and they can be easily reproduced in animal models [403]. The biological response to spinal lesions has been extensively investigated and it includes a primary injury usually of traumatic origin, followed by a delayed and prolonged secondary injury which can last from hours to years (**Figure 15B**). By consequence, such stages are commonly divided in four phases: (1) *immediate phase*, (2) *acute phase*, (3) *intermediate phase* and (4) *chronic phase* [404]. Within the first 2 hours after the primary lesion, the *immediate phase* occurs mainly caused by local hemorrhages and edema. Indeed, at a systemic level, after a very first increase in blood pressure, prolonged hypotension is always observed likely due to reduced blood volume. Swelling and bleeding produce an ischemic environment rapidly resulting in oxygen (and therefore ATP) deprivation, which exacerbates necrosis and exposes neurons to others, non-apoptotic, cell deaths [405–407].

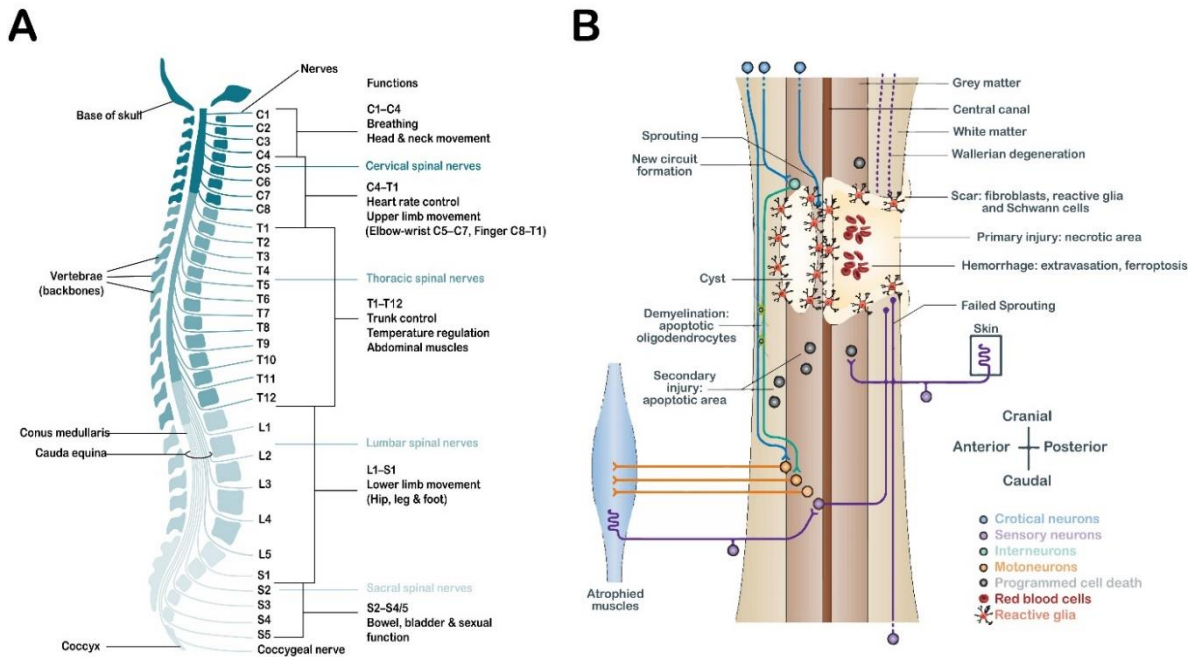


**Figure 15.** Schematic overview of the effects of spinal lesions. **A.** Longitudinal profile of the human spine indicating main nerve functions at different levels. Usually, all nerve functions are impaired under the region of the injury [399]. **B.** Sagittal representation of a contusion lesion adapted from Thuret et al. 2006 [432]. Primary injury site is characterized by neuronal death mainly occurring by various types of programmed cell death (e.g. necrosis, oncosis, necroptosis, parthanatos and ferroptosis); this necrotic area expands over time as consequence of secondary injury processes: extravasation of immune mediators from severed blood vessels dramatically worsen the scenario, macrophages are recruited and together with activated microglia show phagocytic behavior, microglia extending within fiber tracts lead to Wallerian degeneration on distal axons and induce apoptotic processes on oligodendrocytes far from primary lesion areas.

Moreover, resident microglia reactivity rise in minutes after traumatic injuries, leading to phagocytic and pro-inflammatory phenotypes as commonly shown by chemokine (e.g. IL-8 and CCL2) and cytokine (e.g. IL-6, IL-1 $\beta$ , TNF $\alpha$ ) expression profiles [404,408,409]. Also, as soon as neuronal and astrocytic membranes are disrupted right at the lesion site, glutamate leaks and its reuptake fails, thus reaching excitotoxic levels after few minutes [404,410]. At the onset of the *acute phase* (early 2 – 48 h and *subacute* 48 h – 2 weeks), the above described scenario continues and aggravates. Excitotoxicity and ionic dysregulation start spreading from the primary injury area to farther districts, leading to apoptotic and necrotic cascades; in particular, loss of Ca<sup>2+</sup> homeostasis is known to be a common trigger for programmed cell death [411]. Aberrant intracellular Ca<sup>2+</sup> concentrations are soon reached after glutamate receptors



hyperactivation, mainly through AMPA/kainate and N-methyl-D-aspartate (NMDA) receptors, but also after early mitochondrial impairment and the subsequent formation of mitochondrial permeability transition pores (mPTP), thus initiating calpains- and caspases-mediated apoptosis [412–415]. By consequence, malfunctioning of the electron transport chain (ETC) results in molecular oxygen (O<sub>2</sub>) reduction by leaked electrons and in superoxide production, which degenerates in the production of further reactive oxygen species (ROS) [416]. This event peaks already at 12 hours post-trauma and prolongs for one week before returning to basal levels at the fourth week after injury [404]. Such an oxidative environment is also deleterious for proteins by carbonylation, that exacerbates immune responses and for cell membranes and organelles, which rapidly undergo lipid peroxidation [412,416]. On another hand, if immune cells such as neutrophils and reactive microglia contributes to inflammation at early stages of the acute phase, their effects protract resulting in blood monocytes chemoattraction from disrupted BBB [404,417]. At first week and further on, TNF $\alpha$  from microglia considerably affects oligodendrocytes survival through the Fas-ligand apoptotic pathway, and recruited macrophages start exhibiting phagocytic behavior towards cellular and myelin debris; both events are known to sustain Wallerian degeneration for months [418,419]. At the end of the *subacute phase*, survived astrocytes at the periphery of the lesion site become hypertrophic, increase glial fibrillary acidic protein (GFAP) expression and start proliferating, thus starting a fibrotic response [420,421]. Importantly, also infiltrating Schwann cells play an important and controversial role in such a response [422]. This phenotype persists over the *intermediate phase* (2 weeks – 6 months) until the wound is totally filled with a meshwork of tightly packed astrocytes, but also meningeal and perivascular fibroblasts, and ECM molecules, forming the so-called glial scar [404,420,423]; alternatively or concomitantly, a CSF-filled

cavity (a.k.a. cyst or syrinx) might form, a condition referred as syringomyelia and known to worsen the clinical course in a delayed fashion [424]. During this phase, also considerable axonal sprouting might occur and therefore rehabilitation therapies should be implemented to improve functional recovery at this stage [425]. Indeed, Hill and colleagues showed that, in rat models, corticospinal tract fibers are able to regenerate from 3 weeks to 3 months post-injury, while reticulospinal tract regrowth is delayed, within 3 to 8 months post-injury [426]. This process in the CNS is anyhow limited by the presence of myelin-associated and glial scar-associated inhibitors of axonal regrowth, which biochemistry has been exhaustively reviewed elsewhere [427]. Over 6 months post-injury, the *chronic phase* begins and lasts for years, or possibly throughout patients' lifetime. At early stages (1 – 2 years post-lesion), such period is characterized by consolidation of glial scar and cyst, wound stabilization and cessation of Wallerian degeneration processes, together with partial plasticity of spared synapses [404]. At the macroscopic level, these events might result in compensatory mechanisms producing some degree of functional recovery, but also in the further loss of motor feedback control, generation of muscle spasticity and appearance of neuropathic, visceral and nociceptive pains [428].

All “characters” described above were thoroughly considered as a potential target for therapeutic intervention, with contentious effectiveness: most of pharmacological treatments ameliorated patients' prognosis only when administrated within 72 hours after injury, which implies fast transport system to the hospital, fast recognition of spinal lesion site, type and severity, and availability of dedicated drugs [429]. Moreover, such approach would logically, but unfairly exclude already affected (chronic) people from being part of the actual matter. For these and other reasons, neurotechnologies


are nowadays trying to bridge the gap in SCI treatment. Neuroimmune modulation by nanomaterials is starting to be elucidated and glial reactivity can be tuned with nanopatterning and other strategies. Comparably axonal sprouting can be induced by proper topographies, but also by moderate electric field application. On the other hand, neuromodulation technologies are displaying an unprecedented potential in assisting patients at the intermediate to chronic phases, thus justifying scientific efforts in this direction [430,431].

### 4.3 Implantable devices for spinal cord restoration

Due to its heterogeneous nature and complexity, spinal cord damage is considered a multifaceted issue, where applicable solutions strongly depend on the stage of degenerating processes after injury. By consequence, possible strategies are oriented towards modulating the contribution of each cell type present within, or close to, the lesion site at the examined stage.

At earliest phases cellular transplantation and pharmacological therapies have been largely studied either *in vitro* or in animal models, and in some case promising results were achieved also during clinical trials [404,429,432]. Concurrently, many studies have addressed the possibility of rewiring the impaired fiber tracts and neuronal networks by means of fibrous or porous micro- and nano-matrices implanted within the lesion [98,433,434]. Importantly, the combination of these strategies has been shown to improve recovery after lesion [435-439]. Thanks to nanotechnologies and advancements in molecular medicine, these features can be to date integrated in multifunctional regenerative implants which can actively interact with the tissue preventing proinflammatory processes, while enhancing reconnection and healing. Remarkable attempts of such cutting-edge technologies can be found in recent studies where injectable hydrogels and self-assembling scaffolds were used to simultaneously fill lesion cavities and locally release therapeutic compounds [440-442]; or in the work of Koffler and colleagues, which reported locomotion recovery after spinal lesions filling with 3D printed hydrogel scaffolds loaded with NPCs [55]. Also Nguyen and coworkers highlighted the potential of 3D nanofibers hydrogels, this time enriched with miRNAs and trophic factors, to demonstrate that local gene/drug release can be accomplished with bioactive 3D spinal cord implants [99]. Comparably, Gong et al. observed that

downregulation of inflammatory processes through biomimetic scaffolds produce a favorable environment for co-grafted neural stem cells, leading to increased locomotor recovery in implanted SCI animal models [443]. Despite their beneficial effects, regenerative implants are tarrying to reach clinical trials and their translatability is debated. This is probably due, among other things, to variability in the pathophysiological evolution of traumatic SCI observed in humans, which further complicates clinical studies, usually based on the comparison among intrinsically different control lesions. The situation is worsened by unavoidable large times required for clinical testing of new compounds (**Table 2**).



Stage	Purpose	Average stage duration	Test population	Success rate
Discovery and preclinical testing	File patent (20 yr); assess safety, biological activity and formulations; verify effectiveness	3 to 7 yr	from <i>in vitro</i> to <i>in vivo</i> studies	5 of 5000 (0.1%) of screened compounds enter clinical trials
<b>File investigational new drug application (IND) with FDA</b>				
Phase I clinical trial	Determine safety and dosage	2 to 3 yr	20 to 100 healthy volunteers	75% enter Phase II
Phase II clinical trial	Evaluate effectiveness and look for side effects	2 to 4 yr	100 to 500 volunteer patients	61.2 % enter Phase III
Phase III clinical trial	Confirm effectiveness and monitor long-term adverse reactions	1 to 4 yr	1000 to 5000 volunteer patients	86.8 % file NDA
<b>File new drug application (NDA) and Biological License Application (BLA) with FDA</b>				
FDA	Review process and approval	1 to 2 yr		1 compound approved out of the original 5100 (0.02% success)
Phase IV clinical trial	Additional postmarketing testing required by FDA			

**Table 2.** Schematic research pipeline for FDA approval of novel therapeutic compounds (*adapted from <http://phrma-docs.phrma.org/sites/default/files/pdf/biopharmaceutical-industry-profile.pdf>*).

On the other hand, after the lesion is consolidated as in chronic SCI patients, regenerative approaches are unapplicable. For this reason, pioneering research on the field are exploring the possibility to restore lost functions by delivering electrical stimulation to muscles or nerves and to record signals from spared neural tissue or from volitional muscle contraction for feedforward control [444]. Functional electrical stimulation (FES) and related neuroprostheses represent to date a promising approach to bypass several impairing conditions resulting from SCI, such as bladder and bowel disfunctions, but also to sustain autonomic functions such as respiration and cardiac rhythm [444,445]. Importantly, electrical stimulation of the dorsal column in the spinal cord can be used to modulate nociceptive neurotransmission, and it has been indeed suggested for drug-resistant chronic pain treatment [253,254]. Regardless, one of the major challenges after SCI remains the recovery of some voluntary motor function, ranging from hand grasping and postural muscle use, rise-to-stand movements, but also sustained standing and perhaps walking [446–449]. This possibility relates to the existence, within the lesioned spinal cord, of anatomically and functionally preserved propriospinal circuitry, which acts as a source of facilitatory inputs on the so called spinal central pattern generator (CPG) [450,451]. Moreover, there is large evidence for improved rehabilitative outcomes upon periodic sessions of spinal cord stimulation [249,449]. This is overall due to neuroplastic, regenerative and galvanotactic behavior resulting from the evoked electrical activity [452–455]. Epidural stimulation and intraspinal microstimulation are the most common configurations to target the spinal tissue and their long-term efficacy is bound by electrode features described above (2.1 “*Advances in electrode design*”). Interestingly, implantable stimulators are evolving towards a new generation of neuroprosthetic devices that will be able to couple electrical stimuli with chemical release within the target area to increase the level of

excitability, thus pushing residual sensory information to become a source of feedback for stepping [455,456]. Current attempts to bypass deficits induced by spinal lesions encompass a wide range of FES and brain-computer interfaces (BCI) designed to record neural activity, thus providing intuitive control signals for the user [444,457]. To date, the objective is to improve devices architecture by including feedback signals recording usually from cortical structure, by EEG, electrocorticography (ECoG) or intracortical microelectrodes, but also from muscles by electromyography (EMG) [446,447,458–461]. Encouragingly, also electrical recording from DRG has been recently indicated as an exploitable source of natural sensory signals after SCI [462–464]. Sensory feedback incorporation in new closed-loop systems is becoming an imperative requirement, to provide more dynamic and adaptive control over functions [446,457,465]. This of course requires additional support from *in silico* modeling and algorithm design, for clustering and processing recorded activity in real-time and accordingly tuning stimulus parameters [459,466,467]. To conclude, further studies explored also the restoration of proprioceptive and tactile sensations by intracortical microstimulation of somatosensory areas in the postcentral gyrus, but yet this chance will require additional work [468–470].

To summarize, implantable neural technologies hold a particular potential for circuitry repair after SCI and should be considered for their capability of inducing axonal growth and the upregulation of several genes known to regulate neuronal plasticity and survival. The availability of both electrical and chemical stimulation systems and the incorporation of recording elements are crucial to the optimal operation of next-generation neuroprostheses acting on closed-loop architectures to recover and sustain impaired functions in the most automated, intuitive or natural way.



## AIMS OF THE STUDY

The purpose of my thesis is to explore the perspective of nanomaterials in the context of neuroprosthetics formulation. Interfacing the CNS is an arduous challenge, but worth to be investigated to improve healing of damaged CNS. Novel materials showing outstanding physical properties or providing particular chemical, topographical or electrical cues are excellent candidates for the development of next generation implantable devices able to sustain physiological behaviors over pathological states. Our lab has been exploring the use of various nanostructured materials of biotechnological interest to improve the scientific knowledge about their applicability in biological contexts [314,315,317,375,434,471]. In particular, we study neurons at the interface with nanotools by electrophysiological means, live imaging and fluorescent microscopy, using *in vitro* dissociated and organotypic cultures, *ex vivo* acute slices, but also *in vivo* animal models.

In this framework:

I contributed to *in vitro* research within different projects and collaborations, where I was expected to gain expertise with various electrophysiological techniques, from whole cell patch-clamp recordings and live Ca<sup>2+</sup> imaging to extracellular field potential recordings and electrical stimulation. With the aim of improving interfacing performance of new generation devices, I participated in the development of sensors and electrodes based on nanostructured materials for neural interfacing.

I actively worked on the setting of a non-contact sensing devices (magnetophysiology recording) to detect magnetic field of neuronal origin and of nanostructured electrodes

of enhanced adhesion and efficiency for stimulations delivery. In doing so, I have explored the biocompatibility and biological impact of several nanostructures, bridging physics and engineering to neurobiology. In particular I achieved the following steps: Monitor the physiology of isolated hippocampal dissociated neurons and organotypic tissues grown onto suitable materials for implantable electrode fabrication and to design a protocol to stimulate the neuronal tissue across such conductive materials.

I addressed fibers regrowth and reconnection in organotypic entorhino-hippocampal and DRG-spinal cord slice models interfaced with various micro and nanostructured materials intended for biomedical devices encapsulation. I ultimately explored (*in vitro*) the use of innovative non-invasive neural recording tools.

THE RESULTS SECTION OF THIS THESIS INCLUDES 3 PUBLISHED WORKS, 1 SUBMITTED MANUSCRIPT AND 1 MANUSCRIPT IN PREPARATION. ADDITIONAL EXPERIMENTAL STUDIES AND PUBLISHED COLLABORATION WORKS ARE REPORTED AS *APPENDIX*.

# RESULTS

Received: 22 May 2019 | Revised: 10 July 2019 | Accepted: 11 July 2019

DOI: 10.1002/dneu.22711

RESEARCH ARTICLE

WILEY

## Transparent carbon nanotubes promote the outgrowth of entorhino-dentate projections in lesioned organ slice cultures

Niccolò P. Pampaloni<sup>1</sup> | Ilaria Rago<sup>2,3</sup> | Ivo Calaresu<sup>1</sup> | Luca Cozzarini<sup>2,4</sup> |  
Loredana Casalis<sup>2</sup> | Andrea Goldoni<sup>2</sup> | Laura Ballerini<sup>1</sup> | Denis Scaini<sup>1,2</sup>

<sup>1</sup>International School for Advanced Studies (SISSA), Trieste, Italy

<sup>2</sup>Elettra Sincrotrone Trieste, Trieste, Italy

<sup>3</sup>Department of Physics, University of Trieste, Trieste, Italy

<sup>4</sup>Department of Engineering and Architecture, University of Trieste, Trieste, Italy

### Correspondence

Laura Ballerini and Denis Scaini, International School for Advanced Studies (SISSA), Trieste, Italy.  
Email: laura.ballerini@sissa.it (L. B.) and dscaini@sissa.it (D. S.)

### Present address

Niccolò P. Pampaloni, Leibniz-Forschungsinstitut für Molekulare Pharmakologie, Berlin, Germany

### Funding information

The authors acknowledge the t ByAxon No. 737116 to L.B.; A.G. would like to acknowledge the NATO for the project G5140

### Abstract

The increasing engineering of carbon-based nanomaterials as components of neuroregenerative interfaces is motivated by their dimensional compatibility with sub-cellular compartments of excitable cells, such as axons and synapses. In neuroscience applications, carbon nanotubes (CNTs) have been used to improve electronic device performance by exploiting their physical properties. Besides, when manufactured to interface neuronal networks formation in vitro, CNT carpets have shown their unique ability to potentiate synaptic networks formation and function. Due to the low optical transparency of CNTs films, further developments of these materials in neural prosthesis fabrication or in implementing interfacing devices to be paired with in vivo imaging or in vitro optogenetic approaches are currently limited. In the present work, we exploit a new method to fabricate CNTs by growing them on a fused silica surface, which results in a transparent CNT-based substrate (tCNTs). We show that tCNTs favor dissociated primary neurons network formation and function, an effect comparable to the one observed for their dark counterparts. We further adopt tCNTs to support the growth of intact or lesioned entorhinal–hippocampal complex organotypic cultures (EHCs). Through immunocytochemistry and electrophysiological field potential recordings, we show here that tCNTs platforms are suitable substrates for the growth of EHCs and we unmask their ability to significantly increase the signal synchronization and fiber sprouting between the cortex and the hippocampus with respect to Controls. tCNTs transparency and ability to enhance recovery of lesioned brain cultures, make them optimal candidates to implement implantable devices in regenerative medicine and tissue engineering.

### KEYWORDS

hippocampus, injured brain, nanomaterials, neural interfaces, regeneration, synaptic enhancement

## 1 | INTRODUCTION

In modern neuroscience, a large amount of (interdisciplinary) research is devoted to the development of novel therapeutic

Niccolò P. Pampaloni, Ilaria Rago, and Ivo Calaresu contributed equally to this study.

approaches to treat a variety of pathological conditions, ranging from neurodegenerative diseases (Perlmutter & Mink, 2006) to traumatic brain injuries (Finnie & Blumbergs, 2002; Girgis, Pace, Sweet, & Miller, 2016; Maas, Stocchetti, & Bullock, 2008) and psychiatric disorders (Perlmutter & Mink, 2006). An attractive strategy involves the development

of assistive implantable devices, such as electrodes or interfaces, aimed at restoring the lost functions (Guggenmos et al., 2013). In the engineering of neuroprosthetic devices, nanotechnology demonstrated to play an important role (Cetin, Gumru, & Aricioglu, 2012), by enriching artificial scaffolds with controlled nano-sized features/cues, improving the interfacing stability with neuronal tissues at the cellular and subcellular level (Lee et al., 2006; Vidu et al., 2014; Wang et al., 2017), and providing a potential regenerative guidance. In this framework, electrically conductive nanomaterials such as carbon nanotubes (CNTs) (Iijima, 1991), are still promising, because of their tunable physicochemical features (O'Connell, 2006) and their ability to finely interact with neuronal cells (Cellot et al., 2011; Lovat et al., 2005) and neural tissues (Fabbro et al., 2012; Usmani et al., 2016). Because of these properties, CNT-endowed surfaces have been employed in the fabrication of diverse neural interfaces (Bareket-Keren & Hanein, 2013; Vidu et al., 2014), such as retinal implants (Eleftheriou et al., 2017) or deep brain stimulators (Vitale, Summerson, Aazhang, Kemere, & Pasquali, 2015). Intriguingly, CNTs were shown to improve axons regeneration and functional reconnection among segregated mammal spinal cord explants in vitro (Aurand et al., 2017; Fabbro et al., 2012; Usmani et al., 2016). However, their ability to trigger similar effects when challenged with other central nervous system (CNS) areas has yet to be shown. Besides, two significant factors that limit CNTs engineering in brain interfaces, namely their lack of optical transparency and their unstable adhesion to nanostructured films, need to be addressed. Until now, the opaqueness of CNT films directly grown via chemical vapor deposition (CVD) (Rago et al., 2019), hindering the passage of visible light, restrained the exploitation of such substrates in live imaging or optogenetic applications. On the other hand, the limited mechanical stability of CNTs films prepared following the drop casting procedure (Hokkanen, Lautala, Flahaut, & Ahlskog, 2017) to the supporting substrate may result in support detachment due to shear stresses induced by cell growth and motion (Nelson, 2017), muscular tissue contractility (Tschertter, Heuschkel, Renaud, & Streit, 2001), and/or culturing media replacement (Huber, Oskooei, Casadevall i Solvas, DeMello, Kaigala, 2018).

In this study, we take advantage of direct growth of a thin layer of CNTs on fused silica slides, which results in transparent substrates endowed with tightly bonded CNTs suitable for the assessment of functional reconnection in complex CNS organ explants. Through patch-clamp electrophysiology and immunocytochemistry experiments, we investigate whether the novel CNT-endowed substrates retain the ability to support the maturation and growth of dissociated neurons and glial cells from rat hippocampus and, more importantly, we evaluate their impact on the emerging circuit activity. We demonstrate that the novel CNT-endowed substrates can sustain the development of synaptic networks characterized

by improved activity (Cellot et al., 2009, 2011; Lovat et al., 2005).

We further address the potential of tCNTs in supporting axons regeneration when coupled to complex CNS structures (Usmani et al., 2016), by interfacing tCNTs with entorhinal-hippocampal organotypic cultures (EHCs) containing the entorhinal cortex (EC), the perforant path, and the dentate gyrus. To investigate the regenerative potential of tCNTs platforms, we mimic a CNS lesion by transecting the perforant pathway, (Del Turco & Deller, 2007; Li, Field, Yoshioka, & Raisman, 1994; Parnavelas, Lynch, Brecha, Cotman, & Globus, 1974; Perederiy, Luikart, Schnell, & Westbrook, 2013; Li et al., 1993; Steward & Vinsant, 1983; Woodhams & Atkinson, 1996; Woodhams, Atkinson, & Raisman, 1993). To better reproduce a severe mechanical injury (Finnie & Blumbergs, 2002), we introduced a remarkable gap between the two portions of tissue: the hippocampus (H) was placed at 0.5 mm far apart from the EC. We show that tCNTs boost EHCs fiber sprouting ability, which ultimately leads to functional and anatomical reconnection of the two separated brain structures.

## 2 | RESULTS

### 2.1 | tCNTs synthesis and characterization

Transparent CNTs (tCNTs) were synthesized via catalytic chemical vapor deposition (CCVD) directly on fused silica slices. The synthesis was done taking advantage of the catalytic effect of iron nanoparticles (NPs) thermally obtained from a thin iron film deposited (without the employment of any adhesion layer) on the fused silica substrates. The thermal synthesis required just 90 s resulting in an ultra-thin layer of entangled CNTs decorating the slices. In our CCVD synthesis of CNTs, catalyst plays a crucial role since NPs result from a thermal annealing treatment of the substrates and they act as starting sites for the subsequent CNTs growth (Shah & Tali, 2016). Size and density of these NPs are strongly related to annealing treatment parameters (i.e., temperature and time) and the features of the initial catalyst layer (i.e., starting film thickness and its adhesion to the underneath substrate (Chiang & Sankarana, 2007). In the attempt to enhance CNT synthesis yield, one or even more intermediate metallic layers could be used as adhesion and/or anti-diffusion layer between the catalyst and the underneath support (Bayer et al., 2011; Michaelis et al., 2014). Moreover, it was reported that by setting the annealing treatment conditions at 720°C for 3 hr and the growth parameters at 720°C for 1 hr, it is possible to obtain long vertically aligned CNTs (LVA-CNTs) on various supports (Morassutto, Tiggelaara, Smithers, & Gardeniers, 2016). Anyhow, we here demonstrated that, although any adhesion metal was employed and even if the growth time was limited to just 90 s, the yield, reproducibility, and density of the as-produced CNTs are comparable

with that of similar carbon nanostructures produced by using more time-consuming methods. Just the length of the resulting CNTs is limited and, consequently, the total thickness of the CNTs film covering the supporting substrate. Scanning electron microscopy (SEM) imaging was performed on CNTs mat to assess CNT dimensions, length, uniformity, and density. SEM micrographs (Figure 1a, left) showed a uniform carpet of short CNTs (star mark) covering a flat supporting surface of fused silica (hash mark) exposed scratching CNTs away with a razor blade. The enlargement of the dashed line-marked area pointed out a crumpled portion of the CNTs film (Figure 1a, center) allowing to estimate a film thickness of about 1  $\mu\text{m}$ . A high-magnification image in correspondence of the star mark made visible the single CNTs constituting the carpet and their random orientation (Figure 1a, right) due to the absence of proximity effects (Zhang et al., 2006). Transmission electron microscopy (TEM) characterization was conducted on CNTs to explore their structure and crystallinity. It has been found that CNTs consist of multi-walled carbon nanotubes (MWNTs) with a variable number of walls. Specifically, Figure 1b shows an isolated MWNT with an outer diameter (OD) of less than 30 nm and inner diameter (ID) of approximately 10 nm. These measurements are consistent with 15 nanotube walls (Chiodarelli et al., 2012). In addition, TEM analysis revealed the presence of structural defects (Figure 1b, right), generally imperfections of conjugated  $\text{sp}^2$  carbon along the tubes (i.e., breaks),  $\text{sp}^3$  hybridized carbon atoms, Stone–Wales defects (i.e., two heptagons and two pentagons), presumably ascribable to the low synthesis temperature used (730°C) (Charlier, 2002; Lee, Park, Huh, & Lee, 2001). Interestingly, <2- $\mu\text{m}$ -thick CNT films covering the fused silica do not prevent the light from passing through the sample (see the transmittance plot for samples of CNT film with different thickness shown in Figure 1c, left) resulting in (quasi) transparent CNT substrates. An increase in the synthesis time (e.g., 4 min) gives rise to almost opaque CNT films (Figure 1c, right). In this work, we used samples characterized by a CNT film thickness in the range of 0.2–2  $\mu\text{m}$ , ultimately able to guarantee the needed optical transparency. The degree of structural ordering and the quality of our CCVD CNTs were evaluated by Raman spectroscopy. The two main bands typical of all graphite-like materials, including MWNTs, present in Raman spectra (Figure 1d) correspond to the G band at  $\sim 1,583\text{ cm}^{-1}$ . This band related to the in-plane tangential vibration of  $\text{sp}^2$  carbon atoms resulting from the graphitic nature of CNTs and the D band at  $\sim 1,330\text{ cm}^{-1}$  indicating the presence of amorphous and/or low-ordered carbon structure (carbonaceous impurities with  $\text{sp}^3$  bonding, and broken  $\text{sp}^2$  bonds in the sidewalls (Costa, Borowiak-Palen, Kruszyńska, Bachmatiuk, & Kalenczuk, 2008). The ratio between the D ( $I_D$ ) and G ( $I_G$ ) band integral intensities was usually adopted as an indicator of CNTs quality. Specifically, similar intensities of these bands (Antunes,

Lobo, Corat, & Trava-Airoldi, 2007), as in our case, suggested the presence of non-graphitic carbon in nanotubes, typical for low-temperature CVD-grown CNTs (Bulusheva et al., 2008). Together with the G band, the second-order Raman peak  $G'$  is characteristic of graphitic  $\text{sp}^2$  materials and is located at  $\sim 2,700\text{ cm}^{-1}$ . The  $G'$  band, an overtone mode of the D band (Saito et al., 2003), is associated with defect density, but not as crucially as the first order mode. It was also reported that the intensity of this peak depends significantly on the metallicity of CNTs (Kim et al., 2007). Other peaks located at  $\sim 1,698\text{ cm}^{-1}$  and  $\sim 1,759\text{ cm}^{-1}$  are related to C = O bond vibration (Long, 1997; Roeges, 1997) and indicate possible partial oxidation of MWNTs. From the XPS survey spectrum of CNTs (Figure 1e) three elements can be discriminated: carbon (C1s), oxygen (O1s) and silicon (Si2s and Si2p). The atomic percentage of C and O are 87.6 at% and 10 at%, respectively. Only a small amount of Si was detected (2.4 at%). The presence of oxygen on CNTs surface is intrinsically related to our CVD procedure and, specifically, to defects originated during CNTs synthesis showing the tendency to adsorb oxygen when exposed to air. Figure 1f indicates the C1s core level for a  $\sim 8\text{ }\mu\text{m}$  thick CNT film. The most intense peaks located at 284.7 eV and 285.8 eV can be assigned to  $\text{sp}^2$ -hybridized graphitic carbon atoms located on CNTs walls and to amorphous carbon ( $\text{sp}^3$ -hybridized carbon atoms), respectively (Hofmann et al., 2009; Mattevi et al., 2008). The amorphous carbon is likely due to the CNTs synthesis process, as confirmed by the structural defects identified via TEM (Figure 1b) and Raman spectroscopy (Figure 1d). The peak at 290.8 eV corresponds to the electron energy loss peak due to  $\pi$ -plasmon excitations. These three peaks are characteristics of C1s core level from CNTs (Mudimela et al., 2014; Okpalugo, Papakonstantinou, Murphy, McLaughlin, & Brown, 2005). The additional small peaks at 287.15 eV and 288.4 eV were assigned to the presence of oxygen (Okpalugo et al., 2005).

## 2.2 | tCNTs biocompatibility: dissociated primary neurons growth and synaptic activity

CNTs carpets have been since long characterized as platforms enriched with nano-scaled topology able to support neural cultures development, and their effects on cultured hippocampal primary cells are well described (Cellot et al., 2009, 2011; Lovat et al., 2005). Anyway, being the result of a novel fabrication process, our first concern was to understand if the new tCNTs carpets were biocompatible and able to sustain the development of healthy and functional neural networks, potentiating the emerging synaptic activity in respect to Control cultures, as reported for opaque CNTs interfaces (Cellot et al., 2011; Lovat et al., 2005; Mazzatenta et al., 2007; Rago et al., 2019). To this aim, we compared cultured dissociated primary neurons from rat hippocampus interfaced



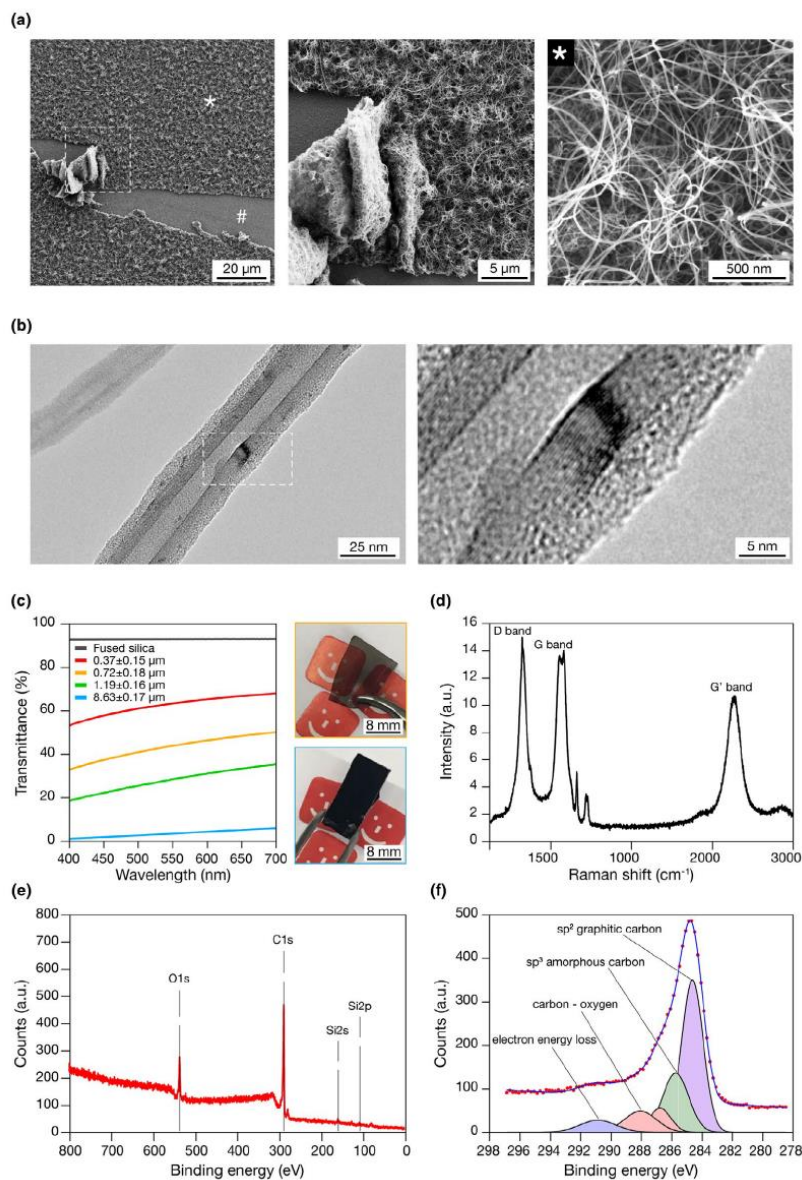


**FIGURE 1** Morphological, structural, and chemical characterization of CNTs synthesized by CCVD on fused silica substrates. (a) SEM investigation of CCVD tCNT substrates reveals the uniformity of the so obtained films (left), characterized by a thickness of about 1 μm, visible in the crumpled portion of the film (center), and a random orientation of the entangled nanotubes (right). (b) TEM images of tCNTs reveals their multi-walled characteristic (left) with all the different walls constituting the tube and structural defects well visible (right). (c) Transmittance analysis in the visible spectrum of four samples characterized by different CNT film thickness compared to the pristine fused silica substrate (left); on the right, two representative optical images of a thin CNT film grown on fused silica (top, about 0.7 μm in thickness) and of a thick CNT film (bottom, about 9 μm in thickness), pointing out the good transparency of the former one. (d) Raman spectra exhibiting the characteristic D, G, and G' peaks of CVD grown MWNTs. (e) XPS survey and C1s core level (f) spectra of tCNTs grown on fused silica substrates



to tCNTs-decorated substrates with glass supported Controls. To evaluate if tCNTs were allowing the correct adhesion and growth of primary cells, we quantified the neuronal and glial cell densities after 8–10 days of in vitro growth (DIVs). Neurons and glial cells were imaged by immunofluorescence of the specific cytoskeletal components  $\beta$ -Tubulin III, to visualize neurons, and glial fibrillary acidic protein (GFAP)

to visualize glial cells; as shown in Figure 2a, the cellular composition of the networks developed onto Controls (left) and tCNTs (right) substrates are qualitatively comparable. We quantify the number of neurons and astrocytes composing the networks and no statistical difference in terms of cell densities were pointed out (bar plots in Figure 2b) indicating that tCNTs can sustain hippocampal cells growth in a fashion

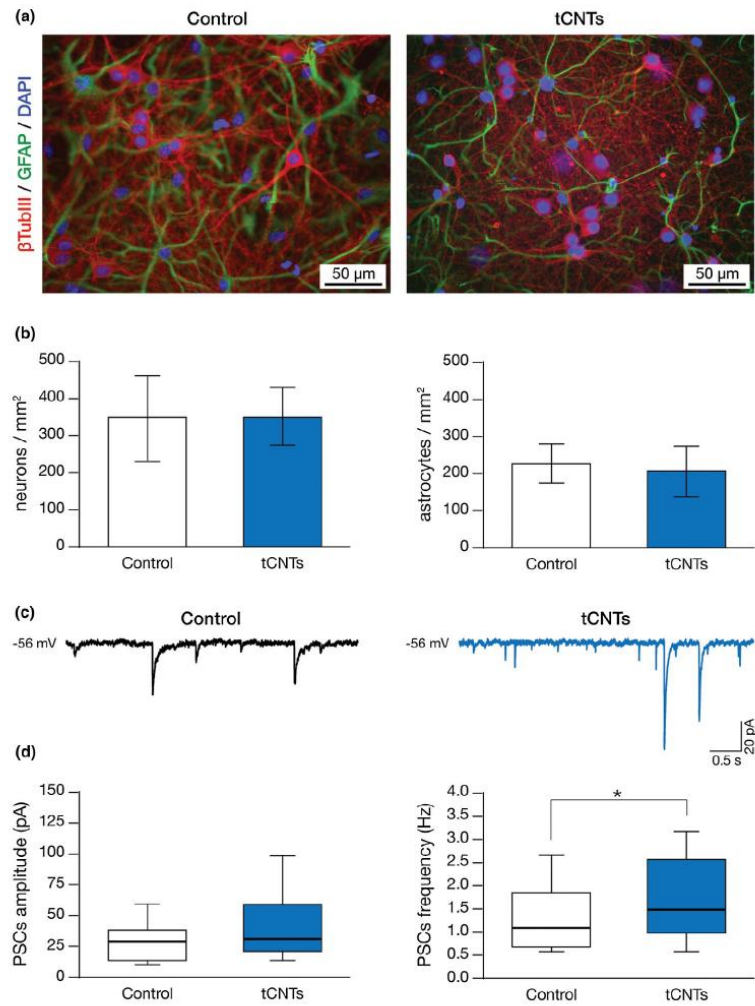


**FIGURE 2** tCNTs boost the spontaneous synaptic activity of hippocampal neurons. (a) representative fluorescent micrographs depicting dissociated primary cells networks grown on glass Control substrates (left) and on tCNTs substrates (right) stained against  $\beta$ -Tubulin III to point out neurons (in red), GFAP to highlight astrocytes (in green) and DAPI to stain cell nuclei (in blue). (b) Bar plots summarize the density values for neuron and glia in the two growth conditions, note the absence of differences. (c) Two representative current tracings from a Control neuron (in black) and from a tCNTs neuron (in blue). (d) Box plots summarize PSCs amplitudes and frequency values. Despite no significant changes in PSCs amplitudes, a significantly higher frequency of the PSC currents related to the tCNTs condition is visible (right,  $p = .03$ )

similar to Control substrates. We further addressed network synaptic activity by means of single neuron, whole-cell patch clamp recordings. Figure 2c shows sample current tracings of the basal spontaneous synaptic activity of Control and tCNTs neurons, characterized by the occurrence of heterogeneous events of inward currents, displaying variable amplitudes (Mazzatenta et al., 2007). We did not detect any significant variation in the mean amplitude values of the postsynaptic currents (PSCs) in tCNT-interfaced neurons ( $n = 59$  cells) when compared to Controls ( $n = 40$  cells; Controls:  $30 \pm 2.8$  pA; tCNTs  $44 \pm 5$  pA;  $p = .10$ ; box plots in Figure 2d, left), as well as in the membrane passive properties, such as the input resistance (Controls:  $790 \pm 104$  M $\Omega$ ; tCNTs:  $587 \pm 67$  M $\Omega$ ;  $p = .10$ ) and membrane capacitance (Controls:  $34 \pm 2$  pF; tCNTs:  $39 \pm 3$  pF;  $p = .20$ ). Conversely, we measured a significant ( $p = .03$ ) increase in the PSCs frequencies when comparing the two conditions (Controls:  $1.3 \pm 0.1$  Hz; tCNTs:  $1.8 \pm 0.1$  Hz; Figure 2d, right). By these preliminary tests, we concluded that the newly manufactured tCNTs allow hippocampal cell adhesion, viability, synaptic network development and promote enhanced synaptic activity, an effect reminiscent of what reported when interfacing neurons to CNT carpets (drop casted or thick CVD growth films; Cellot et al., 2009, 2011; Lovat et al., 2005; Mazzatenta et al., 2007; Rago et al., 2019).

### 2.3 | Organotypic entorhinal–hippocampal cultures growth interfaced to tCNTs

In the second set of experiments, we tested tCNTs, characterized by transparency and strong adhesion to the underneath fused silica substrate, as growth interfaces for intact and injured CNS explants. In particular, we focused on the entorhinal–hippocampal system. As shown by low-magnification immunofluorescence images in Figure 3a, intact EHC successfully grew interfaced to tCNTs, in a way similar to Controls EHCs (Figure 3a, right and left, respectively). To challenge the regenerative potential of the new tCNTs, we simulated a severe mechanical lesion at the subicular level by surgical complete transection. After transecting the tissue, the EC and hippocampus (H) components were cultured (8–12 DIV) at a distance of  $500 \pm 100$   $\mu$ m apart (Figure 3b; see Methods). Also after denervation, we detected adhesion, survival, and growth of the organotypic cultures on both tCNTs and Control (Figure 3b, right and left, respectively). We adopted this configuration to reproduce in vitro a traumatic event due to mechanical injury, resulting in anatomical and functional disconnection of the two brain regions. A severe perforant pathway (PP) transection at the subicular level is a widely exploited and generally accepted model to investigate neural circuits plasticity in response to brain injury, adopted in vivo and in organotypic slices (Perederiy & Westbrook, 2013; Vlachos et al., 2012; Vuksic et al., 2011).

We next investigated the functional impairments following the lesion and the residual neuronal activity in both the EC and H slices (Perederiy & Westbrook, 2013).

### 2.4 | tCNTs enhance the entorhinal–hippocampal field potential synchronization

We performed simultaneous local field potential (LFP) recordings by placing one electrode in the H within the molecular layer of the dentate gyrus (DG), and a second one within the deep layer (IV/V) of the EC. LFPs are voltage signals that reflect collective multiple neurons membrane activities. We compared the spontaneous basal activities emerging upon 8–12 DIV between intact EHC and the lesioned one, in which the PP was totally resected and the two (emi)-portions of the EHC displaced (see the cartoon in Figure 3c). Field recordings were performed in standard saline solution (see Methods) for intact and lesioned EHCs developed on glass substrates (sketched in Figure 4a;  $n = 7$  and  $n = 9$ , respectively) or interfaced with tCNTs (sketched in Figure 4b;  $n = 5$  and  $n = 6$ , respectively).

We quantified DG spontaneous activity when grown on Control glass substrates, by measuring the LFPs inter-event intervals (IEIs). Upon prolonged denervation, IEIs show a significant (cumulative distribution in Figure 4c, top plot for DG;  $p < .001$ ) increase in duration in lesioned EHCs when compared to the intact slices, testifying a reduction in DG excitation. Similarly, LFPs in EC on Control substrates showed a significant increase in IEIs duration in lesioned EHCs when compared to the intact slices (cumulative distribution in Figure 4c, bottom plot;  $p < .001$ ). Thus, in Control conditions, denervation usually determined a reduction in the occurrence of LFPs. When analyzing EHCs interfaced to tCNTs, in the intact organ slices we detected higher LFPs occurrence in DG when compared to glass Controls (cumulative distribution in Figure 4c, top plot;  $p < .001$ ). To note, in DG, LFPs activity was further enhanced after 8–12 DIV of denervation, even when compared to intact tCNTs cultures (i.e., lower IEI values; cumulative distribution in Figure 4c, top plot;  $p < .01$ ). A similar behavior was observed when measuring the distribution of IEIs values of LFPs recorded from the EC interfaced to tCNTs, in intact or injured EHC (cumulative distribution in Figure 4c, bottom plot;  $p < .001$ ). These results suggest that in intact slices, tCNTs interfacing promote an increase in spontaneous activity, reminiscent of the material effect detected in spinal slice cultures (Fabbro et al., 2012), and presumably due to the reported ability of CNT-based interfaces to enhance synaptic networks (Cellot et al., 2011; Fabbro et al., 2012; Lovat et al., 2005; Mazzatenta et al., 2007).

Regardless of the intact EHCs, in lesion ones tCNTs interfacing has the ability to promote LFP occurrence in both DG and EC slices when compared to injured glass Controls

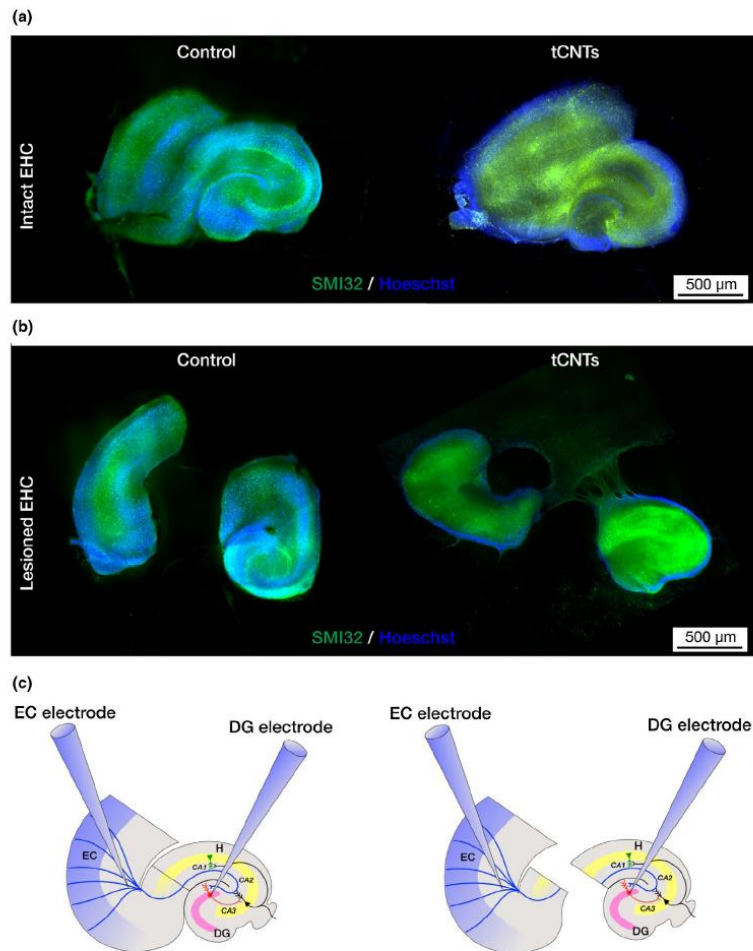


**FIGURE 3** tCNTs are suitable substrates for the development of healthy EHCs organotypic cultures. (a) Representative epifluorescence stitched images showing 8-day-old organotypic EHCs cultures stained with Hoetsch to make visible all cell nuclei (blue) and NeuN to highlight just neuronal nuclei (green) in the intact organotypic slice when cultured on glass Control (left) and tCNTs (right). (b) Representative images of 8-day-old lesioned EHCs organotypic cultures stained with Hoetsch (blue) and NeuN (green) and cultured on glass Control (left) and tCNTs (right). Both intact and lesioned EHC organotypic cultures displayed a similar morphology when grown on Control and tCNTs substrates. (c) Representative sketch depicting the experimental setup: entorhinal cortex (EC), the dentate gyrus (DG) in the hippocampus (H) and a clear vision of the perforant pathway (blue path) together with the Shaffer collaterals (black path) and mossy fiber pathway (red path). Field potential extracellular recordings were simultaneously performed from the EC (left electrode) and the hippocampal DG (right electrode) in the intact (left) and injured (right) EHC slice

(Figure 4d, blue and red box plots, respectively; Control:  $n = 9$ , tCNT:  $n = 6$ ;  $p < .001$ ), a result that might indicate the ability of tCNTs in promoting functional changes in excitatory synapses post-denervation, alternatively tCNTs might also favor regeneration and synaptic targeting of the injured PP axons (Usmani et al., 2016).

To assess whether tCNTs have the ability to promote PP regeneration and synaptic targeting, we assessed the functional connectivity between the DG and the EC in intact and lesion EHC when interfaced to the two different substrates by cross-correlation analysis of the simultaneously recorded, spontaneous LFPs. Interestingly, in intact EHC,



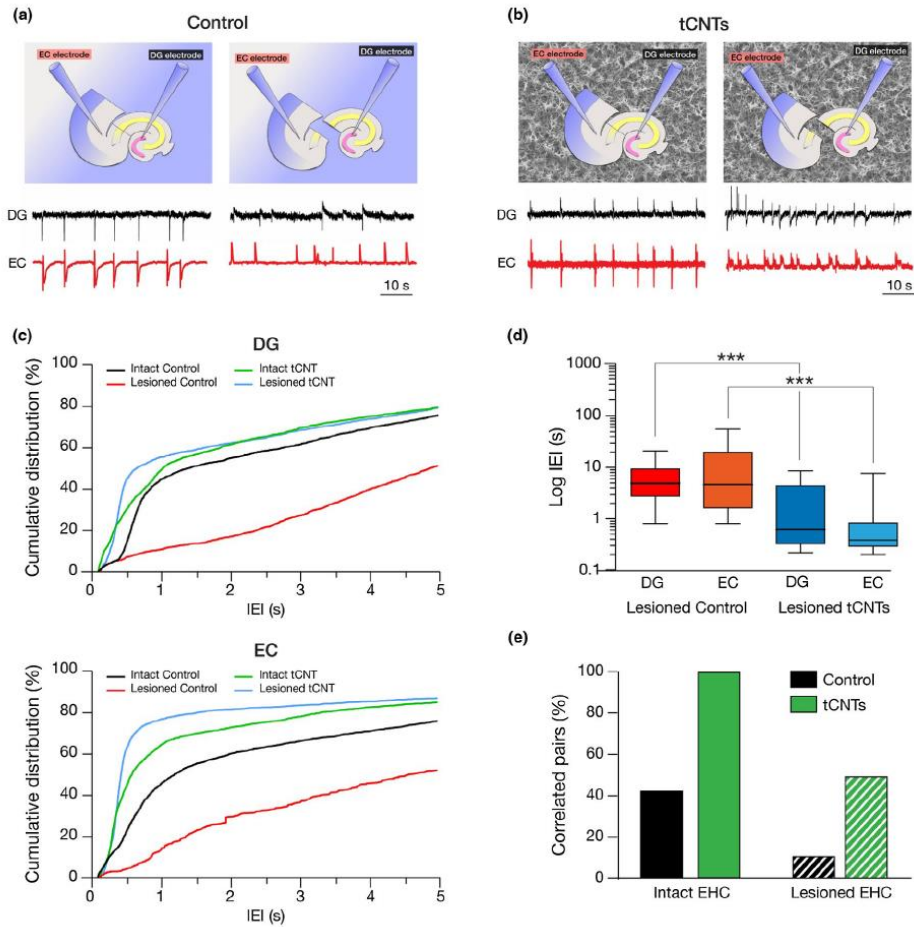


**FIGURE 4** tCNTs enhance the EC–DG signal synchronization in EHCs. (a) A sketch of the intact EHC (left) and the lesioned one (right) when cultured on glass slide Controls. Below, two representative voltage traces for the DG (black trace) and EC (red trace) are shown in standard saline solution. (b) A similar sketch of the intact EHC (left) and the lesioned one (right) when interfaced to tCNTs. Below, two representative voltage traces for the DG (black trace) and EC (red trace) are shown in standard saline solution. (c) The cumulative distribution function of IELs up to 5 s is shown for DG (top) and EC (bottom). When interfaced to tCNTs, the activity of both DG and EC is accelerated, as appreciable from the IELs cumulative distributions (green and blue lines), characterized by a significantly larger population of brief IELs when compared to glass Controls (black and red lines). (d) Box plots of IEL values for the lesioned EHC shown in logarithmic scale for Controls and tCNTs, note the significant drop in IELs duration in tCNTs-interfaced tissues. (e) Bar plots summarize the correlated DG and H pair recordings in intact and injured EHCs, both in Control and tCNT substrates

only 43% of Controls DG and EC displayed a Pearson's correlation coefficient (CCF) that was significantly larger than that expected by chance (see Methods; Usmani et al., 2016), such a value was increased to 100% in intact tCNT recordings (summarized by bar plot in Figure 4e). In lesioned EHCs, correlated LFPs dropped to 11% of Controls, while 50% of tCNTs LFPs recordings were still correlated

(bar plot in Figure 4e). Thus, injured EHC, upon 8–12 DIV interfaced to tCNTs, displayed a lower impairment in spontaneous LFPs characterized by a larger connectivity, as supported by the higher synchronization of the two segregated EHC portions. These results suggest that tCNTs enhanced the regeneration of PP fibers and promote synaptic targeting when interfacing lesioned EHC.

## 2.5 | tCNTs favor regrowth of active fibers in injured EHC slices

To assess whether tCNTs promoted new fibers sprouting leading to a more functional bridge between the EC and H sections, we tested the ability of stimulating EC superficial layers, where the PP is known to originate (Jacobson & Marcus, 2008; Witter, 2007; Witter & Amaral, 2004) in evoking LFPs in injured EHC. The two recording electrodes were positioned in the same configuration used for simultaneous recordings of DG and EC spontaneous LFPs, while an additional stimulating electrode was placed in the superficial

layers of the EC (see sketches in Figure 5a, left). We, therefore, proceeded with the PP stimulation (see Methods), and we grouped the evoked LFPs into three categories: the first, when the stimulation evoked successful responses from both EC and DG; the second, when the response was evoked only in the EC; or, third, only in the DG. Tracings in Figure 5a, right panel, shows sample voltage tracings depicting these three responses (in blue, green, and magenta, respectively), for the lesioned EHC.

In intact ECHs, regardless the presence of tCNTs, PP stimuli always evoked LFPs in both EC and DG (Figure 5b, top; Control:  $n = 4$ ; tCNTs:  $n = 4$ ). On the opposite,

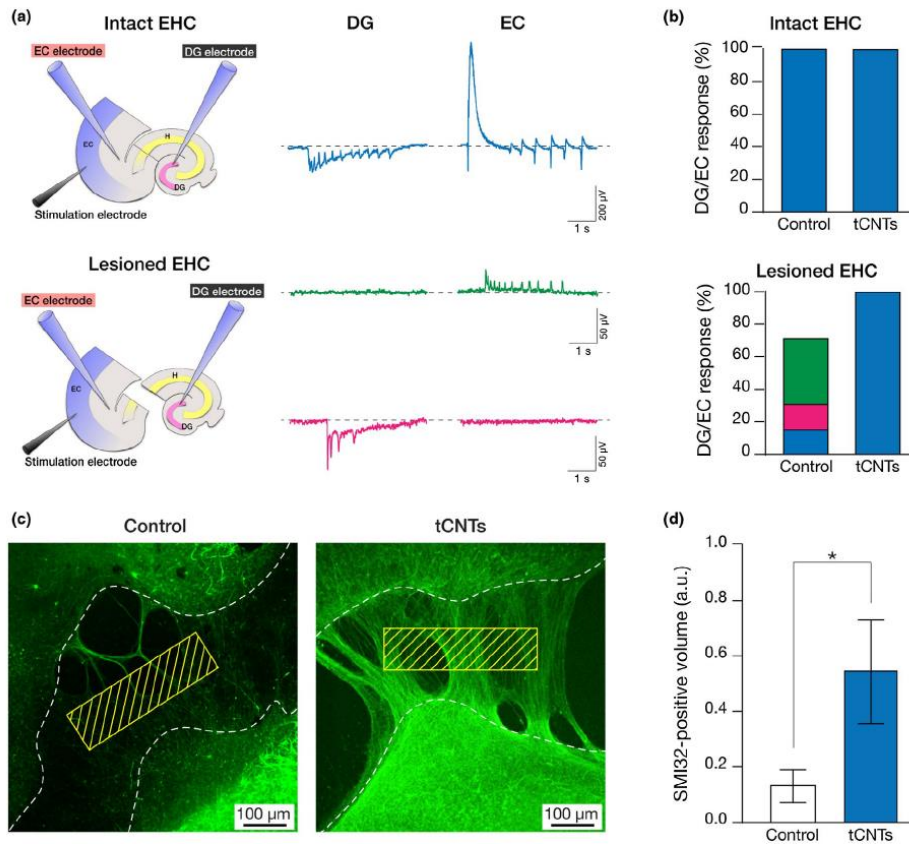


**FIGURE 5** tCNTs induce the sprouting of functionally active fibers crossing the lesioned area. (a) A sketch (left) of the experimental configuration used to evaluate EC/DG intercommunication ability through the PP in intact and lesioned EHC using a stimulation electrode inserted into the EC superficial layer. Some representative traces from DG and EC recordings of a lesioned EHC were shown (right). Note the three kind of evoked responses we could observe: simultaneously from both areas (in blue), just from EC (in green), and just from DG (in magenta). (b) Bar plots summarizing the distribution of the three categories of evoked responses in intact (top) and injured (bottom) EHC, both for Controls and tCNTs. (c) Representative confocal images showing the sprouting of SMI32-positive fibers (in green) into the lesioned area. As summarized in the bar plot in (d) cultures grown onto tCNTs displayed a significantly higher percentage of SMI32-positive volume with respect to Controls

in injured EHCs, evoked responses in the two groups diverged. In injured Control organ slices, only in 12.5% of cases PP stimulation evoked a LFP in both EC and DG, while in the majority of cases (50%) only EC responses were evoked. Intriguingly, in 12.5% of cases only LFP in DG was evoked, with the remaining 25% of slices unresponsive. Notably, in injured EHCs interfaced to tCNTs, we elicited evoked LFPs from both areas in 100% of cases, as in intact slices (Figure 5b, bottom; Control:  $n = 8$ ; tCNTs:  $n = 6$ ). This evidence further strengthens the hypothesis that the slices recovered a 1 (re)connection with similar evoked LFPs of the intact (i.e., not lesioned) structure when cultured onto tCNT platforms. Eventually, we investigated if the tCNT-related increase in EC/H synchronized activity and PP stimulation evoked responses were attributable to an increased number of newly generated fibers interconnecting the EC and H sections and able to carry effective electrochemical signals. To address this point, we performed via immunohistochemistry a quantification of SMI32-positive axons (see Methods) crossing the gap separating H and EC (Figure 5c). In injured EHC interfaced to tCNTs, we detected a significantly larger amount of SMI32-positive “crossing-fibers” sprouting into the lesioned area with respect to the Control counterparts (Control:  $n = 7$ , tCNT:  $n = 6$ ;  $p = .02$ ; Figure 5d). Together with the previous electrophysiological findings, this result shows that tCNTs enhanced the regeneration of axons and their synaptic targeting between EC and DG, re-establishing an active crosstalk between the two separated areas of the sectioned tissue.

### 3 | DISCUSSION

CNTs have contributed considerably to developments in tissue engineering (Edwards, Werkmeister, & Ramshaw, 2009) and nanomedicine (Erol et al., 2017; Marchesan, Kostarelos, Bianco, & Prato, 2015) due to their unique physical features (O’Connell, 2006) and hold the potential to further contribute to the design of novel nanodevices and neural interfaces (Bareket-Keren & Hanein, 2013; Pancrazio, 2008). In this study, we report a novel CCVD-based approach in CNT synthesis generating uniform carpets of entangled nanotubes on fused silica supporting substrates. Differently from commonly used CVD or drop casting CNT decorating methodologies (Chena, Lib, Linc, Hsud, & Wange, 2012; Lovat et al., 2005; Mazzatenta et al., 2007; Rago et al., 2019) by our new approach we manufactured optically transparent (Anguita et al., 2013) CNT substrates characterized by mechanical stability due to their strong adhesion to the underneath surface. These features made our novel films of tCNTs of particular interest in (neuro)-biology applications where the substrate mechanical stability and the use of techniques demanding

transmission of visible light through the samples are required. Our main results are that tCNT-based substrates when challenged with dissociated and organ CNS cultures were biocompatible, allowing the development of neuronal synaptic networks, and maintained CNT characterizing features of potentiating neural transmission at the interface (Cellot et al., 2011; Lovat et al., 2005; Rago et al., 2019) and promoting axons regrowth (Fabbro et al., 2012; Usmani et al., 2016).

Hippocampal dissociated cultures interfaced to tCNTs were characterized by CNS cell densities and neuron/glia ratios comparable to Controls; the viability of neurons on tCNTs was also supported by the values of the cell passive membrane properties, accepted indicators of neuronal health (Carp, 1992; Gao, Liu, Li, & Wang, 2015). Despite the similarities in network size, tCNTs neurons displayed increased synaptic activity, probably due to the described synaptogenic effects of CNTs, acting as artificial biomimetic clues (Cellot et al., 2011; Pampaloni et al., 2018; Rago et al., 2019).

We scaled up the system by developing organotypic cultures, to investigate the regenerative potentials of tCNTs. Organotypic CNS explants are a well-established technique, such slice cultures maintain a three-dimensional (3D) organization, preserve the cytoarchitecture and cell populations of the organ of origin and provide excellent experimental access to electrophysiology, live imaging, and morphology analyses (Fabbro et al., 2012; Usmani et al., 2016). Accordingly, EHC organ cultures are 3D explants of the CNS in which the overall functional and anatomical neuronal connections are preserved (Del Turco & Deller, 2007; Vlachos et al., 2012). In accordance with our previous studies (Fabbro et al., 2012) interfacing EHCs to tCNTs improved spontaneous network activity and potentiated LFP synchronization. We hypothesize that these effects are ultimately related to an increase in synaptic efficacy due to increased synapse formation at the interface with the large surface, roughness, and conductivity of tCNTs (Fabbro et al., 2012), although we cannot exclude other mechanisms, such as ability of the conductive tCNTs to mediate a direct electrical transmission within the cultured EHC areas.

To address the regenerative ability of tCNTs interfaces, we adopted the perforant patch lesion model, a brain injury model that disrupts the main excitatory input to the DG (Vlachos et al., 2012). Upon a complete transection of the PP, we cultured surgically separated H and EC components to the end of assessing denervation-induced regenerative activity reconnecting the two structures and eventually leading to functional recovery. Indeed in Controls such a procedure leads to a loss of activity in DG and EC structures, indicative of a limited regenerative ability. We did not detect any form of synaptic plasticity, such as homeostatic synaptic scaling, due to denervation (Vlachos et al., 2012). Although we cannot exclude that such changes need single cell recording approaches for being detected, it is also feasible that at the time



of recordings (>1 week after denervation) this transient adaptation to the loss of excitatory drive had returned to baseline values (Vlachos et al., 2012). tCNTs, upon axonal regeneration re-established the appropriate excitatory connections, at least in part, as indicated by evoked LFPs, synchronization of spontaneous LFPs and frequency of LFPs. The latter increase in activity, even higher than in intact structures, might indicate an overall increase in excitability, potentially due to long-lasting plasticity compensation, again sustained by the conductive substrates. In previous studies, we have shown that CNT-based interfaces possess regenerative abilities when interfaced to spinal cord explants (Fabbro et al., 2012; Usmani et al., 2016). In particular, an increased growth cone activity was associated to direct interactions among axons and CNTs, via formation of membrane/material tight junctions (Fabbro et al., 2012). Modulating mechanical forces and adhesion may activate cascades of biochemical signaling relevant to CNS reconstruction.

In conclusion, by introducing a new method to synthesize CNTs and demonstrating for the first time the benefits that this substrate is bringing to lesioned organotypic EHCs cultures, we strengthened the notion of the use of physical features alone to guide different biological responses: tCNTs, with their peculiar transparency coupled to the regenerative effects, stand as a promising material to be exploited in a broad range of applications, from the development of new research tools to the design of devices able to actively interface neural tissue reconstruction.

## 4 | MATERIALS AND METHODS

### 4.1 | tCNTs synthesis

MWNTs were synthesized by the decomposition of acetylene (carbon source) catalyzed by iron NPs. NPs were obtained thermally annealing a thin layer of iron evaporated on fused silica (SiO<sub>2</sub>) wafer chips, acting as transparent supporting substrates (Ward, Wei, & Ajayan, 2003). Fused silica wafers were manually cleaved into 15 × 15 mm<sup>2</sup> slices using a diamond scribe and cleaned following the Radio Corporation of America (RCA) method (Kern & Puotinen, 1970). Subsequently, a thin layer of iron (0.2–1 nm in thickness) was deposited directly above the SiO<sub>2</sub> chips surfaces using an electron beam (e-beam) evaporator. Iron film thickness was monitored using an in situ quartz crystal microbalance. Since catalyst layer uniformity plays a crucial role in CNTs synthesis and growth, an average deposition rate of 0.2 Å/s was adopted. The as-evaporated substrates were placed above the heating element of a high-vacuum reaction chamber. An annealing treatment (4 min at 660 ± 10°C in H<sub>2</sub> atmosphere) was performed to: (i) reduce iron oxides resulting from the exposition of the samples to the atmospheric

air during the transfer from the e-beam deposition system to the high-vacuum CVD reactor and (ii) to induce the nucleation from the continuous iron layer of homogeneously distributed NPs which will act as nucleation sites for the CNTs growth. Once this treatment process was over, acetylene was introduced in the reaction chamber up to a partial pressure of about 10–20 mbar. Sample temperature was increased to 730°C and reaction time was limited to 90 s, resulting in the formation of a uniform carpet of CNTs of less than 2 μm in thickness. After that, samples were let to cool down to room temperature (RT) and employed as removed from the reaction chamber.

### 4.2 | tCNTs characterization

Field emission scanning electron microscopy (FE-SEM) imaging was performed on the as-produced CNTs using a Gemini SUPRA 40 SEM (Carl Zeiss NTS GmbH, Oberkochen, Germany) operating at an accelerating voltage of 5 keV. Transmission electron microscopy (TEM) of CNT carpets was performed using an EM 208-Philips TEM system equipped with Quemesa (Olympus Soft Imaging Solutions) camera. Before TEM imaging, samples were released from the substrates, dispersed in ethanol and drop casted onto a commercial lacey carbon TEM grid. Transmission spectra in the visible spectral range (400–700 nm) were acquired with an Agilent Technologies Cary-60 UV-VIS spectrophotometer at a scan speed of 600 nm/min and 1-nm resolution. CCVD CNT film thicknesses were evaluated performing atomic force microscopy (Solver Pro, NT-MDT, RU) across a scratch in the film done with a scalpel and exposing the underneath fused silica substrate. Raman spectroscopy was conducted on the as-produced CNTs at RT employing a Renishaw inVia Raman microscope with a 60× objective lens at 632.8-nm laser excitation and a laser power of about 2 mW. In order to evaluate the CNTs surface composition, X-ray photoelectron spectroscopy (XPS) was carried out on a VG Escalab II spectrometer, in constant pass energy mode. Non-monochromatized Al Kα exciting radiation (1,486.6 eV, 225 W) was used. Core-level XPS data analysis was performed after the removal of nonlinear Shirley background and deconvolution into Gaussian/Lorentzian components using Igor Pro 6.36 software (Wavemetrics Co., US).

### 4.3 | Ethics

All procedures were approved by the local veterinary authorities and performed in accordance with the Italian law (decree 26/14) and the UE guidelines (2007/526/CE and 2010/63/UE). The animal use was approved by the Italian Ministry of Health. All efforts were made to minimize suffering and to reduce the number of animals used.



#### 4.4 | Primary cultures

Hippocampal neurons were obtained from neonatal Wistar rats (postnatal day: P2–P3) as previously reported (Cellot et al., 2009; Lovat et al., 2005). Briefly, cells were plated either on poly-L-ornithine-coated (Sigma Aldrich; Controls) or on tCNTs-coated glass coverslips and incubated at 37°C, 5% CO<sub>2</sub>, in Neurobasal-A (Thermo Fischer) medium containing B27 2% (Gibco), Glutamax 10 mM, and Gentamycin 0.5 μM (Gibco). Cultured neurons were used for experiments at 8–10 DIV.

#### 4.5 | Organotypic cultures

Organotypic slice cultures were prepared according to the roller tube technique, previously described (Gähwiler, 1988; Mohajerani & Cherubini, 2005). Briefly, 400-μm-thick EHCs slices were obtained from P6 to P8-old Wistar rats (the perforant pathway is described to be fully developed in rats from P6; Fricke & Cowan, 1977) by means of a tissue chopper (McIlwan) and stored for 1h in cold (4°C) Gey's Balanced Salt Solution medium (GBSS) enriched with glucose and kynurenic acid to limit excitotoxic processes. The slices were subsequently plated onto glass Control coverslips or tCNTs covered fused silica slices and embedded in chicken plasma (16 μl; SIGMA), which was coagulated with the addition of a drop of thrombin (23 μl). The lesion was made with a scalpel and under microscopy at the subicular level and the EC portion was placed from 400 to 600 μm far from the hippocampus one. This was accomplished taking advantage of a graduated ruler placed below the coverslips during plating. Cultures were then left for 1 hr at RT and then placed in Nunc™ tubes filled with 750 ml of Neurobasal-A (Thermo Fischer) medium containing B27 2% (Gibco), Glutamax 10 mM and Gentamycin 0.5 μM (Gibco). Tubes were incubated at 37°C in a roller drum (0.17 RPM) and used for experiments after 8–12 DIV. The medium was completely replaced every 3 days.

#### 4.6 | Patch-clamp experiments

Patch-clamp, whole-cell recordings were achieved with glass micropipettes with a resistance of 4–7 MΩ. The intracellular pipette solution was the following: 120 mM K-glucuronate, 20 mM KCl, 10 mM HEPES, 10 mM EGTA, 2 mM MgCl<sub>2</sub>, 2 mM Na<sub>2</sub>ATP, and pH 7.3. Cultures were positioned in a custom-made chamber mounted on an inverted microscope (Eclipse TE-200, Nikon, Japan) and continuously superfused with external solution at a rate of 5 ml/min. The external saline solution contained: 150 mM NaCl, 4 mM KCl, 1 mM MgCl<sub>2</sub>, 2 mM CaCl<sub>2</sub>, 10 mM HEPES, 10 mM glucose, and pH 7.4. Cells were voltage clamped at a holding potential of −56 mV (not corrected for liquid

junction potential, that was calculated to be 13.7 mV at 20°C in our experimental conditions). The (uncompensated) series resistance had values lower than 8 MΩ. All recordings were performed at RT. Data were collected using a Multiclamp 700A patch amplifier connected to a PC through a Digidata 1440 (Molecular Devices, US) and subsequently analyzed using Clampfit 10.4 software suite (Molecular Devices, US).

#### 4.7 | Field potential recordings

Simultaneous extracellular field potential recordings from visually identified molecular layer of the DG and the superficial layers of the EC were performed on slices at 8–12 DIV at RT using low resistance (4–6 MΩ) glass micropipettes filled with extracellular solution. For each experiment, the organotypic slices were cultured onto Control glass coverslips and tCNT-decorated fused silica slides, positioned into a recording chamber, mounted onto an upright microscope (Eclipse TE-200, Nikon, Japan) and superfused with standard saline solution containing: 152 mM NaCl, 4 mM KCl, 1 mM MgCl<sub>2</sub>, 2 mM CaCl<sub>2</sub>, 10 mM HEPES, and 10 mM glucose. The pH was adjusted to 7.4 with NaOH. After a stabilization period of about 20 min, the recordings of the spontaneous activity were sampled for additional 45 min in standard saline solution. Finally, as control of the excitatory nature of the recorded neuronal signals, we evaluated the activity for 15 min in the presence of CNQX (10 μM) and no LFPs were detected. All data were collected using a Multiclamp 700A amplifier connected to a PC through a Digidata 1440 (Molecular Devices, US) and subsequently analyzed using Clampfit 10.4 software suite (Molecular Devices, US). To stimulate the PP we placed a bipolar electrode, made by a low-resistance patch pipette containing normal saline solution, into the EC superficial layers, no changes in the electrode position were made. Voltage pulses (from 200 to 1,000 μs) of increasing amplitude (from 1 to 50 V) were delivered by an isolated voltage stimulator (DS2A; Digitimer Ltd.) until a response was evoked and detected. The synchrony between DG and EC LFPs was assessed through a MATLAB custom-made script, as previously described (Usmani et al., 2016). Briefly, for each pair of voltage time series, the Pearson correlation coefficient (CCF) was assessed and its statistical significance was determined by performing a permutation test. This test measures the distribution of correlation coefficients that one would expect to observe if the voltage signals recorded from a pair of explants happened to correlate purely by chance. By measuring how likely it was for the values of this null distribution to be larger or equal than the real correlation coefficient, it was possible to understand whether the correlation between the pair of time series was significantly larger than expected by chance. This procedure allowed for determining what fraction of cocultured slices exhibited a significantly

synchronous LFPs, for all the tested conditions (Aurand et al., 2017; Usmani et al., 2016).

#### 4.8 | Immunocytochemistry and microscopy

To visualize dissociated hippocampal neurons, we fixed cultures in 4% formaldehyde (prepared from fresh paraformaldehyde; Sigma) in PBS for 20 min, permeabilized with 0.3% Triton X-100 and incubated with primary antibodies for 30 min at RT. After washing in PBS, cultures were incubated with secondary antibodies for 45 min and then mounted with Vectashield® (Vector Laboratories) on 1-mm-thick microscope glass slides. To visualize neurons and glial cells, we used the following: rabbit anti- $\beta$ -Tubulin III primary antibody (Sigma T2200, 1:250 dilution), and Alexa 594 goat anti-rabbit secondary antibody (Thermo-Fisher, 1:500); anti-GFAP mouse primary antibody (SIGMA, 1:250) and Alexa 488-goat anti-mouse secondary antibody (Thermo-Fisher, 1:500). Cell nuclei were visualized with the nuclear marker DAPI (1:1,000). Cultures were imaged with an epifluorescence microscope using 10 $\times$  and 20 $\times$  objectives (DM 6000, Leica) and analyzed with the open-source software ImageJ (<http://rsb.info.nih.gov/ij/>). To stain Organotypic cultures we fixed them for 1h at RT as described above. After PBS washes, cultures were incubated with mouse SMI32 (1:250) and rabbit NeuN (SIGMA; 1:200) primary antibodies, and Alexa 594 goat anti-rabbit (Invitrogen, 1:500), Alexa 488 goat anti-mouse (Invitrogen, 1:500) secondary antibodies and Hoechst (Invitrogen; 1:1,000). Cultures were then mounted with Vectashield® (Vector Laboratories) on 1-mm-thick microscope glass slides, visualized with a confocal microscope (Nikon Eclipse Ti-E; 10 $\times$  objective) and analyzed with the Volocity image analysis software (Perkin Elmer). To quantify the SMI32-positive “crossing-fibers,” we selected 3D region of interest (ROI) (500  $\mu$ m  $\times$  50  $\mu$ m  $\times$  15  $\mu$ m) in the gap between the H and the HC (with the ROI longitudinal axis perpendicular to the segment connecting the centers of the two EHC emi-sections, see Figure 5c) in both Controls and tCNTs cultures. The amount of SMI32-positive voxel within each ROI was quantified for each image, and normalized to the overall ROI volume. All the image values from the same condition were then averaged together and plotted.

#### 4.9 | Statistics

All reported values are expressed as means  $\pm$  SD, with n indicating the number of cultures, unless otherwise specified. Statistically significant differences between pairs of data sets were assessed by Student's *t*-test (after validation of variance homogeneity by Levene's test) for parametric data and by either the Mann–Whitney U test or the Kolmogorov–Smirnov test for nonparametric data. When multiple groups were compared, Kruskal–Wallis test was used. Correlation and IIEs of

local field potentials were measured through two different custom programs wrote in MATLAB (The MathWorks, Inc., Natick, Massachusetts, United States) (Usmani et al., 2016). Statistical significance was determined at  $p < .05$ .

#### ACKNOWLEDGMENTS

The authors would like to thank TASC-IOM for Clean Room assistance, Alois Bonifacio for technical support and discussion in Raman spectroscopy experiments, Paolo Bertoncin for technical support in TEM characterization, Alessio Ansuini and Gianfranco Fortunato for MATLAB scripting, and Beatrice Pastore for her technical support in the organotypic culturing.

#### CONFLICT OF INTEREST

The authors declare that they have no competing interests.

#### AUTHOR CONTRIBUTIONS

D.S., L.B., and A.G. conceived the study and wrote the MS; N.P.P., I.R., and I.C. carried out the experiments and analysis. L.C. contributed to the XPS characterization and analysis.

#### DATA AVAILABILITY STATEMENT

All data needed to evaluate the conclusions in the paper are present in the paper. Additional data related to this paper may be requested from the authors.

#### ORCID

Laura Ballerini  <https://orcid.org/0000-0001-8420-0787>

#### REFERENCES

- Anguita, J. V., Cox, D. C., Ahmad, M., Tan, Y. Y., Allam, J., & Silva, S. R. P. (2013). Highly transmissive carbon nanotube forests grown at low substrate temperature. *Advanced Functional Materials*, 23, 5502–5509. <https://doi.org/10.1002/adfm.201300400>
- Antunes, E. F., Lobo, A. O., Corat, E. J., & Trava-Airoldi, V. J. (2007). Influence of diameter in the Raman spectra of aligned multi-walled carbon nanotubes. *Carbon*, 45(5), 913–921. <https://doi.org/10.1016/j.carbon.2007.01.003>
- Aurand, E. R., Usmani, S., Medelin, M., Scaini, D., Bosi, S., Rosselli, F., ... Ballerini, L. (2017). Nanostructures to engineer 3D neural interfaces: Directing axonal navigation toward successful bridging of spinal segments. *Advanced Functional Materials*, 28, 1700550. <https://doi.org/10.1002/adfm.201700550>
- Bareket-Keren, L., & Hanein, Y. (2013). Carbon nanotube-based multi electrode arrays for neuronal interfacing: Progress and prospects. *Frontiers in Neural Circuits*, 9, 122. <https://doi.org/10.3389/fncir.2012.00122>

- Bayer, B. C., Hofmann, S., Castellarin-Cudia, C., Blume, R., Baecht, C., Esconjauregui, S., ... Robertson, J. (2011). Support-catalyst-gas interactions during carbon nanotube growth on metallic Ta films. *The Journal of Physical Chemistry C*, *115*, 4359–4369. <https://doi.org/10.1021/jp102986f>
- Bulusheva, L. G., Okotrub, A. V., Kinloch, I. A., Asanov, I. P., Kurennya, A. G., Kudashov, A. G., ... Song, H. (2008). Effect of nitrogen doping on Raman spectra of multi-walled carbon nanotubes. *Physica Status Solidi (B) Basic Research*, *245*, 1971–1974.
- Carp, J. S. (1992). Physiological properties of primate lumbar motoneurons. *Journal of Neurophysiology*, *68*, 1121–1132. <https://doi.org/10.1152/jn.1992.68.4.1121>
- Cellot, G., Cilia, E., Cipollone, S., Rancic, V., Sucapane, A., Giordani, S., ... Ballerini, L. (2009). Carbon nanotubes might improve neuronal performance by favouring electrical shortcuts. *Nature Nanotechnology*, *4*, 126–133. <https://doi.org/10.1038/nnano.2008.374>
- Cellot, G., Toma, F. M., Varley, Z. K., Laishram, J., Villari, A., Quintana, M., ... Ballerini, L. (2011). Carbon nanotube scaffolds tune synaptic strength in cultured neural circuits: Novel frontiers in nanomaterial-tissue interactions. *Journal of Neuroscience*, *31*, 12945–12953. <https://doi.org/10.1523/JNEUROSCI.1332-11.2011>
- Cetin, M., Gumru, S., & Aricioglu, F. (2012). Nanotechnology applications in neuroscience: Advances, opportunities and challenges. *Bulletin of Clinical Psychopharmacology*, *22*, 115–120. <https://doi.org/10.5455/bcp.20120621044747>
- Charlier, J. C. (2002). Defects in carbon nanotubes. *Accounts of Chemical Research*, *35*, 1063–1069.
- Chena, C., Lib, C., Linc, K., Hsud, T., & Wange, S. (2012). A green process to prepare hydrophobic and transparent CNT-based surface. *Key Engineering Materials*, *521*, 171–178. <https://doi.org/10.4028/www.scientific.net/KEM.521.171>
- Chiang, W.-H., & Sankarana, R. M. (2007). Microplasma synthesis of metal nanoparticles for gas-phase studies of catalyzed carbon nanotube growth. *Applied Physics Letters*, *91*, 121503.
- Chiodarelli, N., Richard, O., Bender, H., Heyns, M., De Gendt, S., Groeseneken, G., & Vereecken, P. M. (2012). Correlation between number of walls and diameter in multiwall carbon nanotubes grown by chemical vapor deposition. *Carbon*, *50*, 1748–1752. <https://doi.org/10.1016/j.carbon.2011.12.020>
- Costa, S., Borowiak-Palen, E., Kruszyńska, M., Bachmatiuk, A., & Kalenczuk, R. J. (2008). Characterization of carbon nanotubes by Raman spectroscopy. *Materials Science-Poland*, *26*, 433–441.
- Del Turco, D., & Deller, T. (2007). Organotypic entorhino-hippocampal slice cultures—a tool to study the molecular and cellular regulation of axonal regeneration and collateral sprouting in vitro. *Methods in Molecular Biology*, *399*, 55–66.
- Edwards, S. L., Werkmeister, J. A., & Ramshaw, J. A. (2009). Carbon nanotubes in scaffolds for tissue engineering. *Expert Review of Medical Devices*, *6*, 499–505. <https://doi.org/10.1586/erd.09.29>
- Eleftheriou, C. G., Zimmermann, J. B., Kjeldsen, H. D., David-Pur, M., Hanein, Y., & Sernagora, E. (2017). Carbon nanotube electrodes for retinal implants: A study of structural and functional integration over time. *Biomaterials*, *112*, 108–121. <https://doi.org/10.1016/j.biomaterials.2016.10.018>
- Erol, O., Uyan, I., Hatip, M., Yilmaz, C., Tekinay, A. B., & Guler, M. O. (2017). Recent advances in bioactive 1D and 2D carbon nanomaterials for biomedical applications. *Nanomedicine*, *17*, 30089.
- Fabbro, A., Villari, A., Laishram, J., Scaini, D., Toma, F. M., Turco, A., ... Ballerini, L. (2012). Spinal cord explants use carbon nanotube interfaces to enhance neurite outgrowth and to fortify synaptic inputs. *ACS Nano*, *6*, 2041–2055. <https://doi.org/10.1021/nn203519r>
- Finnie, J. W., & Blumbergs, P. C. (2002). Traumatic Brain Injury. *Veterinary Pathology*, *39*, 679–689. <https://doi.org/10.1354/vp.39-6-679>
- Fricke, R., & Cowan, W. M. (1977). An autoradiographic study of the development of the entorhinal and commissural afferents to the dentate gyrus of the rat. *The Journal of Comparative Neurology*, *173*, 231–250.
- Gähwiler, B. H. (1988). Organotypic cultures of neural tissue. *Trends in Neuroscience*, *11*, 484–489. [https://doi.org/10.1016/0166-2236\(88\)90007-0](https://doi.org/10.1016/0166-2236(88)90007-0)
- Gao, Y., Liu, L., Li, Q., & Wang, Y. (2015). Differential alterations in the morphology and electrophysiology of layer II pyramidal cells in the primary visual cortex of a mouse model prenatally exposed to LPS. *Neuroscience Letters*, *591*, 138–143. <https://doi.org/10.1016/j.neulet.2015.02.043>
- Girgis, F., Pace, J., Sweet, J., & Miller, J. P. (2016). Hippocampal neurophysiologic changes after mild traumatic brain injury and potential neuromodulation treatment approaches. *Frontiers in Systems Neuroscience*, *10*, 8.
- Guggenmos, D. J., Azin, M., Barbay, S., Mahnken, J. D., Dunham, C., Mohseni, P., & Nudo, R. J. (2013). Restoration of function after brain damage using a neural prosthesis. *Proceedings of the National Academy of Sciences*, *110*, 21177–21182.
- Hofmann, S., Blume, R., Wirth, C. T., Cantoro, M., Sharma, R., Ducafi, C., ... Robertson, J. (2009). State of transition metal catalysts during carbon nanotube growth. *Journal of Physical Chemistry C*, *113*, 1648–1656.
- Hokkanen, M., Lautala, S., Flahaut, E., & Ahlskog, M. (2017). Experimental studies on the detachment of multi-walled carbon nanotubes by a mobile liquid interface. *Colloids and Surfaces A: Physicochemical and Engineering Aspects*, *533*, 109–115. <https://doi.org/10.1016/j.colsurfa.2017.08.029>
- Huber, D., Oskooei, A., Casadevall i Solvas, X., DeMello, A., & Kaigala, G. V. (2018). Hydrodynamics in cell studies. *Chemical Reviews*, *118*, 2042–2079.
- Iijima, S. (1991). Helical microtubules of graphitic carbon. *Nature*, *354*, 56–58. <https://doi.org/10.1038/354056a0>
- Jacobson, S., & Marcus, E. M. (2008). *Neuroanatomy for the neuroscientist*. New York, NY: Springer.
- Kern, W., & Puotinen, D. A. (1970). Cleaning solutions based on hydrogen peroxide for use in silicon semiconductor technology. *RCA Review*, *31*, 187–206.
- Kim, K. K., Park, J. S., Kim, S. J., Geng, H. Z., An, K. H., Yang, C. M., ... Lee, Y. H. (2007). Dependence of Raman spectra G band intensity on metallicity of single-wall carbon nanotubes. *Physical Review B*, *76*, 205426.
- Lee, C. J., Park, J., Huh, Y., & Lee, J. Y. (2001). Temperature effect on the growth of carbon nanotubes using thermal chemical vapor deposition. *Chemical Physics Letters*, *343*, 33–38. [https://doi.org/10.1016/S0009-2614\(01\)00680-7](https://doi.org/10.1016/S0009-2614(01)00680-7)
- Lee, J. K., Baac, H., Song, S. H., Jang, E., Lee, S. D., Park, D., & Kim, S. J. (2006). Neural prosthesis in the wake of nanotechnology: Controlled growth of neurons using surface nanostructures. *Acta Neurochirurgica Supplementum*, *99*, 141–144.



- Li, D., Field, P. M., Starega, U., Li, Y., & Raisman, G. (1993). Entorhinal axons project to dentate gyrus in organotypic slice co-culture. *Neuroscience*, *52*, 799–813. [https://doi.org/10.1016/0306-4522\(93\)90530-S](https://doi.org/10.1016/0306-4522(93)90530-S)
- Li, D., Field, P. M., Yoshioka, N., & Raisman, G. (1994). Axons regenerate with correct specificity in horizontal slice culture of the postnatal rat entorhino-hippocampal system. *European Journal of Neuroscience*, *6*, 1026–1037.
- Long, D. A. (1997). *Raman spectroscopy*. London, UK: McGraw-Hill.
- Lovat, V., Pantarotto, D., Lagostena, L., Cacciari, B., Grandolfo, M., Righi, M., ... Ballerini, L. (2005). Carbon nanotube substrates boost neuronal electrical signaling. *Nano Letters*, *5*, 1107–1110. <https://doi.org/10.1021/nl050637m>
- Maas, A. I., Stocchetti, N., & Bullock, R. (2008). Moderate and severe traumatic brain injury in adults. *The Lancet Neurology*, *7*, 728–741.
- Marchesan, S., Kostarelos, K., Bianco, A., & Prato, M. (2015). The winding road for carbon nanotubes in nanomedicine. *Materials Today*, *18*, 12–19. <https://doi.org/10.1016/j.mattod.2014.07.009>
- Mattevi, C., Wirth, C. T., Hofmann, S., Blume, R., Cantoro, M., Ducati, C., ... Robertson, J. (2008). In-situ X-ray photoelectron spectroscopy study of catalyst–support interactions and growth of carbon nanotube forests. *Journal of Physical Chemistry C*, *112*, 12207–12213.
- Mazzatenta, A., Giugliano, M., Campidelli, S., Gambazzi, L., Businaro, L., Markram, H., ... Ballerini, L. (2007). Interfacing neurons with carbon nanotubes: Electrical signal transfer and synaptic stimulation in cultured brain circuits. *Journal of Neuroscience*, *27*, 6931–6936. <https://doi.org/10.1523/JNEUROSCI.1051-07.2007>
- Michaelis, F. B., Weatherup, R. S., Bayer, B. C., Bock, M. C., Sugime, H., Caneva, S., ... Hofmann, S. (2014). Co-catalytic absorption layers for controlled laser-induced chemical vapor deposition of carbon nanotubes. *ACS Applied Materials & Interfaces*, *6*, 4025–4032. <https://doi.org/10.1021/am405460r>
- Mohajerani, M. H., & Cherubini, E. (2005). Spontaneous recurrent network activity in organotypic rat hippocampal slices. *European Journal of Neuroscience*, *22*, 107–118.
- Morassutto, M., Tiggelaar, R. M., Smithers, M. A., & Gardeniers, G. E. (2016). Vertically aligned carbon nanotube field emitter arrays with Ohmic base contact to silicon by Fe-catalyzed chemical vapor deposition. *Materials Today Communications*, *7*, 89–100. <https://doi.org/10.1016/j.mtcomm.2016.04.007>
- Mudimela, P. R., Scardamaglia, M., González-León, O., Reckinger, N., Snyders, R., Llobet, E., ... Colomer, J. (2014). Gas sensing with gold-decorated vertically aligned carbon nanotubes. *Beilstein Journal of Nanotechnology*, *5*, 910–918.
- Nelson, C. (2017). From static to animated: Measuring mechanical forces in tissues. *Journal of Cell Biology*, *216*, 29–30.
- O'Connell, M. J. (2006). *Carbon nanotubes: Properties and applications* (1st ed.). CRC Press, Taylor e Francis Group.
- Okpalugo, T. I. T., Papakonstantinou, P., Murphy, H., McLaughlin, J. A. D., & Brown, N. M. D. (2005). High resolution XPS characterization of chemical functionalised MWCNTs and SWCNTs. *Carbon*, *43*, 153–161. <https://doi.org/10.1016/j.carbon.2004.08.033>
- Pampaloni, N. P., Scaini, D., Perissinotto, F., Bosi, S., Prato, M., & Ballerini, L. (2018). Sculpting neurotransmission during synaptic development by 2D nanostructured interfaces. *Nanomedicine*, *14*, 2521–2532. <https://doi.org/10.1016/j.nano.2017.01.020>
- Pancrazio, J. J. (2008). Neural interfaces at the nanoscale. *Nanomedicine (London)*, *3*, 823–830. <https://doi.org/10.2217/17435889.3.6.823>
- Parnavelas, J., Lynch, G., Brecha, N., Cotman, C., & Globus, A. (1974). Spine loss and regrowth in hippocampus following deafferentation. *Nature*, *248*, 71–73. <https://doi.org/10.1038/248071a0>
- Perederiy, J. V., Luikart, B. W., Schnell, E., & Westbrook, G. L. (2013). Neural injury alters proliferation and integration of adult-generated neurons in the dentate gyrus. *Journal of Neuroscience*, *33*, 4754–4767.
- Perederiy, J. V., & Westbrook, G. L. (2013). Structural plasticity in the dentate gyrus—Revisiting a classic injury model. *Frontiers in Neural Circuits*, *7*, 17. <https://doi.org/10.3389/fncir.2013.00017>
- Perlmutter, J. S., & Mink, J. W. (2006). Deep brain stimulation. *Annual Review of Neuroscience*, *29*, 229–257.
- Rago, I., Rauti, R., Bevilacqua, M., Calaresu, I., Pozzato, A., Cibinel, M., ... Scaini, D. (2019). Carbon nanotubes, directly grown on supporting surfaces, improve neuronal activity in hippocampal neuronal networks. *Advanced Biosystems*, *3*(5), 1800286–https://doi.org/10.1002/adbi.201800286.
- Roeges, N. P. G. (1997). *A guide to the complete interpretation of infrared spectra of organic structures*. Chichester, UK: John Wiley and Sons.
- Saito, R., Grüneis, A., Samsonidze, G. G., Brar, V. W., Dresselhaus, G., Dresselhaus, M. S., ... Filho, A. G. S. (2003). Double resonance Raman spectroscopy of single-wall carbon nanotubes. *New Journal of Physics*, *5*, 157.
- Shah, K. A., & Tali, B. A. (2016). Synthesis of carbon nanotubes by catalytic chemical vapour deposition: A review on carbon sources, catalysts and substrates. *Materials Science in Semiconductor Processing*, *41*, 67–82. <https://doi.org/10.1016/j.mssp.2015.08.013>
- Steward, O., & Vinsant, S. L. (1983). The process of reinnervation in the dentate gyrus of the adult rat: A quantitative electron microscopic analysis of terminal proliferation and reactive synaptogenesis. *Journal of Comparative Neurology*, *214*, 370–386.
- Tscherter, A., Heuschkel, M., Renaud, P., & Streit, J. (2001). Spatiotemporal characterization of rhythmic activity in rat spinal cord slice cultures. *European Journal of Neuroscience*, *14*, 179–190.
- Usmani, S., Aurand, E. R., Medelin, M., Fabbro, A., Scaini, D., Laishram, J., ... Ballerini, L. (2016). 3D meshes of carbon nanotubes guide functional reconnection of segregated spinal explants. *Science Advances*, *2*, e1600087. <https://doi.org/10.1126/sciadv.1600087>
- Vidu, R., Rahman, M., Mahmoudi, M., Enachescu, M., Poteca, T. D., & Opris, I. (2014). Nanostructures: A platform for brain repair and augmentation. *Frontiers in Systems Neuroscience*, *8*, 91.
- Vitale, F., Summerson, S. R., Aazhang, B., Kemere, C., & Pasquali, M. (2015). Neural stimulation and recording with bidirectional, soft carbon nanotube fiber microelectrodes. *ACS Nano*, *9*, 4465–4474. <https://doi.org/10.1021/acs.nano.5b01060>
- Vlachos, A., Becker, D., Jedlicka, P., Winkels, R., Roeper, J., & Deller, T. (2012). Entorhinal denervation induces homeostatic synaptic scaling of excitatory postsynapses of dentate granule cells in mouse organotypic slice cultures. *PLoS ONE*, *7*, e32883. <https://doi.org/10.1371/journal.pone.0032883>
- Vuksic, M., Del Turco, D., Vlachos, A., Schuldt, G., Müller, C. M., Schneider, G., & Deller, T. (2011). Unilateral entorhinal denervation leads to long-lasting dendritic alterations of mouse hippocampal granule cells. *Experimental Neurology*, *230*, 176–185.

- Wang, M., Mi, G., Shi, D., Bassous, N., Hickey, D., & Webster, T. J. (2017). Nanotechnology and nanomaterials for improving neural interfaces. *Advanced Functional Materials*, *28*, 1700905.
- Ward, J. W., Wei, B. Q., & Ajayan, P. M. (2003). Substrate effects on the growth of carbon nanotubes by thermal decomposition of methane. *Chemical Physics Letters*, *376*, 717–725.
- Witter, M. P. (2007). The perforant path: Projections from the entorhinal cortex to the dentate gyrus. *Progress in Brain Research*, *163*, 43–61.
- Witter, M. P., & Amaral, D. G. (2004). Hippocampal formation. In G. Paxinos (Ed.), *The rat nervous system* (3rd ed., Vol. 3, pp. 511–573). Amsterdam, The Netherlands: Elsevier.
- Woodhams, P. L., & Atkinson, D. J. (1996). Regeneration of entorhino-dentate projections in organotypic slice cultures: Mode of axonal regrowth and effects of growth factors. *Experimental Neurology*, *140*, 68–78. <https://doi.org/10.1006/exnr.1996.0116>
- Woodhams, P. L., Atkinson, D. J., & Raisman, G. (1993). Rapid decline in the ability of entorhinal axons to innervate the dentate gyrus with increasing time in organotypic co-culture. *European Journal of Neuroscience*, *5*, 1596–1609. <https://doi.org/10.1111/j.1460-9568.1993.tb00229.x>
- Zhang, L., Li, Z., Tan, Y., Lolli, G., Sakulchaichroen, N., Requejo, F. G., ... Resasco, E. D. (2006). Influence of a top crust of entangled nanotubes on the structure of vertically aligned forests of single-walled carbon nanotubes. *Chemistry of Materials*, *18*, 5624–5629. <https://doi.org/10.1021/cm061783b>

**How to cite this article:** Pampaloni NP, Rago I, Calaresu I, et al. Transparent carbon nanotubes promote the outgrowth of entorhino-dentate projections in lesioned organ slice cultures. *Develop Neurobiol.* 2019;00:1–16. <https://doi.org/10.1002/dneu.22711>

# Carbon Nanotubes, Directly Grown on Supporting Surfaces, Improve Neuronal Activity in Hippocampal Neuronal Networks

Ilaria Rago, Rossana Rauti, Manuela Bevilacqua, Ivo Calaresu, Alessandro Pozzato, Matteo Cibinel, Matteo Dalmiglio, Claudio Tavagnacco, Andrea Goldoni, and Denis Scaini\*

Carbon nanotube (CNT)-modified surfaces unequivocally demonstrate their biocompatibility and ability to boost the electrical activity of neuronal cells cultured on them. Reasons for this effect are still under debate. However, the intimate contact at the membrane level between these thready nanostructures and cells, in combination with their unique electrical properties, seems to play an important role. The entire existing literature exploiting the effect of CNTs on modulating cellular behavior deals with cell cultures grown on purified multiwalled carbon nanotubes (MWNs) deposited on a supporting surface via drop-casting or mechanical entrapment. Here, for the first time, it is demonstrated that CNTs directly grown on a supporting silicon surface by a chemical vapor deposition (CVD)-assisted technique have the same effect. It is shown that primary neuronal cells developed above a carpet of CVD CNTs form a healthy and functional network. The resulting neuronal network shows increased electrical activity when compared to a similar network developed on a control glass surface. The low cost and high versatility of the here presented CVD-based synthesis process, together with the possibility to create on supporting substrate patterns of any arbitrary shape of CNTs, open up new opportunities for brain-machine interfaces or neuroprosthetic devices.

## 1. Introduction

In the last two decades, research focusing on integrating carbon nanomaterials (CNMs) into the nervous system experienced an exponential increase, demonstrating unexpected results.<sup>[1–3]</sup> The ability to interface nerve cells with novel (nano)materials capable of efficiently modulating the electrical activity of the entire neuronal network opens novel approaches in neuroscience research and future applications in neurology and neuroprosthetics. Within this category, carbon nanotubes (CNTs) are well-known and widely studied CNMs and, thanks to their extensively investigated physicochemical and biological properties,<sup>[4–6]</sup> found application in many fields ranging from biology to nanomedicine.<sup>[7–11]</sup> CNTs could be thought as hollow cylinders made of one (single-walled) or more (multi-walled) layers of graphene (one atom-thick sheet of graphite).<sup>[12]</sup> Their innate characteristics, combined with the ease of chemical modifications<sup>[13,14]</sup> and a (nano)morphology

Dr. I. Rago  
Department of Physics  
University of Trieste  
Piazzale Europa 1, 34127 Trieste, Italy  
Dr. R. Rauti, I. Calaresu, Dr. D. Scaini  
Neurobiology Sector  
International School for Advanced Studies (SISSA/ISAS)  
Via Bonomea 265, 34136 Trieste, Italy  
E-mail: dscaini@sissa.it  
Prof. M. Bevilacqua, Dr. C. Tavagnacco  
Department of Chemical and Pharmaceutical Sciences  
University of Trieste  
Via Giorgieri 1, 34127 Trieste, Italy  
Prof. M. Bevilacqua  
CNR-ICCOM  
Via Madonna del Piano 10, 50019 Sesto Fiorentino, Italy

Prof. M. Bevilacqua  
ICCOM-CNR Trieste Research Unit  
Via Giorgieri 1, 34127 Trieste, Italy  
Dr. A. Pozzato  
ThunderNIL srl  
Via Foscolo 8, I-35131 Padova, Italy  
Dr. A. Pozzato  
IOM-CNR Area Science Park  
Basovizza, S.S. 14, km 163.5, 34149 Trieste, Italy  
Dr. M. Dalmiglio, Dr. A. Goldoni, Dr. D. Scaini  
Elettra-Sincrotrone Trieste  
Area Science Park, S.S. 14, km 163.5, 34149 Trieste, Italy  
Dr. Matteo Cibinel  
Department of Engineering and Architecture  
University of Trieste  
Via Valerio 6/1, 34127 Trieste, Italy

 The ORCID identification number(s) for the author(s) of this article can be found under <https://doi.org/10.1002/adbi.201800286>.

DOI: 10.1002/adbi.201800286

resembling extracellular matrix structure,<sup>[15]</sup> make CNTs an excellent candidate for interfacing neuronal systems.<sup>[16–19]</sup> Indeed, biocompatible, durable, and robust CNT-based substrates/scaffolds and devices have demonstrated to affect neuronal development providing new opportunities for central nervous system disorders therapies.<sup>[20,21]</sup>

The ability of CNT-modified substrates to modulate neuronal functionality at either systemic level (e.g., inducing neuronal processes growth and/or synaptogenesis)<sup>[14,17,21,22]</sup> or functional level (e.g., improving synaptic transmission effectiveness)<sup>[3,16–19]</sup> is well established. In this framework, the possibility of interfacing neuronal systems with CNTs emerged as an intriguing and successful approach to manipulate electrical activity in single neuronal cells, in synaptically connected networks, and in complex tissue explants.<sup>[3,16–19,23]</sup>

Despite cytotoxicity of free-floating CNTs being still under debate (spanning from good tolerance to strong toxicity mainly determined by CNT dimensions, concentration, and surface functionalization<sup>[24–26]</sup>), when CNTs are firmly immobilized on surfaces, no evidence of (cyto)toxicity was pointed out.<sup>[16,17,19,27]</sup> Many different strategies were exploited in order to have surfaces decorated with a stable carpet of CNTs, ranging from laying down CNTs by drop casting<sup>[16]</sup> to surface embedding via elastomeric entrapment<sup>[19]</sup> or by chemical vapor deposition (CVD)-assisted growth of CNTs directly on target surfaces.<sup>[28]</sup>

The majority of the studies demonstrating CNT ability to modulate neuronal activity relates to drop-casted carpets of CNTs. Despite the large amount of work done, the use of glass surfaces modified by drop-casted CNTs still presents drawbacks, strongly limiting the scaling up of their use for biomedical or industrial applications. These shortcomings include a low control of surface coverage that might result in large portions of the supporting sample (e.g., glass) totally lacking CNTs. More crucial, drop-casted CNTs are usually just physisorbed on the supporting surface. This results in easy detachment if tangential strains are induced as, for example, in the case of cell migration, contraction or, simply, intense flow of liquids. In this respect, chemical vapor deposition technique represents a valuable approach to overcome the above-mentioned issues.

CVD gives the possibility, in the presence of a carbon precursor, of thermally growing CNTs on whatever surface—or portion of surface—previously covered by a catalytic element (e.g., iron nanoparticles) resulting in extremely uniform films of aligned CNTs.<sup>[29,30]</sup> The obtained layers of CNTs demonstrated to be strongly bound to the surface of the supporting material reducing the possibility of CNTs' mechanical detachment or release in the surrounding environment. Although different CVD fabrication methods are possible, in this work we used a catalytic-assisted CVD (CCVD) using hydrocarbons (acetylene) as feed material and iron nanoparticles as catalyst.<sup>[31–33]</sup> Such an approach combines fabrication simplicity with the possibility to easily scale up the procedure, making it extremely attractive not only for research but also for large-scale applications.

Herein we first showed that uniform and patterned carpets of pure multiwalled carbon nanotubes (MWNTs) can be easily produced by CCVD on supporting silicon substrates as highlighted by a combination of electron microscopy and spectroscopic techniques. Subsequently, uniform CNT carpets were used as supporting substrates for the development of neuronal

networks from rat hippocampus primary cells. Immunofluorescence experiments showed that our MWNT films are biocompatible and not cytotoxic resulting in an extended and functional neuronal network. Interestingly, calcium imaging experiments, intending to evaluate the electrical activity of the resulting neuronal network, demonstrated that neurons interfaced with our MWNTs were characterized by potentiated electrical activity in a way very similar to what was observed in literature for drop-casted CNT carpets.<sup>[16,17,34]</sup> This was done using just uniform carpets of CNTs, and not patterned ones, in order to highlight the intrinsic CNT neuromodulation effect from alterations in network dynamics due to differences in the morphology of the network induced by a patterned surface. Uniform carpets of CNTs had in glass slides their natural control surface, without the difficulty in reproducing complex network morphologies on glass.

We demonstrated that our activity-boosting CNT mats are characterized by better electrochemical and charge injection properties than drop-casted ones and are more versatile being patternable with CNTs localized only on specific areas of any arbitrary shape and size of a supporting surface.

Approaches toward a deeper analysis of the interactions between surface-immobilized CNTs and brain cells and their circuitry offer great opportunities for boosting nanotechnological applications for the nervous system.

## 2. Results and Discussion

### 2.1. Fabrication of MWNT Carpets for Neuronal Network Growing

Multiwalled carbon nanotubes were grown on silicon wafer chip (Si/SiO<sub>2</sub>) substrates following an iron nanoparticle-catalyzed CCVD process.<sup>[35]</sup> Detailed description of the entire process is available in the Experimental Section. Briefly, MWNT synthesis was carried out at about 700 °C in the presence of acetylene as carbon precursor for just 90 s. Nanotube growth is catalyzed by the formation of iron nanoparticles obtained from a uniform thin (2±5 nm in thickness) iron layer deposited on the wafer and subsequently annealed at 670 °C in reducing conditions (H<sub>2</sub> atmosphere). It is well known from literature that, at high temperatures, the direct coating of a silicon substrate by catalyst can induce silicide formation deactivating the catalyst and, in turn, compromising nanotubes growth.<sup>[36]</sup> Therefore, in order to avoid silicidation of the metal catalyst, buffer layers, such as deposited Al<sub>2</sub>O<sub>3</sub> and TiO<sub>2</sub>, or thermally grown SiO<sub>2</sub> can be used.<sup>[37,38]</sup> Moreover, previous studies have reported methods to enhance nanotube yields by employing two<sup>[31,39]</sup> or even more catalyst layers.<sup>[29,40]</sup> Notably, in our synthesis method, although no metal other than iron has been used as catalyst layer and no other buffer layer besides the native SiO<sub>2</sub> layer spontaneously formed on the silicon surface has been employed, the density and reproducibility of the as-produced CNTs forest were comparable to similar structures found in the literature, grown by using more sophisticated techniques (up to 1.4 × 10<sup>10</sup> cm<sup>-2</sup>).<sup>[41]</sup> The ease and reproducibility of our method will allow a more straightforward scaling up of the entire process.

In order to investigate the morphology and size distribution of the iron nanoparticles, on which depend the density



and the dimension of CNTs constituting the mat, the wafer surface was characterized by means of atomic force microscopy (AFM) imaging before and after the annealing. Figure S1 (Supporting Information) showed typical AFM microscopic images of an as-evaporated 2 nm thick film of iron before (Figure S1a, Supporting Information) and after (Figure S1b, Supporting Information) annealing. Prior to annealing, Fe films have been found relatively smooth and with a root-mean-square (rms) surface roughness (mediated over three samples) of  $0.37 \pm 0.06$  nm; on the other hand, after the annealing treatment, a completely different surface morphology characterized by a significant increase in the rms roughness ( $5.30 \pm 0.19$  nm) was observed (see AFM line profile in Figure S1 in the Supporting Information). AFM particle analysis—performed by taking into consideration AFM tip surface deconvolution—revealed average particle size of about  $13.2 \pm 7.8$  nm in diameter. The nucleation of nanoparticles, acting as CNTs' growing seeds, is driven by a minimization of the surface free energies connected to the difference in surface energy between the metal catalyst and the supporting layer.<sup>[42–44]</sup>

Scanning electron microscopy (SEM) and transmission electron microscopy (TEM) imaging were performed on the as-obtained CNT carpets to address their morphology and uniformity and provide information about nanotube dimensions, alignment, and density. Analysis revealed that as-grown nanotubes have diameters ranging between 15 and 25 nm and lengths up to 300  $\mu\text{m}$ . It is worth noting that CNTs' diameter is strongly related to catalyst particle size,<sup>[45]</sup> while CNTs' length depends mainly upon the growth time.<sup>[46]</sup>

TEM characterization was carried out to investigate CNTs' structure and crystallinity, catalyst particles' size, and their localization along the tubes. It has been found that CNTs consist of multiwalled carbon nanotubes with variable number of walls. Specifically, Figure 1a (top) shows an isolated MWNT with an outer diameter (OD) of about 22 nm and an inner diameter (ID) of nearly 12 nm. These measurements are consistent with 14 nanotube walls.<sup>[47]</sup> TEM observations reveal a non-full encapsulation of Fe nanoparticles into the tubes and, as a matter of fact, their localization at one end of different nanotubes was instead verified. In particular, Figure 1a (bottom) revealed a 24 nm catalyst nanoparticle (highlighted in red) at the endcap of a carbon nanotube. Nanoparticles diameter coincides roughly with MWNTs' inner diameter. The same microscopic image showed several overlapping CNTs with diameters ranging from 8 to 22 nm. Additionally, TEM analysis pointed out that CNTs exhibit structural defects as imperfections of carbon sheet in tubes, such as breaks,  $\text{sp}^3$  hybridized carbon atoms, Stone–Wales defects (i.e., two heptagons and two pentagons), probably related to the relatively low growth temperature used.<sup>[48,49]</sup>

Analysis of SEM images (Figure 1b) revealed that nanotubes' carpets are composed by vertical aligned CNTs, oriented perpendicularly to the surface substrate, with a very high packing density forcing their vertical orientation (side view in bottom-left inset). Instead, from the top, CNTs appear randomly oriented (top view in top-right inset). This “spaghetti-like” aspect is due to the proximity effect of densely distributed catalyst nanoparticles forcing initially randomly oriented CNTs to assume a vertical alignment.<sup>[50]</sup>

Raman spectroscopy was performed to investigate the purity, structure, and defects of CNTs combined with the possibility to discriminate MWNTs from other allotropic forms of carbon. The first- and second-order Raman spectra recorded on as-grown CNTs (Figure 1c) revealed MWNT characteristic peaks with a D band at  $\approx 1330$   $\text{cm}^{-1}$  indicating the presence of crystal disorder in the hexagonal rings, such as amorphous carbon<sup>[51]</sup> and a G band at  $\approx 1583$   $\text{cm}^{-1}$  related to the in-plane tangential vibration of  $\text{sp}^2$ -hybridized carbon atoms within the graphene sheets.<sup>[52]</sup> The ratio between the D ( $I_D$ ) and G ( $I_G$ ) bands' integral intensities is generally exploited to evaluate the quality of MWNTs. Specifically, similar intensities of these bands,<sup>[53]</sup> as in our case ( $I_D/I_G = 0.97$ ), suggested the presence of nongraphitic carbon in nanotubes, a typical condition encountered in low-temperature CVD-grown CNTs.<sup>[54,55]</sup> Together with the G band, the second-order Raman peak  $G'$  is a signature of graphitic  $\text{sp}^2$  materials and is located at  $\approx 2700$   $\text{cm}^{-1}$ .

Additionally, in order to determine CNTs' surface composition, X-ray photoelectron spectroscopy (XPS) analysis was carried out. From the XPS survey spectrum of CNTs (Figure 1d), three elements were discriminated: carbon ( $\text{C}_{1s}$ ), oxygen ( $\text{O}_{1s}$ ), and silicon ( $\text{Si}_{2s}$  and  $\text{Si}_{2p}$ ). The detected amount of C and O are 87.29% and 8.90%, respectively. Moreover, a small amount (3.8%) of Si was detected. The presence of oxygen on CNTs surface is intrinsically related to the CCVD fabrication method and, more in particular, to defects formed during CNTs' synthesis since they tend to adsorb oxygen when exposed to air. The most intense peaks, shown in the  $\text{C}_{1s}$  core level (Figure 1e), located at 284.6 and 285.8 eV can be assigned to  $\text{sp}^2$ -hybridized graphitic carbon atoms on CNTs' walls and to amorphous carbon ( $\text{sp}^3$ -hybridized carbon atoms), respectively.<sup>[56,57]</sup>

The amorphous carbon is likely due to the CNTs' synthesis process, as confirmed by the structural defects identified via TEM (Figure 1a) and Raman spectroscopy (Figure 1d). The peak at 290.8 eV corresponds to the electron energy loss peak due to  $\pi$ -plasmon excitations. These three peaks are characteristics of  $\text{C}_{1s}$  core level from the carbon nanotubes.<sup>[58]</sup> The additional small peaks at 287.15 and 288.4 eV are related to the presence of oxygen.<sup>[59]</sup>

Electrochemical investigation of CCVD synthesized CNTs' carpets by means of cyclic voltammetry (CV) and electrochemical impedance spectroscopy (EIS) pointed out the better performance of our CNT surfaces in terms of conductivity and charge-transfer properties when compared to drop-casted CNTs or gold surfaces (Figure 1f; Figure S2, Supporting Information). Chronopotentiometric analysis was performed to determine the charge injection capacity (CIC) of the three different samples (Figure 1g). Detailed electrochemical measurements were performed on each electrode type (macro-electrode type) at least twice to gain good reproducibility. The impedance value of CCVD synthesized electrode at 1 kHz was found to be  $\approx 1.5$  orders of magnitude smaller than a comparable-sized Au electrode and less than one half with respect to DC electrodes (Figure 1g).

According to the different water windows for the Au electrode ( $-0.8$  to  $+0.8$  V), CCVD CNTs' electrode ( $-1.2$  to  $+1.2$  V), and drop-casted CNTs' electrode ( $-1.4$  to  $+1.4$  V) (see ref. [60] and also Figure S2, Supporting Information), the calculated CIC values from the voltage transient for the three electrode types showed

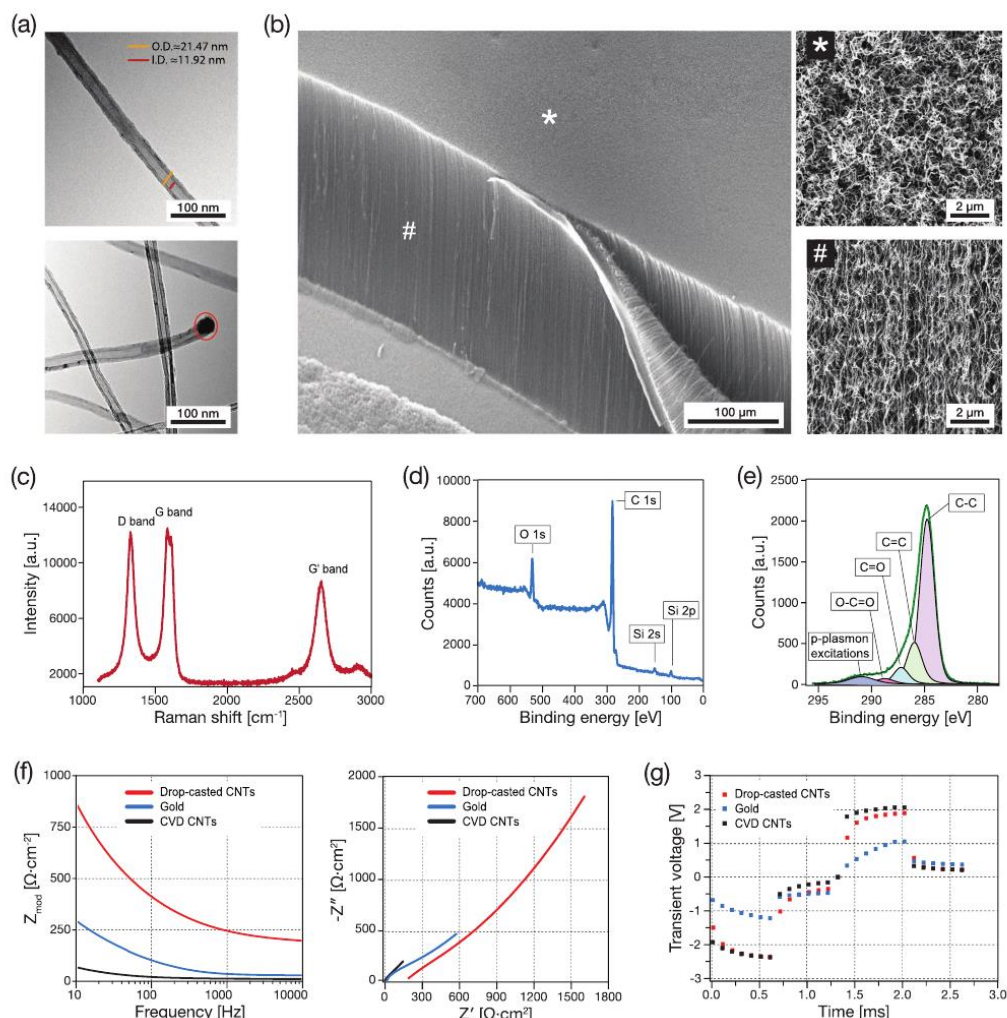


**Figure 1.** Morphological and chemico-structural characterization of CCVD grown CNTs. a) TEM images of CNTs showing an isolated MWNT (top), various overlapping CNTs, and a 24 nm catalyst nanoparticle (highlighted in the red ellipsis) standing inside the endcap of a nanotube (bottom). b) SEM images showing a silicon surface covered by a thick layer of aligned CNTs, oriented perpendicularly to the surface substrate (side view, pound-sign inset). Instead, from the top, nanotubes appear randomly oriented (top view, star-sign inset). c) Raman spectra exhibiting typical bands of low-temperature CCVD-grown MWNTs. d) XPS survey and e) C1s core level of CNTs. f) Electrochemical impedance spectroscopy (EIS) analysis in form of a Bode plot (left) and a Nyquist plot (right) comparing a surface decorated with CCVD CNTs (black), with a surface covered by drop-casted CNTs (red), and a reference gold substrate (in blue). g) Current-controlled measurements were performed recording the voltage transients versus time characteristics to determine the charge injection capacity (CIC) of the three different samples.

the following trend: drop-casted CNTs' electrode ( $6.4 \mu\text{C cm}^{-2}$ , corresponding to an injected current of 5 mA) < Au electrode ( $28 \mu\text{C cm}^{-2}$ , corresponding to an injected current of 20 mA) < CCVD CNTs' electrode ( $190 \mu\text{C cm}^{-2}$ , corresponding to a further increased injected current of 24 mA).

As already mentioned, a remarkable aspect of the CCVD synthesis of CNTs carpets is the ease in confining CNTs just on areas of any arbitrary shape and dimension by means of simple patterning of the catalytic film surface.<sup>[61]</sup> In contrast, invasive subtractive pattern generation via chemical or reactive ion



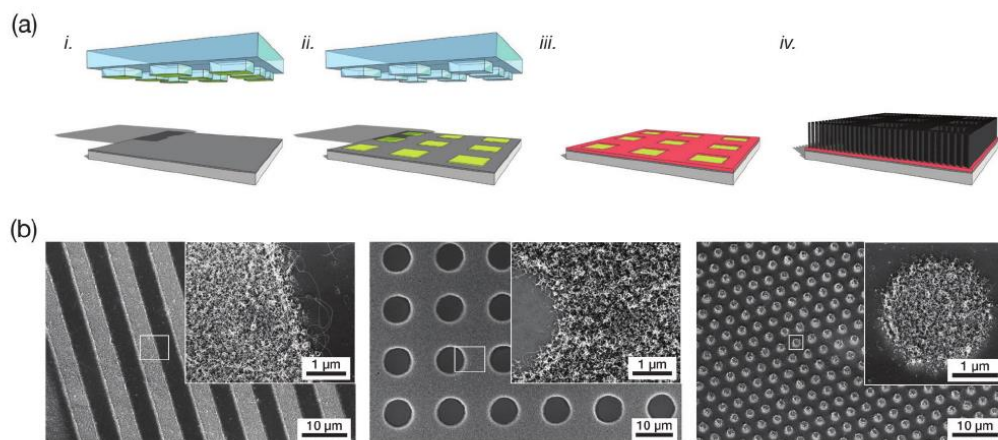


**Figure 2.** a) Schematic overview of the procedure followed to synthesize patterned CNTs on substrates previously decorated with OTS film. a-i) PDMS stamps with relief features are linked with OTS solution and then pressed onto the SiO<sub>2</sub>/Si substrates a-ii) realizing a printed OTS film. Then, a thin layer of iron was selectively deposited on the OTS-patterned SiO<sub>2</sub>/Si substrates leading, due, to hydrophobic exclusion, a-iii) to a selective deposition of iron only around the OTS regions and, a-iv) finally, the subsequent growth of patterned CNTs was carried out following the procedure described in the CNTs' preparation section. b) SEM images showing various micropatterned geometries that could be obtained with CNTs: stripes, wells, and dots.

etching is necessary to achieve the same result from an homogeneous layer of drop-casted CNTs.<sup>[62]</sup> As proof of principle of such possibility, we have here adopted a nonlithographic patterning method based on the microcontact printing ( $\mu$ CP) of octadecyltrichlorosilanes (CH<sub>3</sub>(CH<sub>2</sub>)<sub>17</sub>SiCl<sub>3</sub> (OTS)) (Figure 2a). Catalytic metal patterning performed following this procedure (see the Experimental Section for details) allowed for direct site-selective growth of MWNTs giving rise to reproducible and large-scale CNT-based micrometric patterns of various geometries with a lateral resolution of about 1  $\mu$ m (Figure 2b). Compared to conventional subtractive patterning methods,  $\mu$ CP technique reduces process steps, costs, and chemical wastes. This enables a more rapid fabrication of microstructures with a comparable resolution of similar patterns realized with traditional optical lithographic strategies but at a fraction of the final cost.

## 2.2. Culturing Primary Neurons above CNTs' Substrates

Primary neurons from rat hippocampus were plated above uniform carpets of CNTs and, as control condition, above flat glass slides. Cells were allowed to grow and develop functional networks. Effectiveness of cell morphology, network extension, and adhesion to CNT mats were assessed in a first set of experiments by means of SEM analysis (Figure 3a). Cells demonstrated to possess nice globular healthy shapes extending numerous neurites and to be part of a large network embedded in a diffused extracellular matrix film covering all the CNTs' carpet. Tears in the extracellular matrix film, presumably occurred during sample preparation for SEM investigation, reveal the top portion of the underneath carbon nanotubes' carpet and the intimate contact within them and the cellular phase as visible in Figure 3a (right).

In a second set of experiments we used immunofluorescence technique to compare cells grown on control glass with those grown on CNT substrates. To prove the in vitro formation of comparable hippocampal network on both glass controls and CNT substrates, we imaged by immunofluorescence the cellular components of the network. The specific cytoskeletal component  $\beta$ -tubulin III was marked to point out neurons, while the glial fibrillary acidic protein (GFAP) was targeted to visualize instead astrocytes.<sup>[19,22,63]</sup> At the left-hand side of Figure 3b, two representative confocal reconstructions of the network displaying  $\beta$ -tubulin III positive cells (in red) developed above a control glass coverslip (top image) or above a CNTs' substrate (bottom image) are shown. In both images, nuclei were pointed out by 4',6-diamidino-2-phenylindole (DAPI, in blue). Remarkably, CNTs' presence did not affect neuronal cells' density (histogram in Figure 3c,  $n = 10$  visual fields per condition, three independent culture series). Control cultures present a neuronal density of  $138 \pm 30$   $\beta$ -tubulin-positive cells mm<sup>-2</sup> comparable to that measured in CNT ones ( $130 \pm 25$   $\beta$ -tubulin-positive cells mm<sup>-2</sup>, Student *t*-test). We then investigated the presence and morphology of glial cells. GFAP is the main component of astrocyte intermediate filament cytoskeleton, and its expression increases as the cell matures.<sup>[64]</sup> These cells had a characteristic stellate-like morphology (see confocal reconstructions in Figure 3b, central part) and we measured GFAP-positive cells' density both in control and CNT samples. Again, CNTs did not affect astrocytes' shape (Figure 3b) nor density (histogram in Figure 3d;  $n = 10$  visual fields per condition, three independent culture series). Control cultures present a glial density of  $110 \pm 28$  GFAP-positive cells mm<sup>-2</sup> not significantly different (Student *t*-test) from that measured in CNT ones ( $130 \pm 28$  GFAP-positive cells mm<sup>-2</sup>).

These results clearly indicate that our CNT carpets support both neuronal and glial survival, allowing the development of

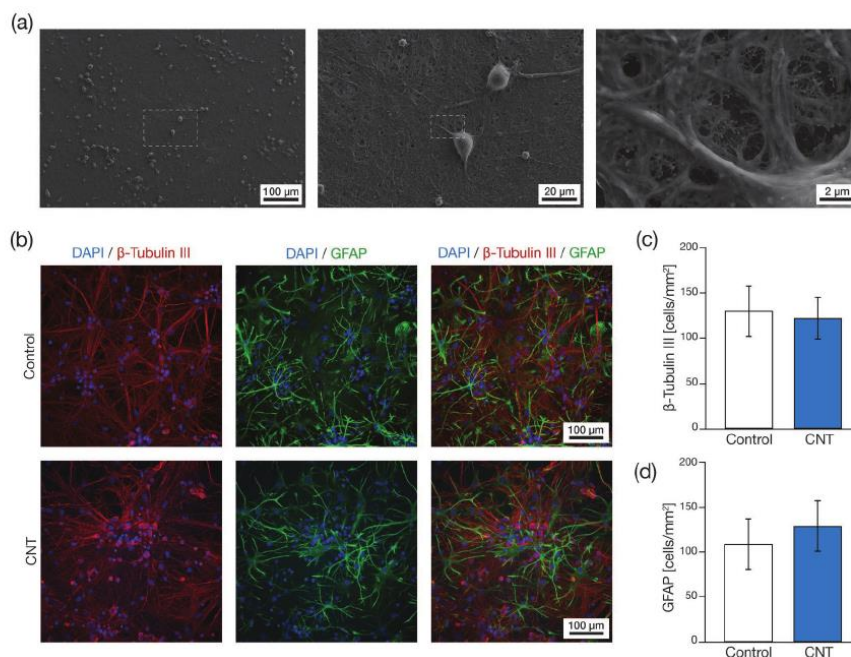


**Figure 3.** a) SEM images at different magnifications where a large portion of the neuronal network developed above a CNT carpet is visible (left). Neurons are characterized by rounded soma and by numerous processes spreading out (center) while, in the cracks in the extracellular matrix covering all the surface underneath CNTs are clearly visible (right). b) Confocal microscopic images of two representative fields of hippocampal cultures grown on a flat glass control (top) and on a uniform carpet of CNTs (bottom). Cells were immune-stained for  $\beta$ -tubulin III to point out neurons (in red, left columns), GFAP to visualize astrocytes (in green, central columns), and DAPI for nuclei (in blue). Overlapping of all the three stains reveals the similarity in terms of morphology and cell phenotype between the two conditions (right columns). The average densities of neuronal cells in the two conditions were evaluated and represented as c) histograms while d) glial cells densities are pointed out.

cellular networks comparable to those grown on control polyornithine glass (see  $\beta$ -tubulin III and GFAP stains overlapping in Figure 3b, right part). The fact that CNT substrates do not alter the density of GFAP-positive glial cells suggests a possible application as biointerfacing nanostructured material.<sup>[16,19,34]</sup>

### 2.3. Assessing Network Activity by Calcium Imaging

To investigate how CNT interfacing can impact neuronal network performance, we monitored the emerging network activity by means of fluorescence calcium imaging.<sup>[65,66]</sup> With our imaging setup, we recorded representative fields of  $680 \times 680 \mu\text{m}^2$  in both glass and CNT-supported neuronal networks (see the Experimental Section). At 9+10 days in vitro (DIV), neurons are usually synaptically connected and display spontaneous activity including bursts emerging by irregular synchronized firing epochs.<sup>[17,22,63]</sup> Figure 4a shows a representative frame extrapolated from a  $\text{Ca}^{2+}$  imaging recording revealing the spatial resolution of the used camera allowing many cells' simultaneous tracing within the same field of view, thanks to single cell resolution. In Figure 4b, examples of fluorescent recordings

of two representative cells under each condition (glass controls and CNTs) are depicted. Traces, shown in normal extracellular saline solution and in bicuculline (BIC; a competitive antagonist of inhibitory  $\text{GABA}_A$  receptors) enriched one, are representative of the spontaneous electrical activity of the cells. Neuronal origin of such activity was assessed taking into account the fact that episodes of neuronal activity are represented by bursts of activity fully blocked by tetrodotoxin (TTX, a potent blocker of voltage-gated sodium channels) application ( $1 \times 10^{-6} \text{ M}$ ; see the Experimental Section).

In our recordings, spontaneous  $\text{Ca}^{2+}$  activity was detected in 40% of cells present in each field visualized on glass coverslips. Notably, in CNTs around virtually all (>98%) of the visualized cells were active and generate spontaneous  $\text{Ca}^{2+}$  episodes. Data relative to control and CNTs conditions are summarized in the histogram in Figure 4c ( $n = 32$  and 36 cells, respectively).

We measure the occurrence of spontaneous  $\text{Ca}^{2+}$  episodes in active cells by quantifying the interevent interval (IEI) that is significantly ( $p < 0.001$ , two way analysis of variance (ANOVA)) shorter in CNTs' cultures ( $10 \pm 5 \text{ s}$ ,  $n = 36$  cells, from six different visual fields of three independent cell cultures) when compared to controls ( $32 \pm 9 \text{ s}$ ,  $n = 32$  cells from six different

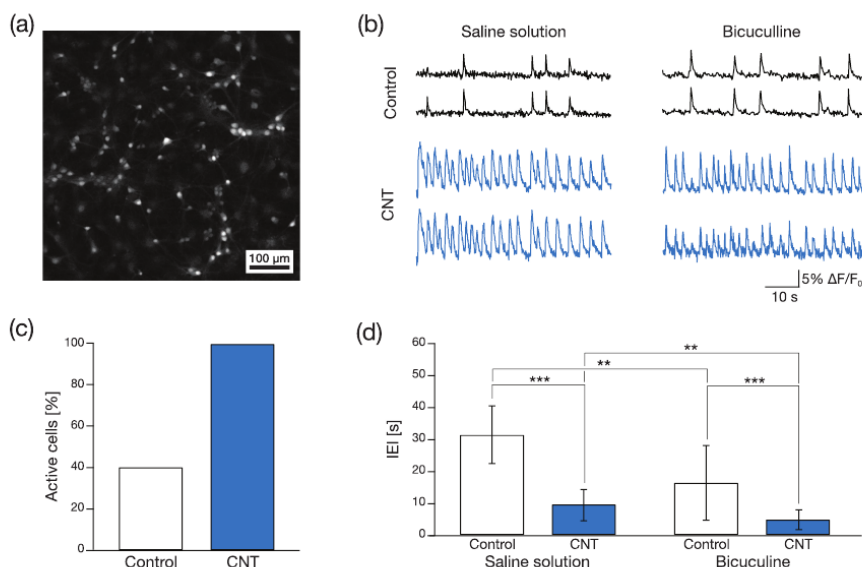


**Figure 4.** a) Snapshot of representative field of neuronal cultures grown on a CNTs' carpet, stained with the Oregon Green 488-BAPTA-1 AM calcium indicator. b) Repetitive Ca<sup>2+</sup> events spontaneously (left) or bicuculline-induced (right) recorded in hippocampal cultures (two sample neurons were selected from the same field). c) A histogram of the percentage of spontaneous active cells in control and CNT conditions. d) Average of interevent interval (IEI) values of control and CNT cells in normal saline solution and in disinhibiting bicuculline solution ( $n = 32$  cells for controls and  $n = 36$  cells for CNTs, six different visual fields from three independent cell cultures per condition; \*\* =  $p < 0.01$ , \*\*\* =  $p < 0.001$ , two-way ANOVA).

visual fields of three independent cell cultures), thus suggesting a different activity modulation induced by the presence of CNTs (plot in Figure 4d).

In an additional set of experiments, we pharmacologically blocked GABA<sub>A</sub> receptors by bicuculline ( $20 \times 10^{-6}$  M; 20 min) application. This antagonist of inhibitory connections is known to alter network patterns of activity.<sup>[67,68]</sup> In both groups, in respect to spontaneous activity, bicuculline addition resulted in boosted neuronal activity as evident by the significant decrease in the average IEI of episodes detected in control ( $p < 0.01$ , two-way ANOVA) or in CNTs ( $p < 0.01$ , two-way ANOVA) cultures (Figure 4d).

As pointed out, as well, by the calcium tracings in Figure 4b, active cells treated with bicuculline give rise to the appearance of Ca<sup>2+</sup> episodes displaying an IEI of  $5 \pm 3$  s in CNTs' cultures ( $n = 36$ ), a value significantly ( $p < 0.001$ ) lower when compared to that of control cultures ( $17 \pm 12$  s;  $n = 32$  cells). All data are summarized in the plot in Figure 4d. According to the neuronal nature of such disinhibited episodes, further applications of TTX completely removed all Ca<sup>2+</sup> activity (data not shown).

### 3. Conclusion

Herein, we have demonstrated a CCVD-based approach to fabricate carbon nanotube-decorated surfaces for cellular applications. Resulting carpets are composed by vertically aligned MWNTs with woven heads uniformly covering a supporting

glass surface (Figure 1). CNT film thickness (from few hundreds of nanometers to hundreds of micrometers) is controlled by tuning CVD reaction parameters. CVD-grown nanotubes are strongly attached by one end to the supporting glass surface. Consequently, different from other CNT surface-decorating techniques, operators are not exposed to free-standing or floating CNTs during both fabrication and utilization phases.

CCVD CNT carpets, when compared to drop-casted CNT carpets or flat gold, demonstrated to have lower impedance in physiological conditions. Interestingly, this difference is more pronounced at low frequencies (10–100 Hz), a regime more representative of neuronal network spike rates.<sup>[2,17,23]</sup> Similarly, CIC is significantly higher for CVD CNT carpets (Figure 1).

Comparing the morphology and cell phenotype distribution of hippocampal networks developed on standard glass surfaces or on uniform carpets of CNTs, we could not point out any significant difference. The fact that the two cellular networks were characterized by healthy and functional cells highlighted the good cytocompatibility of CCVD synthesized CNTs' carpets (Figure 3).

Remarkably, although we demonstrated that patterned CNT surfaces were able to sustain the development of a healthy and functional neuronal network, we observed an alteration of network topology and processes orientation presumably due to a preferential cell/neurite adhesion on CNTs' decorated portions of the sample (see Figure 5). Directionality analysis pointed out an evident peak of directionality of the neuronal processes when neurons were plated on a CCVD CNT-patterned surface composed of aligned CNT stripes.



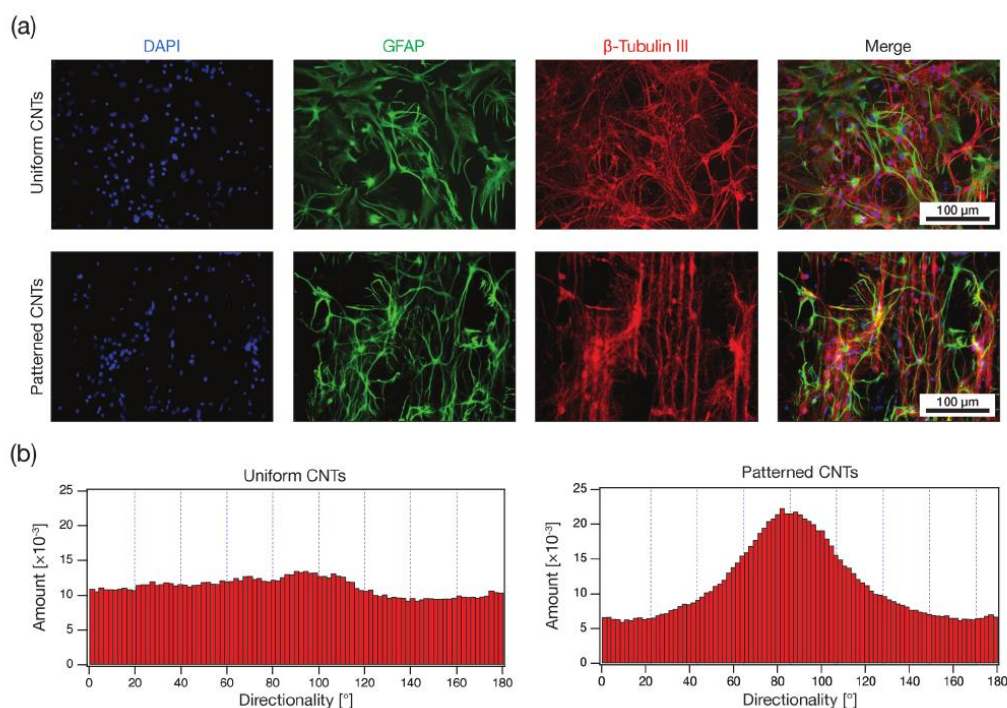


**Figure 5.** a) Two examples of neuronal networks developed above a uniform carpet of CCVD CNTs (top) and on a silicon surface where CNTs (2  $\mu$ m in length) were vertically grown on stripes (7.5  $\mu$ m width, 15  $\mu$ m pitch) giving rise to a patterned substrate (bottom). Cells were immune-stained with DAPI for nuclei (in blue), for GFAP to visualize astrocytes (in green), and for  $\beta$ -tubulin III to point out neurons (in red). On the right, the merging of all three channels pointing out the extremely different network morphology induced by the CNT-patterned surface. The presence of many cell nuclei on CNT covered surface areas as well as a preferential orientation of cell processes along CNT stripes was observable. b) Directionality analysis of neuronal processes performed on the same samples pointed out a homogeneous distribution of directionality, an indication of erratic spread of neuronal processes, in the case of the uniform CNT carpet (left) and an evident peak of directionality for the CNT patterned one along the same direction of the stripes. Directionality analysis performed using Fiji open source software.<sup>[3,80]</sup>

From an electrophysiological point of view, we demonstrated for the first time that CCVD-synthesized CNT carpets, in a way similar to what happen on drop-casted CNTs, increase the overall number of active cells as well the efficacy of neural signaling by boosting, by a threefold increase, the frequency of network electrical activity (Figure 4). This without inducing any change in network size or morphology (if uniform CNT carpets are used). The neuronal and glial densities were, in fact, similar to the control substrates, as shown by our immunocytochemistry measurements. We can hypothesize that altered cellular excitability by the CNT carpets could be, at least in part, responsible for our results. In fact, improving cellular excitability would increase the probability of active cells.<sup>[7,69]</sup> Furthermore, the impact of CNTs on network activity was preserved in the presence of bicuculline, highlighting a change in the excitation/inhibition ratio.

Since a significant increase in terms of  $\text{Ca}^{2+}$ -events frequency was detected, we can postulate that the observed boosting in overall neuronal activity could be related to modifications

occurring at presynaptic level.<sup>[70]</sup> Physico-chemical mechanisms governing such neuronal potentiation could reasonably be the same faced by neurons interfaced to drop-casted CNTs. However, the exact reason of such an effect remains elusive and not well addressed. In fact, the improved neuronal signaling transmission might be related to general properties of MWNTs, such as the high electrical conductivity,<sup>[71]</sup> their electrochemical properties,<sup>[72,73]</sup> and/or their morphology. Thanks to the intimate contact taking place at cell-membrane/nanotube level, as shown in Figure 3a, CNTs could probably induce an extremely fast propagation of local charges related to electronic currents along nearest areas of cell membranes. This could result in a sort of immediate availability of mirror charges in the CNT carpet resulting in ease of membrane cross-polarization between proximal neurons.

More accurate investigations are necessary to highlight this phenomenon as, for example, to understand if CNT-related synaptogenicity or any change at pre- and postsynaptic level takes place in neurons interfaced with CVD CNTs. To clarify these

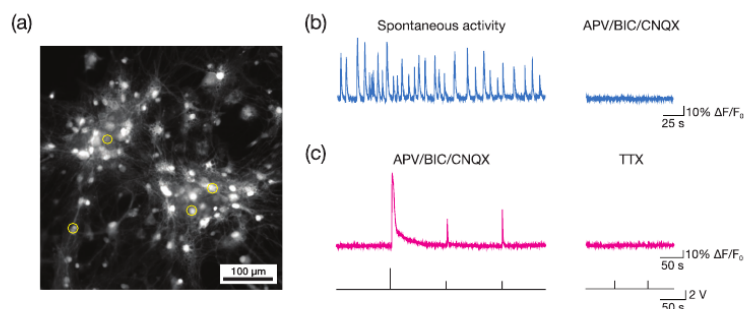


**Figure 6.** Live calcium imaging experiments were used to validate the possibility to induce an evoked activity in neuronal networks through the electrical stimulation of the underneath carpet of CNTs. a) A snapshot of a representative field of hippocampal dissociated cultures developed above an uniform carpet of CCVD CNTs and labeled with Oregon green 488-BAPTA-1 AM calcium probe. Yellow circular markers indicate the neurons (ROI, region of interest) from which calcium events were recorded. b) A representative example of physiological spontaneous synaptic activity of the network (left trace), fully blocked (right trace) by a drug cocktail containing the NMDA receptor antagonist APV ( $25 \times 10^{-6}$  M), the GABA<sub>A</sub> receptor antagonist bicuculline (BIC,  $10 \times 10^{-6}$  M) and the AMPA/kainate receptor antagonist CNQX ( $10 \times 10^{-6}$  M). In this condition only artificially-evoked activity could be observed. c) A representative trace where neuronal responses were induced by extracellular pulse stimulations applied through the CNTs (see the Experimental Section) in the presence of the synaptic blocker drug cocktail (left trace). Below the trace the representation of three, manually delivered, anodic voltage pulses (5, 2, and 2 V, respectively, 300 ms each). By the fact that 5 V stimulation induced abrupt calcium transients in neurons, we reduced stimulus intensity to 2 V in order to prevent strong alterations in cell calcium homeostasis. Neuronal network propensity to be stimulated to fire an action potential after voltage stimuli was totally abolished by tetrodotoxin (TTX) treatment (right trace) ensuring the neuronal origin of the signals evoked in APV/BIC/CNQX condition. Below the trace the representation of the two anodic voltage pulses (2 V each, 300 ms in duration) delivered. Calcium transients are expressed as fractional amplitude increase in the fluorescence signal ( $\Delta F/F_0$ ).

issues, further studies will be necessary. Moreover, the impact of patterned CNT surfaces in altering the network morphology and, consequently, network electrical activity is a pivoting point necessary to be addressed in future studies. In this context, our approach is extremely promising; in that, it allows fabrication of not continuous carpets of CNTs (Figure 2). Such substrates could be an important tool to highlight CNT carpet contribution in the whole potentiation mechanism that we observed as well lay the foundations for a possible use of such substrates to deliver complex spatiotemporal electrical stimulations. From this perspective, as a proof-of-concept study, we demonstrated that our uniform CCVD CNT carpets could be successfully used to electrically stimulate the overlaying neuronal network via short monophasic voltage pulses (2–5 V, 300 ms) evoking  $\text{Ca}^{2+}$ -related signals of proved neuronal origin (see Figure 6 and the Experimental Section).

Taken together, our findings demonstrate the possibility of using on-surface synthesized CNTs to perturb the electrical behavior of a neural network in vitro, an essential step for the design of innovative synthetic biomaterials. Neuroprosthetic devices, ranging from innovative neuronal scaffolds of complex shapes to neuronal probes for electrical recording/stimulation, characterized by strong interaction with neuronal cells and reduced inflammatory response,<sup>[18]</sup> could effectively emerge taking advantage of CVD-based synthesis procedure.

#### 4. Experimental Section

**CNTs' Preparation:** CNTs were synthesized in the Carbon Micro- and Nano-laboratory via CCVD of acetylene over a Fe-coated Si substrate running the growth for just 90 s. The wafers were manually cleaved into

$15 \times 15 \text{ mm}^2$  chips using a diamond scribe and cleaned by rinsing in ultrasonic baths of acetone and ethanol for 15 min. Since CVD-assisted CNTs' synthesis on a supporting substrate needs a catalytic element, iron was deposited as a thin layer (2–5 nm in thickness) directly on the  $\text{SiO}_2/\text{Si}$  chips via thermal evaporation.<sup>[74]</sup> Subsequently, supporting substrates (Fe/ $\text{SiO}_2/\text{Si}$ ) were mounted on the heating element inside a high vacuum reaction chamber. Before the CVD process, samples were thermally annealed at 670 °C in  $\text{H}_2$  atmosphere for 4 min. This serves two purposes: i) reduce iron oxides that might be formed on sample surface during transfer from the metal deposition system to the CVD reactor and ii) de-wet the iron layer inducing nanoparticle formation. Subsequently, acetylene gas (carbon source) was delivered through a flow meter system in the reaction chamber in which the supporting chips were located. Thereafter, sample temperature was raised to 700 °C, and acetylene was introduced into the chamber up to a partial pressure of  $10 \pm 20$  mbar. Reaction time was limited to merely 90 s, resulting in the formation of a uniform network of CNTs of about 10 μm in thickness. Samples were used as removed from the reaction chamber. It is important to highlight the fact that the thickness of the resulting layer of vertically aligned CNTs was tuned by the reaction time. Reaction times shorter than 90 s usually lead to entangled networks of CNTs, showing no preferential alignment. On the other hand, by increasing the reaction time from 90 to 240 s, aligned CNTs of different length (CNTs' carpet thickness from 10 up to 200 μm) can be obtained. A further increase of the reaction time beyond 240 and up to 600 s does not result in an appreciable increase of carpet thickness indicating the onset of a saturation effect.

**Patterned CNTs:** A selective growth of CNTs was performed on silicon wafer chip ( $\text{SiO}_2/\text{Si}$ ) substrates patterned with OTS by the  $\mu\text{CP}$  method.<sup>[75]</sup> OTS's ability to form self-assembled monolayers (SAMs) on a  $\text{SiO}_2/\text{Si}$  substrate<sup>[75]</sup> was usually adopted to modify specific surface properties.<sup>[76]</sup> Accordingly, CNT-based micropatterns were fabricated by a site-selective deposition of the catalytic element (iron as thin layer) by exploiting the OTS's capability to create a barrier for metal nucleation and growth during the deposition.<sup>[77]</sup> Figure 2a shows the general procedure scheme that was adopted to fabricate CNT patterns. It combines the formation of an iron pattern by site-selective Fe deposition on an OTS-patterned  $\text{SiO}_2/\text{Si}$  substrate and subsequently the



selective growth of CNTs over just the Fe-patterned regions. In short, polydimethylsiloxane (PDMS) stamps with a relief microsize-patterned structure were realized according to a previous procedure.<sup>[78]</sup> Afterward, the patterns were transferred onto the SiO<sub>2</sub>/Si substrates, previously cleaned using acetone and isopropanol, by  $\mu$ CP using OTS, prepared in reagent grade toluene with a concentration  $10 \times 10^{-3}$  M, as ink solution. Polyester applicators were used to ink the PDMS stamps with the OTS solutions, and N<sub>2</sub> gun was employed to remove from the stamps the excess of solvent. The stamps were kept in contact with substrates for 5 min and then cleaned using acetone followed by N<sub>2</sub> blowing. After that, the site-selective deposition of the catalyst layer over the as-realized OTS-patterned substrates and the subsequent growth of patterned CNTs were carried out following the same procedure described in the previous section (CNTs' Preparation).

**Materials' Characterization:** The morphology of the continuous catalyst layer deposited on the supporting substrate and the Fe nanoparticles resulting after the thermal annealing treatment were investigated by means of atomic force microscopy using an XE-100 AFM (Park System). For this purpose, samples were processed under the same preparatory steps adopted before CCVD CNTs' synthesis. Topographic measurements were performed in contact mode in air using a MikroMasch NSC36/CR-AU AFM tip (spring constant  $2 \text{ nN nm}^{-1}$ ) collecting images of  $512 \times 512$  pixels at a cantilever speed of about 0.5 Hz. Image processing was performed using Gwyddion open source analysis software (version 2.40).<sup>[79]</sup> SEM imaging was conducted on the as-produced materials collecting secondary electrons on a Gemini SUPRA 40 SEM (Carl Zeiss NTS GmbH, Oberkochen, Germany) operating at an accelerating voltage of 5 keV. TEM investigations of CNT carpets were carried out using an EM 208-Philips TEM system equipped with a Quemesa (Olympus Soft Imaging Solutions) camera. Before TEM imaging, samples were mechanically removed from the substrates, dispersed in ethanol by sonication, and, subsequently, a drop of the so-obtained suspension was deposited onto a commercial lacey-carbon grid. Raman spectroscopy was performed on the as-produced CNTs at room temperature (RT) employing a Renishaw inVia Raman microscope endowed with a 60 $\times$  objective lens (numerical aperture (N.A.) 1.0) at 632.8 nm laser excitation and about 2 mW of laser power. In order to evaluate the composition of the CNTs' carpet covering these samples, XPS analysis was conducted using a commercial X-ray photoelectron spectrometer (VG-ESCALAB-II) equipped with a monochromatic Al K $\alpha$  X-ray source (1486.6 eV) and a hemispherical energy analyzer with a base pressure below  $1 \times 10^{-10}$  mbar. Core-level XPS data analysis was performed after the removal of nonlinear Shirley background and deconvolution into Gaussian/Lorentzian components using Casa-XPS software.

CVs, EIS, and chronopotentiometry fast measurements were performed with an Autolab 302 N electrochemical workstation (Metrohm, The Netherlands) at room temperature in argon atmosphere and in 0.1 M phosphate buffered saline (PBS) electrolyte solution, using a conventional three-electrode cell composed by the sample under investigation as a working electrode, a platinum wire as auxiliary electrode, and a saturated calomel (SCE) as a reference electrode that was separated from the solution by a salt bridge with a Vycor frit and filled with the PBS solution. Electrochemical investigation compared these CVD CNTs to two substrates already used and described as supporting substrates for neuronal network development: drop-casted CNTs<sup>[17,23]</sup> and a thin layer of gold.<sup>[2]</sup>

EIS experiments were taken between 1 Hz to 10 kHz using 10 mV RMS AC voltage. CV tests were performed at a scan rate of  $50 \text{ mV s}^{-1}$  across the water window.

In current-controlled measurements, a biphasic current pulse of 700  $\mu$ s combined to an interphase period of 700  $\mu$ s was applied to the system, and the simultaneous voltage transient was recorded. The magnitude of the current pulse must allow safe stimulation to avoid redox processes in water environment and/or electrode damage (i.e., exfoliation). CIC was calculated from the current pulse divided by the geometrical surface area of the electrode.

**Preparation of Primary Hippocampal Cultures:** Primary dissociated cultures were obtained from postnatal rats (P2+P3) as previously described.<sup>[17,19,63]</sup> All experiments were approved by the local authority and performed in accordance with the Italian law (decree 116/92) and the EU guidelines (86/609/CE, 2007/526/CE and 2010/63/UE). The Italian Ministry of Health approved the use of animals. All efforts were made to minimize animal suffering and to reduce the number of animals used.

Cells were plated on poly-L-ornithine-coated glass coverslips and on CCVD-grown CNT substrates (uniform flat carpets or patterned). Before using for culturing, CNT substrates were mounted on  $12 \times 24 \text{ mm}^2$  glass coverslips ( $0.13 \pm 0.16 \text{ mm}$  in thickness, Kindler, EU) by a thin adhesive layer of PDMS cured at 100 °C. In order to increase cell adhesion, an air plasma-cleaner treatment was performed on glass and CNT substrates, 1 h before plating cells. Subsequently, both substrates were sterilized with UV light for 20 min. Cultures were incubated at 37 °C, in a humidified atmosphere enriched with 5% CO<sub>2</sub>, in a culture medium containing Neurobasal Medium (Gibco), supplemented with B27 (2%; Gibco), Glutamax ( $10 \times 10^{-3}$  M; Gibco), and Gentamycin ( $500 \times 10^{-9}$  M; Gibco). Culture medium was renewed (60%) after 4 days from seeding. Plating was carried out at a nominal density of  $200,000 \pm 16,000 \text{ cells mL}^{-1}$  ( $n = 4$  different series of cultures). Cultures were then used for experiments after 9+10 DIV.

**Immuno-cytochemistry, Confocal Microscopy, and Electron Microscopy:** Cells cultured on CCVD-grown CNT carpets and on glass controls were fixed after 9+10 DIV in a PBS solution containing 4% formaldehyde (prepared from fresh paraformaldehyde) for 20 min at RT. Cells were subsequently blocked and permeabilized in 1% Triton X-100, 5% fetal bovine serum (FBS) in PBS for 30 min at RT. Samples were incubated with primary antibodies (rabbit polyclonal anti- $\beta$ -tubulin III, Sigma-Aldrich, 1:250 dilution; mouse monoclonal anti-GFAP, Sigma-Aldrich, 1:200 dilution) diluted in PBS with 5% FBS, for 30 min at RT.<sup>[19,63]</sup> Samples were then incubated with secondary antibodies (Alexa 594 goat anti rabbit, Invitrogen, dilution 1:500; Alexa 488 goat anti mouse, Invitrogen, dilution 1:500) and with DAPI (Invitrogen, 1:200 dilution) to stain the nuclei, for 30 min at RT. Samples were mounted using Vectashield mounting medium (Vector Laboratories) or with anti-fade medium Fluoromount (Sigma-Aldrich) on rectangular coverslips of 0.120 mm in thickness, to overcome the limitation introduced by CNT samples' opaqueness preventing direct observation through the supporting surface. Upon immunofluorescence staining, hippocampal cultures on both CNTs and glass controls were imaged using an inverted confocal microscope (Leica Microsystems GmbH, Wetzlar, Germany—HCX PL APO CS 40 $\times$ , N.A. 1.25, oil). Images were analyzed offline using the image-processing package Fiji.<sup>[80]</sup> To get insight into neuronal network morphology when plated on patterned CNT substrates, images of immunolabeled cultures were obtained using a Nikon Eclipse Ti2 inverted microscope connected to a ATR confocal system (Nikon Instruments—CFI Apochromat Lambda S 60 $\times$  Oil, N.A. 1.4, Oil). Acquisition, images reconstruction and analysis were accomplished using both NIS-Elements (Nikon) and Fiji software.

SEM characterization was performed on a Gemini SUPRA 40 SEM (Carl Zeiss GmbH, Oberkochen, DE) collecting just secondary electrons. Prior to SEM visualization all cellular samples were washed with 0.1 M cacodylate buffer (pH = 7.2) and subsequently fixed for 1 h at RT with 2% glutaraldehyde (Fluka, Italy) in a 0.1 M cacodylate buffered solution. Cultures were carefully rinsed with cacodylate buffer and dehydrated soaking them in a sequence of water/ethanol solutions at progressively higher alcohol concentrations (30%, 50%, 70%, 80%, 90%, 95%, and 100% ethanol) for 10 min each. Samples were then let to dry at 4 °C overnight. In order to avoid charge accumulation during SEM analysis all samples were Au metalized in a metal sputter coater (Polaron SC7620). An accelerating voltage of about 5 keV was used for sample visualization.

**Calcium Imaging and Data Analysis:** Ca<sup>2+</sup> imaging experiments were performed by loading hippocampal cells with the cell permeable Ca<sup>2+</sup> dye Oregon Green 488 BAPTA I-AM (Molecular Probes, final concentration  $4 \times 10^{-6}$  M) for 30 min.<sup>[19,63]</sup> Cultures were then positioned in a recording

chamber on an inverted microscope (Nikon Eclipse TiU), where they were continuously superfused with physiological saline solution containing (in  $\times 10^{-3}$  M): 150 NaCl, 4 KCl, 2 CaCl<sub>2</sub>, 1 MgCl<sub>2</sub>, 10 HEPES, 10 glucose (pH adjusted to 7.4 with NaOH; osmolarity 300 mOsm) at 5 mL min<sup>-1</sup>.<sup>[19,63]</sup> Video microscopy and Ca<sup>2+</sup>-imaging measurements were performed at RT. The Oregon Green-loaded cultures were observed with a 20 $\times$  air objective (0.45 N.A., Nikon, Japan). All the recordings were taken from randomly selected visual fields and performed from visual fields (512  $\times$  512 pixels<sup>2</sup>, binning 4). Images were continuously acquired by means of a Hamamatsu ORCA Flash4.0 V2 sCMOS camera, exciting the Ca<sup>2+</sup> dye at 488 nm wavelength by means of a fluorescence cube filter set (Ex = 480/20 nm, Em = 520/40 nm, Dic = 500–510 nm, Semrock) coupled to a high-pressure Hg lamp (Nikon). Images were recorded at 6 Hz for 30 min at 200 ms exposure time and simultaneously displayed on a color monitor.

The imaging system was controlled by an integrating imaging software (HCLImage Live) using a dedicated workstation.

In order to induce rhythmic bursts, 20  $\times 10^{-6}$  M bicuculline methiodide (Sigma-Aldrich), diluted in the saline solution, was added after 10 min recording; at the end of each experiment, 1  $\times 10^{-6}$  M TTX (a voltage-gated, fast Na<sup>+</sup> channel blocker) was added to the recording solution to confirm the neuronal nature of the recorded signals.<sup>[19,63]</sup> Recorded images were analyzed off-line with Fiji (selecting region of interest, ROI, around cell bodies), Clampfit (pClamp software, 10.2 version; Axon Instruments), and Igor Pro Software (6.32A version; WaveMetrics, Lake Oswego, Oregon, USA).

Intracellular Ca<sup>2+</sup> transients were detected as signals that exceed at least five times the standard deviation of the noise and were expressed as fractional amplitude increase ( $\Delta F/F_0$ , where  $F_0$  is the baseline fluorescence level and  $\Delta F$  is the rise over baseline).<sup>[19,63]</sup> The IEI, reciprocal of frequency, as the difference between the onset of consecutive Ca<sup>2+</sup> events, was then calculated.<sup>[19,63]</sup> IEI values recorded under the same experimental conditions were pooled together and averaged for further comparison.

Fraction of active cells per field of view was evaluated for both CNT and controls as the ratio between the number of cells showing an electrical bursting activity and the total number of cells present in the field.

**Electrical Stimulation through CNTs:** Dissociated hippocampal neurons were obtained from P2+P3 Wistar rats as previously reported.<sup>[16]</sup> Cultures were plated above a uniform carpet of CCVD CNTs and grown at 37 °C, 5% CO<sub>2</sub> in neurobasal medium (Invitrogen) added with B-27 supplement (Thermo Fisher) and GlutaMAX (Thermo Fisher) to a 1 $\times$  final concentration. Gentamicin (Thermo Fisher) to a final concentration of 5  $\mu$ g mL<sup>-1</sup> was added to prevent culture contaminations. After 10 DIV, cells were loaded with the Ca<sup>2+</sup> dye Oregon Green 488 BAPTA-1 AM (Molecular Probes). 10  $\mu$ L DMSO (Sigma-Aldrich) was added to the 50  $\mu$ g stock of the dye, and cultures were incubated with a final concentration of 4  $\times 10^{-6}$  M for 40 min at 37 °C, 5% CO<sub>2</sub>. Samples were therefore mounted on a fixed-stage upright microscope (Eclipse FN1, Nikon). Cultures were continuously perfused at 5 mL min<sup>-1</sup> rate and at RT with extracellular saline solution of composition ( $\times 10^{-3}$  M): 150  $\times 10^{-3}$  M NaCl, 4  $\times 10^{-3}$  M KCl, 2  $\times 10^{-3}$  M CaCl<sub>2</sub>, 1  $\times 10^{-3}$  M MgCl<sub>2</sub>, 10  $\times 10^{-3}$  M HEPES, and 10  $\times 10^{-3}$  M glucose (pH adjusted to 7.4 with NaOH; osmolarity 300 mOsm). Ca<sup>2+</sup>-dye was excited at 488 nm with a mercury lamp; excitation light was filtered with a ND filter (1/32) and separated from the light emitted from the sample using a 505 nm dichroic mirror. Spontaneous calcium transients were recorded with a 20 $\times$  water immersion objective (UMPlanFL, 0.5 N.A., Olympus) using an EMCCD camera (iXon Ultra 897, Andor, Oxford Instruments) controlled by a computer through NIS-elements D (Nikon). Images were acquired every 150 ms at 10 MHz readout compensating the read noise with  $\times 250$  electron multiplying gain. After 8 min of recording of spontaneous activity, the application of the synaptic blockers (all from Sigma-Aldrich) DL-2-amino-5-phosphonovaleric acid (APV) 25  $\times 10^{-6}$  M (N-methyl-D-aspartate (NMDA) receptors selective antagonist), bicuculline 10  $\times 10^{-6}$  M ( $\gamma$ -Aminobutyric acid type A (GABA<sub>A</sub>) receptors antagonist), and cyanquinoxaline (CNQX) 10  $\times 10^{-6}$  M ( $\alpha$ -amino-3-hydroxy-5-methyl-4-isoxazolepropionic acid (AMPA)/kainate receptors antagonist) completely silenced the network, as previously reported.<sup>[81]</sup>

In these conditions only evoked signals are visible in a Ca<sup>2+</sup> imaging experiment.<sup>[82]</sup>

In order to perform neuronal network stimulation experiments the sample (8  $\times$  8 mm<sup>2</sup>) was glued at the bottom of a polystyrene 35 mm Petri dish. A Kapton insulated platinum wire was inserted through a hole into the Petri and glued to the top conductive CNT layer of the sample using conductive silver-paste (Ted Pella, Inc.). All the bottom of the Petri-dish with the exception of the active CNT surface of the sample not being covered by silver paste was insulated with PDMS (Sylgard 184, Dow Corning). The contacting wire was plugged into the active output of the stimulating apparatus while its ground was plugged to an Ag/AgCl pellet electrode immersed in the extracellular saline solution. Therefore, a voltage pulse train with an isolated stimulator (Digitimer DS2A) was manually triggered. At the end of each session, 1  $\times 10^{-6}$  M TTX (a voltage-gated, fast Na<sup>+</sup> channel blocker; Latoxan) was added to impair also the evoked activity and to confirm the neuronal nature of the recorded signals (see Figure 6b,c). Analysis was accomplished with ImageJ (NIH) and Clampfit (pClamp suite, 10.4 version; Axon Instruments) software in off-line mode. Intracellular Ca<sup>2+</sup> transients were expressed as fractional amplitude increase ( $\Delta F/F_0$ , where  $F_0$  is the baseline fluorescence level and  $\Delta F$  is the rise over baseline). The onset time of neuronal activation was determined by detecting those events in the fluorescence signal that exceeded at least five times the standard deviation of the noise.

**Statistical Analysis:** All data were presented as mean  $\pm$  standard deviation (SD) of the mean ( $n$  is the number of cells, if not otherwise indicated). Statistically significant difference between two data sets was assessed using Student's *t*-test (after checking variances homogeneity by Leven's test) where a value of  $p < 0.05$  was accepted as indicative of statistically significant difference. Differences among multiple groups were evaluated by F-statistic with two-way ANOVA, followed by the Holm–Sidak test for multiple comparison.

## Supporting Information

Supporting Information is available from the Wiley Online Library or from the author.

## Acknowledgements

I.R. and R.R. contributed equally to this work. D.S. and I.R. acknowledge support by the Italian Health Ministry (GR-2011-02348707) and A.G. for the NATO–G5140 project. C.T. acknowledges the support from the University of Trieste through the FRA2016 research funding. The authors would like to thank TASC-IOM for Clean Room assistance, Laura Ballerini for the support in electrophysiological experiments, Alois Bonifacio for technical support and discussion in Raman spectroscopy experiments, Paolo Fornasiero for the advice and helpful discussion about electrochemical analysis, Paolo Bertoncin for technical support in TEM characterization and Loredana Casalis for discussions and proofreading the manuscript.

## Conflict of Interest

The authors declare no conflict of interest.

## Keywords

carbon nanotubes, CVD, electrical activity, neuronal network, surface patterning

Received: October 10, 2018

Revised: February 28, 2019

Published online:

- [1] D. Scaini, L. Ballerini, *Curr. Opin. Neurobiol.* **2018**, *50*, 50.
- [2] N. P. Pampaloni, M. Lottner, M. Giugliano, A. Matruggio, F. D'Amico, M. Prato, J. A. Garrido, L. Ballerini, D. Scaini, *Nat. Nanotechnol.* **2018**, *13*, 755.
- [3] S. Usmani, E. A. Aurand, M. Medelin, A. Fabbro, D. Scaini, J. Laishram, F. B. Rosselli, A. Ansuini, D. Zoccolan, M. Scarselli, M. De Crescenzi, S. Bosi, M. Prato, L. Ballerini, *Sci. Adv.* **2016**, *2*, e1600087.
- [4] J. W. Mintmire, C. T. White, *Carbon* **1995**, *33*, 893.
- [5] R. S. Ruoff, D. C. Lorentz, *Carbon* **1995**, *33*, 925.
- [6] J.-P. Salvetat, J.-M. Bonard, N. H. Thomson, A. J. Kulik, L. Forró, W. Benoit, L. Zuppiroli, *Appl. Phys. A: Mater. Sci. Process.* **1999**, *69*, 255.
- [7] N. Yang, X. Chen, T. Ren, P. Zhang, D. Yang, *Sens. Actuators, B* **2015**, *207*, 690.
- [8] H. E. Unalan, M. Chhowalla, *Nanotechnology* **2005**, *16*, 2153.
- [9] W. Feng, P. Ji, *Biotechnol. Adv.* **2011**, *29*, 889.
- [10] S. R. Ji, C. Liu, B. Zhang, F. Yang, J. Xu, J. Long, C. Jin, D. L. Fu, Q. X. Ni, X. J. Yu, *Biochim. Biophys. Acta* **2010**, *1806*, 29.
- [11] H. He, L. A. Pham-Huy, P. Dramou, D. Xiao, P. Zuo, C. Pham-Huy, *BioMed. Res. Int.* **2013**, *8*, 578290.
- [12] M. Baldrighi, M. Trusel, R. Tonini, S. Giordani, *Front. Neurosci.* **2016**, *10*, 250.
- [13] D. Tasis, N. Tagmatarchis, A. Bianco, M. Prato, *Chem. Rev.* **2006**, *106*, 1105.
- [14] A. Battigelli, C. Ménard-Moyon, T. Da Ros, M. Prato, A. Bianco, *Adv. Drug Delivery Rev.* **2013**, *65*, 1899.
- [15] F. M. Tonelli, A. K. Santos, K. N. Gomes, E. Lorençon, S. Guatimosim, L. O. Ladeira, R. R. Resende, *Int. J. Nanomed.* **2012**, *7*, 4511.
- [16] V. Lovat, D. Pantarotto, L. Lagostena, B. Cacciari, M. Grandolfo, M. Righi, G. Spalluto, M. Prato, L. Ballerini, *Nano Lett.* **2005**, *5*, 1107.
- [17] G. Cellot, E. Cilia, S. Cipollone, V. Rancic, A. Sucapane, S. Giordani, L. Gambazzi, H. Markram, M. Grandolfo, D. Scaini, F. Gelain, L. Casalis, M. Prato, M. Giugliano, L. Ballerini, *Nat. Nanotechnol.* **2009**, *4*, 126.
- [18] E. R. Aurand, S. Usmani, M. Medelin, D. Scaini, S. Bosi, F. B. Rosselli, S. Donato, G. Tromba, M. Prato, L. Ballerini, *Adv. Funct. Mater.* **2017**, *28*, 1700550.
- [19] S. Bosi, R. Rauti, J. Laishram, A. Turco, D. Lonardoni, T. Nieuw, M. Prato, D. Scaini, L. Ballerini, *Sci. Rep.* **2015**, *5*, 9562.
- [20] E. B. Malarkey, V. Parpura, *Neurodegener. Dis.* **2007**, *4*, 292.
- [21] E. B. Malarkey, V. Parpura, *Acta Neurochir. Suppl.* **2010**, *106*, 337.
- [22] G. Cellot, F. M. Toma, Z. K. Varley, J. Laishram, A. Villari, M. Quintana, S. Cipollone, M. Prato, L. Ballerini, *J. Neurosci.* **2011**, *31*, 12945.
- [23] A. Fabbro, A. Villari, J. Laishram, D. Scaini, F. M. Toma, A. Turco, M. Prato, L. Ballerini, *ACS Nano* **2012**, *6*, 2041.
- [24] M. Allegri, D. K. Perivoliotis, M. G. Bianchi, M. Chiu, A. Pagliaro, M. A. Koklioti, A. A. Trompeta, E. Bergamaschi, O. Bussolati, C. A. Charitidis, *Toxicol. Rep.* **2016**, *3*, 230.
- [25] Y. Liu, Y. Zhao, B. Sun, C. Chen, *Acc. Chem. Res.* **2013**, *46*, 702.
- [26] N. Kobayashi, H. Izumi, Y. Morimoto, *J. Occup. Health.* **2017**, *59*, 394.
- [27] N. P. Pampaloni, D. Scaini, F. Perissinotto, S. Bosi, M. Prato, L. Ballerini, *Nanomedicine* **2017**, *S1549-9634*, 30082.
- [28] K. A. Shah, B. A. Tali, *Mater. Sci. Semicond. Process.* **2016**, *41*, 67.
- [29] T. Ng, B. Chen, J. E. Koehne, A. M. Cassell, J. Li, J. Han, M. Meyyappan, *J. Phys. Chem. B* **2003**, *107*, 8484.
- [30] J. J. Schneider, *Adv. Biosyst.* **2017**, *1*, 1700101.
- [31] A. M. Cassell, J. A. Raymakers, J. Kong, H. Dai, *J. Phys. Chem. B* **1999**, *103*, 6484.
- [32] R. Andrews, D. Jacques, D. Qian, T. Rantell, *Acc. Chem. Res.* **2002**, *35*, 1008.
- [33] V. O. Khavrus, N. V. Lemesh, S. V. Gordijchuk, A. I. Tripolsky, T. S. Ivashchenko, M. M. Bilyi, P. E. Strizhak, *React. Kinet. Catal. Lett.* **2008**, *93*, 295.
- [34] A. Mazzatenta, M. Giugliano, S. Campidelli, L. Gambazzi, L. Businaro, H. Markram, M. Prato, L. Ballerini, *J. Neurosci.* **2007**, *27*, 6931.
- [35] W. Z. Li, S. S. Xie, L. X. Qian, B. H. Chang, B. S. Zou, W. Y. Zhou, R. A. Zhao, G. Wang, *Science* **1996**, *274*, 1701.
- [36] Y. J. Jung, B. Wei, R. Vajtai, P. M. Ajayan, Y. Homma, K. Prabhakaran, T. Ogino, *Nano Lett.* **2003**, *3*, 561.
- [37] P. M. Parthangal, R. E. Cavicchi, M. R. Zachariah, *Nanotechnology* **2007**, *18*, 185605.
- [38] M. K. Lai, N. M. Mohamed, K. M. Begam, *Adv. Mater. Res.* **2008**, *32*, 29.
- [39] D. E. Resasco, W. E. Alvarez, F. Pompeo, L. Balzano, J. E. Herrera, B. Kitiyanan, A. Borgna, *J. Nanopart. Res.* **2002**, *4*, 131.
- [40] M. Horibe, M. Nihei, D. Kondo, A. Kawabata, Y. Awano, *Jpn. J. Appl. Phys.* **2005**, *44*, 5309.
- [41] J. Robertson, G. Zhong, C. S. Esconjauregui, B. C. Bayer, C. Zhang, M. Fouquet, S. Hofmann, *Jpn. J. Appl. Phys.* **2012**, *51*, 01AH01.
- [42] J. M. Wen, J. W. Evans, M. C. Bartelt, J. W. Burnett, P. A. Thiel, *Phys. Rev. Lett.* **1996**, *76*, 652.
- [43] E. Jiran, C. V. J. Thompson, *J. Electron. Mater.* **1990**, *19*, 1153.
- [44] P. R. Gadkari, A. P. Warren, R. M. Todi, R. V. Petrova, K. R. Coffey, *J. Vac. Sci. Technol., A* **2005**, *23*, 1152.
- [45] Y. M. Li, W. Kim, Y. G. Zhang, M. Rolandi, D. W. Wang, H. J. Dai, *J. Phys. Chem. B* **2001**, *105*, 11424.
- [46] J. F. Colomer, B. Ruelle, N. Moreau, S. Lucas, R. Snyders, T. Godfroid, C. Navio, C. Bittencourt, *Surf. Coat. Technol.* **2011**, *205*, S592.
- [47] R. C. Batra, A. Sears, *Modell. Simul. Mater. Sci. Eng.* **2007**, *15*, 835.
- [48] C. J. Lee, J. Park, Y. Huh, L. Yong, *Chem. Phys. Lett.* **2001**, *343*, 33.
- [49] J. C. Charlier, *Acc. Chem. Res.* **2002**, *35*, 1063.
- [50] L. Zhang, Z. Li, Y. Tan, G. Loll, N. Sakulchaicharoen, F. G. Requejo, B. S. Mun, D. E. Resasco, *Chem. Mater.* **2006**, *18*, 5624.
- [51] M. S. Dresselhaus, P. Eklund, *Adv. Phys.* **2000**, *49*, 705.
- [52] P. C. Eklund, J. M. Holden, R. A. Jishi, *Carbon* **1995**, *33*, 959.
- [53] E. F. Antunes, A. O. Lobo, E. J. Corat, V. J. Trava-Airoldi, *Carbon* **2007**, *45*, 913.
- [54] W. Li, H. Zhang, C. Wang, Y. Zhang, L. Xu, K. Zhu, *Appl. Phys. Lett.* **1997**, *70*, 2684.
- [55] R. A. DiLeo, B. J. Landi, R. P. Raffaele, *J. Appl. Phys.* **2007**, *101*, 064307.
- [56] C. Mattevi, C. T. Wirth, S. Hofmann, R. Blume, M. Cantoro, C. Ducati, C. Cepek, A. Knop-Gericke, S. Milne, C. Castellarin-Cudia, S. Dolafi, A. Goldoni, R. Schloegl, J. Robertson, *J. Phys. Chem. C* **2008**, *112*, 12207.
- [57] S. Hofmann, R. Blume, C. T. Wirth, M. Cantoro, R. Sharma, C. Ducati, M. Haevecker, S. Zafeirotos, P. Schnoerch, A. Oesterreich, D. Teschner, M. Albrecht, A. Knop-Gericke, R. Schloegl, J. Robertson, *J. Phys. Chem. C* **2009**, *113*, 1648.
- [58] M. Scardamaglia, M. Amati, B. Llorente, P. Mudimela, J.-F. Colomer, J. Ghijsen, C. Ewels, R. Snyders, L. Gregoratti, C. Bittencourt, *Carbon* **2014**, *77*, 319.
- [59] T. I. T. Okpalugo, P. Papakonstantinou, H. Murphy, J. McLaughlin, N. M. D. Brown, *Carbon* **2005**, *43*, 153.
- [60] Y. Lu, H. Lyu, A. G. Richardson, T. H. Lucas, D. Kuzum, *Sci. Rep.* **2016**, *6*, 33526.
- [61] Y. J. Jung, Y. Homma, T. Ogino, Y. Kobayashi, D. Takagi, B. Wei, R. Vajtai, P. M. Ajayan, *J. Phys. Chem. B* **2003**, *107*, 6859.
- [62] H. M. Saavedra, T. J. Mullen, P. Zhang, D. C. Dewey, S. A. Claridge, P. S. Weiss, *Rep. Prog. Phys.* **2010**, *73*, 036501.
- [63] R. Rauti, N. Lozano, V. León, D. Scaini, M. Musto, I. Rago, F. P. Ulloa Severino, A. Fabbro, L. Casalis, E. Vázquez, K. Kostarelos, M. Prato, L. Ballerini, *ACS Nano* **2016**, *10*, 4459.

- [64] D. Avossa, M. D. Rosato-Siri, F. Mazzarol, L. Ballerini, *Neuroscience* **2003**, 122, 391.
- [65] W. N. Ross, *Nat. Rev. Neurosci.* **2012**, 13, 157.
- [66] C. Grienberger, A. Konnerth, *Neuron* **2012**, 73, 862.
- [67] E. Tibau, M. Valencia, J. Soriano, *Front. Neural Circuits* **2013**, 7, 199.
- [68] D. M. Sokal, R. Mason, T. L. Parker, *Neuropharmacology* **2000**, 39, 2408.
- [69] F. Aguado, M. A. Carmona, E. Pozas, A. Aguiló, F. J. Martínez-Guijarro, S. Alcantara, V. Borrell, R. Yuste, C. F. Ibañez, E. Soriano, *Development* **2003**, 130, 1267.
- [70] M. Raastad, J. F. Storm, P. Andersen, *Eur. J. Neurosci.* **1992**, 4, 113.
- [71] D. Mattia, M. P. Rossi, B. M. Kim, G. Korneva, H. H. Bau, Y. Gogotsi, *J. Phys. Chem. B* **2006**, 110, 9850.
- [72] C. Vallejo-Giraldo, E. Pugliese, A. Larrañaga, M. A. Fernandez-Yague, J. J. Britton, A. Trotier, G. Tadayyon, A. Kelly, I. Rago, J. R. Sarasua, E. Dowd, L. R. Quinlan, A. Pandit, M. J. Biggs, *Nanomedicine* **2016**, 11, 2547.
- [73] N. Gaio, C. Silvestri, B. van Meer, S. Vollebregt, C. L. Mummery, R. Dekker, *IEEE Sens. J.* **2016**, 16, 8685.
- [74] K. L. Kepplea, G. P. Sanborn, P. A. Lacasse, K. M. Gruenberg, W. J. Ready, *Carbon* **2008**, 46, 2026.
- [75] Y. Xia, G. M. Whitesides, *Angew. Chem., Int. Ed.* **1998**, 37, 550.
- [76] P. M. Mendes, J. A. Preece, *Curr. Opin. Colloid Interface Sci.* **2004**, 9, 236.
- [77] J. Huang, M. Lee, J. Kim, *J. Vac. Sci. Technol., A* **2012**, 30, 01A128.
- [78] A. Kumar, H. A. Biebuyck, G. M. Whitesides, *Langmuir* **1994**, 10, 1498.
- [79] P. Klapetek, M. Valtr, D. Nečas, O. Salyk, P. Dzik, *Nanoscale Res. Lett.* **2011**, 6, 514.
- [80] J. Schindelin, I. Arganda-Carreras, E. Frise, V. Kaynig, M. Longair, T. Pietzsch, S. Preibisch, C. Rueden, S. Saalfeld, B. Schmid, J. Y. Tinevez, D. J. White, V. Hartenstein, K. Eliceiri, P. Tomancak, A. Cardona, *Nat. Methods* **2012**, 9, 676.
- [81] I. Breskin, J. Soriano, E. Moses, T. Tlusty, *Phys. Rev. Lett.* **2006**, 97, 188102.
- [82] S. Stern, A. Agudelo-Toro, A. Rotem, E. Moses, A. Neef, *PLoS One* **2015**, 10, e0132577.



# Interfacing Neurons with Nanostructured Electrodes Modulates Synaptic Circuit Features

Ana Domínguez-Bajo, Beatriz Loreto Rodilla, Ivo Calaresu, Ana Arché-Núñez, Ankor González-Mayorga, Denis Scaini, Lucas Pérez, Julio Camarero, Rodolfo Miranda, Elisa López-Dolado, María Teresa González,\* Laura Ballerini,\* and María Concepción Serrano\*


Understanding neural physiopathology requires advances in nanotechnology-based interfaces, engineered to monitor the functional state of mammalian nervous cells. Such interfaces typically contain nanometer-size features for stimulation and recording as in cell-non-invasive extracellular microelectrode arrays. In such devices, it turns crucial to understand specific interactions of neural cells with physicochemical features of electrodes, which could be designed to optimize performance. Herein, versatile flexible nanostructured electrodes covered by arrays of metallic nanowires are fabricated and used to investigate the role of chemical composition and nanotopography on rat brain cells *in vitro*. By using Au and Ni as exemplary materials, nanostructure and chemical composition are demonstrated to play major roles in the interaction of neural cells with electrodes. Nanostructured devices are interfaced to rat embryonic cortical cells and postnatal hippocampal neurons forming synaptic circuits. It is shown that Au-based electrodes behave similarly to controls. Contrarily, Ni-based nanostructured electrodes increase cell survival, boost neuronal differentiation, and reduce glial cells with respect to flat counterparts. Nonetheless, Au-based electrodes perform superiorly compared to Ni-based ones. Under electrical stimulation, Au-based nanostructured substrates evoke intracellular calcium dynamics compatible with neural networks activation. These studies highlight the opportunity for these electrodes to excite a silent neural network by direct neuronal membranes depolarization.

## 1. Introduction

For decades, scientists have been interested in understanding the state of mammalian cells from different perspectives (e.g., molecular, mechanical, structural, electrical, and functional), as it highly relates to physiology and pathology. In this scenario, recent advances in nanotechnology tools are broadening the technical possibilities to do so. One particular example is the fabrication of interfaces with nanometer-size features for neural stimulation and recording. At present, neural activity can be monitored locally by using intracellular sharp/patch electrodes, extracellular substrate-integrated microelectrode arrays, and fluorescent indicators/genetically encoded probes.<sup>[1]</sup> Although advances at the level of individual cells have provided unprecedented knowledge on neuronal functioning, unraveling the connectivity routes of nervous system nuclei and circuits must rely more on the use of cell-non-invasive extracellular microelectrode arrays.<sup>[2–4]</sup> By means of nano- and micro-technologies,

A. Domínguez-Bajo, Dr. M. C. Serrano  
Instituto de Ciencia de Materiales de Madrid (ICMM)  
CSIC  
Calle Sor Juana Inés de la Cruz 3  
Madrid 28049, Spain  
E-mail: mc.terradas@csic.es

B. L. Rodilla, A. Arché-Núñez, Dr. L. Pérez, Prof. J. Camarero,  
Prof. R. Miranda, Dr. M. T. González  
Fundación IMDEA Nanociencia  
Calle Faraday 9  
Madrid 28049, Spain  
E-mail: teresa.gonzalez@imdea.org

 The ORCID identification number(s) for the author(s) of this article can be found under <https://doi.org/10.1002/adbi.202000117>.

© 2020 The Authors. Published by Wiley-VCH GmbH. This is an open access article under the terms of the Creative Commons Attribution-NonCommercial License, which permits use, distribution and reproduction in any medium, provided the original work is properly cited and is not used for commercial purposes.

DOI: 10.1002/adbi.202000117

B. L. Rodilla, Dr. L. Pérez  
Departamento de Física de Materiales  
Universidad Complutense de Madrid  
Plaza de las Ciencias s/n  
Madrid 28040, Spain

I. Calaresu, Dr. D. Scaini, Prof. L. Ballerini  
International School for Advanced Studies (SISSA/ISAS)  
Via Bonomea 265  
Trieste 34136, Italy  
E-mail: laura.ballerini@sissa.it

A. González-Mayorga, Dr. E. López-Dolado  
Hospital Nacional de Paraplégicos  
SESCAM

Finca La Peraleda s/n  
Toledo 45071, Spain

Prof. J. Camarero, Prof. R. Miranda  
Instituto "Nicolas Cabrera" and Condensed Matter Physics Center (IFIMAC)  
Departamento de Física de la Materia Condensada  
Universidad Autónoma de Madrid (UAM)  
Campus de Cantoblanco  
Madrid 28049, Spain

the benefits of substrate-integrated extracellular electrode arrays are being combined with those of intracellular electrodes to improve the quality and performance of neural interfaces.<sup>[15,5]</sup> Importantly, nanotechnology allows for an improved design of lower impedance and a more intimate interface with individual neurons by better mimicking the native extracellular environment.<sup>[6]</sup> Early studies reported the ability of high-density silicon nanowire (NW) transistor arrays to record signals from up to 50 different spatial points in a single axon.<sup>[7]</sup> Recent advances in the field include gold mushroom-shaped microelectrodes functionalized with RGD peptides,<sup>[8]</sup> vertical NW electrode arrays,<sup>[9]</sup> and platinum-black electrodes with nanoscale roughness,<sup>[10]</sup> to name a few. Specifically, vertical nanoscale structures have demonstrated to support the growth of a variety of mammalian cells in vitro.<sup>[11]</sup> From the chemical point of view, nanoelectrode fabrication has explored materials such as gold (Au),<sup>[12,13]</sup> platinum,<sup>[14]</sup> silicon,<sup>[9]</sup> iridium oxide,<sup>[15]</sup> and gallium phosphide.<sup>[16]</sup> In these approaches, the reduction in electrode size to the nanometer scale enhances the precision of the stimulation point and then optimizes the efficiency of the stimulating devices.<sup>[17]</sup>

Aiming to biomedical applications, the flexibility of the electrodes becomes an essential factor to minimize the mechanical mismatch at the interface and guarantee an effective coupling.<sup>[5]</sup> In this line, a series of flexible electrodes have been proposed,<sup>[18–20]</sup> but only a few combine flexibility with nanostructure.<sup>[21,22,23]</sup> For instance, Rogers and colleagues described a bio-interfaced system based on ultrathin electronics supported by bioresorbable substrates of silk fibroin,<sup>[18]</sup> which assures minimal stresses on the tissue and highly conformal coverage. Authors proved the utility of these interfaces to record neural activity in the feline visual cortex. By using a transparent silicone substrate, Minev et al. patterned microfluidic channels for drug delivery and soft platinum/silicone electrodes and stretchable gold interconnects for electrical stimulation and transferring electrophysiological signals.<sup>[21]</sup> This e-dura proved utility for brain-machine interfaces and electrochemical spinal neuromodulation. Differently, vertically aligned carbon nanotubes (CNTs) have been integrated on a flexible and biocompatible parylene substrate to serve as flexible nanostructured electrodes with lower impedance and larger interfacial capacitance for extracellular neuronal recording and stimulation in rats.<sup>[22]</sup> On the basis of hydrothermally grown ZnO NWs over a metalized polyimide layer, Ryu et al. described stable flexible neural probes with low impedance after a two steps coating process with gold and PEDOT.<sup>[23]</sup> So, in order to achieve flexibility, either non-metallic solutions are used, at the cost of an increase in impedance, or a many-step growth process is required to finally metalize the sample.

In this context, it turns crucial as well to understand the specific interaction of neural cells with topographical features so electrodes can be designed and manipulated to achieve optimized performance and biological responses. Indeed, cells have the ability to respond to topography,<sup>[24]</sup> especially in the fate of

progenitor and stem cells.<sup>[25,26]</sup> In this sense, Carlberg et al. first demonstrated that topographical cues could be used to induce dopaminergic differentiation of human embryonic stem cells (ESCs) by means of an electrospun polyurethane nanofiber scaffold in the presence of neurotrophic factors.<sup>[27]</sup> Other works that followed supported this finding,<sup>[28,29]</sup> with polymeric grooved substrates being one of the first and most extensively explored.<sup>[30]</sup> Regarding the use of metallic substrates, Au films varying in surface nano-roughness have been proved to induce differential responses in ESCs,<sup>[31]</sup> with higher adhesion and differentiation profiles on those films with root mean square surface roughness of  $\approx 21$  nm rather than 30 nm and plane (0.40 nm). In general terms, surface nanotopography has been stated to significantly accelerate neuronal development in vitro and induce a preferential differentiation of stem cells to neuronal lineages, along with a remarkable impact on neuronal guidance, neurite outgrowth and alignment.<sup>[32,33]</sup> In this scenario, pillar structures and NWs are being pursued as a source of “interrupted” topographical features for neural cells, with a wide range of customizable configurations including isotropic and anisotropic forms.<sup>[34]</sup> Thus, topographical cues in the shape of pillar structures at the nanoscale are desirable advances to improve spatial control in neural interfacing and to guide relevant biological behaviors.

In this work, we have designed thin metal electrodes whose surface is nanostructured by arrays of vertical metallic NWs grown by template-assisted electrodeposition to improve performance by reducing impedance and more intimately interfacing individual neurons. Differently from most previously reported nanostructured metallic electrodes, the ones presented herein are flexible, allowing an easier implementation in medical interfaces by improving conformal implantation and reducing mechanical stresses on the neural tissue. On the other hand, our technique allows to produce metallic nanostructures in a simple way, guaranteeing a good electrode conductance and low impedance without the need of a multiple-layer growth process. We have investigated the role that both chemical composition and nanotopography play on the biological behavior of rat brain cells in vitro. Morphology, viability and neural differentiation parameters are first studied. We then extend this investigation by challenging the nanostructured electrodes with postnatal hippocampal cultures. Neuronal and glial cells are seeded at the interface of NW arrays to investigate, by confocal microscopy and live calcium imaging, the formation and function of postnatal synaptic networks together with glial cell reactivity. Finally, we verify the ability of these flexible arrays to evoke neuronal action potentials by delivering electrical stimulation and monitoring single cell responses by live calcium imaging.

## 2. Results and Discussion

### 2.1. Nanostructured Metallic Arrays Fabrication and Characterization

We fabricated flexible nanostructured electrodes composed of vertical arrays of either gold (Au-NWs) or nickel (Ni-NWs) NWs grown on top of Au substrates. These two different metals were selected to form two different kinds of nanostructured electrodes based on their largely different physicochemical properties.

Dr. E. López-Dolado  
Research Unit of “Design and development of biomaterials for neural regeneration”  
Hospital Nacional de Paraplégicos  
Joint Research Unit with CSIC  
Toledo 45071, Spain



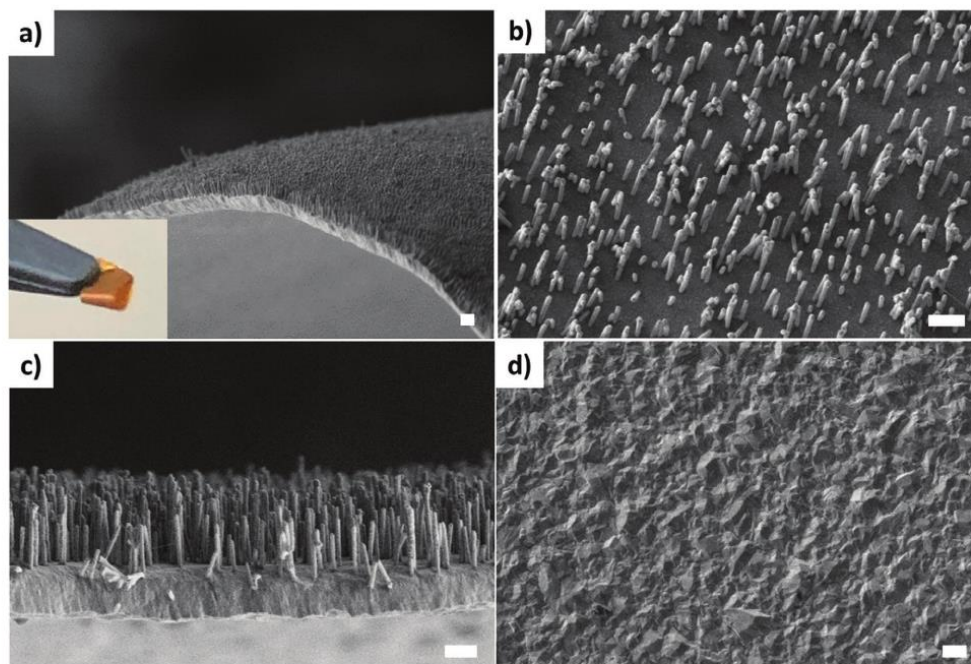


**Figure 1.** a) Representative SEM image showing the flexibility of the electrodes. SEM image in b) top view and c) cross-section of an Au-NWs electrode in which both, the base and the nanostructured active part can be seen. d) Representative SEM image of a planar Au-Flat electrode. Scale bars represent 1  $\mu\text{m}$  in all the images.

Specifically, the selection of Au was driven by its extensive applicability and biocompatibility, while Ni was chosen by its superior robustness and better mechanical properties than Au. We determined the optimum thickness of the Au substrate to be 1  $\mu\text{m}$ . This is the minimum thickness that preserves both the substrate and the NW-network integrity, allowing the electrode manipulation without damages, while maximizing their flexibility. As illustrated in **Figure 1**, we observed no damage, plastic deformation, break or crack after bending our electrodes with a curvature radius down to 0.3 mm. Importantly, this makes the electrodes adaptable and, therefore, versatile as part of applied neural interfaces.

These arrays were fabricated by template-assisted electrodeposition using polycarbonate nanoporous membranes as templates (details described in the Experimental Section and Figure S1, Supporting Information). After the growth, the template was chemically dissolved, leaving a network of vertical NWs attached at their bottom to the Au flat base. By this methodology, homogeneous and reproducible nanostructured electrodes composed of either Au or Ni NWs were fabricated. Figure 1 shows a representative scanning electron microscopy (SEM) image in top view (panel b) and cross-section (panel c) of an Au-NWs electrode in which both, the base and the nanostructured active part can be seen. Similar images were obtained for Ni-NWs electrodes (Figure S2, Supporting Information). For proper evaluation of the nanostructure effect, we

also fabricated flat electrodes, either composed of Au (Au-Flat) or Ni (Ni-Flat), as reference samples (Figure 1d). Interestingly, we found the impedance of both Au-NWs and Ni-NWs electrodes to be very similar,  $106 \pm 3$  and  $108 \pm 3$   $\Omega$ , respectively, which is less than half of the impedance measured in a planar Au electrode of the same area ( $232 \pm 3$   $\Omega$ ), showing that nanostructure clearly reduced the impedance of the electrode as expected, due to a larger electrode effective area. Also, impedance values a 10% lower were observed when bending the NWs electrodes as described above. A denser NWs network covering more tightly the base surface would reduce further the final electrode impedance. We are presently working on obtaining this type of nanostructure.

## 2.2. Nanotopography and Chemical Composition affect Embryonic Cortical Cell Differentiation In Vitro

To initially assess mammalian brain progenitor fate in contact with the electrodes fabricated, neural cells derived from progenitor cells isolated from the cerebral cortices of rat embryos (rNCCs) were used. Preliminary studies on bare electrodes, either Au-NWs or Ni-NWs, revealed a poor adhesion of these cells, with high-size spheroid-like clumps (Figure S3, Supporting Information). In order to facilitate rNCCs adhesion, samples

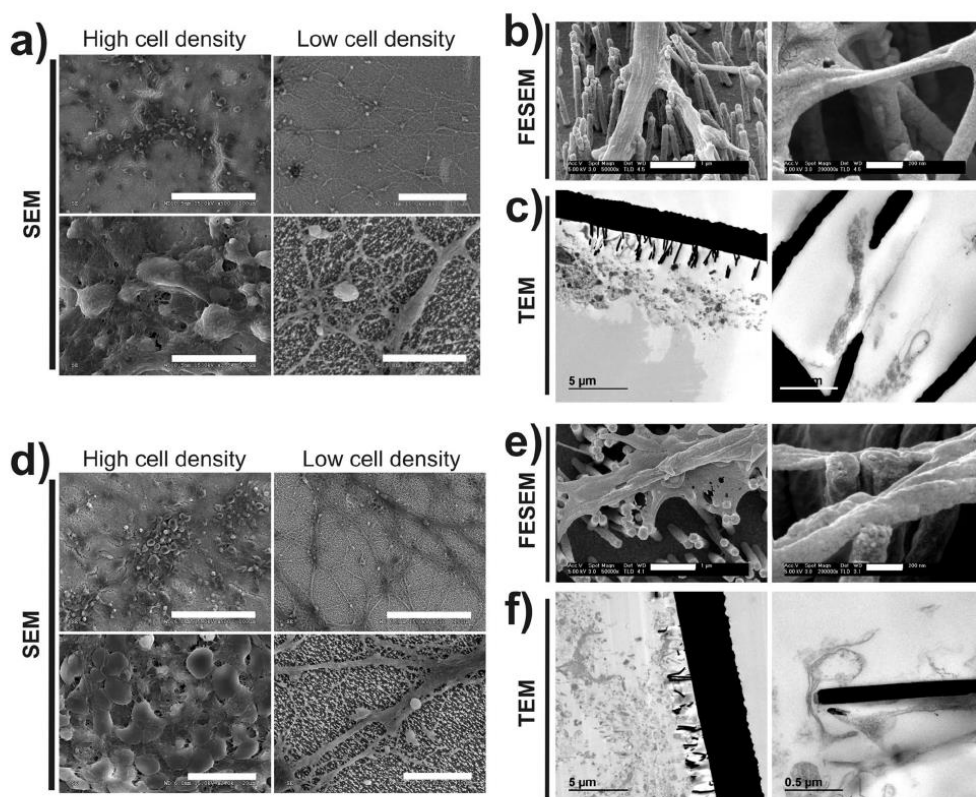


**Figure 2.** Morphological evaluation of rNCC cultures at high- and low-density seeding conditions on a–c) Au-NWs and d–f) Ni-NWs electrodes. Representative SEM, FESEM, and TEM micrographs of cultures at 14 DIV are shown. Scale bars represent: (a,d) 100  $\mu\text{m}$  (top) and 20  $\mu\text{m}$  (bottom); (b,e): 1  $\mu\text{m}$  (left) and 200 nm (right); and (c,f): 5  $\mu\text{m}$  (left) and 0.5  $\mu\text{m}$  (right).

were thereafter functionalized with poly-L-lysine (PLL) molecules. Immunofluorescence studies with PLL-FITC confirmed the homogeneous functionalization of the arrays surfaces when coated with PLL (Figure S4, Supporting Information). After 14 days in vitro (DIV), rNCCs properly attached and spread on top of PLL-coated Au-NWs platforms colonizing the totality of the substrate surface (Figure 2a) when cultured at favorable high density conditions ( $75\,000\text{ cells cm}^{-2}$ ) as shown by SEM. When challenged at low density ( $25\,000\text{ cells cm}^{-2}$ ), these cells also adhered to the arrays retaining their typical neural morphology and forming interconnected cultures. Detailed observation by field-emission scanning electron microscopy (FESEM) revealed a close contact of both somata and neurites with the Au-NWs (Figure 2b), without evidences of either neural cell membrane piercing or perforation, as also confirmed by transmission electron microscopy (TEM) studies (Figure 2c). Standard glass coverslips served as a reference control material for comparison (Figure S5, Supporting Information). When Ni-NWs electrodes were investigated, a comparable degree of cell adhesion

and close interaction with the NWs arrays surface was found (Figure 2d–f), both at high and low density seeding conditions. Importantly, both Au-NWs and Ni-NWs substrates supported the growth of highly confluent cultures of rNCCs at 21 DIV (Figure S6, Supporting Information). At 28 DIV, however, Ni-NWs electrodes seemed less adhesive to cells than Au-NWs ones so highly compact cell monolayers started to detach (Figure S7, Supporting Information). This inferior performance of Ni substrates with brain cells could be related to some toxicity effects derived from their chemical composition. To this regard, individual Ni NWs produced deleterious effects on diverse cell types such as human WI-38 fibroblasts,<sup>[34]</sup> monocytic THP-1 cells<sup>[35]</sup> and rat marrow stroma cells.<sup>[36]</sup> In HeLa cells, individual Ni NWs (1  $\mu\text{m}$  in length and 50 nm in diameter) induced cell cycle arrest and apoptosis, with significant dose- and length-dependent effects.<sup>[37]</sup> We hypothesize that, in our case, the fact of being arranged in a nanostructured array, in which individual wires cannot be internalized by cells, significantly improved cell responses with respect to previous work by others.



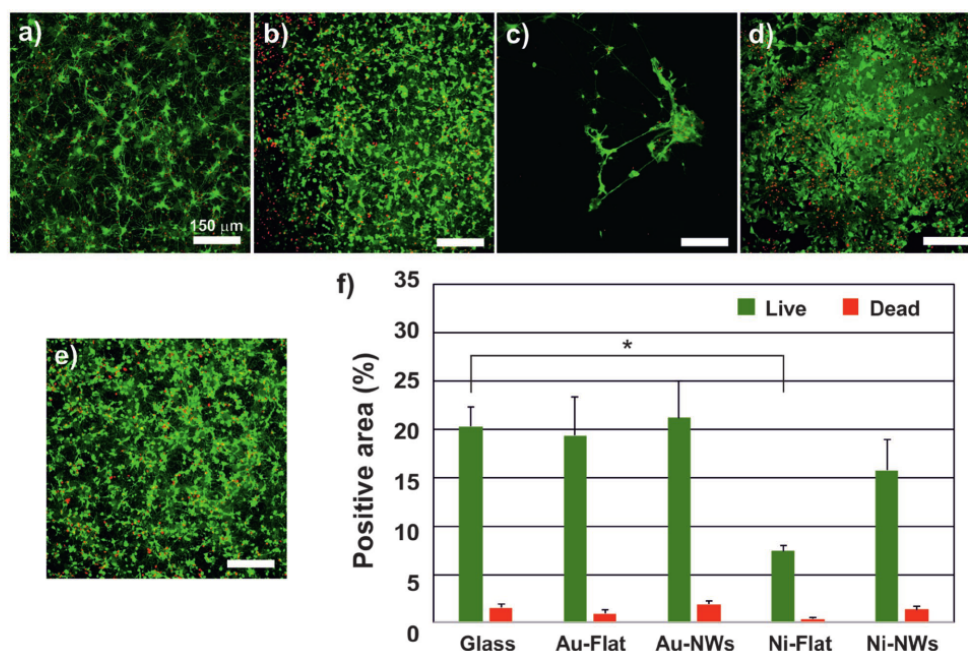


**Figure 3.** Viability studies of rNCC cultures on the different electrode substrates at 14 DIV by CLSM. Alive cells are labeled in green (calcein) and dead cells in red (EthD-1). a) Au-Flat, b) Au-NWs, c) Ni-Flat, d) Ni-NWs electrodes, and e) glass coverslips (control). f) Normalized positive area for alive and dead cells (mean  $\pm$  standard deviation;  $n \geq 5$  for each condition). Statistics:  $*p = 0.021$  (Ni-Flat vs control); one-way ANOVA followed by Games-Howell post-hoc test. For the rest of comparisons, not statistically significant differences were found (one-way ANOVA). Significance symbol:  $*p < 0.05$ .

In order to elucidate the role that nanotopography might be playing on the neural cell responses found, we next explored equivalent flat electrodes, either fabricated as Au-Flat or Ni-Flat, in comparison to NWs-based ones. rNCC cultures were formed on both flat materials, although cells on Ni-Flat showed a pronounced tendency to clump and fasciculate neurites, as demonstrated by morphological SEM studies (Figure S8, Supporting Information). Then, cell viability was evaluated in all four substrates (Au-Flat, Au-NWs, Ni-Flat, and Ni-NWs) (Figure 3a–e). As these neural cells tend to group in culture and slightly vary in size, it becomes difficult to accurately identify the number of individual live cells, so viability was measured from the images as the area covered by calcein-labelled cells (i.e., live cells). In both types of nanostructured electrodes (Au-NWs and Ni-NWs), a majority of the surface was covered by live cells (green fluorescent as labelled with calcein). When quantified (Figure 3f), cells cultured on nanostructured electrodes were similarly viable to those on control glass substrates (104.3% for Au-NWs and 77.4% for Ni-NWs;  $p > 0.999$ , Au-NWs vs control, and  $p = 0.739$ , Ni-NWs vs control). Regarding flat electrodes, while Au-Flat electrodes reached control values, Ni-Flat ones were more poorly colonized than the control with a significantly inferior surface area covered by viable cells ( $*p = 0.021$ , Ni-Flat vs control), thus demonstrating a significant impact of nanotopography on the survival of rNCCs in the case of Ni-based

electrodes. In agreement with this finding, neural cells in contact with epitaxial gallium phosphide NWs (2.5  $\mu\text{m}$  long and 50 nm wide) also experienced an improvement in cell survival with respect to respective planar substrates.<sup>[38]</sup> No statistically significant differences were found when comparing the area of live cells between flat and nanostructured electrodes for each chemical composition (either Au or Ni), although found in the case of Ni-Flat with respect to the control. The area of dead cells was statistically similar in all substrates, including the control, thus indicating an equal degree of cell death sustained in the cultures at 14 DIV.

Differentiation to either neuronal or non-neuronal phenotypes was then investigated by immunofluorescence studies of map-2 (neuronal cytoskeleton protein) and vimentin (non-neuronal cytoskeleton protein) (Figure 4a–e). In both nanostructured electrodes, there was a predominant presence of neuron-differentiated cells, as occurred on control substrates and expected for this cell type and these culture conditions. When quantified (Figure 4f), cells on Au electrodes (both flat and nanostructured) displayed a similar differentiation profile than that found on glass coverslips (map-2:  $p = 0.794$ , Au-Flat vs control, and  $p = 0.248$ , Au-NWs vs control; vimentin:  $p = 0.380$ , Au-Flat vs control, and  $p = 0.886$ , Au-NWs vs control). On the contrary, on Ni electrodes, rNCC differentiation profiles seemed dependent on both chemical and nanotopography features. While Ni-Flat

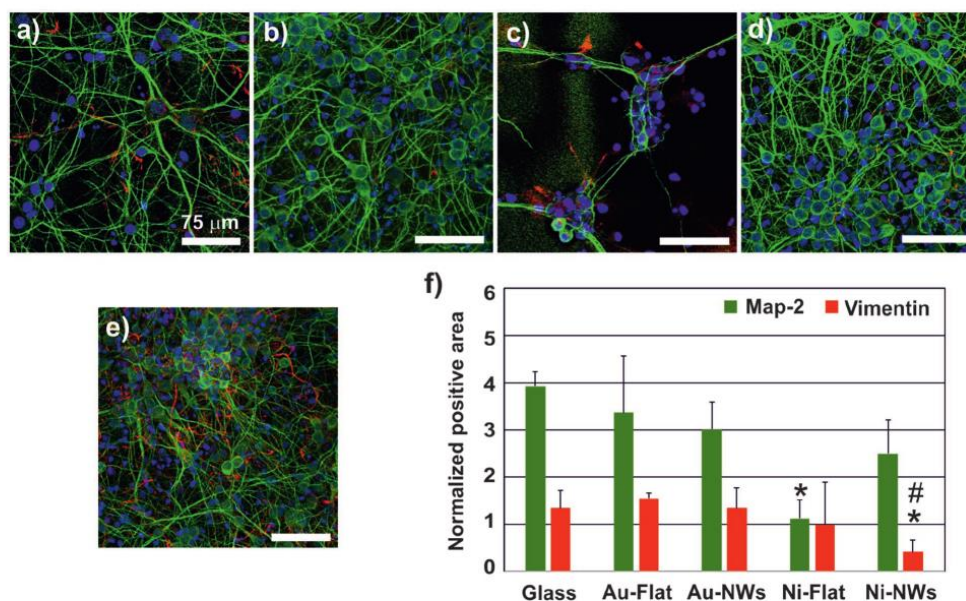


**Figure 4.** Differentiation studies of rNCC cultures on different electrode substrates at 14 DIV by CLSM. Neurons are labeled for map-2 (green) and non-neuronal cells including glial cells for vimentin (red). In all cases, cell nuclei were stained with DAPI (blue). a) Au-Flat, b) Au-NWs, c) Ni-Flat, d) Ni-NWs electrodes, and e) glass coverslips (control). f) Normalized positive area for neurons (map2<sup>+</sup>) and non-neuronal cells (vimentin<sup>+</sup>) (mean  $\pm$  standard deviation;  $n \geq 5$  for each condition). Statistics: \* $p = 0.037$  (Ni-Flat vs control), \* $p = 0.035$  (Ni-NWs vs control) and # $p = 0.032$  (Ni-NWs vs Au-NWs); in all cases, one-way ANOVA, followed by Games-Howell post-hoc tests. For the rest of comparisons, not statistically significant differences were found (one-way ANOVA). Significance symbol: \*  $p < 0.05$  in comparisons with respect to control and #  $p < 0.05$  in comparisons to Au-NWs.

substrates hampered neuronal cells appearance (\* $p = 0.037$ , Ni-Flat vs control), nanostructured ones significantly reduced the presence of glial phenotypes (\* $p = 0.035$ , Ni-NWs vs control, and \* $p = 0.032$ , Ni-NWs vs Au-NWs). Based on this, nanotopography features of Ni-based substrates seemed to promote a higher predominance of neurons in comparison to their plane counterparts. This effect, however, was not observed in Au-based electrodes, thus pointing toward an additional role of chemical features on these responses. To this regard, Cho and colleagues described a preferential neuronal differentiation of neural stem cells induced by hierarchically patterned substrates containing both microgroove (1.5  $\mu\text{m}$ ) and nanopore (10 nm in diameter) patterns.<sup>[39]</sup> At the molecular level, they related these effects to the  $\beta 1$  integrin-mediated binding and the intracellular Rho-associated protein kinase pathway. Topography-dependent differentiation patterns have been also described for human ESCs.<sup>[40]</sup> Specifically, hESCs preferentially differentiated into neural phenotypes when cultured in anisotropic substrates like gratings, while isotropic patterns including pillars and wells favored their glial differentiation. In this particular approach, topography and size were identified as key parameters to induce cell lineage differentiation. The significant differences in terms of cell type and material configuration (composition, size and inter-distance) of pillars (1  $\mu\text{m}$  in length, 6.5  $\mu\text{m}$  of pitch, and 1  $\mu\text{m}$  in height) with respect to NWs in our study make difficult a direct comparison

and expected the differing biological impact. Interestingly, studies by Stevens and colleagues pointed out toward a synergistic action of nanoscale chemistry and topography on ESCs differentiation when cultured on metallic thin films.<sup>[41]</sup>

### 2.3. Au-NWs Impact Glial Cell Density and Synaptic Activity in Postnatal Hippocampal Cell Cultures

Previous experiments on neural progenitor cells suggested Au-based NWs as the most advantageous material for neural interfacing; so we next challenged such substrates by postnatal hippocampal network. Hippocampal dissociated cultures obtained from rat pups have been extensively used as a standard model for functional studies of nanomaterial-to-neuron interfaces.<sup>[42–46]</sup> The morphological adaptation of the most represented cell types in this culture model, namely mature neurons and astrocytes, was therefore investigated. Figure 5a shows the appearance of cultured neurons on Au-NWs and compared with Au-Flat and control (glass) substrates, visualized by  $\beta$ -tubulin III immunofluorescence (in red). In all cases, we observed an extensive regrowth of neurites and axons (Figure 5a, left column) and neuronal cell densities were comparable in the three conditions, summarized in the box plot of Figure 5b. When investigating astrocytes by GFAP immunolabelling



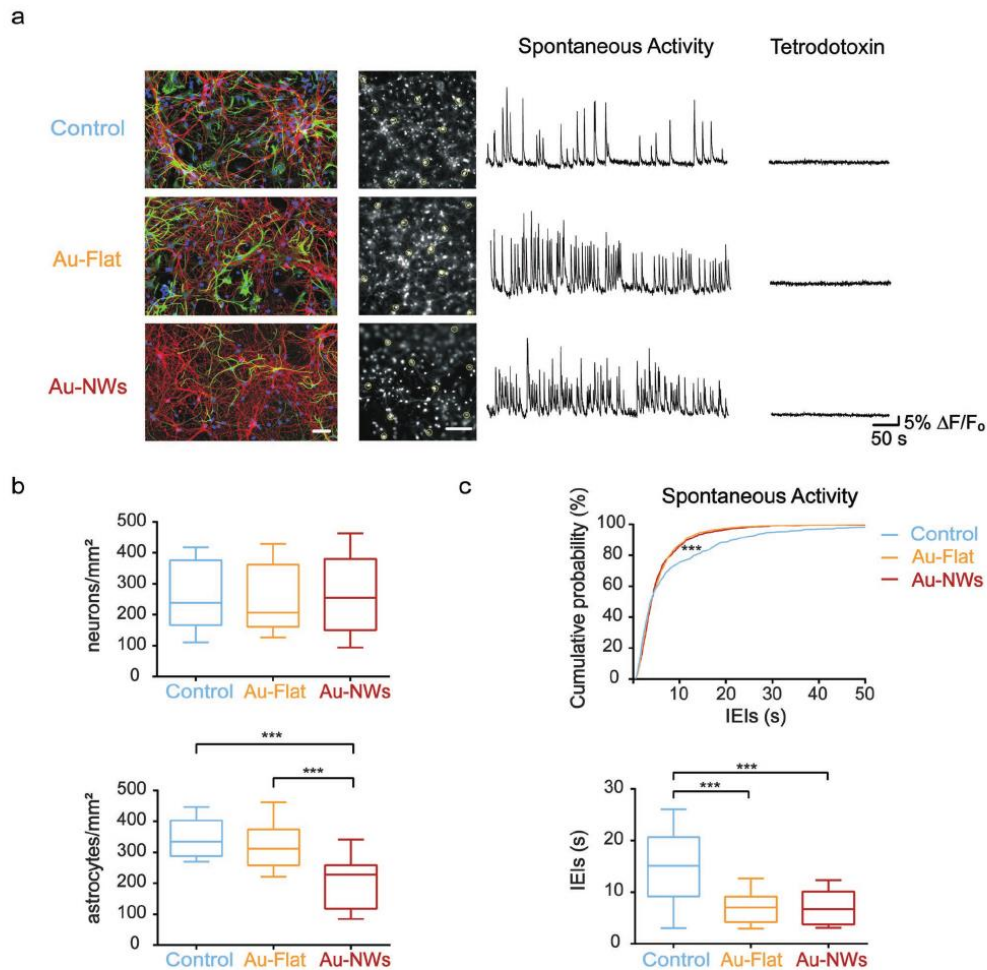


**Figure 5.** Hippocampal synaptic network formation onto Au-NWs electrodes studied by immunocytochemistry and calcium imaging experiments. a) From left to right, confocal micrographs of immunolabeled cultures, large fields are shown in the first column. Neurons are visualized by anti  $\beta$ -tubulin III, in red, glial cells by anti-GFAP, in green, and nuclei by DAPI, in blue. Scale bar = 100  $\mu$ m. Snapshots of 3 representative fields of hippocampal dissociated cultures labeled with Oregon green 488-BAPTA-1 AM. Scale bar = 100  $\mu$ m. Yellow circles indicate the selected regions of interest (ROI) from which calcium events were measured. On the right of each field, representative traces of spontaneous network activity for each condition are also shown. TTX was used at the end of each recording to assess the neuronal nature of the signals. Calcium transients are expressed as fractional amplitude increase ( $\Delta F/F_0$ ). b) Left box plots summarize neuronal (top) and astrocytes (bottom) densities in the three conditions ( $n = 47$  for control,  $n = 39$  for Au-Flat and  $n = 44$  for Au-NWs). Statistics:  $***p < 0.001$ ; Kruskal–Wallis test,  $p$ -value was adjusted for multiple comparisons with Dunn’s correction. c) Top, cumulative probability distribution of the interevent intervals (IELs); bottom, box plot highlights IELs distribution around the median values ( $n = 42$  for control,  $n = 53$  for Au-Flat and  $n = 49$  for Au-NWs). Statistics:  $***p < 0.001$ ; both Kolmogorov–Smirnov test and Kruskal–Wallis test on ranks suggested a marked difference in the IELs distribution among the different substrates, Dunn’s correction for multiple comparisons was also used. Significant symbol:  $***p < 0.001$  (for both b,c).

(Figure 5a, in green), we detected a significant and selective reduction in GFAP<sup>+</sup> cell density when cultures were interfaced to the nanostructured surfaces (Au-NWs,  $202 \pm 96$  cells mm<sup>-2</sup>) in comparison with glass ( $348 \pm 67$  cells mm<sup>-2</sup>) or plane Au

(Au-Flat,  $327 \pm 88$  cells mm<sup>-2</sup>; summarized in Figure 5b, lower left box plot,  $***p < 0.001$ ). The lower amount of GFAP<sup>+</sup> cells in Au-NWs might be relevant for future applications requiring diminished glial reactivity. This seems to be a well-known



feature of nanoscale surface patterning, consisting in a selective reduction of astroglial cell adhesion.<sup>[47]</sup> Nonetheless, this was unrelated to Au interaction with cells, since plane Au surfaces showed a comparable astrocyte density to glass. This preferential reduction in glial cells was also found previously with rNCCs cultured on Ni-NWs, not on Au-NWs though, thus evidencing that the specific cell source and inherent characteristics of each neural cell type play a relevant role in the overall biological responses found.

Primary cultured neurons display spontaneous and temporally structured electrical activity.<sup>[45]</sup> We explored the network dynamics in hippocampal cultures by calcium imaging, that allows monitoring simultaneously single-cell calcium transients in a population of neurons.<sup>[45]</sup> Neurons, stained by a membrane permeable calcium dye, were visualized within the sampled area (Figure 5a, right panels). In all culture groups, we detected spontaneous and repetitive calcium events emerging from episodes of synaptic, action potential-dependent, bursts of activity, fully blocked by tetrodotoxin (TTX) application (Figure 5a, fluorescence tracings). Next, we quantified the occurrence of spontaneous calcium episodes in active cells by measuring the inter-event interval (IEI), the time interval between the onset of a calcium burst and the beginning of the next one. As shown by the cumulative probability distribution and box plots in Figure 5b, Au-Flat and Au-NW substrates increased spontaneous activity, when compared to control, detected as a shift of the IEI toward smaller values ( $***p < 0.001$ ). This peculiar feature was not observed in prior reports where the interaction between plane Au surfaces and hippocampal dissociated cultures was studied at the single-cell level by means of patch-clamp technique.<sup>[46]</sup> In this previous study from our group, only PSCs (post-synaptic currents) frequency was monitored via voltage-clamp of single neurons and no indication was provided about the calcium-related collective behavior of the network, which is predominant in our conditions. Indeed, monitoring isolated PSCs provides a measure of synaptic inputs with high temporal resolution, allowing the investigation of individual synaptic changes. Conversely, calcium activity, whose neuronal and synaptic nature was supported by TTX experiments, are reflecting synaptic event due to synchronous firing of neurons, thus reporting neuronal activity occurring at network, more than at cellular resolution.<sup>[45]</sup>

#### 2.4. Nanostructured Electrodes Enable Electrical Stimulation of Brain Cell Cultures

Finally, we provide a proof-of-concept for the Au-based substrates to electrically stimulate neural networks *in vitro*. Regardless the improved network signaling, apparently due to the Au substrates (chemical composition), we further investigated the functionality of Au-based nanoelectrodes in delivering electrical stimulations leading to evoked depolarizations in neurons reaching the threshold for the generation of action potentials. To this aim, we customized a recording chamber to deliver a charge injection from the Au substrates while cultured neurons were monitored by fluorescence calcium imaging (Figure 6a,b, sketch and stimulation protocol). After 10 min of recording of sustained spontaneous synaptic

activity (Figure 6c), a cocktail of synaptic receptor antagonists, containing APV ( $25 \times 10^{-6}$  M), BIC ( $10 \times 10^{-6}$  M), and CNQX ( $10 \times 10^{-6}$  M), was applied to functionally disconnect neurons from the network activity.<sup>[48,49]</sup> This condition allowed testing the efficacy of electrical stimuli delivered via the Au substrates in directly depolarizing the monitored neurons, eventually inducing a burst of action potentials. Figure 6d shows such recordings where five biphasic low-voltage steps, repeated three times (Figure 6b, lower left sketch), were delivered either via Au-Flat or Au-NWs electrodes. The observed positive responses are a straightforward link to the ability of Au electrodes to directly depolarize neuronal cell membranes, ultimately leading to evoked action potentials, as confirmed by subsequent TTX application removing all the evoked activity (Figure 6d, underneath traces). These results highlight the possibility to excite a silent network through this novel Au-NWs array by direct neuronal membranes depolarization, leading to action potential propagation. In line with this result, a recent work described a device formed by a forest of randomly oriented Au-coated silicon NWs to enable non-invasive extracellular recording of the slow-frequency oscillations generated by differentiated primary astrocytes.<sup>[50]</sup> In this case, flat electrodes failed on recording signals from undifferentiated cells. Differing from array-like configurations, single Au NWs, with a similar diameter to ours but longer lengths (100–200 nm in diameter and over 10  $\mu$ m in length), have been also proposed as stimulator/detector systems for electrical stimulation and electrochemical analysis of dopamine exocytosis from PC-12 cells.<sup>[51]</sup> These individual electrodes, fabricated by using a vapor transport method,<sup>[52]</sup> promoted dopamine release attributed to  $Ca^{2+}$  channels opening (pulse voltage tuned from 0.3 to  $-0.3$  V).

Besides their intrinsic interest as advanced platforms for neural stimulation and recording, this type of NWs could also be incorporated into scaffolds to recreate 3D environments for optimal cellular interactions. For example, comparable Au NWs arrays fabricated by template-assisted electrodeposition have been described as highly efficient platforms for the capture and electrochemical release of circulating human leukemic lymphoblasts (tumor cells) when functionalized with aptamers.<sup>[53]</sup> By using electrochemical deposition on anodic aluminum oxide as a template, the arrays fabricated were able to capture target cells with much higher yield and to release them with little damage through an electrochemical desorption process. Silicon NWs (150 nm in diameter and 2.6  $\mu$ m in length) decorated with Au are being also explored as highly efficient near-infrared (NIR) hyperthermia and photothermal agents for cancer treatment.<sup>[54]</sup> Other than metallic, free-standing single coaxial silicon NWs have been recently described as useful materials for photoelectrochemical modulation of neuronal activity.<sup>[55]</sup> Curiously, these authors demonstrated that the presence of atomic Au diffused on the NW surface during material growth (where Au nanoclusters were used as a catalyst in a chemical vapor deposition process) enhanced the photoelectrochemical process involved in the stimulation of action potentials in primary rat dorsal root ganglion neurons. The versatility of our fabrication system allow us for the configuration of NWs in the shape of flexible millimeter size arrays as well as individual electrodes if needed, so they can be customized for a plethora of biomedical applications.

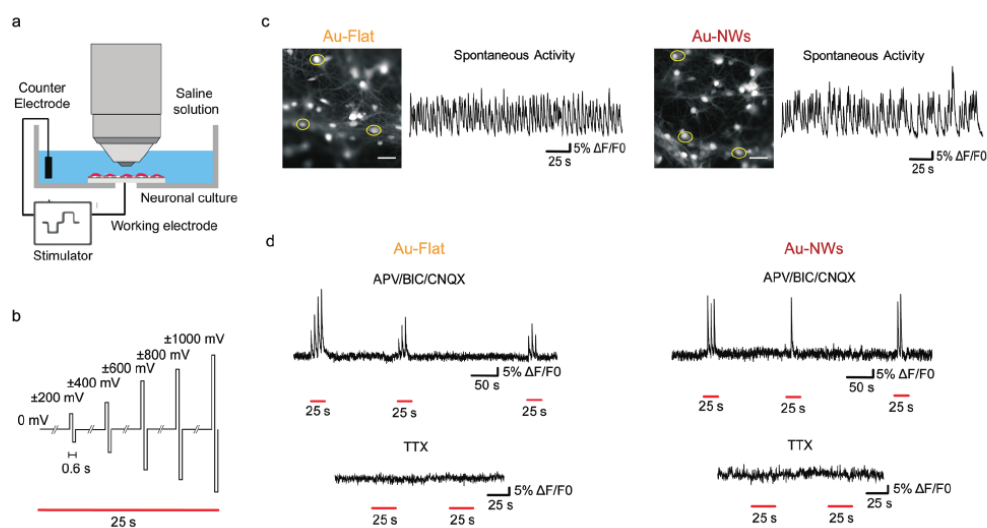


**Figure 6.** Au-Flat and Au-NWs act as electrode delivering electrical stimulation to cultured neurons. a) A sketch of the experimental setting: a dry connection was ensured between the stimulating electrode and the gold sheets. b) The stimulation protocol applied in this proof-of-concept consisted of five biphasic voltage steps repeated three outdistanced times. Increasing bipolar steps from 0 to 1000 mV were sent at 0.2 Hz and each phase lasted 300  $\mu$ s for a total stimulus length of 25 s. c) Two representative snapshot of the imaged field of hippocampal dissociated cultures (scale bar = 50  $\mu$ m) grown for 10 DIV onto Au-Flat and Au-NWs electrodes are shown. Cells were labelled with Oregon green 488-BAPTA-1 AM and a circular ROI (region of interest, yellow circle) was drawn around spiking neurons, the mean grey value of the pixels in the ROIs was used to plot the calcium transient course over the time. On the right side of the snapshots a representative trace of the sustained spontaneous synaptic activity corroborates the state of health of tested cells in both conditions. d) The physiological spontaneous synaptic activity of the network was fully blocked (upper traces) by a drug cocktail containing the NMDA receptor antagonist APV ( $25 \times 10^{-6}$  M), the GABA<sub>A</sub> receptor antagonist BIC ( $10 \times 10^{-6}$  M) and the AMPA/kainate receptor antagonist CNQX ( $10 \times 10^{-6}$  M). In this condition only stimulus-evoked activity could be observed. Representative fluorescence tracings depict neuronal responses evoked by extracellular pulse stimulations (25 s long red dashes) applied through the Au-Flat (left traces) or Au-NWs electrodes (right traces). Neuronal cells ability to fire action potentials after voltage stimuli was totally abolished by TTX ( $1 \times 10^{-6}$  M) treatment (underneath traces) ensuring the neuronal origin of the signals evoked in APV/BIC/CNQX condition. Calcium transients are expressed as fractional amplitude increase in the fluorescence signal ( $\Delta F/F_0$ , where  $F_0$  is the baseline fluorescence level and  $\Delta F$  is the rise over baseline).

### 3. Conclusion

By using Au and Ni as exemplary materials, we have demonstrated that both nanostructure and chemical composition, along with biological features such as cell source and type, play a major role in the interaction of neural cells with electrode arrays. Particularly, Ni-NWs increase neural cell survival, boost neuronal differentiation and reduce glial cell content with respect to their flat counterparts. For Au-based substrates, nanotopography seems to have negligible effects on the survival and differentiation of cortical neural cells. However, Au-NWs induce a significant reduction in glial cell density on primary hippocampal cell cultures when compared to Au-Flat substrates, as also identified on Ni-NWs electrodes. When challenged under electrical stimulation, these Au-NWs substrates sustain intracellular calcium dynamics compatible with functional neural networks. Moreover, our studies highlight the possibility to excite a silent network through these nanostructured arrays by direct neuronal membranes depolarization, leading to action potential propagation.

### 4. Experimental Section

**Material:** Chemical reagents and biological molecules were purchased from Sigma-Aldrich and Panreac and used as received, unless otherwise indicated. Antibodies were bought from Sigma-Aldrich and Invitrogen. Neurobasal media and B-27 supplement were purchased from Invitrogen and Thermo Fisher. All additional cell culture media supplements and reagents were obtained from Lonza. All materials and biological samples in this study were manipulated according to standard regulations so no safety concerns arise.

**Fabrication and Characterization of Electrodes Covered by Arrays of Metallic NWs:** Nanostructured electrodes were prepared by template-assisted electrochemical deposition (schematics shown in Figure S1, Supporting Information) using as templates polycarbonate nanoporous membranes, with 100 nm pore diameter (Whatman). The pores density of the template was  $10^8$  cm<sup>-2</sup>. Electrodeposition was carried out in a three-electrode electrochemical cell with a Metrohm Autolab PGSTAT204 potentiostat, using a Pt mesh as a counter electrode and an Ag/AgCl (3 M NaCl) electrode as a reference electrode. Before electrodeposition, a 100 nm thick Au film was sputtered on one side of the membrane using a Leica EM ACE600 sputtering, which was thickened to 1  $\mu$ m using pulse-plating Au electrodeposition, with an on pulse at  $-1.5$  V and an off/rest pulse of 0 V. The use of pulsed electrodeposition allowed to release the stresses during Au thickening, so noncracked flexible Au

thin layers could be obtained. This Au film constituted the base of the final electrode over which the nanowires were deposited. Electrodes with nanowires of either Au (Au-NWs) or Ni (Ni-NWs) were prepared, in order to explore two materials with significantly different physico-chemical properties. For Au electrodeposition, an Orosene commercial electrolyte (ORE-4, Italogalvano) was used at room temperature (RT), with a growth potential of  $-1.5$  V versus RE; whereas for Ni growth a Watts-type electrolyte composed by  $\text{NiSO}_4$  (0.8 M),  $\text{NiCl}_2$  (0.2 M), and  $\text{H}_2\text{BO}_3$  (0.4 M), working at  $45$  °C was used, with a growth potential of  $-1.0$  V versus RE. Finally, dichloromethane was used to remove the templates, followed by extensive washing in acetone, ethanol and deionized water, while leaving the network of vertical NWs attached to the Au base. After growth, the morphology of the arrays of metallic NWs was studied by SEM using a ZEISS EVO HD15 microscope. Plane flat Au (Au-Flat) and Ni (Ni-Flat) electrodes were also prepared as reference materials. For Au-Flat, the bases described above were used without performing NW growth, while, for Ni-Flat, a thin Ni layer was deposited on top of the Au bases under the same electrochemical conditions as those used for Ni-NWs growth.

**Electrochemical Impedance:** The impedance of the electrodes was measured at room temperature by a three-electrode cell using a Metrohm Autolab PGSTAT204 potentiostat with a Pt mesh as a counter electrode and an Ag/AgCl (3 M NaCl) electrode as reference. Measurements were carried out in phosphate buffer saline (PBS) with bovine serum albumin ( $0.2$  mg  $\text{mL}^{-1}$ ), with a modulation of  $10$  mV at  $250$  Hz, in circular electrodes of  $4$  mm in diameter.

**Cell Isolation and Culture: Rat Neural Cortical Cells (rNCCs):** Neural progenitor cells were obtained from cerebral cortices of E18 Wistar rat embryos as previously described.<sup>[56]</sup> All the experimental protocols for cell collection adhered to the regulations of the European Commission (directives 2010/63/EU and 86/609/EEC) and the Spanish government (RD53/2013 and ECC/566/2015) for the protection of animals used for scientific purposes. Adult female Wistar rats were provided by a commercial supplier (Harlan Ibérica, Spain) and sacrificed when gestation reached 16–18 days. A total of 5 independent cell cultures from 5 different animals with a minimum of 3 replicates per condition in each culture were carried out ( $N \geq 15$  arrays per condition). The viability of the so-isolated cells was  $90 \pm 4\%$  in all cases. For high-density assays, a total of  $7.5 \times 10^4$  cells contained in a small fraction of media (typically 20–50  $\mu\text{L}$ ) was seeded on the top part of each array and allowed to attach for 10 min. Immediately after, samples were completely covered with 500  $\mu\text{L}$  of complete Neurobasal media containing: B-27 supplement (2%), streptomycin ( $100$  UI  $\text{mL}^{-1}$ ), penicillin ( $100$  UI  $\text{mL}^{-1}$ ), and L-glutamine ( $1 \times 10^{-3}$  M). For low-density assays, cells were seeded at a density of  $2.5 \times 10^4$  cells  $\text{cm}^{-2}$ . After 2 h of adhesion in a sterile incubator at  $37$  °C in a  $\text{CO}_2$  atmosphere (5%), culture media were replaced and cultures maintained for up to 2 weeks. Culture media were half replaced every 3–4 days. Cell culture was monitored in the periphery of the substrates and control samples by using an Axiovert CFL-40 optical microscope with a coupled Axiocam ICC-1 digital camera (Zeiss). Prior to cell culture, all electrodes were first sterilized by UV radiation in a biosafety cabinet and then functionalized by adsorbing low molecular weight PLL molecules (30 000–70 000 Da;  $45$   $\mu\text{g}$   $\text{mL}^{-1}$ ). The homogeneity of the coating was confirmed by immunofluorescence by using PLL-FITC. Control glass substrates were functionalized following the same protocol as for metallic electrodes.

**Cell Isolation and Culture: Rat Hippocampal Cells:** Dissociated hippocampal neurons were isolated from post-natal 2–3 days old Wistar rats as previously reported.<sup>[45]</sup> Au-Flat and Au-NWs electrodes were washed preliminarily with 5 min long washes on milliQ  $\text{H}_2\text{O}$  and then in ethanol 90%,  $\text{H}_2\text{O}$  and ethanol were previously filtered with  $0.22$   $\mu\text{m}$  cutoff filter (Merck Millipore). The electrodes were dried at  $90$  °C and their surfaces were activated under low-pressure air plasma (Harrick PDC-32G Plasma Cleaner) for 7 min at RT ( $20$ – $22$  °C), with RF coil powers of 9 W. A 20 min long exposure to ultraviolet (UV)-radiation was finally used to sterilize the substrates. One hour prior to cell culturing, PLL ( $50$   $\mu\text{g}$   $\text{mL}^{-1}$ , Merck) coating was performed onto all tested substrates, including control glass, to enhance positive surface charging,

thus facilitating cell adhesion. About  $600$  cells  $\text{mm}^{-2}$  were plated onto control glass, Au-Flat and Au-NWs electrodes, then incubated at  $37$  °C, 5%  $\text{CO}_2$  in Neurobasal medium added with B-27 supplement (Thermo Fisher) and GlutaMAX (Thermo Fisher) both to a  $1 \times$  final concentration. Gentamicin ( $5$   $\mu\text{g}$   $\text{mL}^{-1}$ ; Thermo Fisher) was also added. Cultured cells were grown until 8–12 DIV by renewing half of the medium once in this period.

**Cell Morphological Studies by Electron Microscopies:** All studied samples were rinsed in PBS twice and fixed with glutaraldehyde (2.5% in PBS) for 45 min as a conventional fixation method for examination by electron microscopy. After washing in distilled water, dehydration was performed by using series of ethanol solutions for 15 min (2 washes) and a final dehydration in absolute ethanol for 30 min. Samples were then dried at RT for at least 24 h. After mounting in stubs and gold coating under vacuum, the morphology of the samples was characterized by using a Hitachi S-3000N electron microscope and a field-emission Philips XL30 S-FEG microscope.

Alternatively, in vitro culture samples were first fixed with a mixture of paraformaldehyde 4% and glutaraldehyde 1% in phosphate buffer for 1 h and then post-fixed in osmic tetroxide (1% in distilled water) for an additional hour. Dehydration was then carried out by immersion in successive solutions of ethanol at increasing concentrations (30%, 50%, 70%, 95%, and 100%), with a final step in pure acetone. Samples were included in the resin Durcupán by consecutive immersion steps at increasing concentrations (1:3, 1:1, 3:1 in acetone). The final samples in pure resin were then polymerized at  $60$  °C for 48 h. Ultrathin sections ( $\approx 60$  nm) were obtained and subsequently stained with uracil acetate and lead citrate. The visualization was carried out by using a Jeol JEM 1010 microscope (Japan) at 80 kV with a coupled camera (Gatan SC200, USA) for image acquisition.

**Cell Viability Studies by Confocal Laser Scanning Microscopy (CLSM):** To test cell viability, cells cultured on the different substrates were analyzed by using a Live/Dead Viability kit according to manufacturer's instructions. This kit is based on the use of calcein and ethidium homodimer-1 (EthD-1). Calcein is a non-fluorescent cell-permeable dye that gets converted into a strongly green-light emitting compound after contact with intracellular esterases and so retained inside live cells. On the contrary, EthD-1 is a DNA-intercalating agent that penetrates cell membranes in dead cells and emits orange/red fluorescence when inserted into the DNA double helix. After staining, samples were visualized by using a Leica SP5 CLSM. The fluorescence of both probes was excited by an Argon laser tuned to 488 nm. After excitation, emitted fluorescence was separated by using a triple dichroic filter 488/561/633 and measured at 505–570 nm for green fluorescence (calcein) and 630–750 nm for red fluorescence (EthD-1). Physical reflection from the metallic electrodes (non-transparent) after excitation at 488 nm was also recorded and used to visualize the material structure and the relative cellular location.

**Brain Cells Differentiation Studies by CLSM:** rNCC cultures on the different substrates were fixed with paraformaldehyde (4% in PBS) at RT for 12 min and then incubated with the following primary antibodies: 1) Map-2 for somas and dendrites in neurons and 2) Vimentin for non-neuron cells including glial cells. The secondary antibodies used were: Alexa Fluor 488 anti-mouse in goat IgG (H+L) and Alexa Fluor 594 anti-rabbit in goat IgG (H+L) (Life technologies). Both primary and secondary antibodies were dissolved in PBS containing saponin (0.25%) and fetal goat serum (2%) to guarantee cell permeability and to block any non-specific bindings, respectively. Each antibody was incubated for 1 h at RT in darkness. Cell nuclei were labeled with 4',6-diamidino-2-phenylindole (DAPI,  $3 \times 10^{-6}$  M, 5 min). After immunostaining, samples were visualized by using a Leica TCS SP5 microscope. The fluorescence of the different fluorochromes was excited and measured as follows: Alexa Fluor 488 excitation at 488 nm with an argon laser and detection in the range 507–576 nm, Alexa Fluor 594 excitation at 594 nm with a helium-neon laser and detection in the range 625–689 nm and DAPI excitation at 405 nm with a diode UV laser and detection in the range 423–476 nm. Capture conditions in each case were established by using appropriate positive and negative controls and maintained during the



acquisition of all the images. Reflection mode images were taken to observe the metallic electrodes surface in all cases.

Hippocampal cultures were fixed in 4% formaldehyde (prepared from fresh paraformaldehyde) in PBS and permeabilized for 30 min with 0.3% Triton-X-100 (Carlo Erba) in PBS added with 5% FBS (Gibco) and 4% BSA to prevent non-specific binding of primary antibodies. Samples were subsequently incubated with primary antibodies for 30 min at RT and, after being washed with PBS, with secondary antibodies for 45 min. Mounting was performed with anti-fade medium Fluoromount on 1 mm thick microscope glass slides. Neurons were labeled for anti- $\beta$ -tubulin III and visualized with Alexa 594 anti-rabbit in goat as secondary antibody. Astrocytes were instead stained for GFAP and visualized with Alexa 488 anti-mouse in goat as secondary antibody. Nuclei were stained with DAPI. Nikon Eclipse Ti2 inverted microscope connected to a AIR confocal system was used to acquire confocal reconstructed images ( $20 \times$  Plan Apo HL, 0.75 NA).

**Calcium Imaging:** Hippocampal dissociated cultures were loaded with cell permeable  $\text{Ca}^{2+}$  dye Oregon Green 488 BAPTA-1 AM (Molecular Probes); 10  $\mu\text{L}$  DMSO was added to the stock 50  $\mu\text{g}$  of the dye and cultures were incubated with a final concentration of  $4 \times 10^{-6}$  M for 30 min at 37 °C, 5%  $\text{CO}_2$ . Samples were therefore placed in a recording chamber mounted on an inverted microscope (Nikon Eclipse Ti-U). Cultures were continuously perfused at 5  $\text{mL min}^{-1}$  rate at RT with extracellular saline solution of composition ( $\times 10^{-3}$  M): 150 NaCl, 4 KCl, 2  $\text{CaCl}_2$ , 1  $\text{MgCl}_2$ , 10 HEPES, 10 glucose (pH adjusted to 7.4 with NaOH; osmolarity 300 mOsm).  $\text{Ca}^{2+}$ -dye was excited at 488 nm with a mercury lamp; excitation light was separated from the light emitted from the sample using a 505 nm dichroic mirror and ND filter (1/32). Oregon loaded cultures were observed with a  $20 \times$  objective (PlanFluor, 0.45 NA) and images were continuously acquired (exposure time 150 ms) using an ORCA-Flash4.0 V2 sCMOS camera (Hamamatsu). The imaging system was controlled by an integrating imaging software (HCLImage Live) and the camera was set to operate on  $2048 \times 2048$  pixels at binning 4. Cultures accustomed to extracellular solution for about 10 min. Spontaneous activity was thereafter recorded for 10 min. At the end of each recording session,  $1 \times 10^{-6}$  M TTX (a voltage-gated, fast  $\text{Na}^+$  channel blocker; Latoxan) was added to confirm the neuronal nature of the recorded signals. 1 field was recorded from each sample and  $12 \pm 2$  cells out of each recording were selected by drawing regions of interest (ROIs) around cell bodies. Images were analyzed with ImageJ software (NIH) and the corresponding traces were studied with Clampfit software (pClamp suite, 10.4 version; Axon Instruments) in off-line mode and with MATLAB (MathWorks, Inc.). The difference between consecutive peaks onset times was computed, to obtain the inter-event interval. Intracellular  $\text{Ca}^{2+}$  transients were expressed as fractional amplitude increase ( $\Delta F/F_0$ , where  $F_0$  is the baseline fluorescence level and  $\Delta F$  is the rise over baseline); the onset time of neuronal activation was determined by detecting those events in the fluorescence signal that exceed at least five times the standard deviation of the noise.<sup>45</sup>

**Spontaneous and Evoked Intracellular Calcium Dynamics Studies under Electrical Stimulation:** For the electrical stimulation of the conductive substrates, the bottom of a 35 mm petri dish (Falcon) was modified to include either Au-Flat or Au-NWs squared electrodes of about  $6 \times 6$  mm. The junction between the petri and the Au-Flat or Au-NWs electrodes was sealed by PDMS silicon elastomer (Sylgard 184 – Down Corning Co.). This setting allowed positioning of a stimulating electrode in direct contact with the Au-Flat and Au-NWs films in a dry environment. In the modified petri dishes, hippocampal cultures were grown for 10 DIV. To deliver stimuli, the positive output of an STG 4002 stimulator (Multi Channel Systems) was plugged to a platinum wire in direct contact with the Au-Flat and Au-NWs electrodes as described above, while the ground output was plugged with an Ag/AgCl pellet electrode submerged in the extracellular saline solution. The extracellular stimulus pattern was designed with MC\_Stimulus II (Multi Channel Systems) and the stimulator was controlled by a computer. In these conditions, for calcium live imaging, cells were loaded with the cell permeable  $\text{Ca}^{2+}$  dye as described above. After incubation, the petri dish with the substrate was mounted in a fixed-stage upright microscope (Eclipse

FNI, Nikon) and was continuously superfused at 5  $\text{mL min}^{-1}$  rate, at RT, with the extracellular saline solution (see above). The  $\text{Ca}^{2+}$ -dye was excited at 488 nm with a mercury lamp; a dichroic mirror and ND filter (1/32) was used to separate the excitation light from the light emitted by the sample. Spontaneous calcium transients were recorded with a  $20 \times$  water immersion objective (UMPlanFl, 0.5 NA, Olympus) using an EMCCD camera (IXon Ultra 897, AndorTM, Oxford Instruments) controlled by a computer through NIS-elements D (Nikon). Images were acquired each 150 ms at 10 MHz readout compensating the read noise with  $250 \times$  electron multiplying (EM) gain. 20 min of basal spontaneous activity was recorded then the following antagonists were applied: APV  $25 \times 10^{-6}$  M (glutamate NMDA receptor selective antagonist), bicuculline  $10 \times 10^{-6}$  M (GABA<sub>A</sub> receptor antagonist) and CNQX  $10 \times 10^{-6}$  M (glutamate AMPA/kainate receptor antagonist) to remove all ongoing synaptic activity.<sup>46</sup> This experimental condition was used to detect the evoked  $\text{Ca}^{2+}$  transients due to direct excitation of cells and generation of action potentials via either Au-Flat or Au-NWs electrodes electrical stimulation. The neuronal nature of the recorded calcium episodes was ensured by applying  $1 \times 10^{-6}$  M TTX which readily abolished any evoked responses. All off line analyses were accomplished by the ImageJ software (NIH) and the Clampfit software (pClamp suite, 10.4 version; Axon Instruments).

**Statistical Analysis:** The procedure used for the quantification of the immunofluorescence images from viability and differentiation studies of rNCCs was based on an automatized protocol created by using the Fiji software in which the observer must only define a threshold of positive staining for each marker established from the negative controls. In order to minimize bias effects, quantifications were carried out blind by two independent observers. The positively stained area for each particular marker was expressed as a percentage of the total image area. Quantified parameters were expressed as the mean  $\pm$  standard deviation. For each parameter under study and substrate, images were randomly acquired from a minimum of 3 independent experiments ( $n \geq 5$ ). For parametric analysis to compare more than 2 groups, one-way analyses of variance (ANOVA) followed by either Scheffé or Games–Howell post-hoc tests (homogeneous and heterogeneous variances, respectively, according to Levene's test) was used. For non-parametric analysis, the Mann-Whitney  $U$  test was used for comparisons between groups. In studies with rNCCs, the statistical significance levels were defined as:  $*p < 0.05$ ,  $**p < 0.01$ , and  $***p < 0.005$ . Statistical analyses were performed by using the Statistical Package for the Social Sciences software (SPSS, version 17.0).

Quantitative data for neuronal and astrocytes densities from hippocampal cells were presented as box plots. Images were randomly acquired from 3 independent culture series, 4 cultures each, and at least 3 fields per culture dish. Statistical comparisons were done by the Kruskal–Wallis test, being the  $p$ -value adjusted for multiple comparisons with Dunn's correction. Distribution of IELs in hippocampal cells was presented as cumulative probability and box plots. Calcium imaging was recorded in hippocampal cells from at least 3 independent cultures per treatment. Statistical comparisons were done by the Kolmogorov–Smirnov test and the Kruskal–Wallis test on ranks, using also Dunn's correction for multiple comparisons. In studies with hippocampal cells, the statistical significance level was defined as:  $***p < 0.001$ . Statistical analyses in this case were performed by using the Prism 6 software.

## Supporting Information

Supporting Information is available from the Wiley Online Library or from the author.

## Acknowledgements

A.D.-B. and B.L.R. contributed equally to this work. This work was funded by the European Union's Horizon 2020 research and innovation

programme under grant agreement No. 737116 (ByAxon). The work was also partially funded by the Spanish Ministry of Science and Innovation through project BiSURE (Grant: DPI2017-90058-R) and the 'Severo Ochoa' Programme for Centers of Excellence in R&D (MINECO, Grant SEV-2016-0686), as well as by the Comunidad de Madrid project NanoMagCOST (CM S2018/NMT-4321). BLR acknowledges UCM for her predoctoral fellowship. Authors are thankful to Dr. Esperanza Salvador, Isidoro Poveda, Gabriel Carro, Enrique Rodríguez, Dr. Francisco Urbano, and Dr. Covadonga Agudo from the Servicio Interdepartamental de Investigación at the Universidad Autónoma de Madrid for respective assistance with SEM, FESEM, and TEM studies. Sylvia Gutiérrez from the Advanced Light Microscopy Service at the Centro Nacional de Biotecnología (CNB-CSIC) is acknowledged for her assistance with CLSM studies.

### Conflict of Interest

The authors declare no conflict of interest.

### Keywords

electrical stimulation, electrode arrays, metallic nanowires, nanotopography, neural interfaces

Received: May 2, 2020

Revised: July 16, 2020

Published online:

- [1] M. E. Spira, A. Hai, *Nat. Nanotechnol.* **2013**, *8*, 83.  
 [2] M. E. Spira, S. H. Huang, N. Shmuel, H. Erez, *Adv. Neurobiol.* **2019**, *22*, 125.  
 [3] D. Eytan, S. Marom, *J. Neurosci.* **2006**, *26*, 8465.  
 [4] T. J. Blanche, M. A. Spacek, J. F. Hetke, N. V. Swindale, *J. Neurophysiol.* **2005**, *93*, 2987.  
 [5] M. N. Hasan, A. N. Radwan, M. Kim, E. Kucukal, D. Maji, V. Pashaei, C.-Y. Chung, A. Kakkar, U. A. Gurkan, *Technology* **2019**, *07*, 57.  
 [6] S. K. Seidlits, J. Y. Lee, C. E. Schmidt, *Nanomedicine* **2008**, *3*, 183.  
 [7] F. Patolsky, B. P. Timbo, G. Yu, Y. Fang, A. B. Greytak, G. Zheng, C. M. Lieber, *Science* **2006**, *313*, 1100.  
 [8] A. Hai, J. Shappir, M. E. Spira, *J. Neurophysiol.* **2010**, *104*, 559.  
 [9] J. T. Robinson, M. Jorgolli, A. K. Shalek, M. H. Yoon, R. S. Gertner, H. Park, *Nat. Nanotechnol.* **2012**, *7*, 180.  
 [10] J. Abbott, T. Ye, K. Krenek, R. S. Gertner, S. Ban, Y. Kim, L. Qin, W. Wu, H. Park, D. Ham, *Nat. Biomed. Eng.* **2020**, *4*, 232.  
 [11] A. F. McGuire, F. Santoro, B. Cui, *Ann. Rev. Anal. Chem.* **2018**, *11*, 101.  
 [12] M. Dipalo, H. Amin, L. Lovato, F. Moia, V. Caprettini, G. C. Messina, F. Tantussi, L. Berdondini, F. De Angels, *Nano Lett.* **2017**, *17*, 3932.  
 [13] D. Brüggemann, B. Wolfrum, V. Maybeck, Y. Mourzina, M. Jansen, A. Offenhäusser, *Nanotechnology* **2011**, *22*, 265104.  
 [14] C. Xie, Z. Lin, L. Hanson, Y. Cui, B. Cui, *Nat. Nanotechnol.* **2012**, *7*, 185.  
 [15] Z. C. Lin, C. Xie, Y. Osakada, Y. Cui, B. Cui, *Nat. Commun.* **2014**, *5*, 3206.  
 [16] D. B. Suyatin, L. Wallman, J. Thelin, C. N. Prinz, H. Jörntell, L. Samuelson, L. Montelius, J. Schouenborg, *PLoS ONE* **2013**, *8*, e56673.  
 [17] G. M. Dittami, R. D. Rabbitt, *Lab Chip* **2010**, *10*, 30.  
 [18] D. H. Kim, J. Viventi, J. J. Amsden, J. Xiao, L. Vigeland, Y. S. Kim, J. A. Blanco, B. Panilaitis, E. S. Frechette, D. Contreras, D. L. Kaplan, F. G. Omenetto, Y. Huang, K. C. Hwang, M. R. Zakin, B. Litt, J. A. Rogers, *Nat. Mater.* **2010**, *9*, 511.  
 [19] Z. J. Sperry, K. Na, S. S. Parizi, H. J. Chiel, J. Seymour, E. Yoon, T. M. Bruns, *J. Neural Eng.* **2018**, *15*, 036027.  
 [20] S. Huang, Y. Liu, Y. Zhao, Z. Ren, C. F. Guo, *Adv. Funct. Mater.* **2019**, *29*, 1805924.  
 [21] I. R. Mineev, P. Musienko, A. Hirsch, Q. Barraud, N. Wenger, E. M. Moraud, J. Gandar, M. Capogrosso, T. Milekovic, L. Asboth, R. F. Torres, N. Vachicouras, Q. Liu, N. Pavlova, S. Duis, A. Larmagnac, J. Vörös, S. Micera, Z. Suo, G. Courtine, S. P. Lacour, *Science* **2015**, *347*, 159.  
 [22] W. Yi, C. Chen, Z. Feng, Y. Xu, C. Zhou, N. Masurkar, J. Cavanaugh, M. M. Cheng, *Nanotechnology* **2015**, *26*, 125301.  
 [23] M. Ryu, J. H. Yang, Y. Ahn, M. Sim, K. H. Lee, K. Kim, T. Lee, S.-J. Yoo, S. Y. Kim, C. Moon, M. Je, J.-W. Choi, Y. Lee, J. E. Jang, *ACS Appl. Mater. Interfaces* **2017**, *9*, 10577.  
 [24] D. Jain, S. Mattiassi, E. L. Goh, E. K. F. Yim, *Neural Regen. Res.* **2020**, *15*, 573.  
 [25] D. E. Discher, D. J. Mooney, P. W. Zandstra, *Science* **2009**, *324*, 1673.  
 [26] D. Hoffman-Kim, J. A. Mitchel, R. V. Bellamkonda, *Annu. Rev. Biomed. Eng.* **2010**, *12*, 203.  
 [27] B. Carlberg, M. Z. Axell, U. Nannmark, J. Liu, H. G. Kuhn, *Biomed. Mater.* **2009**, *4*, 045004.  
 [28] M. R. Lee, K. W. Kwon, H. Jung, H. N. Kim, K. Y. Suh, K. Kim, K. S. Kim, *Biomaterials* **2010**, *31*, 4360.  
 [29] E. Shhbaizi, S. Kiani, H. Gourabi, H. Baharvand, *Tissue Eng., Part A* **2011**, *17*, 3021.  
 [30] C. H. Chen, C. C. Tsai, P. T. Wu, I. K. Wang, J. Yu, W. B. Tsai, *ACS Appl. Mater. Interfaces* **2019**, *2*, 205.  
 [31] G. J. Bakeine, J. Ban, G. Grecni, A. Pozzato, S. Dal Zilio, M. Prasciolu, L. Businaro, M. Tormen, M. E. Ruaro, *Microelectron. Eng.* **2009**, *86*, 1435.  
 [32] H. K. Kim, E. Kim, H. Jang, Y. K. Kim, K. Kang, *ChemNanoMat* **2017**, *3*, 278.  
 [33] M. Marcus, K. Baranes, M. Park, I. S. Choi, K. Kang, O. Shefi, *Adv. Healthc. Mater.* **2017**, *6*, 1700267.  
 [34] L. P. Felix, J. E. Perez, M. F. Contreras, T. Ravasi, J. Kosel, *Toxicol. Rep.* **2016**, *3*, 373.  
 [35] F. Byrne, A. Prina-Mello, A. Whelan, B. M. Mohamed, A. Davies, Y. K. Gurko, J. M. D. Coey, Y. Volkov, *J. Magn. Magn. Mater.* **2009**, *321*, 1341.  
 [36] A. Prina-Mello, Z. Diao, J. M. Coey, *J. Nanobiotechnol.* **2006**, *4*, 9.  
 [37] C. G. Ma, M. M. Song, Y. Zhang, M. Q. Yan, M. Zhang, H. Bi, *Toxicol. Rep.* **2014**, *1*, 114.  
 [38] W. Hällström, T. Martensson, C. Prinz, P. Gustavsson, L. Montelius, M. Kanje, *Nano Lett.* **2007**, *7*, 2960.  
 [39] K. Yang, H. Jung, H. R. Lee, J. S. Lee, S. R. Kim, K. Y. Song, E. Cheong, J. Bang, S. G. Im, S. W. Cho, *ACS Nano* **2014**, *8*, 7809.  
 [40] S. Ankam, M. Suryana, L. Y. Chan, A. A. K. Moe, B. K. K. Teo, J. B. K. Law, M. P. Sheetz, H. Y. Low, E. K. F. Yim, *Acta Biomater.* **2013**, *9*, 4535.  
 [41] V. L. S. LaPointe, A. T. Fernandes, N. C. Bell, F. Stellacci, M. M. Stevens, *Adv. Healthcare Mater.* **2013**, *2*, 1644.  
 [42] G. Cellot, F. M. Toma, Z. K. Varley, J. Laishram, A. Villari, M. Quintana, S. Cipollone, M. Prato, L. Ballerini, *J. Neurosci.* **2011**, *31*, 12945.  
 [43] S. Li, F. P. Ulloa Severino, J. Ban, L. Wang, G. Pinato, V. Torre, Y. Chen, *Biomed. Mater.* **2018**, *13*, 034105.  
 [44] F. P. Ulloa Severino, J. Ban, Q. Song, M. Tang, G. Bianconi, G. Cheng, V. Torre, *Sci. Rep.* **2016**, *6*, 29640.  
 [45] S. Bosi, R. Rauti, J. Laishram, A. Turco, D. Lonardoni, T. Nieuw, M. Prato, D. Scaini, L. Ballerini, *Sci. Rep.* **2015**, *5*, 9562.  
 [46] N. P. Pampaloni, M. Lottner, M. Giugliano, A. Matruggio, F. D'Amico, M. Prato, J. A. Garrido, L. Ballerini, D. Scaini, *Nat. Nanotechnol.* **2018**, *13*, 755.  
 [47] C. Vallejo-Giraldo, K. Krukiewicz, I. Calaresu, J. Zhu, M. Palma, M. Fernandez-Yague, B. W. McDowell, N. Peixoto, N. Farid,



- G. O'Connor, L. Ballerini, A. Pandit, M. J. P. Biggs, *Small* **2018**, *14*, 1800863.
- [48] I. Rago, R. Rauti, M. Bevilacqua, I. Calaresu, A. Pozzato, M. Cibinel, M. Dalmiglio, C. Tavagnacco, A. Goldoni, D. Scaini, *Adv. Biosyst.* **2019**, *3*, 1800286.
- [49] S. Stern, A. Agudelo-Toro, A. Rotem, E. Moses, A. Neef, *PLoS ONE* **2015**, *10*, e0132577.
- [50] E. Saracino, L. Maiolo, D. Polese, M. Semprini, A. I. Borrachero-Conejo, J. Gasparetto, S. Murtagh, M. Sola, L. Tomasi, F. Valle, L. Pazzini, F. Formaggio, M. Chiappalone, S. Hussain, M. Caprini, M. Muccini, L. Ambrosio, G. Fortunato, R. Zamboni, A. Convertino, V. Benfenati, *Adv. Biosyst.* **2020**, *4*, 1900264.
- [51] M. Kang, S. M. Yoo, R. Gwak, G. Eom, J. Kim, S. Y. Lee, B. Kim, *Nanoscale* **2016**, *8*, 214.
- [52] Y. Yoo, K. Seo, S. Han, K. S. K. Varadwaj, H. Y. Kim, J. H. Ryu, H. M. Lee, J. P. Ahn, H. Ihee, B. Kim, *Nano Lett.* **2010**, *10*, 432.
- [53] T. T. Zhai, D. Ye, Q. W. Zhang, Z. Q. Wu, X. H. Xia, *ACS Appl. Mater. Interfaces* **2017**, *9*, 34706.
- [54] A. Convertino, V. Mussi, L. Maiolo, M. Ledda, M. G. Lolli, F. A. Bovino, G. Fortunato, M. Rocchia, A. Lisi, *Nanotechnology* **2018**, *29*, 415102.
- [55] R. Parameswaran, J. L. Carvalho-de-Souza, Y. Juang, M. J. Burke, J. F. Zimmerman, K. Koehler, A. Philips, J. Yi, E. J. Adams, F. Bezanilla, B. Tian, *Nat. Nanotechnol.* **2018**, *13*, 260.
- [56] M. Carballo-Vila, B. Moreno-Burriel, E. Chinarro, J. R. Jurado, N. Casañ-Pastor, J. E. Collazos-Castro, *J. Biomed. Mater. Res., Part A* **2009**, *90A*, 94.

**Polystyrene nanopillars with inbuilt carbon nanotubes enable synaptic modulation and stimulation in interfaced neuronal networks**

Ivo Calaresu, Jaime Hernandez, Rossana Rauti<sup>#</sup>, Beatriz L. Rodilla, Ana Arché-Núñez, Lucas Perez, Julio Camarero, Rodolfo Miranda, M. Teresa González<sup>\*</sup>, Isabel Rodríguez<sup>\*</sup>, Denis Scaini<sup>§</sup> \* and Laura Ballerini<sup>\*</sup>

I. Calaresu, R. Rauti, D. Scaini, L. Ballerini

Scuola Internazionale Superiore di Studi Avanzati (SISSA) Via Bonomea, 265 - 34136 Trieste ITALY

J. Hernandez, B. L. Rodilla, A. Arché-Núñez, L. Perez, J. Camarero, R. Miranda, M.T. González, I. Rodriguez

Madrid Institute for Advanced Studies in Nanoscience (IMDEA Nanoscience), C/Faraday 9, Ciudad Universitaria de Cantoblanco. 28049 Madrid, SPAIN

L. Perez

Dpto. Física de Materiales. Universidad Complutense de Madrid. 28040 Madrid, Spain

J. Camarero, R. Miranda,

Departamento de Física de la Materia Condensada and Instituto de Ciencia de Materiales Nicolás Cabrera, Universidad Autónoma de Madrid, Madrid, Spain

<sup>#</sup>Present affiliation R. Rauti: Department of Biomedical Engineering, Tel Aviv University, Tel Aviv 6997801, Israel.

<sup>§</sup>Present affiliation D. Scaini: Department of Medicine, Imperial College London, Hammersmith Hospital, London, UK

E-mail: [teresa.gonzalez@imdea.org](mailto:teresa.gonzalez@imdea.org), [i.rodriguez@imdea.org](mailto:i.rodriguez@imdea.org), [dscaini@sissa.it](mailto:dscaini@sissa.it),

[lballerini@sissa.it](mailto:lballerini@sissa.it)

Keywords: (nanopillars, carbon nanotubes, electrical stimulation, suspended 2D cultures, hippocampal cultures, spinal cord organotypic slices)

## **Abstract**

The use of nanostructured materials and nanosized-topographies have the potential to impact the performance of implantable biodevices, including neural interfaces, enhancing their sensitivity and selectivity, while reducing tissue reactivity. As a result, current trends in biosensor technology require the effective ability to improve devices with controlled nanostructures. We exploited nanoimprint lithography to pattern surfaces with high-density and high aspect ratio nanopillars (NP) made of polystyrene (PS-NP, insulating), or of a polystyrene/carbon-nanotube nanocomposite (PS-CNT-NP, electrically conductive). Both substrates were challenged with cultured primary neurons. They demonstrated to support the development of suspended synaptic networks at the NPs' interfaces characterized by a reduction in proliferating neuroglia, and a boost in neuronal emergent electrical activity when compared to flat controls. We successfully exploited our conductive PS-CNT-NPs to stimulate cultured cells electrically. We then tested the ability of both nanostructured surfaces to interface tissue explants isolated from the mouse spinal cord. The integration of the neuronal circuits with the NP topology, the suspended nature of the cultured networks, the reduced neuroglia formation, and the higher network activity together with the ability to deliver electrical stimuli via PS-CNT-NP reveal such platforms as promising designs to implement on neuro-prosthetic or neurostimulation devices.

## 1. Introduction

In the design of neural interfaces, nanomaterials and nanostructured topologies are tools which may enable an improved interfacing with the nerve tissue. Nanotechnology-based engineering of neuronal interfaces aims at overcoming some of the current limitations of implantable devices, such as the mechanical matching with the central nervous system (CNS) tissue and the biological tolerance.<sup>[1]</sup> Nanofabrication allows for bio-camouflage of interfacing electrodes via emulating extracellular matrix (ECM) features, or allowing for three-dimensional interfacing.<sup>[2]</sup> Surfaces patterned with vertically aligned nanopillars (NPs) have been exploited as bio-interfaces.<sup>[3]</sup> Mouse embryonic stem cells, neural progenitors and hippocampal neurons, to name a few, were successfully cultured on NP substrates of different size, aspect ratio, shape, or density, with the aim to target the influence of surface topographical features on biological responses, including cell viability, proliferation, morphology, differentiation, adhesion, and motility.<sup>[4-9]</sup>

In particular, for neuronal or progenitor cell cultures, NP patterned substrates have been designed to significantly influence proliferation and guidance, neural differentiation, outgrowth, and development.<sup>[10,11]</sup> In the field of neuroscience, vertical nanowires (NW) or NPs have been shown to support the formation of axons in hippocampal neurons, and that of functional neuronal networks.<sup>[8,12]</sup> Vertical NWs have also been employed for single-cell stimulation and recording in experimental bioelectric interfaces.<sup>[13]</sup> In most cases, NPs have been made out of hard materials like gallium phosphide (GaP) semiconductors, silicon, or metals.<sup>[12,14-16]</sup> Despite their remarkable features, semiconductors or metal NPs require long growth times and their production is time expensive. These materials are characterized by high Young's modulus which renders these NPs stiff and tedious to handle in bioassays, due to their fragility. Moreover, CNS tissues are soft, and as such, there is a substantial difference in stiffness between these NPs and the CNS tissues, leading to low mechanical compatibility. This mismatch in mechanical properties is believed to cause glia

over proliferation and gliosis, once implanted *in vivo*.<sup>[17]</sup> Polymeric, high aspect ratio, nanoscale topographies with a lower effective modulus would be more compliant with a good potential for improved biocompatibility.<sup>[18]</sup>

Here, we developed an easy and affordable fabrication strategy based on nanoimprint lithography to pattern polystyrene (PS) surfaces with high-density, high aspect ratio NPs. Two different substrates were investigated: insulating NP surfaces (PS-NP), fabricated from pristine polystyrene, and conductive NPs (PS-CNT-NP), produced from a polystyrene nanocomposite where single-walled carbon nanotubes (SWCNTs) were used as conducting filler. These NP substrates were optimized to support the development of primary neuronal cultures allowing the growth of planar neuronal circuits comprised of neural cells soma and axons, making functional synapse networks, and having a three-dimensional exposure to the extracellular environment. We discovered that neuronal networks developed on NP substrates, compared to those grown on flat glass or flat PS surfaces, presented a reduction in glial cell density and a boost in spontaneous electrical activity. We suggest that these features result from the 3D-like microenvironment exposure of cells when suspended among NPs, emulating natural surroundings of cells as in *in vivo* conditions.

We successfully validated the possibility of using PS-CNT-NP to deliver electrical stimuli to the neural network and, finally, we showed that PS-NP and PS-CNT-NP were able to interface with and sustain the development of organotypic slices of mouse spinal cord.

## **2. Results and Discussion**

### **2.1 Topography fabrication and characterization**

Dense arrays of high aspect ratio NPs of 500 nm in diameter and 1  $\mu\text{m}$  pitch were selected as cell culture platforms to provide a substrate topography where, due to the small spacing and size exclusion, interaction and adhesion of neuronal cells will be forced to take place only at the top of the topography (**Figure 1**).



An anisotropic square pillar arrangement was chosen rather than a compact hexagonal one to maximize interpillar space, ultimately filled by extracellular solution, while providing physical support for developing a planar neural network suspended at the top of NPs.<sup>[4]</sup> NPs surfaces were prepared by soft thermal nanoimprint lithography (T-NIL). This technology allowed us to imprint NPs with the same dimensions in both insulating PS and in a polystyrene/carbon-nanotubes composite (PS-CNT), thus providing precisely the same spatio-mechanical cue to the neuronal cells cultured on each of the substrates.

In Figure 1A, a scheme of the nanoimprint process is depicted, while Figure 1B shows a scanning electron microscopy (SEM) image of one of our high aspect ratio NP arrays (500 nm in diameter, 2  $\mu\text{m}$  in height, in a square arrangement with a pitch of 1  $\mu\text{m}$ ). PS-NP substrates were produced by imprinting a PDMS working mold onto pristine PS films under optimum time, temperature, and pressure conditions (see Experimental Section for details). PS-CNT-NP substrates were produced in the same way by imprinting the nanopillar structures on a composite material constituted by a polystyrene matrix filled with single-wall carbon nanotubes (SWCNTs, 1% w/w).

Localized confocal Raman spectroscopy was performed to verify the presence of SWCNTs dispersed within the imprinted PS-CNT nanopillars. Specifically, a laser light of 532 nm wavelength, providing a depth resolution of about 400 nm, was utilized to detect the SWCNTs inside the nanopillars.<sup>[19]</sup> Figure 1C compares the Raman spectra of pristine PS nanopillars to PS-CNT ones, confirming SWCNTs' characteristics bands (D, G, and G'). This fingerprint is not present in pristine PS-NPs. The formation within the polymeric matrix of a percolation network of SWCNTs was confirmed by measuring the through-plane conductivity employing dielectric spectroscopy measurements (see Experimental Section). A value in the range of 10–100  $\text{mS}\cdot\text{cm}^{-1}$  was measured for PS-CNT nanocomposite films.

Nanoindentation tests were conducted to determine the changes in surface stiffness upon patterning the substrates under study, and possibly identify a stiffness-dependent cellular adaptation on the different topographies.

**Figure S1** shows representative nanoindentation curves obtained from pristine PS, PS-NP and PS-CNT-NP samples. The apparent stiffness ( $k$ ), defined as the rate of change of probe depth with applied load, was determined from the slope of the unloading curves at the beginning of the loading-unloading nanoindentation cycles (elastic regime, low penetration values). The stiffness of the unstructured PS substrate ( $1.6 \pm 0.15 \mu\text{N}\cdot\text{nm}^{-1}$ ) decreased by 84% after just surface (nano)patterning, and the apparent stiffness on the PS-NP topography set to values down to  $0.25 \pm 0.03 \mu\text{N}\cdot\text{nm}^{-1}$ . Upon the reinforcement of the PS-NP with SWCNT, the PS-CNT-NP patterned surface apparent stiffness increased slightly to  $0.31 \pm 0.03 \mu\text{N}\cdot\text{nm}^{-1}$ . These marked changes in the surface apparent stiffness can be inferred from the nanoindentation graphs displayed in Figure S1.

## **2.2 Characterization of Primary Hippocampal Cultures interfaced to NP substrates**

In our first set of neurobiology experiments, we tested the stability of PS-NP (non-conductive and nanostructured) and PS-CNT-NP (conductive and nanostructured) once exposed to cells grown seeded on top of the NPs and submerged in cell culturing media for days. In particular, we investigated the substrates' ability to support neuronal adhesion and formation of neuronal networks. Neonatal rat hippocampal cells successfully adhered and grew on both substrates and were analyzed after 8 to 12 days *in vitro* (DIV; **Figure 2**), a time known to allow functional synaptic network development in *in vitro* conditions.<sup>[20,21]</sup> The structural stability of both NP platforms, and their interaction with cultured hippocampal cell soma, axons and dendritic arborizations, were assessed by SEM. Figure 2A shows SEM micrographs at increasing magnifications (left to right) of control cells developed on poly-ornithine-coated glass coverslips (top row) and on the two

nanostructured substrates (PS-NP and PS-CNT-NP, second and third rows, respectively). At low magnification (left panels), neuronal cell bodies characterized by prominent neurites and glial cells branching are evident and appear in all three conditions. Higher magnification (Figure 2A, middle) reveals well-formed cell somas and neurites. At this magnification, it is possible to appreciate that NPs are slightly tilted at cell-bodies' boundaries, suggesting cell ability to exert peripheral tangential forces through focal adhesions engagement of the NPs heads and actomyosin-driven cytoskeletal contractions.<sup>[22]</sup> These features are usually correlated to a healthy neuronal adhesion and growth.<sup>[23,24]</sup> Further magnification (Figure 2A, right), allows visualizing distinct neuronal processes. NP substrates induced the formation of planar networks of neuronal processes apparently similar to those developed on Controls. However, neurites ability to navigate by surfing on the top of NPs generated a suspended network architecture, whose axons and dendrites are exposed to the inter-pillars extracellular milieu with cell media flowing below as well on top of them (**Figure S4**). We further investigated the size of the cultured networks and their cellular composition via immunofluorescence microscopy, labeling the specific cytoskeletal components  $\beta$ -tubulin III, to visualize neurons, 4',6-diamidino-2-phenylindole (DAPI), to highlight cell nuclei, and glial fibrillary acidic protein (GFAP) to visualize astrocytes (Figure 2B). We compared Control, PS-NP, and PS-CNT-NP hippocampal networks morphology and cell composition. Control (n = 77, from 5 culture series), PS-NP (n = 73, 5 culture series) and PS-CNT-NP (n = 80, 5 culture series) showed a comparable density of  $\beta$ -tubulin III positive neurons (highlighted in red in Figure 2B, and quantified in the box plot in Figure 2C). The density of neuroglia cells, a heterogeneous population of cells that includes oligodendrocytes, astrocytes, and microglia, was quantified as non-neuronal stained nuclei (Figure 2B, top row; see Experimental Section). This measure pointed out a significant reduction in the overall number of glial cells on both PS-NP and PS-CNT-NP substrates ( $774 \pm 347$  and  $675 \pm 227$  neuroglial

cells/mm<sup>2</sup>, respectively) when compared to Control (1113 ± 249 neuroglial cells/mm<sup>2</sup>; \*\*\*p < 0.001; box plot in Figure 2D). Interestingly, when we focused on the GFAP positive astrocyte (in green in Figure 2B, bottom row), a substantial change in astrocyte morphology between flat and nanostructured substrates was qualitatively observed. In Controls, astrocytes appear more spread and flatten than on both nanostructured substrates where they appear with a stellate shape (see arrows in Figure 2B, second row). In a further set of experiments (4 culture series) we selectively quantified the number of GFAP-positive cells comparing Control, PS-NP, PS-CNT-NP and PS-flat substrates, to rule out the possible contribution of polystyrene *per se* (**Figure S2**). Consistently with our first group of results, both flat substrates (PS-flat, n = 46 fields, and Control, n = 42 fields) showed comparable astrocyte densities (297 ± 49 cells/mm<sup>2</sup> and 274 ± 54 cells/mm<sup>2</sup>, respectively), while in the nanostructured substrates (PS-NP, n = 45 fields, and PS-CNT-NP, n = 45 fields) GFAP positive cells density was significantly reduced (199 ± 42 cells/mm<sup>2</sup> and 138 ± 51 cells/mm<sup>2</sup>, respectively; \*\*\*p<0.001). No difference was depicted in neuronal densities comparing PS-flat substrates with the other conditions (results summarized in Figure S2A and S2B).

We suggest that the decrease in glial cell density brought about by NP-structured substrates may be ascribed to mechanisms related to the cell focal contact modulation by the topography and related mechanotransduction processes.<sup>[25-28]</sup> In addition, other features such as the reduced apparent stiffness of the nano-topographies may induce this cellular response.<sup>[29]</sup> Furthermore, a reduced glial cell proliferation may have been favored by the suspended configuration these cultures adopt in the high aspect ratio topography. In any case we can rule out a mere inhibition of proliferation due to the PS chemical characteristics since the behavior is not consistent in all the substrates being made of the same polymer matrix. Regardless of the mechanisms reducing glial cells

adhesion/proliferation on NPs substrates, this feature might imply a lower reactive gliosis when interfacing CNS tissue with the NP substrates.<sup>[18,30]</sup>

### **2.3 Nanopillars-based substrates increase synaptic network performance**

Upon *ex vivo* reorganization of synaptic networks, primary cultured neurons display spontaneous and temporally structured electrical activity.<sup>[31,32]</sup> We explored the network dynamics in Control, PS-NP, and PS-CNT-NP hippocampal cultures (9 – 12 DIV; 5 culture series) by fluorescent imaging with calcium indicators (**Figure 3**). This is a minimally invasive approach that allows monitoring neuronal activity following the calcium transients occurring in a neuronal network at a single-cell level.<sup>[33]</sup> Living neurons, stained with the membrane-permeable dye Oregon Green 488-BAPTA-1 AM, were visualized within randomly chosen sample areas ( $660 \times 660 \mu\text{m}^2$ , Figure 3A, left images) and, on average,  $135 \pm 30$  fluorescent cells were analyzed for each experimental condition (see Experimental Section).

In all culture groups, we detected spontaneous and repetitive calcium events emerging from episodes of synaptic, action potential-dependent, bursts of activity (Figure 3A, tracings). This electrical activity was entirely blocked by Tetrodotoxin (TTX,  $1 \mu\text{M}$ ; a blocker of fast voltage-gated  $\text{Na}^+$  channels) applications, demonstrating its dependence upon neuronal firing and synaptic activation (Figure 3A, right traces).<sup>[33]</sup> We quantified spontaneous calcium episodes in active cells by measuring the inter-event interval (IEI), the time interval between the onset of a calcium burst and the beginning of the next one. IEI values were significantly reduced (thus activity increased) in PS-NP and PS-CNT-NP substrates compared to Control ones (results summarized in the box plot of Figure 3B;  $**p < 0.01$  and  $***p < 0.001$ , respectively for Control vs. PS-NP, and Control vs. PS-CNT-NP). Network activity was not affected by PS-flat, again ruling out a role of polystyrene *per se* (Figure S2 C, left traces). A distinct feature of network dynamics is the emergence of synchronized calcium events in cells located within the same field of view. We quantified



this parameter by measuring the cross-correlation function among pairs of cells (**Figure S3**, see Experimental Section for details). Neurons displaying a Pearson correlation coefficient (CCF) that was significantly larger than that expected by chance, were considered positively correlated. The bar plot in Figure 3C shows that in Control  $46 \pm 1\%$  of cell pairs ( $n = 661$  pairs) were positively correlated, this value raised to  $86 \pm 2\%$  and  $96 \pm 2\%$  in PS-NP ( $n = 876$  pairs) and PS-CNT-NP ( $n = 983$  pairs), respectively.

To investigate the mechanism responsible for the increased activity observed in NP substrates, we performed single neuron, whole-cell, patch-clamp recordings directly comparing synaptic activity recorded in flat substrates (Control) with the nanostructured ones (PS-NP) (**Figure 4**).

Figure 4A shows current tracings characterized by heterogeneous events of inward currents which represent basal spontaneous synaptic activity of a Control neuron and a PS-NP one.<sup>[20]</sup> No significant variations in the mean amplitude values of the postsynaptic currents (PSCs) was measured between the two conditions ( $n = 11$  cells for Control,  $n = 17$  cells for PS-NP). Conversely, we detected a significant increase (\*\* $p = 0.009$ ) in the PSCs frequencies when comparing the two conditions (Control:  $0.9 \pm 0.3$  Hz; PS-NP:  $2.1 \pm 0.4$  Hz; Figure 4A, right box plot), confirming the presence of increased network activity in NP cultured neurons. In Figure 4B we recorded miniature PSCs (mPSCs) in the presence of TTX ( $1 \mu\text{M}$ ) in both Control and PS-NP conditions. Recording mPSCs allows disambiguating dynamical from structural changes of neural circuit activity. mPSCs, in fact, reflect the stochastic release of vesicles from the presynaptic terminals and mPSC frequency depends on the number of synaptic contacts, while their amplitude depends on postsynaptic receptor sensitivity.<sup>[34]</sup> In these experimental conditions, we did not detect any significant variation in mPSCs mean amplitude values ( $n = 8$  cells for Control,  $n = 9$  cells for PS-NP). Instead, we measured a significant increase ( $p = 0.012$ ) in mPSCs frequencies when comparing Control to PS-NP samples ( $0.6 \pm 0.2$  Hz vs.  $1.6 \pm 0.3$  Hz,

respectively; Figure 4B, right box plot). In all recordings we never detected changes in neuronal passive membrane properties (for capacitance, Control:  $84 \pm 33$  pF; PS-NP:  $97 \pm 32$  pF;  $p = 0.20$ ; and input resistance, Control:  $436 \pm 211$  M $\Omega$ ; PS-NP:  $361 \pm 190$  M $\Omega$ ;  $p = 0.22$ ; Figure 4C).

To estimate whether changes in synaptic density may account for the enhanced mPSC frequency observed in NP neurons, cultured hippocampal neurons were co-immunostained for  $\beta$ -tubulin III, DAPI and the synaptic marker Bassoon.<sup>[35]</sup>

We quantified the number of synaptic contacts in the two conditions evaluating the volumetric ratio between Bassoon's presynaptic marker, which labels the presynaptic active zone, and the neuronal tracer  $\beta$ -tubulin III. Results are summarized in the box plot in Figure 4E, where a significant increase in synaptic-related signal is evincible in PS-NP samples in comparison to the Control condition (Control:  $0.06 \pm 0.01$ ; PS-NP:  $0.16 \pm 0.01$ ;  $n = 23$  and  $25$ , respectively;  $p = 0.0015$ ). All results presented so far indicate that synaptogenic processes are facilitated in neuronal networks developed above nanopillar-surfaces, that is in the suspended bidimensional configuration.

#### **2.4 Carbon-based nanostructures as a platform for effective electrical neurostimulation**

We further evaluated the possibility of exploiting our conductive nanostructured substrates (PS-CNT-NP) as a neuro-stimulating platform (**Figure 5**). We monitored neuronal responses during electrical stimulation through PS-CNT-NP with a two-electrode system.<sup>[36]</sup> For this purpose, we used the experimental setup sketched in Figure 5A, where a PS-CNT-NP surface was exploited concurrently as culturing substrate and planar working electrode against an Ag/AgCl pellet reference electrode, both placed in the physiological saline solution. The emergence of evoked neuronal activity upon external electrical stimulation was monitored via real-time calcium imaging visualization.<sup>[37,38]</sup> Spontaneously active neurons were selected and pharmacologically decoupled from the

network by a cocktail of receptor antagonists (APV/CNQX/bicuculline, see Experimental Section for details), to block ionotropic glutamate receptors subtypes and GABA<sub>A</sub> ones (Figure 5B). Under this recording condition synaptic activity was silenced, allowing to monitor the appearance in the neurons of activity burst only evoked by the electrical stimulation delivered *via* the CNT nanopillars.<sup>[39,40]</sup> We tested a stimulation protocol where five consecutive cathodic voltage squared pulses at 0.2 Hz (1 V/mm<sup>2</sup>, train-to-train frequency 0.01 Hz) were delivered by the PS-CNT-NP extracellular surface/electrode (Figure 5C). As shown in Figure 5D (top calcium imaging trace), such a stimulation reliably evoked calcium bursts that were abolished by tetrodotoxin (TTX, see Experimental Section) administration (Figure 5D, bottom trace), thus confirming the neuronal origins of the observed signals and the ability of PS-CNT-NP substrates to interface the neuronal network electrically. Such a phenomenological observation suggests that PS-CNT-NP platforms might represent a reliable interface to physically and electrically interface neuronal tissues.

## **2.5 Nanopillars interfacing to a complex tissue**

Cultured CNS explants provide an *in vitro* model of a complex neuronal network. In the last set of experiments, we decided to validate the long-term biological tolerance of nanostructured substrates (i.e., PS-NP and PS-CNT-NP) by interfacing them with spinal cord organotypic cultures for weeks. Organotypic spinal slices represent a biological model of segmental microcircuits which is maintained in *in vitro* conditions for weeks (**Figure 6**).<sup>[41]</sup> We used immunofluorescence labeling and confocal microscopy to study the adhesion, development, and final morphology of explanted spinal tissues and their axonal re-growth when chronically interfaced to PS-NP, PS-CNT-NP, and Control substrates for 21 – 24 DIV (see Experimental Section for details). Immunofluorescence confocal images at low magnification of the three conditions are depicted in Figure 6A. It is possible to note the healthy and complex structure of the spinal explants when grown interfaced with the

three substrates. The entire spinal cross-section is visible including the spinal slice, at the center, the peripheral dorsal root ganglia (DRGs), and a dense mesh of neurites in the surrounding outgrowth belt, highlighted by  $\beta$ -tubulin III positive neurites (in red) and the specific antibody against axonal neurofilament H (Smi-32, in green). No alterations in the growth and morphology of explanted spinal cord cultures were observed between the three conditions.

We further tested the functional impact of interfacing spinal slices on both nanostructured substrates. Organotypic spinal cord slices exhibit an intense spontaneous synaptic activity, monitored via live calcium imaging as spontaneous bursts emerging as irregular synchronized firing epochs (Figure 6B and 6C).<sup>[42]</sup> Fluorescent cells can be observed within the ventral area (pre-motor area) of each slice culture (arrows in Figure 6B). Spontaneous neuronal activity was measured by simultaneously imaging the intracellular calcium dynamic of selected neurons; these transients were fully blocked by TTX application demonstrating their neuronal origin (left and right traces in Figure 6C). Spontaneous calcium episodes were analyzed, and the resulting frequency (in Hz) was highly conserved between all tested conditions (Figure 6D). This result provides evidence of an appropriate maturation and development of the spinal cord slice when interfaced to nanostructured substrates.

The absence of a substantial increase in the electrical activity in suspended slices when compared to dissociated hippocampal cultures might be due to the different CNS anatomical origin (spinal cord vs. cortex) and by the long-term interfacing of organ cultures, leading to homeostatic adjustments of neuronal activity.<sup>[43]</sup>

Indeed, differently from a newly formed network of dissociated neurons, organotypic slices are characterized by complex three-dimensional cytoarchitecture governing the electrophysiological behavior of the network. The resulting robust network activity,

reflecting the spinal activity of the original tissue, might be more difficultly altered in the long term by the NP structure.

### **3. Conclusion**

We successfully developed insulating and conductive high aspect ratio nanopillar-based interfaces, constituted by cylindrical structures of 500 nm in diameter square-organized with a pitch of 1  $\mu\text{m}$ , able to successfully support the development of healthy and functional neuronal networks characterized by a suspended topology. These networks show similar cellular organization and neuronal cell content of Control cultures, but a significant reduction in the densities of astrocyte cellular population. This is not due to the mere chemical nature of PS but, more likely, to the combined effect of the surface (nano)morphology and the reduced apparent stiffness of the substrate compared to flat PS surfaces. In addition, the suspended organization of cultured cells might discourage the formation of glial layers interposed between the substrate and the neuronal cells.<sup>[44]</sup> This supportive cell layer could be less needed to the circuit formation due to the nanostructured surfaces of NP inducing submicrometrical surface adhesivity.

Valuably, both the tested substrates (PS-NP and PS-CNT-PS) allowed the development of suspended networks, characterized by increased network activity and higher degree of synchronization among cells pairs. It is tempting to speculate that, in the case of dissociated cultures, this configuration mimics the exposure of cell membrane (Figure S4, left) to a 3D geometry, providing neurons and neuronal connections with an improved efficiency, due to their accessibility to the third dimension.<sup>[33,45]</sup>

Finally, we validated these novel conductive nanostructured substrates (PS-CNT-NP) as a reliable device to electrically interface neural tissues demonstrating the possibility to elicit electrical activity, in the form of evoked calcium bursts, by extracellular stimulation of the conductive NPs. With the possible application of our nanostructured surfaces as a



neuroelectric interface for *in vivo* stimulation in mind, we validated PS-NP and PS-CNT-NP ability to support the long-term growth in vitro of spinal cord explants.

These experiments open to the possible applicability of our high aspect ratio PS-NP and, more interestingly, our PS-CNT-NP patterned substrates as a nerve tissue interfacing platform, with the advantage of inducing low gliosis, preserving intact tissue physiological activity, and the possibility to effectively electrically stimulate the nervous tissue.

#### **4. Experimental Section**

##### **Fabrication and characterization of high aspect ratio nanopillar substrates**

The PS-CNT nanocomposites films with ca. 1% w/w of functionalized single-wall carbon nanotubes (P3-SWCNT, Carbon Solutions Inc.) were prepared beforehand by solution blending, which is a commonly used method for the preparation of polymer-carbon nanotubes nanocomposites.<sup>[46]</sup> Briefly, a stable dispersion of SWCNT was initially prepared in toluene (99.8%, Acros Organics) by tip-sonication. A fixed volume of the dispersion was subsequently added to a PS solution prepared in toluene too. Using a dispersion tool (Ultraturrax, 10000 rpm), three stirring-sonication cycles were carried out to ensure good mixing and dispersion. Next, the nanocomposite was coagulated by the dropwise addition of the solution to cold methanol (reagent grade, Scharlau) under intense stirring. The obtained precipitate was filtered using a Buchner funnel, repeatedly washed with methanol, and dried in vacuum at 80 °C overnight. 200 – 300 µm thick self-standing PS and PS-CNT films were obtained by melt pressing using a hydraulic press with heating plates adapted (Specac Atlas 15T, temperature set at 140 °C and pressure at 10 tons).

PDMS molds with a pore size of 500 nm in diameter and 2 µm in length obtained from a silicon master by soft lithography, were used to fabricate high aspect ratio nanostructured substrates by thermal nanoimprint lithography (T-NIL), employing an EITRE Nano Imprint Lithography system (Obducat AB, Sweden). The thermal imprinting conditions

were  $T = 130\text{ }^{\circ}\text{C}$ ;  $P = 30\text{ bar}$  and  $t = 5\text{ min}$  for pristine PS and  $T = 140\text{ }^{\circ}\text{C}$ ;  $P = 30\text{ bar}$ ;  $t = 5\text{ min}$  for the SWCNT nanocomposite (PS-CNT).

A confocal Raman microscopy (SENTERRA, Bruker) was employed to verify the dispersion and penetration of the SWCNT into the nanopillars working at wavelengths of 532 and 785 nm.

The nanopillars' apparent stiffness was evaluated by performing nanoindentation tests using a Hysitron TI-950 TriboIndenter employing a diamond probe with a tip radius of 10  $\mu\text{m}$ . Nanoindentations measurements were performed by making 20 load-hold-unload cycles (1 second/segment) on different areas of the imprinted substrates. Unloading values up to 50% were employed in each cycle until a maximum load of 40  $\mu\text{N}$  was reached. The minimum critical buckling load for uniaxial compression was estimated through the geometrical parameters of an individual pillar to be about 25  $\mu\text{N}$ , assuming a modulus of 3.2 GPa for the polystyrene (according to manufacturer specifications).

The through-plane conductivity of the nanocomposites was evaluated by broadband dielectric spectroscopy using a Novocontrol broadband dielectric spectrometer. 10 mm diameter gold electrodes were first deposited by sputtering on both surfaces before the measurements.

### **Primary Cultures**

Dissociated hippocampal neurons were obtained from P2 – P3 old Wistar rats, as previously reported.<sup>[20,21]</sup> All procedures were approved by the local veterinary authorities and performed in accordance with the Italian law (decree 26/14) and the UE guidelines (2007/526/CE and 2010/63/UE). Animal use was approved by the Italian Ministry of Health (no. 22DABNQYA). All efforts were made to minimize suffering and to reduce the number of animals used. PS-flat, PS-NP, and PS-CNT-NP substrates were carefully rinsed with three 5 minutes-long washes with milliQ water (Merck Millipore). Samples were therefore dried at 60  $^{\circ}\text{C}$ , and their surfaces were activated under a low-pressure air plasma

(Harrick PDC-32G Plasma Cleaner) for 7 minutes at room temperature (RT), with a radiofrequency (RF) coil power set to 9 Watt. A 20 minutes-long exposition to ultraviolet (UV)-radiation was finally used to sterilize the substrates immediately before cell plating.<sup>[47]</sup> About 800 cells/mm<sup>2</sup> were plated onto poly-L-ornithine-coated (Sigma-Aldrich) glass coverslips (Control), PS-flat, PS-NP, and PS-CNT-NP substrates, and incubated at 37 °C, 5% CO<sub>2</sub> in Neurobasal medium (Invitrogen) added with B-27 supplement (Thermo Fisher) and GlutaMAX (Thermo Fisher) both to a 1× final concentration. Gentamicin (Thermo Fisher) was also added to a final concentration of 5 µg/mL to prevent contamination. Cultured cells were grown until 8 – 12 days in vitro (DIV) by renewing half of the medium once in this period.

### **Immunocytochemistry and Fluorescent Microscopy**

Cultures were fixed in 4% formaldehyde, prepared from fresh paraformaldehyde, in PBS 1× and permeabilized for 30 min with 0.3% Triton-X-100 (Carlo Erba) in PBS 1× added with 5% FBS (Gibco) and 4% BSA (Sigma-Aldrich) to prevent non-specific binding of primary antibodies. Samples were subsequently incubated with primary antibodies for 30 min at RT and, after being washed with PBS 1×, with secondary antibodies for 45 minutes. Mounting was performed with anti-fade medium Fluoromount (Sigma-Aldrich) on 1 mm thick microscope glass slides. Neurons were labeled through anti-β-tubulin III primary antibody (1:800, Sigma-Aldrich) and visualized with Alexa 594 anti-rabbit in goat as the secondary antibody (1:800, Invitrogen). Astrocytes were instead stained with mouse anti-GFAP primary antibodies (1:800, Sigma-Aldrich) and visualized with Alexa 488 anti-mouse in goat as the secondary antibody (1:800, Invitrogen). Nuclei were stained with 4',6-diamidino-2-phenylindole (DAPI, 1:800, Invitrogen). To estimate neurons and astrocytes number, images of immunolabeled cultures were acquired using a Leica DM6000 Epifluorescence Microscope, either using 10× or 20× objectives (HC PL Fluotar, 0.30 NA and 0.50 NA, respectively). We collected 8 – 10 fields per culture in two cultures

per series from 4 – 5 different culture series. We manually counted the total number of nuclei in each field and the number of neurons and astrocytes. Image analysis and reconstruction were accomplished using NIS-Elements (Nikon) and ImageJ (NIH) software.

### **Scanning Electron Microscopy**

The interaction between neurons and pillars was qualitatively assessed through scanning electron microscopy (SEM). Images were acquired collecting secondary electrons on a Gemini SUPRA 40 SEM (Carl Zeiss NTS GmbH, Oberkochen, Germany). Primary cultures onto PS-NP and PS-CNT-NP were fixed in with 2% glutaraldehyde dissolved in cacodylate buffer (0.1 M, pH 7.2) in the dark for 1 hour at room temperature. After fixation, samples were carefully rinsed with cacodylate buffer; the dehydration process followed by dipping the sample in water/ethanol solutions at progressively higher alcohol concentrations (50%, 75%, 95%, and 100% ethanol for 3 minutes each). Samples were left to dry overnight at 4 °C temperature in the dark. Before SEM imaging, samples were metalized in a metal sputter coater (Polaron SC7620). Cells were visualized at low accelerating voltages (1 – 2 keV) to prevent electron-induced surface charging.

### **Calcium Imaging**

Hippocampal dissociated cultures were loaded with cell-permeable Ca<sup>2+</sup> dye Oregon Green 488 BAPTA-1-AM (Molecular Probes); 10 µL DMSO (Sigma-Aldrich) was added to the stock 50 µg of the dye, and cultures were incubated with a final concentration of 4 µM for 30 min at 37 °C, 5% CO<sub>2</sub>. Samples were therefore placed in a recording chamber mounted on an inverted microscope (Nikon Eclipse Ti-U). Cultures were continuously perfused at 5 mL/min rate and room temperature (RT) with an extracellular saline solution of composition (mM): 150 NaCl, 4 KCl, 2 CaCl<sub>2</sub>, 1 MgCl<sub>2</sub>, 10 HEPES, 10 glucose (pH adjusted to 7.4 with NaOH; osmolarity about 300 mOsm). Ca<sup>2+</sup>-dye was excited at 488 nm with a mercury lamp; excitation light was attenuated using an ND filter (1/32) and separated

from the light emitted from the sample using a 505 nm dichroic mirror. Oregon loaded cultures were observed with a 20× objective (PlanFluor, 0.45 NA), and images were continuously acquired (exposure time 150 ms) using an ORCA-Flash4.0 V2 sCMOS camera (Hamamatsu). The imaging system was controlled by an integrated acquisition software (HImage Live), and the camera was set to operate on 2048 x 2048 pixels<sup>2</sup> at binning 4. Cultures were accustomed to extracellular solution for about 10 minutes. Spontaneous activity was, therefore, recorded for 10 minutes. 10 μM bicuculline (GABA<sub>A</sub> antagonist; Sigma-Aldrich) was subsequently perfused for 20 minutes to weaken the synaptic inhibition and increase the synchronization. Finally, 1 μM TTX (a voltage-gated, fast Na<sup>+</sup> channel blocker; Latoxan) was added to confirm the recorded signals' neuronal nature. We recorded 1 field from each sample, and 15 ± 2 cells from each recording were selected by drawing regions of interest (ROIs) around cell bodies (n = 9 cultures from 5 different series). Images were analyzed with ImageJ software (NIH), and the corresponding traces were studied with Clampfit software (pClamp suite, 10.4 version; Axon Instruments) in off-line mode and with MATLAB (MathWorks, Inc.). We computed the difference between consecutive peaks onset times, to obtain the inter-event interval (IEI). Intracellular Ca<sup>2+</sup> transients were expressed as fractional amplitude increase ( $\Delta F/F_0$ , where  $F_0$  is the baseline fluorescence level and  $\Delta F$  is the rise over baseline); we determined the onset time of neuronal activation by detecting those events in the fluorescence signal that exceeded at least five times the standard deviation of the noise.<sup>[33]</sup> Cross-correlation analysis was performed following the methodology described in S. Usmani et al., 2016.<sup>[47]</sup>

### **Electrophysiology**

Patch-clamp, whole-cell, recordings were achieved with glass micropipettes with a resistance of 4 to 7 MΩ. The patch micropipette was filled with intracellular solution containing: 120 mM K-gluconate, 20 mM KCl, 10 mM HEPES, 10 mM EGTA, 2 mM MgCl<sub>2</sub>, 2 mM Na<sub>2</sub>ATP, pH 7.3. Cultures were positioned in a custom-made chamber mounted on



an inverted microscope (Eclipse TE-200, Nikon, Japan) and continuously superfused with the extracellular solution as in *Calcium imaging* experiments. Cells were voltage-clamped at a holding potential of -56 mV (not corrected for liquid junction potential, calculated to be -13.7 mV at 20 °C in our experimental conditions), and spontaneous post-synaptic currents (PSCs) were recorded. Miniature post-synaptic currents (mPSCs) were recorded in the presence of the fast voltage-gated Na<sup>+</sup> channels blocker Tetrodotoxin (TTX 1 μM; Latoxan). Data were collected at a sampling rate of 10 kHz using a Multiclamp 700A patch amplifier (Axon CNS, Molecular Devices LLC, US) connected to a PC through a Digidata 1440 (Molecular Devices LLC, US). Input resistance and cell capacitance were measured offline using Clampfit 10.4 software suite (Molecular Devices LLC, US), while spontaneous and miniatures PSCs were analyzed in Axograph (Axograph Scientific).

### **Synapse Immunolabeling, Spectral Imaging and 3D analysis**

After fixation in 4% formaldehyde, prepared from fresh paraformaldehyde, dissociated hippocampal cultures were incubated for 10 min with 0.1 M glycine in PBS 1× to mask free aldehyde groups, thus preventing unspecific antibodies binding. Permeabilization was performed as described above (see *Immunocytochemistry and Fluorescent Microscopy*). Samples were subsequently incubated with primary antibodies for 30 min at 37 °C, 5% CO<sub>2</sub>, 95% relative humidity (RH), and after being washed with PBS 1×, with secondary antibodies for 45 minutes. Mounting was performed with anti-fade medium Fluoromount (Sigma-Aldrich) on 0.17 μm thick microscope glass slides. Neurons were stained through anti-β-tubulin III primary antibody (1:800, Sigma-Aldrich) and visualized with Alexa 594 anti-rabbit in goat as the secondary antibody (1:800, Invitrogen). Synapses were instead labeled with mouse anti-Bassoon/BSN primary monoclonal antibody (1:400, Abcam) and visualized with Alexa 488 anti-mouse in goat as the secondary antibody (1:800, Invitrogen). Nuclei were stained with 4',6-diamidino-2-phenylindole (DAPI, 1:800, Invitrogen). Spectral images (2048×2048 pixels) acquisition in variable bandpass (VB)

mode was carried out with the A1R confocal system mounted on a Nikon Eclipse Ti2 inverted microscope (60× plan apo  $\lambda$  oil, 1.40 NA). The selected bandpass (10 nm steps) for the aforementioned RGB channels were respectively 590 – 610 nm (R), 510 – 530 nm (G), and 450 – 470 nm (B). Line averaged scans ( $\emptyset \times 2$ ) were used to further increase SNR (signal-to-noise ratio), and 6 – 8 stacks of 700 nm were sufficient to reconstruct neuronal structures and synaptic clusters. 3D image analysis was performed with NIS-Elements AR Analysis software (version 5.20.02, Nikon Instruments); through the 3D object measurement function, it was possible to define a common intensity threshold of 36-bit images for red and green channels. The total volumes corresponding to  $\beta$ -tubulin III<sup>+</sup> and Bassoon<sup>+</sup> structures were evaluated as the sum of connected and contiguous marked objects. The ratio between these volumes allowed us to consistently compare the fraction of neuronal volume occupied by synaptic clusters in cultures grown onto flat *vs.* nanostructured surfaces.

### **Electrical Stimulation**

To perform extracellular stimulation through PS-CNT-NP substrates, we glued a 4 mm × 4 mm square piece of sample on a glass coverslip (16 mm in diameter, 0.22 mm in thickness) with a 1 mm hole drilled at its center, allowing to contact the back of the conductive sample electrically. The sample was mounted using PDMS taking care to avoid that PDMS cover the central part of the sample. The glass slide hole was subsequently filled with a small drop of silver paste (Sigma Aldrich) to assure good conductivity and increase sample robustness (curing time 30 minutes at 60 °C). The PS-CNT-PS sample mounted on the glass slide was subsequently glued on a custom made liquid cell for neuronal extracellular stimulation. The latter was obtained drilling an 8 mm diameter hole in the bottom of a 35 mm PS petri dish (Falcon®).<sup>[38]</sup> To ensure neuronal viability and avoid medium leak during culture the sample assemble was mounted on the petri dish hole using PDMS silicone elastomer (Sylgard® 184 - Dow Corning Co.).<sup>[33]</sup> This assembly offered ease

access for the stimulating electrode to contact in a dry environment the PS-CNT nanopillars from the bottom side (see the sketch in Figure 5A). Cultures were grown for 10 DIV in the same conditions described above (see Experimental Section, Primary Cultures). Cells were loaded with the  $\text{Ca}^{2+}$  dye, and after incubation, the petri dish with the substrate was mounted in a fixed-stage upright microscope (Eclipse FN1, Nikon), and it was used as a perfusion chamber during the experiment (see Experimental Section, Calcium Imaging). Spontaneous calcium transients were recorded with a 20 $\times$  water immersion objective (UMPlanFl, 0.5 NA, Olympus) using an EMCCD camera (iXon Ultra 897, Andor<sup>TM</sup>, Oxford Instruments) controlled by a computer through NIS-Elements D (Nikon). Images were acquired each 150 ms at 10 MHz readouts, compensating the read noise with  $\times 250$  EM gain.

After about 10 minutes of spontaneous activity, the application of the synaptic blockers (all from Sigma-Aldrich) APV 25  $\mu\text{M}$  (NMDA receptor selective antagonist), bicuculline 10  $\mu\text{M}$  (GABA<sub>A</sub> receptor antagonist), and CNQX 10  $\mu\text{M}$  (AMPA/kainate receptor antagonist) completely silenced the network, as previously reported.<sup>[39]</sup> In these conditions, only evoked signals are visible in a  $\text{Ca}^{2+}$  imaging experiment.<sup>[40]</sup> The positive output of an external insulated stimuli generator (Digitimer DS2A) was connected to a stimulating platinum wire contacting the PS-CNT-NP substrate from its bottom side. In contrast, the negative output was plugged into an Ag/AgCl pellet electrode submerged in the extracellular saline solution (Figure 5A). We therefore manually triggered the voltage pulse train through the isolated stimulator, tuning stimuli according to literature guidelines.<sup>[36,48]</sup> Analysis was accomplished with ImageJ software (NIH) and Clampfit software (pClamp suite, 10.4 version; Axon Instruments) in off-line mode.

### **Organotypic Slice Cultures**

Spinal cord slices were obtained from embryos at 12 – 13 days of gestation (E12 – E13) from a pregnant female mouse (C57Bl/6), as previously reported.<sup>[49]</sup> All procedures were

approved by the local veterinary authorities and performed in accordance with the Italian law (decree 26/14) and the UE guidelines (2007/526/CE and 2010/63/UE). The animal use was approved by the Italian Ministry of Health (22DABN1WO). All efforts were made to minimize suffering and to reduce the number of animals used. Pregnant mice were sacrificed by CO<sub>2</sub> overdose and beheading; fetuses were finally extracted by cesarean section. The spinal cord's thoracolumbar portion was explanted and cut into transversal slices (275 µm) with a tissue chopper (McIlwain TC752, Campden Instruments Ltd.). Slices were dissected from the surrounding tissue and plated either onto glass coverslips or the tested materials (PS-NP and PS-CNT-NP) by clotting 15 µL of chicken plasma with 23 µL of thrombin (both from Sigma-Aldrich). Organotypic Spinal Cords were therefore grown with 1 mL medium containing 66% DMEM 1× (Gibco), 8% sterile water for tissue culture, 25% fetal bovine serum (Gibco), 1% antibiotic-antimycotic (Gibco), 2% B-27 supplement (Gibco) and 20 ng/mL nerve growth factor (NGF, Alomone Laboratories); 300 mOsm; pH 7.35. Cultures were kept in a roller drum (120 revs/min, at 37 °C and 5% CO<sub>2</sub>) for about 14 – 21 days in vitro (DIV).<sup>[56]</sup> After 7 DIV, culture medium was replaced for 24h by fresh medium containing antimetabolites (10 µM ARA-C/Uridine/5-Fl-dU) and reduced NGF concentration (5 ng/mL). At DIV 8, fresh medium with reduced NGF was added and refreshed every 7 days.

### **Organotypic Culture Immunofluorescence and Confocal Microscopy**

Organotypic slices were fixed in 4% formaldehyde, prepared from fresh paraformaldehyde, in PBS 1× for at least 1h. After fixation, slices were incubated for 10 min with 0.1 M glycine in PBS 1× and permeabilized for 1h with 0.3% Triton-X-100 (Carlo Erba) in PBS 1× added with 5% FBS (Gibco) and 4% BSA (Sigma-Aldrich) to prevent non-specific binding of primary antibodies. Samples were subsequently incubated with primary antibodies overnight at 4 °C and with the secondary antibodies for 2h at RT (three washes in PBS 1× preceded each step). Mounting was performed with anti-fade medium Fluoromount

(Sigma-Aldrich) on 1 mm thick microscope glass slides. All neurons were labeled through anti- $\beta$ -tubulin III primary antibody (1:800, Sigma-Aldrich) and visualized with Alexa 594 anti-rabbit in goat as the secondary antibody (1:800, Invitrogen). Exclusive staining of motoneurons was instead achieved with anti-neurofilament H (SMI-32, 1:800, Biolegend) recognized by Alexa 488 anti-mouse in goat as the secondary antibody (1:800, Invitrogen). Nuclei were stained with 4',6-diamidino-2-phenylindole (DAPI, 1:500, Invitrogen). A Nikon Eclipse Ti2 inverted microscope connected to an A1R confocal system (Nikon Instruments) was used to acquire stitched images (10 $\times$  Plan Apo  $\lambda$ , 0.45 NA) to obtain a morphological insight of the stained spinal cord slice cultures.

### **Spinal Cord Calcium Imaging**

Organotypic spinal cord samples, grown in vitro for 2 – 3 weeks, were loaded with cell-permeable  $\text{Ca}^{2+}$  dye Fluo-4 AM (Molecular Probes); 11.6  $\mu\text{L}$  of DMSO (Sigma-Aldrich) was added to the stock 50  $\mu\text{g}$  of the dye, and cultures were incubated with a final concentration of 4  $\mu\text{M}$  for 1h in the roller drum at 37  $^{\circ}\text{C}$ , 5%  $\text{CO}_2$ . After dye loading, a de-esterification period followed, cultures were maintained in extracellular saline solution (described above) in the same incubator for 30 min. Samples were mounted on the previously described inverted microscope (Nikon Eclipse Ti-U). The dye was excited at 488 nm, and the emission was detected at 520 nm. Cultures were continuously perfused with extracellular saline solution, and neurons at the premotor region in the slice's ventral zone were observed with a 40 $\times$  objective (PlanFluor, 0.60 NA). Images were acquired every 150 ms using the ORCA-Flash4.0 V2 sCMOS camera (Hamamatsu) operating at binning 4. After cultures accustomed to the extracellular solution, spontaneous activity was recorded for 10 minutes. 25  $\mu\text{M}$  bicuculline (GABA<sub>A</sub> antagonist; Sigma-Aldrich) and 2  $\mu\text{M}$  strychnine (glycine receptor antagonist; Sigma-Aldrich) were subsequently perfused for 20 minutes to weaken the synaptic inhibition and increase the synchronization. Finally, 1  $\mu\text{M}$  TTX (a voltage-gated, fast  $\text{Na}^+$  channel blocker; Latoxan) was added to confirm the



recorded signals' neuronal nature. Images were analyzed with ImageJ software (NIH), and the corresponding traces were extracted with Clampfit software (pClamp suite, 10.4 version; Axon Instruments) in off-line.

### **Statistical Analysis**

Statistical analysis was accomplished using Prism 6 software (GraphPad): datasets normality was addressed with D'Agostino and Pearson omnibus normality test. Non-parametric tests were used in both non-normally distributed data and unequal variances among tested data sets. Accordingly, statistics between two independent samples were performed with t-test or Mann-Whitney U test. In contrast, three independent samples differences were tested with either one-way ANOVA adjusted for multiple comparisons with Tukey's correction or Kruskal-Wallis test adjusted with Dunn's multiple comparison test. All data are plotted as median with their 25<sup>th</sup> (1<sup>st</sup> quartile, Q<sub>1</sub>) and 75<sup>th</sup> (3<sup>rd</sup> quartile, Q<sub>3</sub>) percentiles, with whiskers representing 10<sup>th</sup> and 90<sup>th</sup> percentiles. Descriptive statistics used in the text express the central tendency as mean  $\pm$  SD for normal distributions and median for non-normal distributions.

### **Acknowledgements**

This work was performed within the framework of the ByAXON project funded by the European Union's Horizon 2020 FET Open program under grant agreement No. 737116.

The work was partially funded by the Spanish Ministry of Science and Innovation through project BiSURE (Grant: DPI2017-90058-R) and the 'Severo Ochoa' Programme for Centres of Excellence in R&D (MINECO, Grant SEV-2016-0686). D. Scaini acknowledges the support of the European Union's Horizon 2020 research and innovation program under the Marie Skłodowska-Curie grant agreement no. 838902. M. A. Monclús, and J. M. Molina-Aldareguia from IMDEA Materials are acknowledged for the nanoindentation testing.

## References

- [1] D. Scaini, L. Ballerini, *Curr. Opin. Neurobiol.* **2018**, *50*, 50.
- [2] T. Dvir, B. P. Timko, D. S. Kohane, R. Langer, *Nat. Nanotechnol.* **2011**, *6*, 13.
- [3] S. G. Higgins, M. Becce, A. Belessiotis-Richards, H. Seong, J. E. Sero, M. M. Stevens, *Adv. Mater.* **2020**, *32*, 1.
- [4] W. Kim, J. K. Ng, M. E. Kunitake, B. R. Conklin, P. Yang, *J. Am. Chem. Soc.* **2007**, *129*, 7228.
- [5] F. Viela, D. Granados, A. Ayuso-Sacido, I. Rodríguez, *Adv. Funct. Mater.* **2016**.
- [6] C. Xie, L. Hanson, W. Xie, Z. Lin, B. Cui, Y. Cui, *Nano Lett.* **2010**, *10*, 4020.
- [7] L. Micholt, A. Gärtner, D. Prodanov, D. Braeken, C. G. Dotti, C. Bartic, *PLoS One* **2013**, *8*, e66170.
- [8] J. Seo, J. Kim, S. Joo, J. Y. Choi, K. Kang, W. K. Cho, I. S. Choi, *Small* **2018**, *14*, 1801763.
- [9] C. J. Bettinger, R. Langer, J. T. Borenstein, *Angew. Chemie - Int. Ed.* **2009**, *48*, 5406.
- [10] A. T. Nguyen, S. R. Sathe, E. K. F. Yim, *J. Phys. Condens. Matter* **2016**, *28*, 183001.
- [11] M. Marcus, K. Baranes, M. Park, I. S. Choi, K. Kang, O. Shefi, *Adv. Healthc. Mater.* **2017**, *6*.
- [12] V. Gautam, S. Naureen, N. Shahid, Q. Gao, Y. Wang, D. Nisbet, C. Jagadish, V. R. Daria, *Nano Lett.* **2017**.
- [13] J. T. Robinson, M. Jorgolli, A. K. Shalek, M. H. Yoon, R. S. Gertner, H. Park, *Nat. Nanotechnol.* **2012**.
- [14] K. Kang, Y.-S. Park, M. Park, M. J. Jang, S.-M. Kim, J. Lee, J. Y. Choi, D. H. Jung, Y.-T. Chang, M.-H. Yoon, J. S. Lee, Y. Nam, I. S. Choi, *Nano Lett.* **2016**, *16*, 675.
- [15] K. Tybrandt, D. Khodagholy, B. Dielacher, F. Stauffer, A. F. Renz, G. Buzsáki, J. Vörös, *Adv. Mater.* **2018**.

- [16] C. Nick, S. Quednau, R. Sarwar, H. F. Schlaak, C. Thielemann, *Microsyst. Technol.* **2014**, *20*, 1849.
- [17] J. W. Salatino, K. A. Ludwig, T. D. Y. Kozai, E. K. Purcell, *Nat. Biomed. Eng.* **2017**, *1*, 862.
- [18] C. Vallejo-Giraldo, K. Krukiewicz, I. Calaresu, J. Zhu, M. Palma, M. Fernandez-Yague, B. McDowell, N. Peixoto, N. Farid, G. O'Connor, L. Ballerini, A. Pandit, M. J. P. Biggs, *Small* **2018**, *14*, 1800863.
- [19] J. J. Hernández, M. A. Monclús, I. Navarro-Baena, F. Viela, J. M. Molina-Aldareguia, I. Rodríguez, *Sci. Rep.* **2017**.
- [20] A. Mazzatenta, M. Giugliano, S. Campidelli, L. Gambazzi, L. Businaro, H. Markram, M. Prato, L. Ballerini, *J. Neurosci.* **2007**, *27*, 6931.
- [21] V. Lovat, D. Pantarotto, L. Lagostena, B. Cacciari, M. Grandolfo, M. Righi, G. Spalluto, M. Prato, L. Ballerini, *Nano Lett.* **2005**, *5*.
- [22] W. J. Polacheck, C. S. Chen, *Nat. Methods* **2016**, *13*, 415.
- [23] J. Lantoine, T. Grevesse, A. Villers, G. Delhaye, C. Mestdagh, M. Versaevel, D. Mohammed, C. Bruyère, L. Alaimo, S. P. Lacour, L. Ris, S. Gabriele, *Biomaterials* **2016**, *89*, 14.
- [24] D. M. Suter, K. E. Miller, *Prog. Neurobiol.* **2011**, *94*, 91.
- [25] M. Chighizola, T. Dini, C. Lenardi, P. Milani, A. Podestà, C. Schulte, *Biophys. Rev.* **2019**, *11*, 701.
- [26] S. M. Kim, S. Lee, D. Kim, D. H. Kang, K. Yang, S. W. Cho, J. S. Lee, I. S. Choi, K. Kang, M. H. Yoon, *Nano Res.* **2018**, *11*, 2532.
- [27] C. A. R. Chapman, H. Chen, M. Stamou, J. Biener, M. M. Biener, P. J. Lein, E. Seker, *ACS Appl. Mater. Interfaces* **2015**, *7*, 7093.
- [28] A. E. Hampe, Z. Li, S. Sethi, P. J. Lein, E. Seker, *Nanomaterials* **2018**, *8*, 1.
- [29] P. Moshayedi, G. Ng, J. C. F. Kwok, G. S. H. Yeo, C. E. Bryant, J. W. Fawcett, K.

- Franze, J. Guck, *Biomaterials* **2014**, *35*, 3919.
- [30] M. J. P. Biggs, R. G. Richards, M. J. Dalby, *Nanomedicine Nanotechnology, Biol. Med.* **2010**, *6*, 619.
- [31] N. P. Pampaloni, D. Scaini, F. Perissinotto, S. Bosi, M. Prato, L. Ballerini, N. Paolo, D. Scaini, F. Perissinotto, S. Bosi, M. Prato, L. Ballerini, *Nanomedicine Nanotechnology, Biol. Med.* **2018**, *14*, 2521.
- [32] M. Giugliano, P. Darbon, M. Arsiero, H. R. Lüscher, J. Streit, *J. Neurophysiol.* **2004**, *92*, 977.
- [33] S. Bosi, R. Rauti, J. Laishram, A. Turco, D. Lonardoni, T. Nieuw, M. Prato, D. Scaini, L. Ballerini, *Sci. Rep.* **2015**, *5*, 9562.
- [34] N. P. Pampaloni, M. Lottner, M. Giugliano, A. Matruggio, F. D'Amico, M. Prato, J. A. Garrido, L. Ballerini, D. Scaini, *Nat. Nanotechnol.* **2018**, *13*, 755.
- [35] K. D. Micheva, B. Busse, N. C. Weiler, N. O'Rourke, S. J. Smith, *Neuron* **2010**.
- [36] D. R. Merrill, M. Bikson, J. G. R. R. Jefferys, *J. Neurosci. Methods* **2005**, *141*, 171.
- [37] I. Rago, R. Rauti, M. Bevilacqua, I. Calaresu, A. Pozzato, M. Cibinel, M. Dalmiglio, C. Tavagnacco, A. Goldoni, D. Scaini, *Adv. Biosyst.* **2019**.
- [38] A. Domínguez-Bajo, B. L. Rodilla, I. Calaresu, A. Arché-Núñez, A. González-Mayorga, D. Scaini, L. Pérez, J. Camarero, R. Miranda, E. López-Dolado, M. T. González, L. Ballerini, M. C. Serrano, *Adv. Biosyst.* **2020**, *4*, 2000117.
- [39] I. Breskin, J. Soriano, E. Moses, T. Tlusty, *Phys. Rev. Lett.* **2006**, *97*.
- [40] S. Stern, A. Agudelo-Toro, A. Rotem, E. Moses, A. Neef, *PLoS One* **2015**, *10*.
- [41] D. Avossa, M. D. Rosato-Siri, F. Mazzarol, L. Ballerini, *Neuroscience* **2003**.
- [42] S. Sibilla, A. Fabbro, M. Grandolfo, P. D'Andrea, A. Nistri, L. Ballerini, *Eur. J. Neurosci.* **2009**, *29*, 1543.
- [43] M. Galante, A. Nistri, L. Ballerini, *J. Physiol.* **2000**, *523*, 639.
- [44] M. Grumet, G. M. Edelman, *J. Cell Biol.* **1988**.



- [45] V. Onesto, L. Cancedda, M. L. Coluccio, M. Nanni, M. Pesce, N. Malara, M. Cesarelli, E. DI Fabrizio, F. Amato, F. Gentile, *Sci. Rep.* **2017**, 7, 1.
- [46] S.-H. Park, J. Bae, *Recent Pat. Nanotechnol.* **2017**.
- [47] S. Usmani, E. R. Aurand, M. Medelin, A. Fabbro, D. Scaini, J. Laishram, F. B. Rosselli, A. Ansuini, D. Zoccolan, M. Scarselli, M. De Crescenzi, S. Bosi, M. Prato, L. Ballerini, *Sci. Adv.* **2016**, 2.
- [48] M. A. Meza-Cuevas, *Simulation of Neurons by Electrical Means*; Wolfgang Krautschneider, Ed.; Logos Verlag Berlin, **2015**.
- [49] A. Fabbro, A. Villari, J. Laishram, D. Scaini, F. M. Toma, A. Turco, M. Prato, L. Ballerini, *ACS Nano* **2012**, 6, 2041.

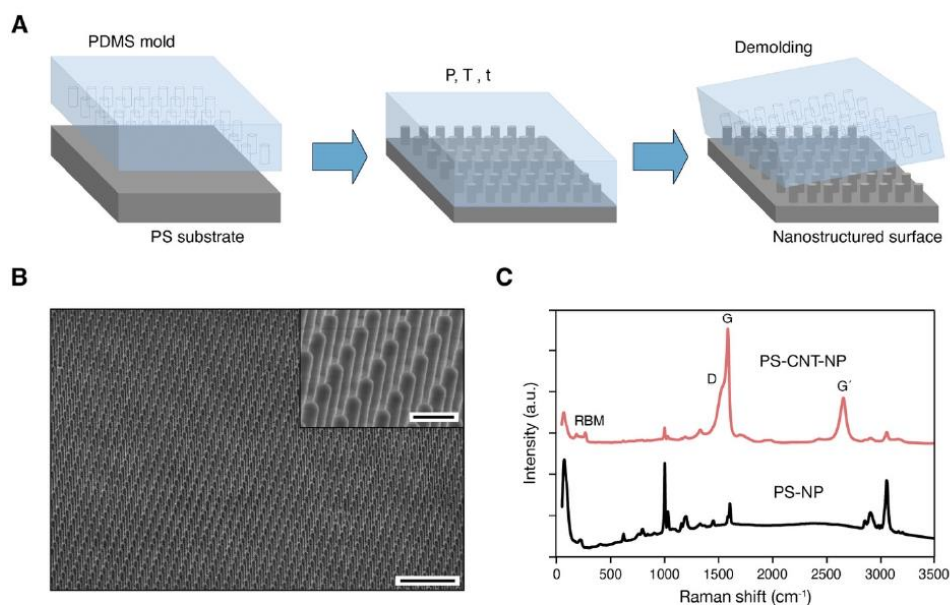


**Figure 1.** Fabrication and characterization of substrates patterned with polystyrene nanopillars (PS-NPs) and polystyrene-SWCNT nanopillars (PS-CNT-NP). A) Outline of the fabrication process of high aspect ratio nanometric pillar topography by nanoimprinting lithography. B) SEM images of a PS-CNT-NP imprinted substrate highlighting long-distance order and anisotropic square pillar arrangement. Image scale bar = 5  $\mu\text{m}$ ; inset scale bar = 1  $\mu\text{m}$ . C) Raman spectra obtained from both PS-NP, and PS-CNT-NP topographies. The carbon nanotubes' characteristic D, G and G' peaks are visible in the PS-CNT-NP sample.

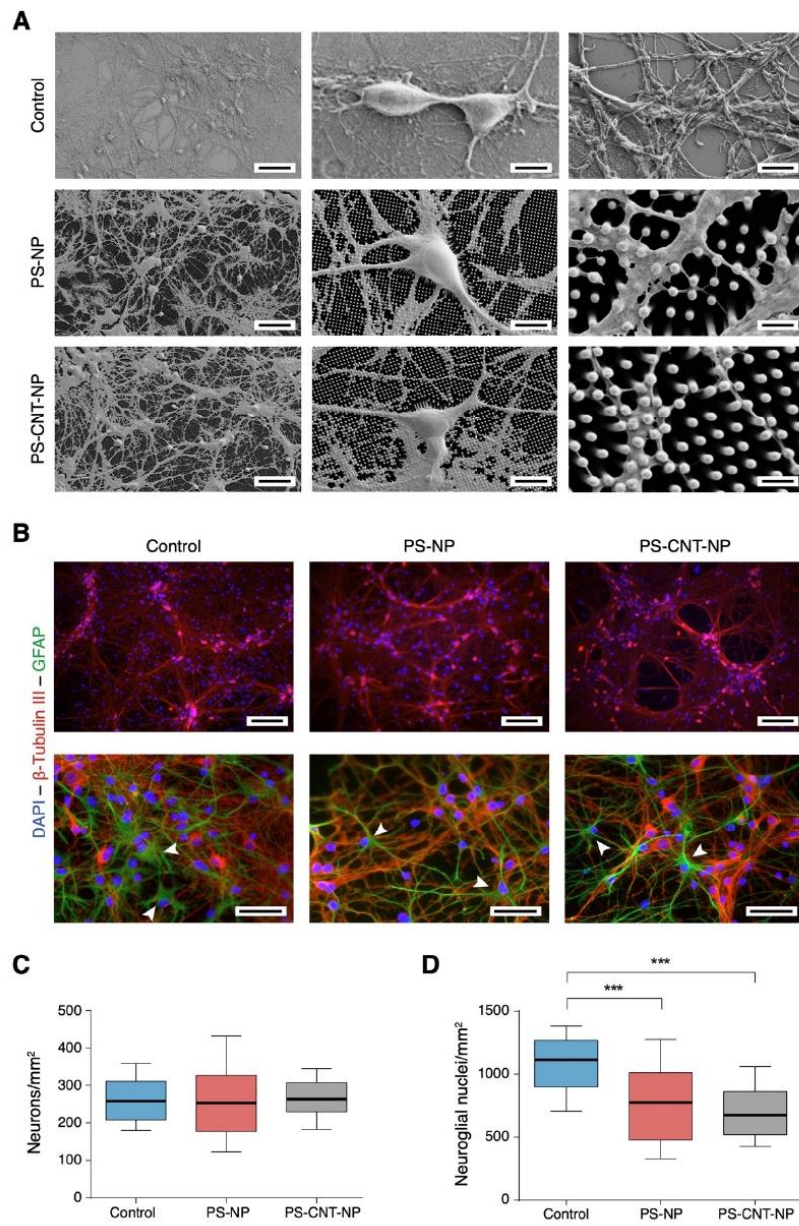


**Figure 2.** Morphology and cellular composition of hippocampal-cells networks developed on poly-L-ornithine coated glass (Control), polystyrene nanopillars (PS-NP), and polystyrene-SWCNT nanopillars (PS-CNT-NP). A) Scanning Electron Microscopy (SEM)

images of dissociated hippocampal cultures grown (9 DIV) onto Control, PS-NP and PS-CNT-NP are shown at three increasing magnifications. Scale bars = 40  $\mu\text{m}$ , 10  $\mu\text{m}$ , and 2  $\mu\text{m}$  from left to right. B) Epifluorescence micrographs of immune-labeled cultures for the three conditions. Neuronal cells are visualized, in the top images, by anti  $\beta$ -tubulin III antibody (red), while all cellular nuclei were pointed out by DAPI staining (blue). Scale bar = 100  $\mu\text{m}$ . On the bottom, enlarged representative fields showing neurons in red (anti  $\beta$ -tubulin III), astrocytes in green (anti-GFAP), and nuclei in blue (DAPI). Scale bar = 50  $\mu\text{m}$ . C) Box plot summarizing neuronal densities for the three conditions. D) A box plot showing the densities of neuroglial cell nuclei (evaluated as the whole non-neuronal sub-population of cells in the samples; \*\*\* $p < 0.001$ ).

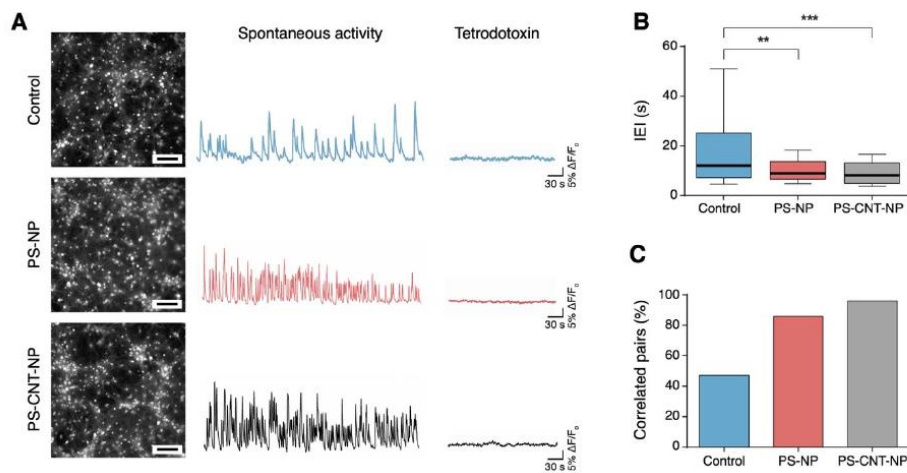


**Figure 3.** Calcium imaging experiments were used to monitor spontaneous network activity onto Control, PS-NP, and PS-CNT-NP samples. A) Snapshots of 3 representative fields of hippocampal dissociated cultures labeled with Oregon Green 488-BAPTA-1 AM. Scale bar = 100  $\mu\text{m}$ . Active cells were manually selected as regions of interest (ROI) from which calcium variations were evaluated. Representative traces for each condition are shown (central traces). Tetrodotoxin was used at the end of each recording to assess the neuronal nature of the signals (right traces). Calcium transients are expressed as fractional amplitude increase ( $\Delta F/F_0$ ). B) Cells grown onto nanopillars exhibited enhanced spontaneous activity depending on substrate topography (\*\* $p < 0.01$ ). C) In the bar chart, the percentages of correlated cell pairs were plotted for each condition. Bars represent the percentage of significantly correlated pairs over the total amount of cells pairs analyzed. Calcium events correlation raised from 46% in Control cultures to 86% and 96% in nanopillars cultures (PS-NP and PS-CNT-NP, respectively).



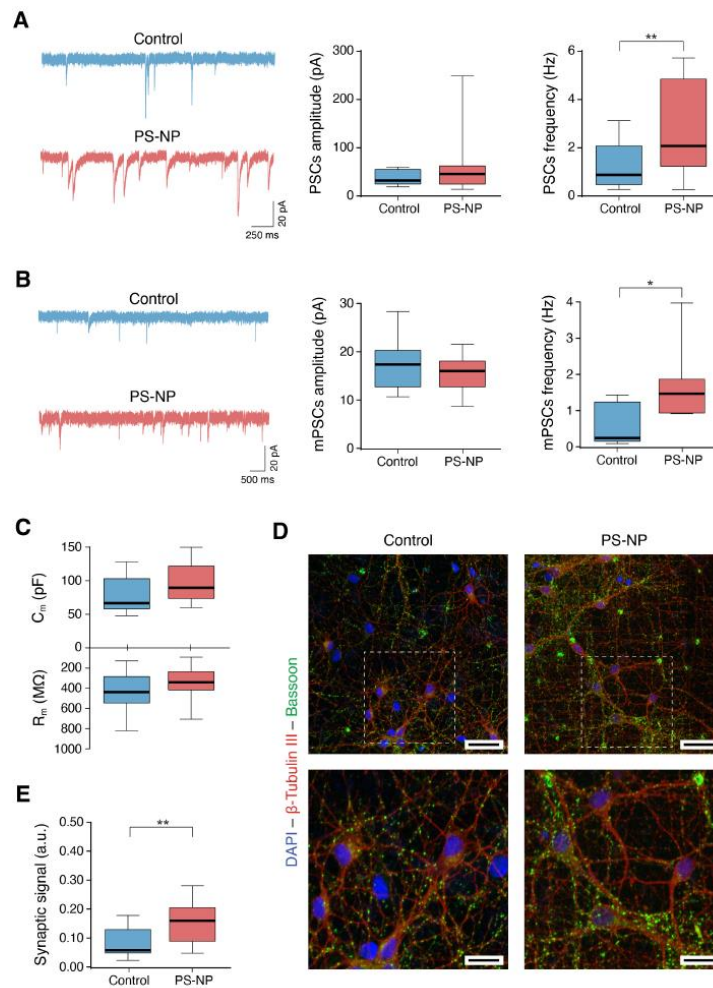


**Figure 4.** Synaptic modifications of nanopillars-interfaced neurons. A) Representative spontaneous post-synaptic currents (PSCs) tracings of patch-clamped neurons onto Control and PS-NP are shown together with the corresponding plots of spontaneous PSCs amplitude (left) and frequency (right). Comparably to what was observed during calcium imaging experiments, spontaneous synaptic activity was boosted by PS-NP (\*\* $p < 0.01$ ). B) Representative tracings of miniature post-synaptic currents (mPSCs) recorded in the presence of 1  $\mu$ M TTX are provided with their amplitude and frequency plots (left and right respectively). Note the increased miniature currents frequency of PS-NP neurons

35

(\* $p < 0.05$ ). C) Passive membrane properties of neurons were comparable in control poly-L-ornithine coated glass and polystyrene nanopillars (PS-NP). D) Confocal Z-projection of fluorescent micrographs at two increasing magnifications were reconstructed to show synapse-labeled cultures grown onto Control and PS-NP. Increased synaptic clustering onto PS-NP can be observed by the greater Bassoon (green) reactivity, while neuronal cells are visualized by anti  $\beta$ -tubulin III antibody (red), nuclei are marked with the classical DAPI staining (blue). Scale bar = 25 and 10  $\mu\text{m}$ . E) The box plot showing the fraction of neuronal volume occupied by synaptic clusters summarizes such an observation (\*\* $p = 0.0015$ ).

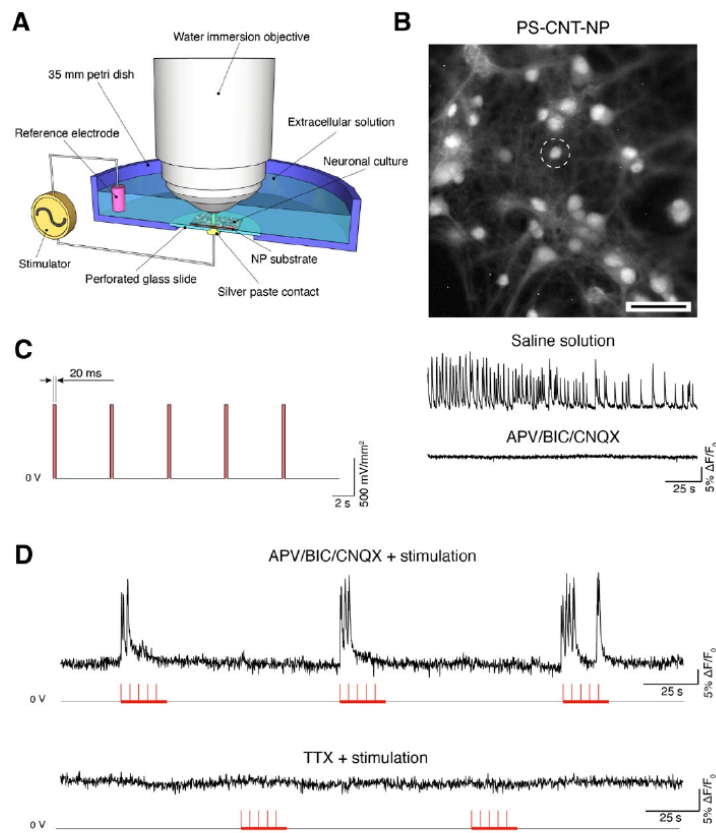


**Figure 5.** Electrical stimulation from conductive PS-CNT nanopillars composite. A) A sketch of the experimental setting used to electrically stimulate neuronal tissues through our PS-CNT-NP substrates is depicted. B) A snapshot of a representative field of hippocampal dissociated cultures grown onto PS-CNT-NP and labeled with Oregon Green 488-BAPTA-1-AM (Scale bar = 50  $\mu\text{m}$ ). Typical recordings of spontaneous synaptic activity monitored via live calcium imaging are shown below in the case of saline solution perfusion (top trace), and in the presence of the APV/BIC/CNQX silencing cocktail (bottom trace). C) Schematic of the stimulation protocol used: it consists of three stimulation trains (0.01 Hz) of 5 voltage steps (1  $\text{V}/\text{mm}^2$  and 20 ms in amplitude and duration, at 0.2 Hz). D) A representative trace showing the neuronal response in the

presence of a cocktail of synaptic blockers: in this condition, the network is silenced, and only evoked activity could be visible (top trace). The red lines correspond to the 25 seconds-long pulse trains; the concurrent strong and transient increases in the  $\text{Ca}^{2+}$  dye fluorescence is noticeable. Such responses were entirely abolished by tetrodotoxin administration (bottom trace), thus confirming the neuronal nature of the detected signals, and indicating that evoked action potentials triggered such a rise in  $\text{Ca}^{2+}$ . Calcium transients are expressed as fractional amplitude increase ( $\Delta F/F_0$ ).

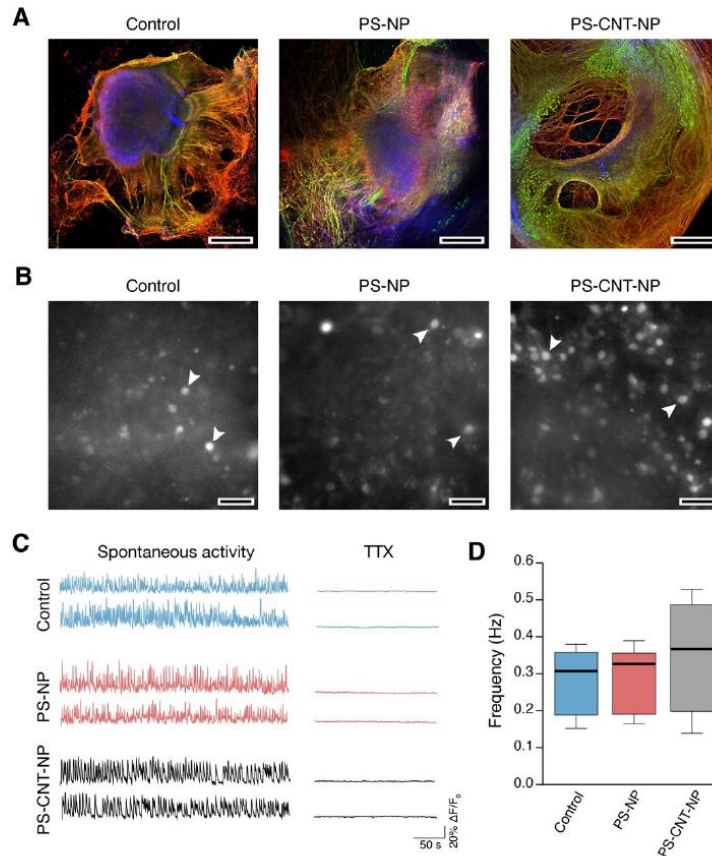


**Figure 6.** Organotypic spinal cord slices development onto polymeric nanopillars. A) Three low-magnification confocal stitching of transversal spinal cord slices grown for 21 DIV are depicted. Neurons are visualized with an anti  $\beta$ -tubulin III antibody (red), specific motoneuron labeling is achieved with SMI-32 (green), while cell nuclei are targeted by DAPI staining (blue). Scale bar = 500  $\mu$ m. B) Representative snapshots of the ventral regions relative to the three substrates after spinal cord slices were loaded with the  $\text{Ca}^{2+}$ -dye Fluo-4 AM. Scale bar = 50  $\mu$ m. C) Two representative traces (from the highlighted couple of neurons in panel B) of the recorded motoneuronal spontaneous activity are given for every condition (left traces). Tetrodotoxin was used at the end of each recording to



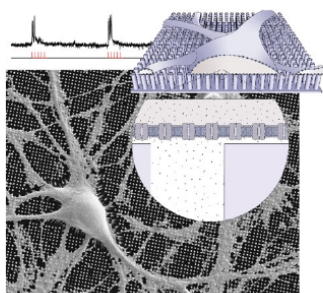
assess the neuronal nature of the signals (right traces). Calcium transients are expressed as fractional amplitude increase ( $\Delta F/F_0$ ). D) The boxplot summarizes calcium spikes frequency (Hz) during spontaneous motoneurons activity.

The ability to improve devices affinity for cellular tissues plays a crucial role in bioengineering and biosensing. We interface neuronal cells and spinal cord explants to surfaces decorated with nanostructures able to reduce neuroglia proliferation and boost neuronal activity. Our carbon-modified nanostructures enable synaptic modulation and stimulation in interfaced neuronal networks, opening to future implementation on neuro-prosthetic or neurostimulation devices.

### **Biomimetics**

Ivo Calaresu, Jaime Hernandez, Rossana Rauti, Beatriz L. Rodilla, Ana Arché-Núñez, Lucas Perez, Julio Camarero, Rodolfo Miranda, M. Teresa González\*, Isabel Rodríguez\*, Denis Scaini \* and Laura Ballerini\*

### **Polystyrene nanopillars with inbuilt carbon nanotubes enable synaptic modulation and stimulation in interfaced neuronal networks**



## Supporting Information

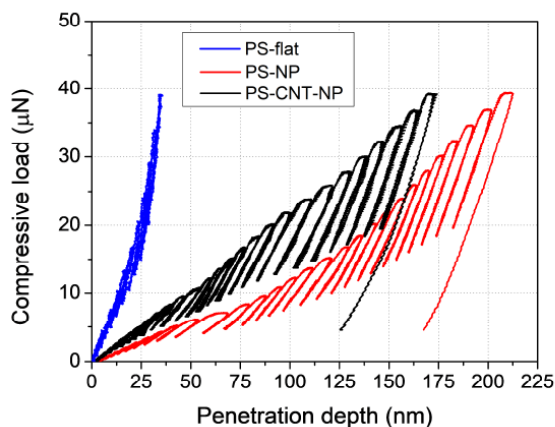


**Figure S1.** Representative nanoindentation loading-unloading profiles for a monotonically increasing nanoindentation load up to a maximum of 40  $\mu\text{N}$  for pristine PS (blue trace), PS-NP (red trace), and PS-CNT-NP reinforced topographies (black trace).

The graph shows that, for an equivalent applied compressive load, the penetration depth observable on the flat PS surface is smaller than on substrates patterned with high aspect ratio pillars. The probe deeply penetrated within the PS-NP substrate, with just a slight reduction on the PS-CNT-NP topography, when the NPs are reinforced with SWCNT.

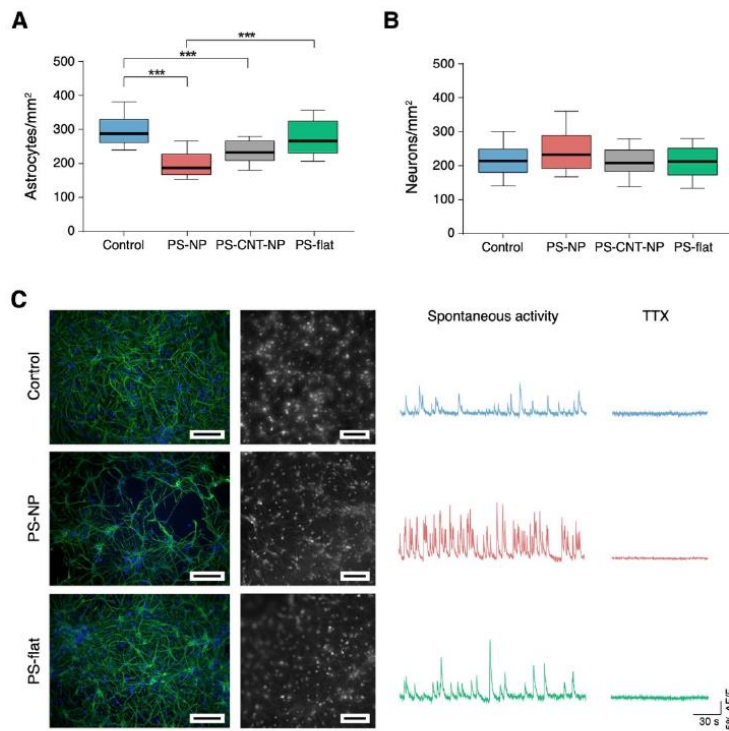


**Figure S2.** Glial cells adhesion changes according to substrate topography but not to its chemistry. A) Boxplot summarizing the diminished ( $***p < 0.001$ ) astroglia density onto nanopatterned surfaces (PS-NP and PS-CNT-NP) compared to flat glass (Control) and flat polystyrene (PS-flat). B) Neuronal densities were also evaluated, finding no significant changes among all the four conditions. C) In order to decouple the effects of surface topography and chemistry, astrocytes density and spontaneous network activity were shown for poly-L-ornithine coated glass (Control), polystyrene nanopillars (PS-NP), and flat polystyrene (PS-flat) surfaces. In the first column, representative immunostainings showing GFAP-positive glial cells in green and nuclei in blue (DAPI). In the second column, snapshots of Oregon green-loaded cultures for all tested conditions. At the right, the corresponding  $\text{Ca}^{2+}$  imaging traces of spontaneous activity. Scale bars = 100  $\mu\text{m}$ . The neuronal nature of such activity was confirmed by tetrodotoxin (TTX) administration.

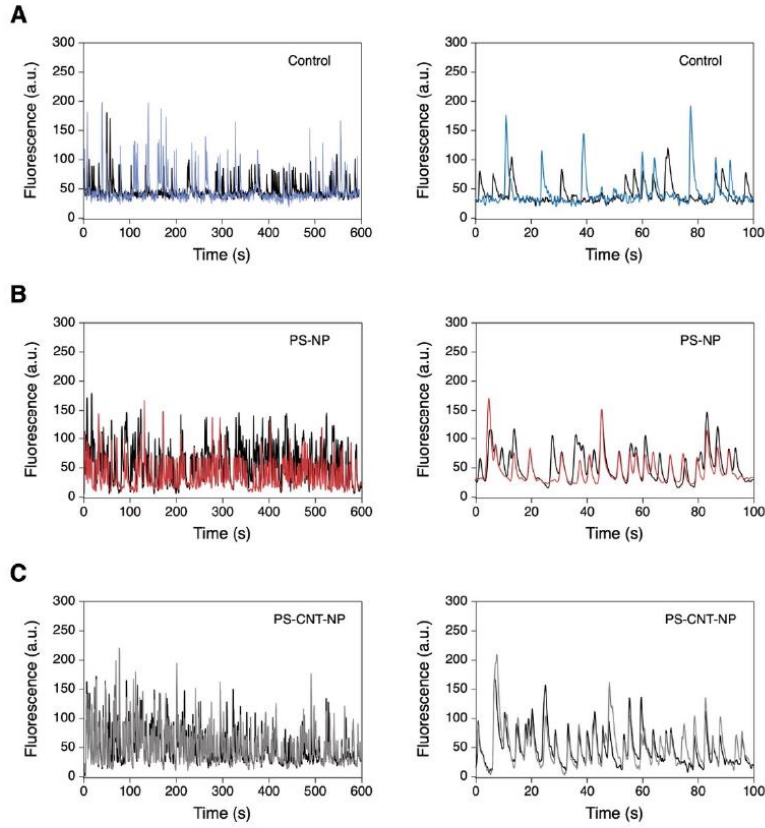


**Figure S3.** Synchronization analysis example. The synchronization analysis was based on a bootstrapping method modified from Ref [41]. With this analysis  $2 \times 10^5$  time windows are generated from each pair of traces and used to obtain a “real CCF (cross-correlation factor)” distribution with its median that is then compared with the distribution of “randomly generated CCFs” obtained by shuffling the  $2 \times 10^5$  time windows. The extent of the area of the “random CCFs” distribution that exceeded the median of the “real CCFs” allowed the calculation of a p-value. Significantly ( $*p < 0.05$ ) correlated pairs were considered synchronized and their count over the total number of cell pairs analyzed was plotted as the percentage of correlated pairs. Red and blue traces for each condition represent the spontaneous synaptic activity of two non-neighboring cells in the same field



of a calcium imaging recording. Left plots provide three snapshots of full traces alignment performed in MATLAB, while the right plots show enlarged views. During spontaneous network activity, calcium events correlation was strongly increased in neuronal networks interfaced with PS-NP and PS-CNT-NP (B and C, respectively) compared to Control samples (A), as shown by traces superposition.

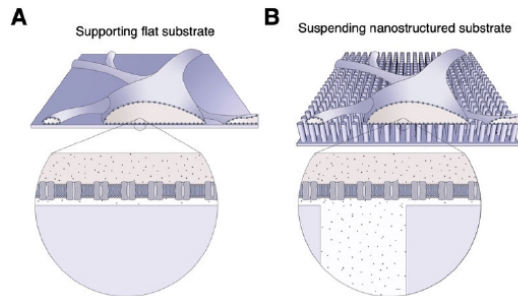


**Figure S4.** Establish quasi-spherical access to the extracellular milieu due to a suspended cellular organization on top of nanopillared surfaces. A) A sketch representative of the condition where a neuronal cell lays on a flat substrate (glass or PS), where the cell could mainly interact with the extracellular milieu through its upper face. The magnified region below highlighted the cell-membrane/substrate interface: here (voltage) channels activity is mainly hindered by the interference of the underneath supporting surface. B) A neuron laying instead on a nanostructured substrate able to confer to it a suspended configuration. Here the cell can interact with the extracellular environment/milieu with the upper face, as in the previous condition, and with a large portion of the inferior face (see magnified image below). This 2  $\mu\text{m}$  thick space below the cell is filled by a two-dimensional square array of cylindrical nanostructure (500 nm in diameter, 1  $\mu\text{m}$  in pitch) and behaves as a bidimensional porous material characterized by a porosity value  $\epsilon$  of about 0.78 ( $\pi \cdot 0.52$ ). The large pores constituting this interpillar space let us suppose that the ionic composition of the extracellular solution here localized is similar to the bulky solution (ion diffusivity  $\sim 2000 \mu\text{m}^2/\text{s}$ ). In particular, in suspended cells, about 80% of the ventral membrane faces the extracellular solution (about 150 mM  $\text{Na}^+$ , 4 mM  $\text{K}^+$  and 2 mM  $\text{Ca}^{2+}$ ), resulting in quasi-spherical cell accessibility when compared to the hemispherical one characterizing the supported cell.

**Real-Time Magnetic Recording of Neuronal Activity is a Suitable Source of Physiological Signals to Entrain Spinal Networks *in Vitro***

Ivo Calaresu<sup>1</sup>, Isidoro Martinez<sup>2</sup>, Arturo Vera<sup>2</sup>, Rubén Guerrero<sup>2</sup>, Denis Scaini<sup>1</sup>, Jaime Hernandez<sup>2</sup>, Isabel Rodriguez<sup>2</sup>, Lucas Perez<sup>2,3</sup>, Julio Camarero<sup>2,4</sup>, Rodolfo Miranda<sup>2,4</sup>, Teresa Gonzalez<sup>2</sup>, Laura Ballerini<sup>1</sup>

<sup>1</sup>International School for Advanced Studies (SISSA), Trieste, Italy

<sup>2</sup>IMDEA Nanociencia, Campus de Cantoblanco, 28049 Madrid, Spain

<sup>3</sup>Normandie Univ, UNICAEN, ENSICAEN, CNRS, GREYC, Caen, France

<sup>4</sup>Dept. Física de Materiales, Universidad Complutense, 28040 Madrid, Spain

## **Abstract**

To record *in vivo* neural signalling originating from action potential activity and synaptic dynamics in the context of complex behaviour has long been a major pursuit in neuroscience in general and in neuroelectronic interfaces, in particular. Interfacing the central nervous system (CNS) is an arduous challenge, but crucial to restore the transmission of electrical signals in the injured CNS. Technological advances in this domain are providing increasingly powerful tools to study, restore, and augment neural functions in health and disease. Conventional electrodes (for direct voltage/current measurements) and emergent optical imaging techniques (using genetically encoded fluorescence indicators/light-gated ion channels) are complementary technologies to monitor neuronal activity *in vivo*, but might be limited by intrinsic physical constraints. Both approaches are characterized by high invasiveness, with, in the case of electrical interfaces, their long-term efficacy limited by tissue reactivity, micromotions and foreign body responses, all drawbacks that might be solved by using appropriate magnetic sensing technologies. Here, we developed and tested the ability of spintronic-based magnetic sensors, designed for room temperature recording in a magnetic shielding-free environment, to detect neuronal activity emerging from spinal explants, namely spinal cord-dorsal root ganglia (SC-DRG) organotypic slices *in vitro*. In particular, we introduce differential measurements, using an improved sensing approach in a gradiometer configuration to record real-time neural activity driven by pharmacological network disinhibition (upon removal of synaptic inhibition by Bicuculline/Strychnine application). In the spinal cord, disinhibited activity is characterized by rhythmic outputs relying on active synaptic networks, abolished by action potential blocker (Tetrodotoxin). The ability to remove spinal activity by tetrodotoxin application was exploited to address the biological origin of the magnetic signals. Live imaging of  $\text{Ca}^{2+}$  dynamics and extracellular field potential electrophysiology were simultaneously

acquired to magnetophysiology and confirmed the real-time insight and the electric origin of the recorded neural activity. These results pave the way towards the development of portable and wearable devices capable of detecting magnetic fields arising from neuronal activity.



## **Introduction**

Spinal cord injury (SCI) treatment has experienced several medical breakthroughs in the last decade, involving different treatments such as stem cell transplantation, engineered materials for tissue support, wearable robotic exoskeletons, functional electrical stimulation (FES) and epidural spinal stimulation (EES).<sup>[1]</sup> In particular, EES has improved the treatment of SCI leading to stunning results.<sup>[2,3]</sup> However, electrical stimulation techniques for SCI usually make use of artificial waveforms to restore functions below the lesion site. The reason for that is linked to the apparent limited source of physiological signals that might be used to trigger stimulating devices. Most of assistive prosthesis are indeed controlled by joysticks, trackpads, switches and eye-tracking tools. To date it is widely agreed that volitional activity can be recorded from brain cortex or muscles, to provide an additional way of controlling neuroprosthesis.<sup>[4]</sup> Yet, it is known that a critical number of neurons within the injured spinal cord survive and current researches are considering the possibility to recruit these spared neuronal population to restore sensory-motor functions in a more physiological manner.<sup>[5]</sup> Therefore, the ability to reliably record signals from specific fibers tracts *in vivo* holds the key to recover the complex tasks performed by the spinal cord. The past decades has witnessed a proliferation of techniques to monitor neural activity not only by electrical means, but also through optical and magnetic technologies.<sup>[6,7]</sup> Electrical recording probes have been so far the sole tool reaching clinical applications, even though their invasiveness strongly limits their long-term performance.<sup>[8]</sup> On the other hand, optical methods can obviate to physical tissue penetration, but their use requires gene transfer approaches resulting in a poor clinical translatability. Moreover, even under ideal conditions, optical monitoring is limited to ~1 mm in depth, as well as by the inherent quantum mechanical randomness of photon emission and detection.<sup>[9]</sup> Magnetic field probing needs either bulky equipment, cryogenic temperatures or special screening systems,

which makes them require special shielding rooms.<sup>[10,11]</sup> Solving these drawbacks could funnel magnetic sensors for spinal activity recording towards the design of a new neuroprosthetic devices generation. Importantly, magnetic fields are able to cross biological tissues with no attenuation since its vacuum permeability is roughly constant, conversely to electric fields, which magnitude is affected by dielectric properties of the electrode-tissue interface.<sup>[12]</sup> This difference has long been recognized as a potential way to non-invasively target neuronal activity in the brain by magnetoencephalography (MEG) using superconducting quantum interference devices (SQUIDs) capable to resolve neural magnetic fields in the femto-to-pico Tesla ( $10^{-15}$  T -  $10^{-12}$  T) range.<sup>[13,14]</sup> Recent advances in the field led to less cumbersome devices based on giant magnetoresistance (GMR) spin electronics.<sup>[15,16]</sup> However, wearability in the absence of tissue penetration is an imperative requirement for novel neural magnetic sensors, and their ability to work in real-time without magnetic shielding is crucial for portable devices to be functional on a daily basis.

We interfaced to new magnetic sensors organotypic cultures of the embryonic mouse spinal cord. Organotypic spinal slices represent a biological model of segmental microcircuit where subsets of interneurons organized in 3D fashion and dorsal root ganglia sensory pathways can be directly investigated. Despite the absence of afferent and supraspinal inputs, this preparation represents a useful model for studying the dynamics of intrasegmental signaling processes that rely on sensory and propriospinal neurons and circuits.<sup>[17-20]</sup> We report the detection of neural magnetic fields in organotypic spinal cord (SC)-DRG slices *in vitro*, with no need for digital post-processing, nor time-series averaging. Reference-free recording can be conducted without magnetic shielding, at room temperature and avoiding sensors insertion within the spinal tissue. Ultimately, we demonstrated that magnetic sensor-recorded

physiological waveforms could be used to entrain premotor network activity in an open-loop configuration through DRG stimulation.

### **Experimental Set-up and Results**

*In vitro* recordings were performed on SC-DRG organotypic slice co-cultures obtained from mouse embryos (E12-13).<sup>[21,22]</sup> Slices were grown onto thin micropatterned substrates (50 – 150  $\mu\text{m}$ ) made of a biocompatible polymeric materials previously used for neural recording devices encapsulation, namely polydimethylsiloxane (PDMS) and polystyrene (PS).<sup>[23,24]</sup>

Magnetic sensor measurements (here referred as magnetophysiology), have been made using a vector magnetometer based on tunnel magnetoresistance (TMR). The fundamental figure of merit of these TMR sensors is their detectivity, which is below  $\text{nT}/\text{Hz}^{1/2}$  at 1Hz. The working commercial sensor has been encapsulated in PDMS to protect its circuits from possible liquid spills. Additionally, a low noise electronic system has been developed in order to amplify the small voltage signals keeping them undisturbed from electronic noise. Sensor output signals were acquired at 1 kHz sampling rate with a homemade set up comprising a dedicated low noise amplifier selected to match the output resistance of the sensor. The signal was therefore amplified and bandpass filtered (0.01 Hz – 100 Hz) by a commercial low noise amplifier (SR560, Stanford Research Systems). The gain was divided between the two amplification stages where the homemade one is usually 250 and the SR560 is set to  $\times 1000$  increasing the overall gain up to  $\times 250000$ .

The SC-DRG sample was directly placed on top of the magnetic sensor to record the magnetic signal without shielding (see **Figure 1**). Differential measurements using two identical magnetic sensors (stacked at  $\sim 1$  cm distance) were performed in a gradiometer configuration, which allowed background noise subtraction (see **Figure 1**). The measuring sensor was the closest to the sample ( $< 500$   $\mu\text{m}$ ) and given that magnetic field is expected to strongly decay

with the distance ( $1/r^2$  or even  $1/r^3$ ), measuring sensor uniquely sensed neural signals. Magnetophysiology recorded traces were downsampled to 500 Hz and selected events were used as noisy stimulus waveforms which were lowpass filtered at 10 Hz as previously described.<sup>[25]</sup> Corresponding waveform duration was time-scaled to the size of synaptic vents, it was transformed in ASCII format and imported in MC\_Stimulus II (to trigger an STG 4002 stimulator, Multi Channel Systems).

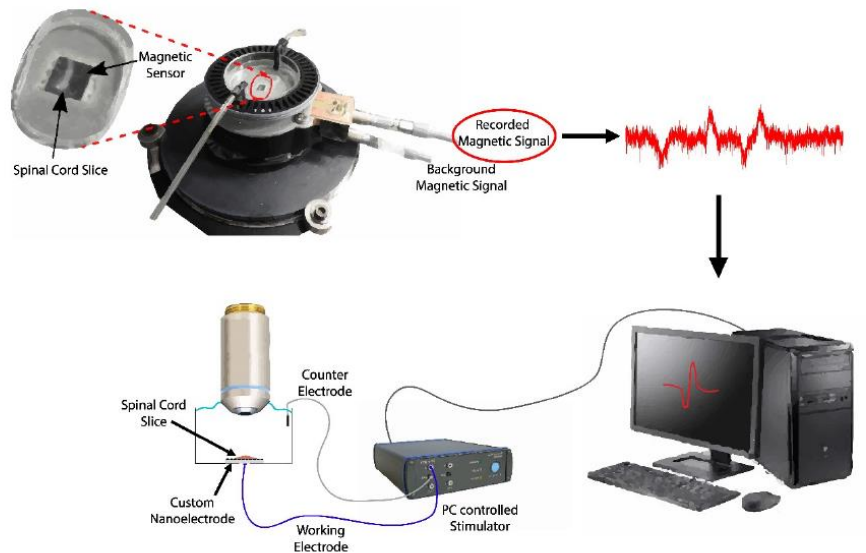


**Figure 1.** Sketch of the open loop recording and stimulation setting. The spinal cord organotypic slice is grown for 2-3 weeks in vitro onto micropatterned (grooved) polymeric substrates. Our custom setup for magnetic sensing (top image) was composed by two tunnel magnetoresistive (TMR) sensors (recording and background). The recorded magnetic signals (red trace) of few nT in amplitude were therefore transferred to a computer and used as stimulus to trigger spinal cord activity in independent experiments. Voltage waveform was injected either through custom nanoelectrodes (e.g. PS-CNTs nanopillars or Au nanowires) or through focal bipolar electrodes on DRGs, by means of a computer-controlled stimulator or an isolated battery stimulator.

To follow-up organotypic SC-DRG slices activity either live  $Ca^{2+}$  imaging or extracellular field potential electrophysiological recordings were carried out in parallel with magnetophysiological recordings.<sup>[26,27]</sup> Network disinhibition through bicuculline/strychnine ( $20 \mu\text{M}/1 \mu\text{M}$ ) application was used to synchronize the network, thereby generating rhythmic

patterns reminiscent of an entire spinal cord activity.<sup>[28,29]</sup> The neural origin of the recorded signals was assessed by tetrodotoxin (1  $\mu$ M) administration, always resulting in physiological signals abolishment, both in electrophysiological and magnetophysiological recordings (**Figure 2A** and **2B** respectively).

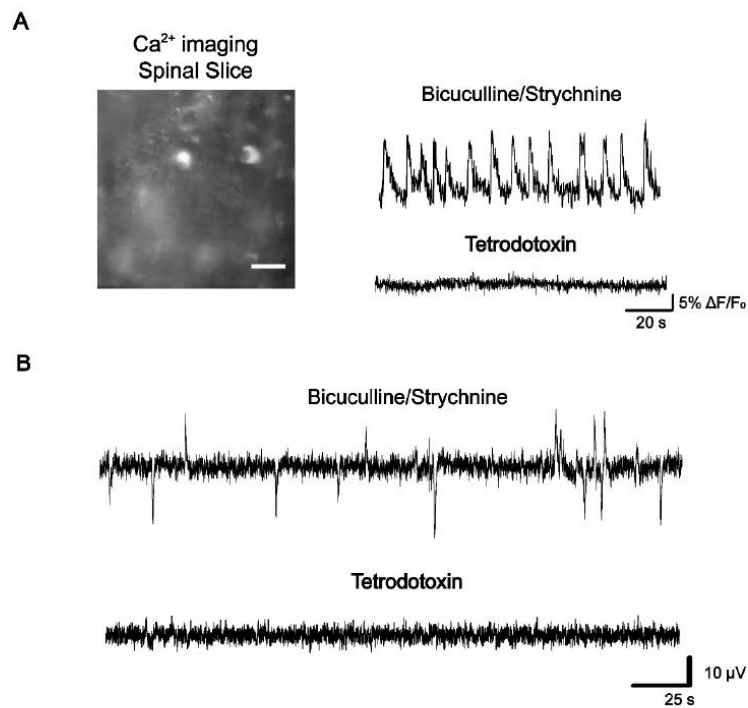


**Figure 2.** Simultaneous Calcium Imaging and Magnetic Sensing. **A.** Live calcium imaging snapshot of the recorded field in the ventral region of a SC-DRG organotypic slice (scale bar = 50  $\mu$ m). Calcium oscillation arising from neuronal activity was isolated using bicuculline/strychnine cocktail and abolished by tetrodotoxin as shown by top right representative tracings. **B.** Parallel magnetic recording of the disinhibited network was achieved with TMR-based sensor, as shown by occasional magnetic field variations (top trace). Tetrodotoxin administration shutdown such activity, thus confirming the neuronal nature of the recorded signals (expressed in voltage).



As in the case of electrophysiological recordings, magnetic field variations within the network are expected to be the resultant of multiple neuronal activities superposing in time.<sup>[30]</sup> Therefore, the duration of TMR-recorded signals was reduced to match the duration of physiological polysynaptic events (10 – 30 ms, **Figure 3A**), also to avoid the eventual electrical damage of the spinal tissue.<sup>[31]</sup> Appropriate DRG electrical stimulation can be used to trigger sensory feedback to the spinal cord and it has been previously used to evoke postsynaptic potentials in the premotor (ventral) region of transversal SC-DRG slices.<sup>[32]</sup> A bipolar stimulating electrode (**Figure 3B**, left micropipette) was gently inserted within DRGs, while the recording electrode (**Figure 3B**, right micropipette) was placed in the ventral premotor region of the spinal slice. Spontaneous, rhythmic extracellular bursts were recorded during network disinhibition, again induced by bicuculline/strychnine application (**Figure 3C**, upper left trace). After 15 minutes recording, electrical stimuli designed from magnetophysiological signals were presented to DRG neurons at 0.1 Hz for 5 minutes, resulting in evoked responses due to network entrainment (**Figure 3C**, upper right trace). Overall, the single burst duration was not affected by the increased burst frequency imposed through electrical stimulation (**Figure 3C**, left and right middle traces). As expected, tetrodotoxin administration totally abolished spontaneous (**Figure 3C**, left trace) and evoked network activity (**Figure 3C**, right trace), ultimately confirming the synaptic origin of the response evoked by DRG stimulations.

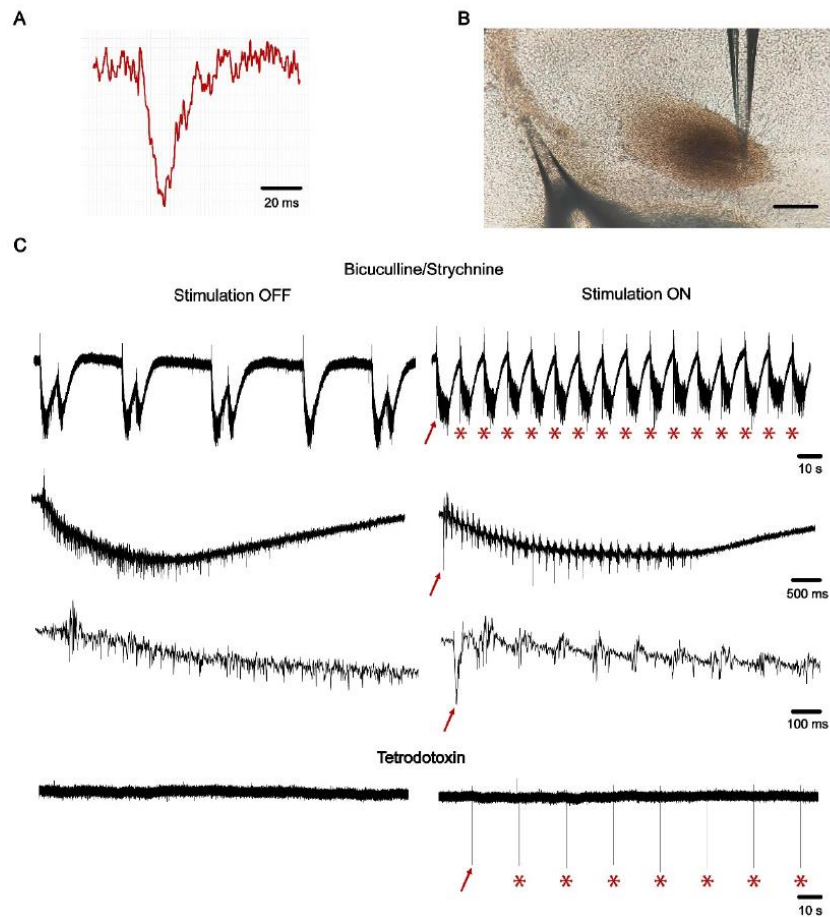


**Figure 3.** Evoked spinal activity by stimulation with recorded magnetophysiological events. **A.** Timeseries of the selected magnetic event produced by neuronal activity and used to evoke postsynaptic potentials in SC-DRG slices. **B.** Bright-field image of an organotypic SC-DRG slice during the experiment: a bipolar stimulating electrode (left micropipette) was placed within DRGs, while recording electrode (right micropipette) was inserted in the ventral region (scale bar = 500  $\mu$ m). **C.** Extracellular field potentials were recorded during network disinhibition produced by bicuculline/strychnine (upper left trace). Electrical stimuli (red asterisks) were therefore injected in the DRG neurons, resulting in timed evoked responses (upper right trace). Burst duration was comparable before and after stimulation (left and right middle traces). At higher magnification, the stimulus artifact (red arrows) matching the magnetic waveform shape is clearly visible before burst initiation (bottom right vs bottom left traces). Tetrodotoxin silenced network activity either in the absence (left trace) or in the presence (right trace) of the stimulation thus ensuring the neuronal source of the recorded spontaneous and evoked signals.

## **Conclusions**

We have shown the possibility to record small synaptic signals by magnetic recordings *in vitro* to monitor neural activity emerging from organotypic SC-DRG co-cultures. The sporadic magnetophysiological events recordings were corroborated by using two extensively recurrent techniques in neurobiology research, live  $\text{Ca}^{2+}$  imaging and extracellular field potential recordings. The magnetic recordings were performed in real time, with no magnetic shielding using commercial sensors based on spin electronics. Disproportion between the occurrence of magnetophysiological and electrophysiological events was always observed, suggesting that variability in instantaneous current densities might affect the actual ability of TMR-sensors to record neuronal signals in this *in vitro* preparation. A solution to such an inconvenient might be to improve the spatial resolution of magnetic sensors by creating a multiplexed array of spintronic sensors. Notwithstanding, we could explore the possibility of using magnetic signals generated by spinal network activity as a physiological source of input that might be potentially used to bypass CNS lesions.

These results are very promising and pave the way to the future design of lab bench or wearable devices capable of detecting magnetic fields created by neuronal activity which will hopefully result in a dramatic impact on both neurobiology research and neural prosthesis engineering.

## References

- [1] T. H. Hutson, S. Di Giovanni, *Nat. Rev. Neurol.* **2019**, *15*, 732.
- [2] N. Wenger, E. M. Moraud, S. Raspopovic, M. Bonizzato, J. DiGiovanna, P. Musienko, M. Morari, S. Micera, G. Courtine, *Sci. Transl. Med.* **2014**, *6*.
- [3] F. B. Wagner, J. B. Mignardot, C. G. Le Goff-Mignardot, R. Demesmaeker, S. Komi, M. Capogrosso, A. Rowald, I. Seáñez, M. Caban, E. Pirondini, M. Vat, L. A. McCracken, R. Heimgartner, I. Fodor, A. Watrin, P. Seguin, E. Paoles, K. Van Den Keybus, G. Eberle, B. Schurch, E. Pralong, F. Becce, J. Prior, N. Buse, R. Buschman, E. Neufeld, N. Kuster, S. Carda, J. von Zitzewitz, V. Delattre, T. Denison, H. Lambert, K. Minassian, J. Bloch, G. Courtine, *Nature* **2018**.
- [4] J. L. Collinger, S. Foldes, T. M. Bruns, B. Wodlinger, R. Gaunt, D. J. Weber, *J. Spinal Cord Med.* **2013**, *36*, 258.
- [5] G. Taccola, D. Sayenko, P. Gad, Y. Gerasimenko, V. R. Edgerton, *Prog. Neurobiol.* **2018**, *160*, 64.
- [6] G. Hong, C. M. Lieber, *Nat. Rev. Neurosci.* **2019**, *20*, 330.
- [7] R. Chen, A. Canales, P. Anikeeva, *Nat. Rev. Mater.* **2017**, *2*, 1.
- [8] J. W. Salatino, K. A. Ludwig, T. D. Y. Kozai, E. K. Purcell, *Nat. Biomed. Eng.* **2017**, *1*, 862.
- [9] W. Yang, R. Yuste, *Nat. Methods* **2017**, *14*, 349.
- [10] E. Boto, S. S. Meyer, V. Shah, O. Alem, S. Knappe, P. Kruger, T. M. Fromhold, M. Lim, P. M. Glover, P. G. Morris, R. Bowtell, G. R. Barnes, M. J. Brookes, *Neuroimage* **2017**, *149*, 404.
- [11] S. Sumiya, S. Kawabata, Y. Hoshino, Y. Adachi, K. Sekihara, S. Tomizawa, M. Tomori, S. Ishii, K. Sakaki, D. Ukegawa, S. Ushio, T. Watanabe, A. Okawa, *Sci. Rep.* **2017**, *7*, 2192.

- [12] B. Greenebaum, F. Barnes, *Biological and Medical Aspects of Electromagnetic Fields*; CRC Press, 2018; Vol. 1.
- [13] D. Cohen, *Science (80-. )*. **1968**, 161, 784.
- [14] D. Cohen, *Science (80-. )*. **1972**, 175, 664.
- [15] F. Barbieri, V. Trauchessec, L. Caruso, J. Trejo-Rosillo, B. Telenczuk, E. Paul, T. Bal, A. Destexhe, C. Fermon, M. Pannetier-Lecoeur, G. Ouanounou, *Sci. Rep.* **2016**, 6, 1.
- [16] L. Caruso, T. Wunderle, C. M. Lewis, J. Valadeiro, V. Trauchessec, J. Trejo Rosillo, J. P. Amaral, J. Ni, P. Jendritza, C. Fermon, S. Cardoso, P. P. Freitas, P. Fries, M. Pannetier-Lecoeur, *Neuron* **2017**, 95, 1283.
- [17] D. Avossa, M. D. Rosato-Siri, F. Mazzarol, L. Ballerini, *Neuroscience* **2003**.
- [18] M. D. Rosato-Siri, D. Zoccolan, F. Furlan, L. Ballerini, *Eur. J. Neurosci.* **2004**, 20, 2697.
- [19] F. Furlan, L. Guasti, D. Avossa, A. Becchetti, E. Cilia, L. Ballerini, A. Arcangeli, *Neuroscience* **2005**, 135, 1179.
- [20] A. Fabbro, B. Pastore, A. Nistri, L. Ballerini, *Cell Calcium* **2007**, 41, 317.
- [21] B. H. Gähwiler, *J. Neurosci. Methods* **1981**, 4, 329.
- [22] U. F. Braschler, A. Iannone, C. Spenger, J. Streit, H. R. Lüscher, *J. Neurosci. Methods* **1989**.
- [23] I. R. Mineev, P. Musienko, A. Hirsch, Q. Barraud, N. Wenger, E. M. Moraud, J. Gandar, M. Capogrosso, T. Milekovic, L. Asboth, R. F. Torres, N. Vachicouras, Q. Liu, N. Pavlova, S. Duis, A. Larmagnac, J. Voros, S. Micera, Z. Suo, G. Courtine, S. P. Lacour, *Science (80-. )*. **2015**, 347, 159.
- [24] A. Hammack, R. T. Rihani, B. J. Black, J. J. Pancrazio, B. E. Gnade, *Biomed. Microdevices* **2018**, 20, 48.



- [25] G. Taccola, *J. Neurophysiol.* **2011**, *106*, 872.
- [26] S. Sibilla, A. Fabbro, M. Grandolfo, P. D'Andrea, A. Nistri, L. Ballerini, *Eur. J. Neurosci.* **2009**, *29*, 1543.
- [27] N. P. Pampaloni, I. Rago, I. Calaresu, L. Cozzarini, L. Casalis, A. Goldoni, L. Ballerini, D. Scaini, *Dev. Neurobiol.* **2019**, *1*.
- [28] J. Streit, *J. Neurophysiol.* **1993**, *70*, 871.
- [29] E. Bracci, L. Ballerini, A. Nistri, *J. Neurosci.* **1996**, *16*, 7063.
- [30] G. Buzsáki, C. A. Anastassiou, C. Koch, The origin of extracellular fields and currents- EEG, ECoG, LFP and spikes. *Nat. Rev. Neurosci.* **2012**.
- [31] K. C. Murray, M. J. Stephens, M. Rank, J. D'Amico, M. A. Gorassini, D. J. Bennett, *J. Neurophysiol.* **2011**, *106*, 925.
- [32] J. Streit, C. Luscher, H. R. Luscher, *J. Neurophysiol.* **1992**, *68*, 1793.

## APPENDIX

### 1. Longitudinal hemi-spinal organotypic culture from mouse embryo

Embryonic spinal cord organotypic cultures are known to maintain their main cytoarchitectural elements for various days in culture [339]. This feature has been largely exploited in transversal slices to study maturation-dependent circuitry behaviors, molecular and electrophysiological responses during inflammatory processes and tissue response to pharmacological treatment [355,360,361,368,374]. Remarkable achievements have been also reached in the field of regenerative and nano-medicine thanks to material science support [106,149,375]. In this context, I revisited an existing organotypic culture model of spinal cord, to a long-term propagation, with the intention of better representing *in vitro* biomedical issues such as spinal cord lesion and spinal neural interfaces testing, which often requires the investigation of physiological responses along the longitudinal axis [354,362,472–474].

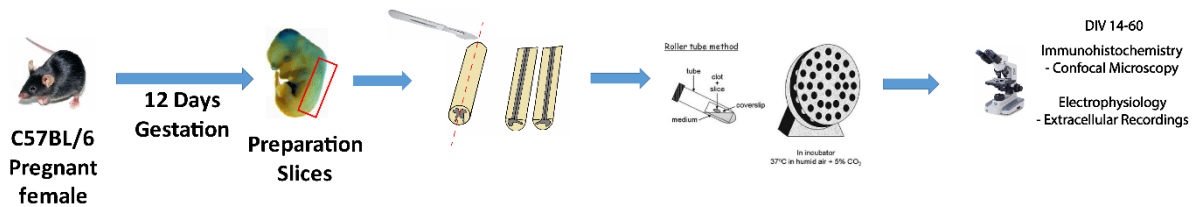


**Figure 16.** Schematic of explant preparation. Spinal cords were obtained from embryos at 12-13 days of gestation (E12-13) from a pregnant female mouse (C57Bl/6). Ventral fissure and the dorsal sulcus are used as reference to perform a longitudinal cut of the two contralateral halves. Cultures were kept in a roller drum at 120 revolution per hour in an incubator at 37°C up to two months *in vitro*. After 7 DIV culture medium was replaced for 24h by fresh medium containing antimetabolites (10  $\mu$ M ARA-C/Uridine/5-Fl-dU) and 20 ng/mL nerve growth factor (NGF). At DIV 8 fresh medium without antimetabolites and with reduced NGF (5 ng/mL) was added and refreshed every 7 days.

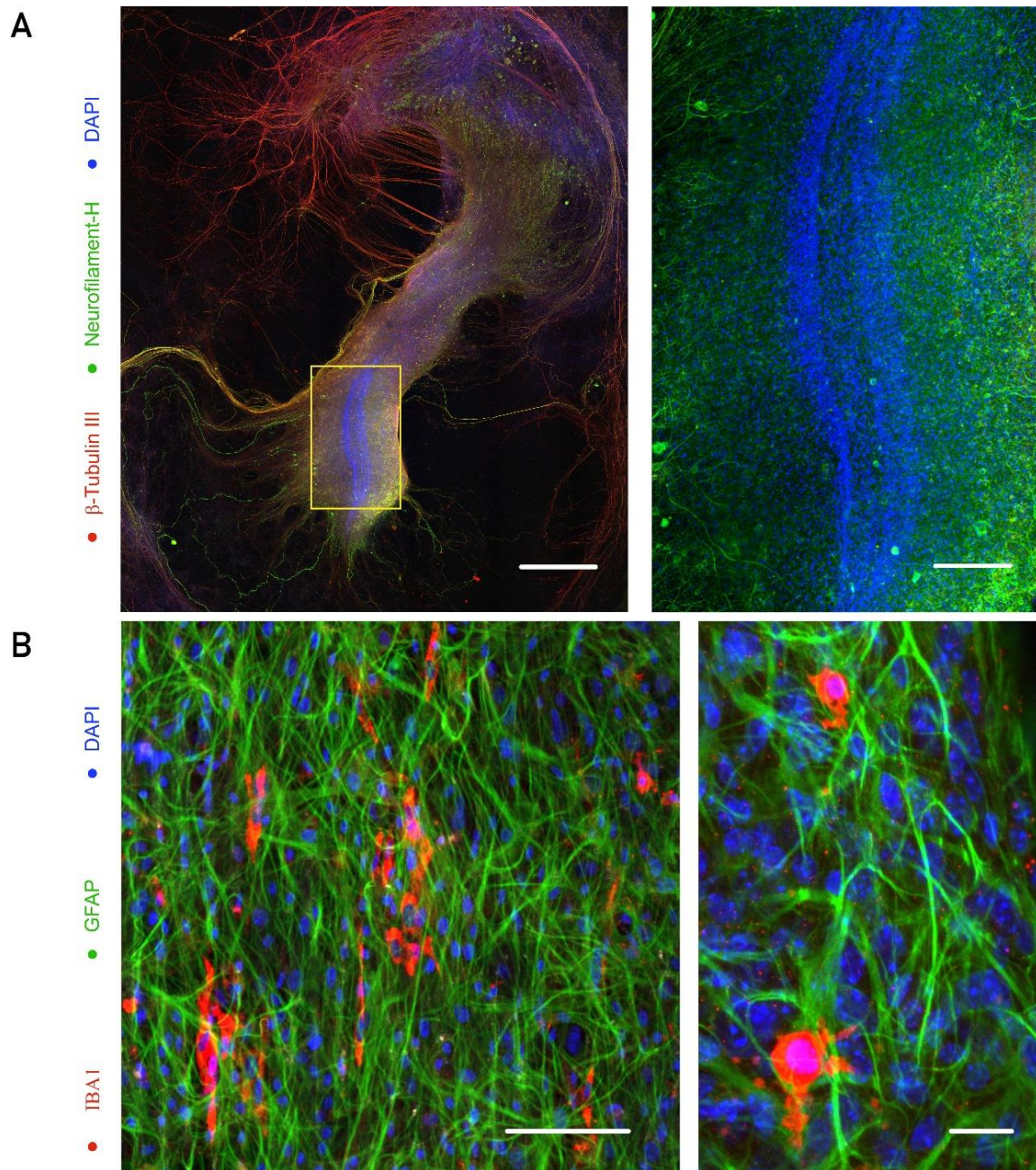


**Figure 17.** Longitudinal spinal cord immunocytochemistry. **A.** Neurons were labeled with  $\beta$ -tubulin III (red), motoneurons with SMI32 (green) and nuclei with DAPI (blue) to observe the longitudinal extent of such preparation. We also observed the presence of defined cytoarchitectural elements such as the nuclei-dense central canal as highlighted by the yellow square on the left image and its magnified view on the right (scale bars = 1000  $\mu\text{m}$  and 250  $\mu\text{m}$  respectively). **B.** In another subset of immunolabeling, we also observed the presence of other cell types such as astrocytes labeled with GFAP (green) and microglial cells with IBA1 (red), again DAPI (blue) was used to visualize nuclei (from left to right scale bars = 100  $\mu\text{m}$  and 50  $\mu\text{m}$ ).

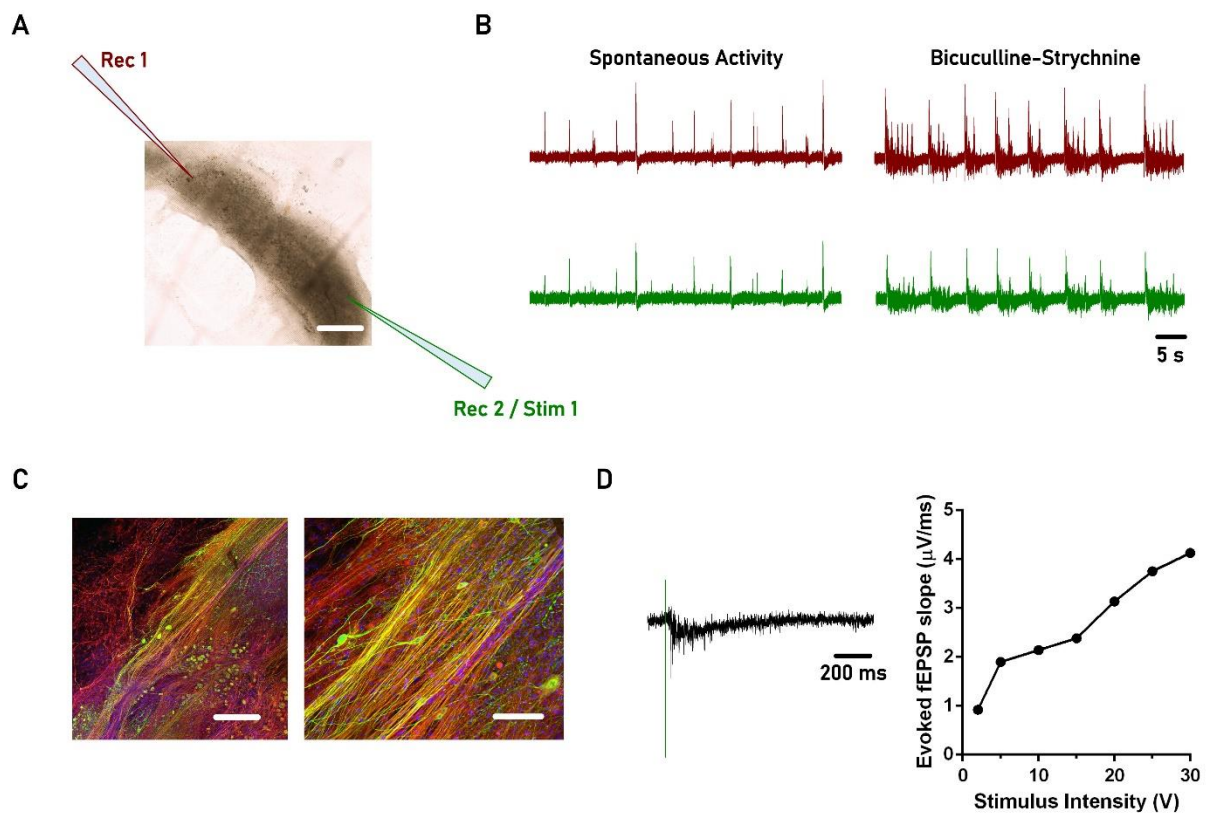


**Figure 18.** Maintenance of long-haul ascending and descending fiber pathways. **A.** To have a functional insight, we studied longitudinal signals spreading in the spinal cord hemisections by extracellular field potential co-recording (scale bar = 800  $\mu\text{m}$ ). **B.** Interestingly we found that a sustained spontaneous activity was highly synchronized even at distant sites of recording (left red and green traces). Moreover, the high correlation and frequency were maintained during bicuculline/strychnine (20  $\mu\text{M}$ /1  $\mu\text{M}$ )-induced bursting (right red and green traces). **C.** This assumption was further supported by the presence of densely packed neuronal and motoneuronal fibers (red and green respectively) longitudinally aligned over 2 mm distances, as highlighted by the confocal reconstruction at two increasing magnifications (from left to right, scale bar = 400  $\mu\text{m}$  and 100  $\mu\text{m}$ ). **D.** In another subset of experiments the second recording electrode (Rec 2) was replaced by a stimulating bipolar electrode (Stim1) connected to a battery stimulator. The longitudinal spinal cords explants ability to respond to stimulation (left representative trace) was therefore studied by measuring the extracellular field post-synaptic potential (fEPSP) slope ( $\mu\text{V}/\text{ms}$ ) versus the stimulus intensity (V). Results were finally plotted in the input-output curve as shown in the right graph.

## 2. Spinal fibers elongation over polymeric micropatterned substrates

Several materials composing implantable neural probes must be usually protected to direct contact with proteinaceous and saline extracellular environment; therefore, we were provided by our collaborators (IMDEA Nanociencia, Madrid) with two polymeric candidates for sensors insulation. These layers were based on anisotropic patterns of grooves thermally imprinted on polystyrene (PS) and PMDS. I therefore interfaced organotypic spinal cord-dorsal root ganglia co-cultures onto these materials and onto flat glass (Control) to observe if such grooved substrates, were long-term biocompatible, if could improve fibers reconnection and if these fibers displayed avoid constitutive and measurable field potentials, this was done by immunocytochemistry, calcium imaging and electrical recordings.



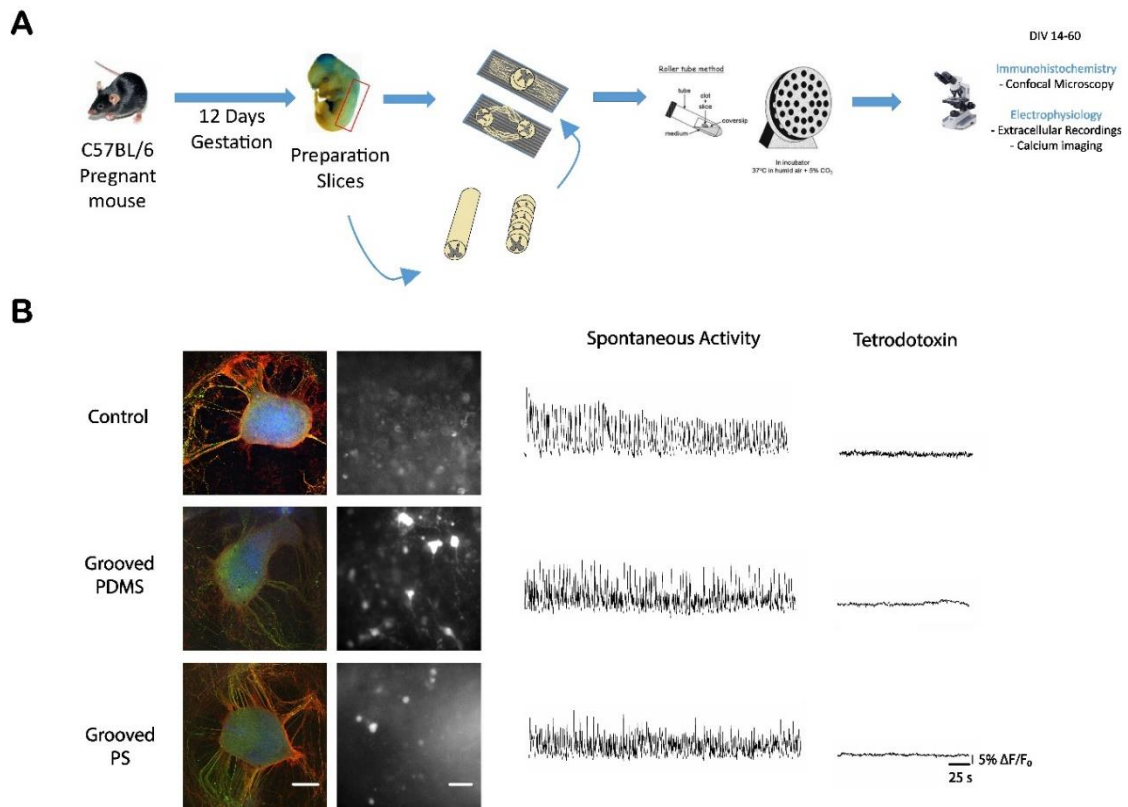


**Figure 19.** Spinal cord-DRG organotypic co-cultures interfacing to micropatterned polymeric substrates. **A.** Schematic of explant preparation: embryonic organotypic transversal slice cultures were grown either alone or in pairs onto grooved substrates, to observe respectively their intrinsic capacity of inducing fiber sprouting and their ability to promote double-slices reconnection. **B.** Morphological observation by immunohistochemistry revealed appropriate slices growth (first column). Live calcium imaging (recorded field snapshot in second column) was used to monitor neuronal activity (representative tracings) until 60 days in vitro (respective scale bars = 500 and 60  $\mu\text{m}$ ).



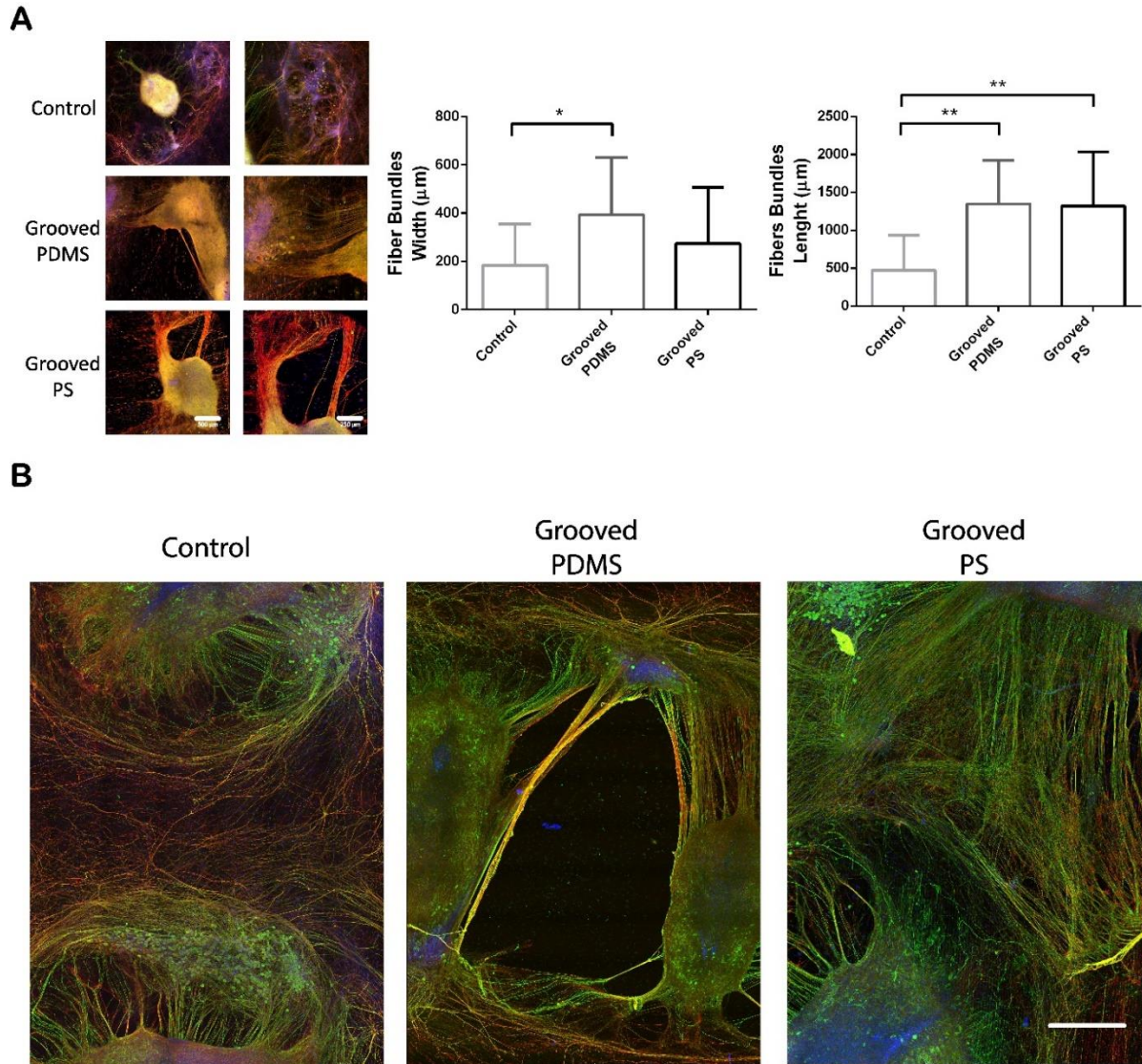


**Figure 20.** Organotypic spinal cord-DRG slices grown alone (top) or in pairs (bottom). **A.** We characterized motor and sensory axons outgrowing from the spinal cord/DRG slice co-culture, by performing double immunostaining for neuron-specific microtubules (anti- $\beta$ -tubulin III antibody) together with anti-neurofilament H (Smi-32) antibody (marker for projecting neurons, DRG neurons and motoneurons). In control spinal slices, in the absence of structured interfaces, axons regrow randomly, with no preferred orientation, usually organized centrifugally around the spinal tissue (first two columns: scale bars = 500 and 250  $\mu\text{m}$ ). Conversely, when the spinal-cord slices were interfaced to patterned substrates, axonal elongation was evident (grooved PDMS and PS). To quantify such phenomenon, fiber bundles width and length were measured (see bar plots). On one hand fibers width was only slightly modified by anisotropic patterning, with a more prominent effect onto grooved PDMS substrates ( $394 \pm 68 \mu\text{m}$ ) than grooved PS or standard glass (respectively,  $274 \pm 56 \mu\text{m}$  and  $184 \pm 49 \mu\text{m}$ ). On the other hand, neuronal fibers at the interface with grooves resulted in a greater bundles length ( $1350 \pm 166 \mu\text{m}$  onto grooved PDMS and  $1320 \pm 174 \mu\text{m}$  onto grooved PS) compared to planar glass ( $472 \pm 134 \mu\text{m}$ ). **B.** Immunolabeling for the same neuronal elements as above was used to address the reconnection between two spinal cord slices. Double slices onto control flat glass showed weak reconnection over about 2 mm distances as shown in the first column, while onto grooved polymeric substrates reconnection was always greater (scale bar = 800  $\mu\text{m}$ ).

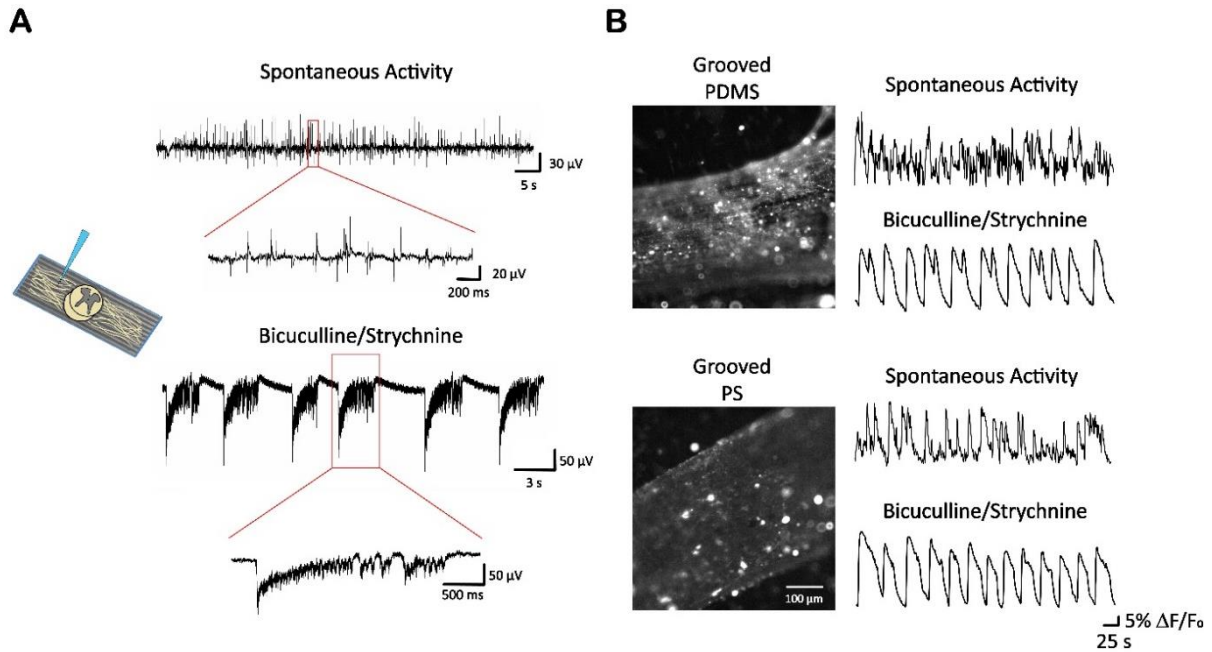


**Figure 21.** Extracellular field potential recordings and live  $\text{Ca}^{2+}$  imaging on fiber bundles. **A.** Glass micropipettes filled with extracellular saline solution were used to record multiple units within the axon bundles as depicted in the cartoon on the left. Spontaneous activity was of variable frequency and intensity depending on the electrode position and the size of the investigated bundle of axons, a remarkable example of such recordings is given (top tracings). To have more reproducibility in the measurements we pharmacologically synchronized the network by disinhibiting it through bicuculline/strychnine ( $25 \mu\text{M}/1 \mu\text{M}$ ). This resulted in a rhythmic and periodic activity of greater intensity and duration if compared to signals found during spontaneous activity (bottom tracing). **B.** Activity monitoring through axon bundles, was possible also by fluorescent  $\text{Ca}^{2+}$ -dynamics imaging (top and bottom snapshots; scale bar =  $500 \mu\text{m}$ ). Projecting axons loaded with the membrane-permeable  $\text{Ca}^{2+}$ -dye revealed typical spontaneous calcium bursts in all field examined (top and bottom spontaneous activity tracing). Again, Bicuculline /Strychnine application increased signals rhythmicity and periodicity (top and bottom Bicuculline/Strychnine tracing) in a similar fashion to what observed in voltage recordings. As usually, at the end of each experiments, either field potential recordings or fluorescent calcium imaging, the voltage-gated  $\text{Na}^+$  channel blocker Tetrodotoxin ( $1 \mu\text{M}$ ) was administrated to abolish any action potential and impair synaptic activity, thus ensuring the neuronal nature of recorded signals (tracing not shown).

## Attenuated Glial Reactivity on Topographically Functionalized Poly(3,4-Ethylenedioxythiophene):P-Toluene Sulfonate (PEDOT:PTS) Neuroelectrodes Fabricated by Microimprint Lithography

Catalina Vallejo-Giraldo,\* Katarzyna Krukiewicz, Ivo Calaresu, Jingyuan Zhu, Matteo Palma, Marc Fernandez-Yague, Benjamin W. McDowell, Nathalia Peixoto, Nazar Farid, Gerard O'Connor, Laura Ballerini, Abhay Pandit, and Manus Jonathan Paul Biggs\*

Following implantation, neuroelectrode functionality is susceptible to deterioration via reactive host cell response and glial scar-induced encapsulation. Within the neuroengineering community, there is a consensus that the induction of selective adhesion and regulated cellular interaction at the tissue–electrode interface can significantly enhance device interfacing and functionality *in vivo*. In particular, topographical modification holds promise for the development of functionalized neural interfaces to mediate initial cell adhesion and the subsequent evolution of gliosis, minimizing the onset of a proinflammatory glial phenotype, to provide long-term stability. Herein, a low-temperature microimprint-lithography technique for the development of micro-topographically functionalized neuroelectrode interfaces in electrodeposited poly(3,4-ethylenedioxythiophene):p-toluene sulfonate (PEDOT:PTS) is described and assessed *in vitro*. Platinum (Pt) microelectrodes are subjected to electrodeposition of a PEDOT:PTS microcoating, which is subsequently topographically functionalized with an ordered array of micropits, inducing a significant reduction in electrode electrical impedance and an increase in charge storage capacity. Furthermore, topographically functionalized electrodes reduce the adhesion of reactive astrocytes *in vitro*, evident from morphological changes in cell area, focal adhesion formation, and the synthesis of proinflammatory cytokines and chemokine factors. This study contributes to the understanding of gliosis in complex primary mixed cell cultures, and describes the role of micro-topographically modified neural interfaces in the development of stable microelectrode interfaces.

### 1. Introduction

Implantable stimulation and recording devices have received significant attention in biomedical engineering and have brought great success in the treatment of central nervous system disorders including paralysis,<sup>[1]</sup> epilepsy,<sup>[2]</sup> and Parkinson's disease.<sup>[3,4]</sup> In order to achieve chronic functionality and integration with surrounding tissue, material functionalization strategies have been employed to provide chemical and physicochemical properties analogous to neural tissues, with an ultimate goal of mitigating electrode deterioration via reactive host cell response and glial scar-induced encapsulation.<sup>[3,5–8]</sup>

From this perspective, the field of neuroelectrode engineering has encouraged the use of alternative electroactive materials over conventional metallic strategies such as gold and platinum<sup>[9,10]</sup> as an approach to provide an electrochemical platform for the immobilization of biological molecules,<sup>[11,12]</sup> or in order to promote physicochemical mimicry through soft or topographically rough interfaces.<sup>[13,14]</sup> Specifically, semiconducting polymers,<sup>[6,15–20]</sup> including polypyrrole<sup>[21–23]</sup>

Dr. C. Vallejo-Giraldo, Dr. K. Krukiewicz, M. Fernandez-Yague, Prof. A. Pandit, Dr. M. J. P. Biggs  
CÚRAM—Centre for Research in Medical Devices—Galway  
Biosciences Research Building  
118 Corrib Village, Newcastle, Galway H91 D577, Ireland  
E-mail: catalina.vallejogiraldo@nuigalway.ie; manus.biggs@nuigalway.ie  
Dr. K. Krukiewicz  
Department of Physical Chemistry and Technology of Polymers  
Silesian University of Technology  
Gliwice 44-100, Poland

I. Calaresu, Prof. L. Ballerini  
Scuola Internazionale Superiore di Studi Avanzati (SISSA)  
Via Bonomea, 265, 34136 Trieste, Italy

J. Zhu, Dr. M. Palma  
School of Biological and Chemical Sciences  
Queen Mary University of London  
Mile End Road, London E14NS UK

B. W. McDowell, Dr. N. Peixoto  
Department of Electrical and Computer Engineering  
George Mason University  
4400 University Drive, MS-1G5 Fairfax, VA 22030, USA

Dr. N. Farid, Dr. G. O'Connor  
School of Physics  
National University of Ireland  
Galway, University Road, Galway H91 CF50, Ireland

 The ORCID identification number(s) for the author(s) of this article can be found under <https://doi.org/10.1002/sml.201800863>.

DOI: 10.1002/sml.201800863



and poly(3,4-ethylenedioxythiophene) (PEDOT),<sup>[24–26]</sup> and their hybrids<sup>[27,28]</sup> have been employed widely in neural engineering because of their versatility as electrode coatings through electro-deposition processes,<sup>[29,30]</sup> and have been employed to enhance the neuroelectrode electrochemical profile,<sup>[26,31]</sup> and provide a platform for chemical<sup>[32–34]</sup> and morphological<sup>[35–38]</sup> functionalization to meet particular requirements.<sup>[39–42]</sup>

Ongoing studies into topographical functionalization strategies of the neural interface have explored the micro<sup>[43–45]</sup> to the nanoscale,<sup>[46,47]</sup> and have shown promise in promoting a low impedance profile of implantable electrodes through effects on electrode surface area.<sup>[46,48,49]</sup> Recent studies indicate the cytocompatibility of conducting and semiconducting polymers in vitro and in vivo and the realization that electrodeposited conducting coatings present a nanorough surface that has led to speculation that topography may play a role in directing the cellular functional response to implanted electrodes by modulating cell function through altering integrin distribution<sup>[50]</sup> and differential cell adhesion.<sup>[51,52]</sup> In particular, nano-topographically functionalized materials have been shown to influence the activation of intrinsic cellular processes that lead to more quiescent or reactive cell phenotypes in the onset of a proinflammatory response<sup>[46,50–53]</sup> and glial scar formation.<sup>[54,55]</sup>

Ordered arrays of lithography fabricated nanopit substrates have been consistently shown in previous work to disrupt cell adhesion in vitro by direct or indirect modulation of focal adhesion formation.<sup>[51,52]</sup> Recent in vitro studies exploring topographical modification have been successful in controlling astrocyte adhesion while promoting high neuron integration as strategies to reduce gliosis,<sup>[14,56,57]</sup> with microscale isotropic pit topographies of 1  $\mu\text{m}$  in depth reported to modulate astrocyte adhesion in vitro.<sup>[61]</sup>

Although neural cells are reported to produce sparse and small focal adhesions,<sup>[58]</sup> it has been shown that astrocytes are adhesion dependent,<sup>[59]</sup> and will form a monolayer in culture, providing neurons with physicochemical cues to modulate neural processes extension.<sup>[57]</sup> Consequently, the ability to control astrocyte adhesion and promote a reduction of the reactive astrocyte phenotype at the electrode interface is critical to support neuronal outgrowth,<sup>[60]</sup> and reduce glial scar formation.<sup>[54]</sup>

In this study, PEDOT:p-toluene sulfonate (PTS) coated microelectrodes were topographically functionalized with ordered micropit arrays using a novel low-temperature three-step die imprinting lithography process as a strategy to enhance electrode functionality, cytocompatibility and promote selective adhesion, minimizing the onset of a proinflammatory glial phenotype, in neural applications. The physical, electrochemical, and cytocompatibility effects of topographically functionalized microelectrodes were subsequently explored in vitro. Our results elucidate important topographical effects with regard to microelectrode functionality, cytocompatibility, and astrogliosis toward the generation of neural interfaces with superior electrical and biological properties.

## 2. Results and Discussion

### 2.1. Physical Characterization

A range of techniques have been explored to create defined microstructures on electrode surfaces,<sup>[62]</sup> including laser

ablation,<sup>[63,64]</sup> focused ion beam,<sup>[65,66]</sup> sputter etching,<sup>[67,68]</sup> reactive ion etching,<sup>[69,70]</sup> deep reactive ion etching,<sup>[71,72]</sup> hot embossing,<sup>[73,74]</sup> and electron beam lithography.<sup>[75,76]</sup> Complementary to these techniques, imprint lithography is an especially attractive approach due to its simplicity, nondestructive character, and feasibility of patterning large areas with features down to 10 nm using elevated temperature and/or pressure processes to transfer a pattern into typically thermoplastic materials.<sup>[77–80]</sup> Regarding the variation of imprinting methods, direct die imprinting is of particular interest as patterns are transferred via a stamp/die in a single imprint process.<sup>[81]</sup> However, the quality of the pattern transfer depends on relatively high temperatures and pressures,<sup>[81,82]</sup> and silanization steps are also required to facilitate the separation of the die and imprinted material.<sup>[83–86]</sup>

A study by Tan et al.<sup>[87]</sup> shows the imprinting process of non-thermoplastic materials such as PEDOT and chitosan using plasticizers. Imprinting of PEDOT and chitosan films from the poly(dimethylsiloxane) mold was achieved at a pressure of 10 kPa and 25 °C by controlled addition of glycerol as a plasticizer. In this case, the added glycerol was used to increase the chain mobility of the polymers, resulting in lower imprinting temperature and low pressures.

Further, a room temperature nanoimprint lithography process was shown by Pisignano et al.,<sup>[88]</sup> with the nanoimprinting of patterns in organic semiconductors with poor thermoplastic properties.

A focus of this study was to develop a low-temperature, simple imprinting method to reproduce lithographically fabricated well-defined and ordered topographies into PEDOT:PTS electrodeposited electrode coatings. Critically this approach preserves the ability to introduce coupled biochemical functionalization—an approach which has been explored extensively with PEDOT functionalized microelectrodes.<sup>[89–92]</sup> Arrays of pits possessing a diameter of  $\approx 1 \mu\text{m}$ , a pitch of  $\approx 2 \mu\text{m}$ , and depth of  $\approx 1 \mu\text{m}$  were initially fabricated via photolithography, which was used as a mask for a Ni (Nickel) electroforming process as described previously.<sup>[51]</sup> Fabricated negative Ni masters were used as hard stamps to replicate the original topography into electrodeposited PEDOT:PTS coatings via an imprint process applying 1.9 metric tons per  $\text{cm}^2$  for 15 min to achieve high quality pattern transfer conducted at room temperature. To facilitate substrate separation, a dehydration-assisted process was employed to enhance the cohesion of PEDOT:PTS and prevent topography disruption during the separation step, ensuring high pattern transfer as first described by Yang et al.,<sup>[80]</sup> who also used the dehydration-assisted method for the imprinting of spin-coated PEDOT:PSS nanogratings for photovoltaic applications. In this way, silanization steps were avoided, as they caused neural cell death to our cultures due to insufficient evaporation of fluorides.<sup>[93,94]</sup>

Experimentally, the microimprinting process is outlined in **Figure 1**. Representative scanning electron microscopy (SEM) micrographs of the nickel die used in the imprinting process and the resulting well-ordered arrays of micropits in the microtopographically functionalized PEDOT:PTS coated microelectrodes with respective dimensions are indicated in **Figure S1A** (Supporting Information). The calculated thickness of the electrodeposited PEDOT:PTS coating was of  $1.22 \pm 0.12 \mu\text{m}$ .

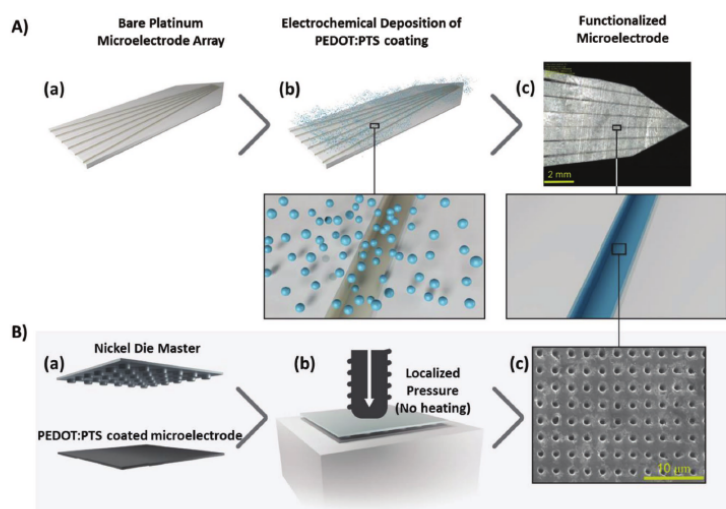


**Figure 1.** Microelectrode functionalization process. Upper panel (A) describes the sequential steps taken on the a) bare platinum electrodes, b) electro-deposition of PEDOT:PTS coating, followed by c) the optical micrograph of the coated PEDOT:PTS microelectrode ready for the functionalization with the topography; Scale bar = 2 mm, 10 $\times$ . Bottom panel (B) outlines the low temperature three-step die imprinting lithography process. a) This process starts with the micropit nickel die master and the PEDOT:PTS coated electrode. b) The nickel die was then pressed against the PEDOT:PTS coated microelectrode at a localized constant pressure of 1.9 metric tons per cm<sup>2</sup> for 15 min at room temperature using parallel pressing plates. Finally, a c) scanning electron micrograph (SEM) of the micro-topographically functionalized PEDOT:PTS coated microelectrode is shown.

Following imprinting, PEDOT:PTS microelectrodes were micro-topographically functionalized with arrays of pits with a diameter of  $0.82 \pm 0.07 \mu\text{m}$  and interpit spacing of  $2.28 \pm 0.06 \mu\text{m}$ . The depth was confirmed by atomic force microscopy (AFM) analysis (Figure S1B, Supporting Information) indicating vertical distances of  $0.96 \pm 0.07 \mu\text{m}$  and high fidelity pattern transfer using a low temperature three-step die imprinting lithography process. No Ni residues from the die master on the micro-topographically functionalized PEDOT:PTS coated microelectrodes were present after the imprinting process (Table S1, Supporting Information).

The topographical profiles of microimprinted PEDOT:PTS coated microelectrodes were subsequently analyzed by AFM and results presented relative to pristine PEDOT:PTS and to a PEDOT:PTS coated microelectrode flattened via imprinting with a planar glass substrate; these control groups serving as pristine electrodeposited PEDOT:PTS surface and a topographically planar PEDOT:PTS surface, respectively. A sputtered platinum (Pt) group was also used as a representative electrode control material (images shown in Figure S2, Supporting Information). Representative SEM and AFM images of experimental groups are depicted in Figure 2A,B. Micro-topographically functionalized PEDOT:PTS coated microelectrodes resulted in a nonsignificant decrease in surface roughness ( $R_a$ ) relative to pristine PEDOT:PTS coated microelectrode but in a significant increase when compared to the control flattened PEDOT:PTS coated microelectrodes (Table 1). Pristine PEDOT:PTS coated microelectrodes exhibited an average roughness of 85 nm over

$10 \mu\text{m}^2$ , and average roughnesses of 53 and 76 nm were noted on flattened and micro-topographically functionalized electrodes, respectively. All PEDOT:PTS coated electrodes exhibited a significant increase in surface roughness ( $R_a$ ) relative to Pt microelectrodes, which possessed an experimental  $R_a$  of 2 nm over  $10 \mu\text{m}^2$ .<sup>[49]</sup>

The microimprinting process resulted in a reduction in  $R_a$  of the interpit surface to levels similar to flattened PEDOT:PTS electrodes, indicating that the application of the mechanical imprinting eliminated nanoroughness while producing a regular micropit topography.<sup>[95]</sup> Significantly, the calculated physical surface area of the micro-topographically functionalized PEDOT:PTS coated microelectrodes was of  $2.35 \times 10^{10} \pm 51.77 \times 10^6 \text{ nm}^2$ ,  $1.74 \times 10^{10} \pm 93.34 \times 10^6 \text{ nm}^2$  for the pristine PEDOT:PTS coated microelectrodes  $1.32 \times 10^{10} \pm 71.42 \times 10^6 \text{ nm}^2$  for the flattened PEDOT:PTS coated microelectrodes, and  $1.05 \times 10^{10} \pm 35.35 \times 10^6 \text{ nm}^2$  for sputtered Pt electrodes indicating that through microimprinting the surface area of electrodeposited PEDOT:PTS was significantly increased relative to nanorough pristine electrodeposited materials and uncoated Pt electrodes, as shown in Table 1. These results suggest that microimprinting functionalization of PEDOT:PTS coated microelectrodes can be employed to induce a 135.06% greater surface area relative to pristine PEDOT:PEDOT coated microelectrodes and a 178.03% greater surface area relative to flattened control microelectrodes. Critically, micro-topographically modified PEDOT:PTS coated microelectrodes represented a 223.81% increase in surface area over that of Pt microelectrodes.

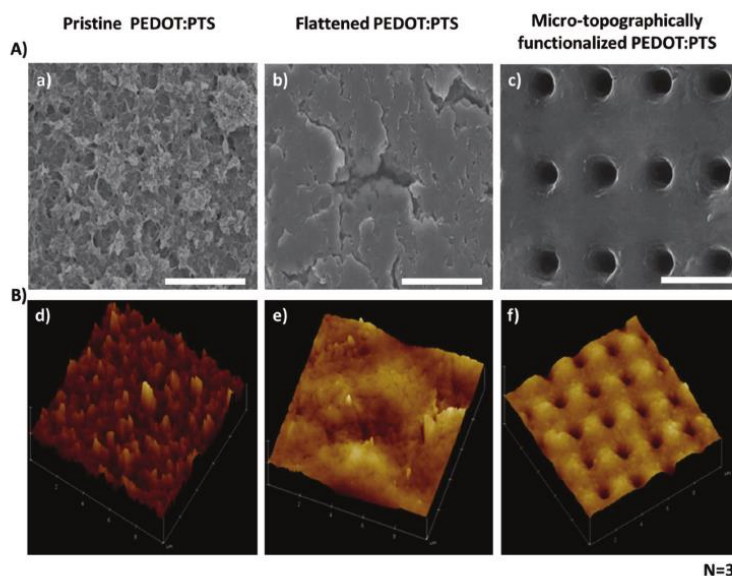


**Figure 2.** Microelectrode morphological physical characterization. Upper panel (A) describes a–c) scanning electron micrographs (SEM) of pristine PEDOT:PTS, flattened PEDOT:PTS, and the micro-topographically functionalized PEDOT:PTS coated microelectrodes. Scale bar = 3  $\mu\text{m}$ . B) d–f) Corresponding surface plots of pristine PEDOT:PTS, flattened PEDOT:PTS, and the micro-topographically functionalized microelectrodes on 10  $\mu\text{m}^2$  regions.

## 2.2. Electrochemical Characterization

Topographical surface modification of the neural electrodes has shown promise in improving the electrochemical performance through high aspect ratio structures, increasing the active surface area of the electrodes.<sup>[13,62]</sup> The electrochemical performance and the evaluation of the resulting effective-active surface area of the functionalized microelectrodes were subsequently assessed. To allow comparison, the evaluation of the electrochemical profile of in-house fabricated sputtered Pt microelectrodes was compared to topographically and non-topographically modified electrodeposited PEDOT:PTS electrodes and to electrodeposited gold coated microelectrodes

**Table 1.** Microelectrode physical properties. Values of experimental mean surface roughness ( $R_a$ ) and mean surface area (SA) measurements over 10  $\mu\text{m}^2$  regions. The data represent the mean of 15 measurements from three different replicas. Results are  $\pm$  SD,  $N = 3$ .

Microelectrodes	Average roughness $R_a$ [nm]	Average surface area [ $\text{nm}^2$ ]
Bare platinum (Pt)	1.96 $\pm$ 0.22	1.05 $\times 10^{10} \pm 35.35 \times 10^6$
Pristine PEDOT:PTS	85.16 $\pm$ 16.94	1.74 $\times 10^{10} \pm 93.34 \times 10^6$
Flattened PEDOT:PTS	52.59 $\pm$ 6.16	1.32 $\times 10^{10} \pm 71.42 \times 10^6$
Micro-topographically functionalized PEDOT:PTS	76.10 $\pm$ 17.21	2.35 $\times 10^{10} \pm 51.77 \times 10^6$

with a similar experimental coating thickness of the as-formed PEDOT:PTS coatings, which possessed approximated thicknesses of 1.21  $\pm$  0.08 and 1.22  $\pm$  0.12  $\mu\text{m}$ , respectively.

**Figure 3A** shows the cyclic voltammograms (CVs) for each of the experimental and control groups in 1 $\times$  phosphate-buffered saline (PBS) evaluated with a microelectrode area of 0.287  $\text{mm}^2$ . The increase in charge storage capacity (CSC) (**Table 2**), which was approximated through the integration of the charge passed within one CV scan, confirmed the presence of highly conducting PEDOT:PTS coatings with improvement in the electrochemical performance of the microelectrodes over that of bare platinum and gold coated microelectrode controls.<sup>[96,97]</sup> In addition, and owing to the topographical functionalization, further enhancement of electrical performance was observed over that of the CSC of the PEDOT:PTS coated microelectrodes. The highest CSC was obtained with the micro-topographically functionalized PEDOT:PTS coated microelectrodes with a capacitance of 131.01  $\pm$  8.05  $\mu\text{C mm}^{-2}$  followed by the pristine PEDOT:PTS coated microelectrodes with a CSC of 48.82  $\pm$  0.49  $\mu\text{C mm}^{-2}$  and finally the controlled nonpatterned surface, flattened PEDOT:PTS coated microelectrodes, with a CSC of 19.09  $\pm$  0.77  $\mu\text{C mm}^{-2}$  (**Table 2**). Of note is that these wide ranges of the aforementioned CSC values suggest that film structure plays a major role in determining the capacitance, more specifically, this may be related to the role of volumetric capacitance, significantly reduced on the flattened PEDOT:PTS coated microelectrodes.<sup>[98]</sup> The flattening geometry may be limiting the volume fraction



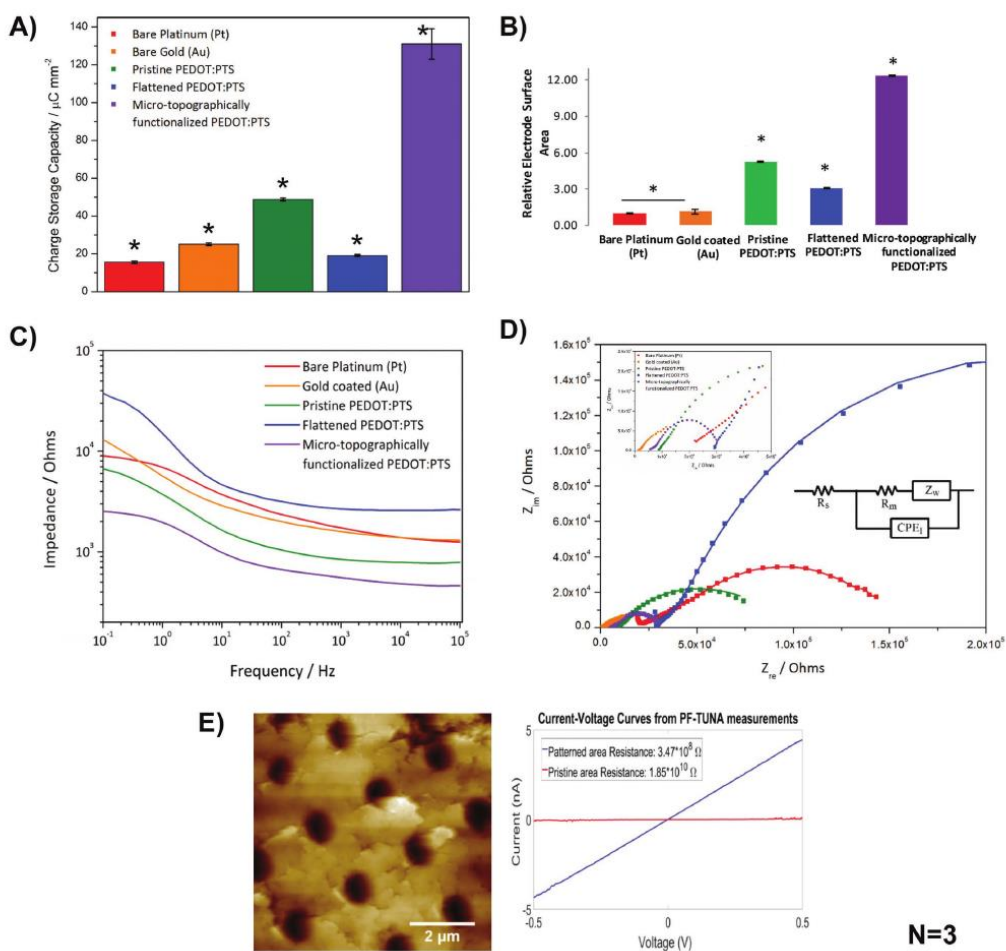


**Figure 3.** Electrochemical analysis of functionalized PEDOT:PTS coated microelectrodes. A) Cyclic voltammograms (CVs) bare platinum (Pt) and gold coated (Au) microelectrodes and pristine PEDOT:PTS, flattened PEDOT:PTS, and micro-topographically functionalized PEDOT:PTS coated microelectrodes. CVs were recorded in  $1 \times$  phosphate-buffered saline (PBS) at a scan rate of  $100 \text{ mV s}^{-1}$ . B) Relative electrode surface area calculated based on cyclic voltammograms (CVs) in  $2.5 \text{ mol dm}^{-3} \text{ K}_3[\text{Fe}(\text{CN})_6]$  in  $0.1 \text{ M KCl}$  solution at a scan rate of  $100 \text{ mV s}^{-1}$ . The relative electrode surface area was estimated according to the Randles–Sevcik equation and the bare platinum (Pt) microelectrode was used as a reference. C) Bode and D) Nyquist plots comparing the EIS spectra of bare platinum (Pt) and gold coated (Au) microelectrodes and pristine PEDOT:PTS, flattened PEDOT:PTS, and micro-topographically functionalized PEDOT:PTS coated microelectrodes. In addition, in (D) is shown the electrical equivalent circuit used to analyze experimental data and the low impedance regions. E) C-AFM micrograph of micro-topographically functionalized PEDOT:PTS coated microelectrode used for analysis and the corresponding  $I$ - $V$  curves recorded at selective positions, nonpatterned region and patterned region (pit) on the micro-topographically functionalized microelectrode. C-AFM tips (coated with platinum/iridium) were used as the mobile counter electrode to contact the SWCNTs (PeakForce-TUNA tips, Bruker). For a schematic of the set-up, see Figure S4 (Supporting Information). The voltage bias was ramped between  $-500$  and  $500 \text{ mV}$ . The data were then analyzed by NanoScope Analysis (version 1.5, Bruker) and Matlab (version 2016 a). Results are  $\pm$  STD,  $\star = p < 0.05$ .  $N = 3$ .

of the coating, hence limiting the favorable packing of the polymeric coating for facile ion transport affecting the capacitance.<sup>[98]</sup>

Furthermore, and together with the increased charge storage capacity, micro-topographically functionalized PEDOT:PTS coated microelectrodes possessed a significantly increased

**Table 2.** Electrochemical performance and stability of functionalized PEDOT:PTS coated microelectrodes. The initial and the final charge storage capacity (CSC) was evaluated from the cathodic region of cyclic voltammograms (CVs) recorded in 1× phosphate-buffered saline (PBS) at 100 mV s<sup>-1</sup> scan rate (potential range: -1 to 0.4 V vs Ag/AgCl). The corresponding loss was calculated after 500 cycles. Results are ±SD, N = 3.

	Bare platinum (Pt)	Gold coated (Au)	Pristine PEDOT:PTS	Flattened PEDOT:PTS	Micro-topographically functionalized PEDOT:PTS
Initial CSC [ $\mu\text{C mm}^{-2}$ ]	15.57 ± 0.66	25.12 ± 0.66	48.82 ± 0.49	19.09 ± 0.77	131.01 ± 8.05
Final CSC [ $\mu\text{C mm}^{-2}$ ]	4.36 ± 0.17	15.79 ± 0.31	31.01 ± 0.11	0.38 ± 0.04	96.41 ± 22.23
Electroactivity loss [%]	72.10 ± 1.61	37.17 ± 0.23	36.50 ± 0.41	98.1 ± 1.52	26.42 ± 6.33

effective electroactive surface area relative to pristine and flattened PEDOT:PTS coated microelectrodes, and increased even further when compared with the bare platinum and gold coated microelectrodes. The electroactive surface area was measured using a redox probe (2.5 mol dm<sup>-3</sup> K<sub>4</sub>[Fe(CN)<sub>6</sub>] in 0.1 M KCl) solution and estimated according to the Randles–Sevcik equation (Equation (1)). Figure 3B shows that it is enough to deposit an electroactive PEDOT:PTS layer on the surface of Pt microelectrodes to observe a 5× increase in effective surface area, also reported in previous studies into electroactive polymers.<sup>[99,100]</sup> Further, micropit functionalization resulted in a 2× increase in the microelectrode electroactive surface area relative to pristine PEDOT:PTS coated microelectrodes. Likewise, the micro-topographically functionalized PEDOT:PTS coated microelectrodes induced a significant 12× increase in effective surface area relative to Pt microelectrodes and a significant 11× increase relative to gold coated microelectrodes. It is noteworthy that electroactive surface area between bare platinum and gold coated microelectrode controls was not significantly different.

Following PEDOT:PTS coated microelectrode flattening via imprinting with a planar glass substrate, microelectrode effective surface area was decreased relative to both micro-topographically functionalized and pristine PEDOT:PTS coated microelectrodes. This is due to an overall reduction of microelectrode surface area and lower  $R_a$  when compared to the pristine and PEDOT:PTS functionalized microelectrodes. However, flattened PEDOT:PTS microelectrodes still possessed an increased electroactive surface area relative to bare platinum and gold coated microelectrodes.<sup>[49]</sup> The evolution of electroactive surface area is of importance for microelectrodes, especially because the currents measured with implanted neural recording devices are in the range of  $\mu\text{A}$  or below.<sup>[101–104]</sup> This, together with the nontypical shape of CVs,<sup>[105]</sup> makes the process of optimization of microelectrode modification a challenging task. Complimentary data obtained with larger electrodes (1.6 cm<sup>2</sup>) as part of the optimization process for this work are presented in Figure S3 (Supporting Information).

Comparative electrochemical impedance spectroscopy (EIS) profiles of all experimentally modified microelectrodes are presented in the form of a Bode diagram (Figure 3C) and Nyquist plot (Figure 3D). Overall, micro-topographically functionalized PEDOT:PTS microelectrodes exhibited the lowest impedance profile within the 0.1 Hz to 100 kHz frequency range, lower than that of pristine PEDOT:PTS microelectrodes and significantly lower than that of gold coated and bare platinum microelectrodes. This indicates the superior electrical performance of electrodes subjected to micro-topographical functionalization and the diminishing effect of the process of PEDOT:PTS

flattening on the electrochemical properties of microelectrodes, due to the impact of the former on volumetric changes of the coating.<sup>[98]</sup>

The detailed insight into the process of charge transport was possible by the simulation of EIS data with an equivalent electrical circuit. As shown in Figure 3D, a Randles equivalent circuit<sup>[106,107]</sup> was indicated as the most appropriate and was used to fit the impedance data. The parameters of the equivalent circuit included the solution resistance ( $R_s$ ), resistance of microelectrodes ( $R_m$ ), constant phase element ( $\text{CPE}_1$ ), and the diffusion impedance ( $Z_w$ ) (replaced with  $\text{CPE}_2$  in the case of flattened PEDOT:PTS coated microelectrodes and gold coated microelectrodes). The simulated data confirmed the lowest resistance of micro-topographically functionalized PEDOT:PTS coated microelectrode (3.11 ± 0.13 k $\Omega$ ), when compared to pristine (12.01 ± 1.53 k $\Omega$ ) and flattened (357.77 ± 14.64 k $\Omega$ ) PEDOT:PTS coated microelectrodes, as well as bare platinum (40.28 ± 0.63 k $\Omega$ ) and gold coated (23.61 ± 1.28 k $\Omega$ ) microelectrodes. The summary of resistance calculated values is tabulated in Table 3.

The range of impedance as well as the magnitude of resistance achieved by micro-topographically functionalized PEDOT:PTS microelectrodes place them among the surface-materials suitable for use in neural stimulation and recording.<sup>[108,109]</sup>

To further confirm the effects of micropit topographical functionalization on enhancing the electrical performance of the PEDOT:PTS coated microelectrode through an increase in surface area, force-controlled current–voltage ( $I$ – $V$ ) spectra were recorded employing conductive-AFM (C-AFM) (in PeakForce Tuna mode, PF Tuna, Bruker) using a system detailed in Figure S4 (Supporting Information). Figure 3E shows the surface topography and the corresponding distribution of the electrical profile at the nanoscale level within a micro-topographically functionalized PEDOT:PTS coated microelectrode, respectively. The comparative  $I$ – $V$  curves provide additional insights into the role of the micropit topography in generating lower resistance profiles of the PEDOT:PTS relative to nonimprinted peripit regions. This effect is likely due to a differential response in potential across the pit, resulting in a linear increase in current compared to a steady response seen on the  $I$ – $V$  relationship from the nonpatterned region.

In order to determine the stability of PEDOT:PTS functionalized microelectrodes, substrates were subjected to 500 cycles of continuous potentiodynamic stimulation with the aim of testing, under working conditions, the durability and the electrochemical robustness of the potential neural electrodes.<sup>[8,110,111]</sup> The loss in electroactivity of the microelectrodes was calculated as a percentage based on CSCs recorded before and after

**Table 3.** Summary of the calculated resistance values ( $R_m$ ), solution resistance values ( $R_s$ ), constant phase element parameters ( $P$ : pseudocapacitance,  $n$ : exponent), and Warburg coefficients ( $W_{s1}$ ,  $W_{s2}$ ) of bare platinum (Pt) and gold coated (Au) microelectrodes and pristine PEDOT:PTS, flattened PEDOT:PTS, and micro-topographically functionalized PEDOT:PTS coated microelectrodes after equivalent circuit analysis. Results are  $\pm$  STD.  $N = 3$ .

		Bare platinum (Pt)	Gold coated (Au)	Pristine PEDOT:PTS	Flattened PEDOT:PTS	Micro-topographically functionalized PEDOT:PTS
$R_m$ [kOhms]		40.28 $\pm$ 0.63	23.61 $\pm$ 1.28	12.01 $\pm$ 1.53	357.77 $\pm$ 14.64	3.11 $\pm$ 0.13
$R_s$ [kOhms]		3.00 $\pm$ 0.16	0.92 $\pm$ 0.02	8.59 $\pm$ 0.11	27.50 $\pm$ 0.32	4.41 $\pm$ 0.04
CPE <sub>1</sub>	$P_2$	4.57 $\times 10^{-6} \pm 0.06 \times 10^{-6}$	3.88 $\times 10^{-4} \pm 0.09 \times 10^{-4}$	6.40 $\times 10^{-6} \pm 0.40 \times 10^{-6}$	9.89 $\times 10^{-6} \pm 0.36 \times 10^{-6}$	1.03 $\times 10^{-5} \pm 0.05 \times 10^{-5}$
	$n_2$	0.143 $\pm$ 0.002	0.151 $\pm$ 0.003	0.538 $\pm$ 0.013	0.381 $\pm$ 0.007	0.323 $\pm$ 0.010
$Z_w$	$W_{s1}$	4.50 $\times 10^5 \pm 0.21 \times 10^5$	–	1.45 $\times 10^5 \pm 0.05 \times 10^5$	–	5.01 $\times 10^4 \pm 0.12 \times 10^4$
	$W_{s2}$	0.525 $\pm$ 0.099	–	0.377 $\pm$ 0.015	–	0.422 $\pm$ 0.014
CPE <sub>2</sub>	$P_1$	–	7.39 $\times 10^{-5} \pm 0.19 \times 10^{-5}$	–	1.05 $\times 10^{-6} \pm 0.03 \times 10^{-6}$	–
	$n_1$	–	0.629 $\pm$ 0.009	–	1 $\pm$ 0.015	–

stability studies (Table 2). A high loss in CSC was observed for Pt sputtered microelectrodes due to the thickness differences, with a 72% loss. By contrast, with a comparable working thickness obtained with gold coated microelectrodes, a significantly lower percentage loss of 37% was observed which was similar to the percentage loss obtained with PEDOT:PTS coated microelectrodes. Significantly, flattened PEDOT:PTS coated microelectrodes were associated with a diminution of performance, with a loss of 98%. Overall, superior electrochemical stability and robustness were observed with micro-topographically functionalized PEDOT:PTS coated microelectrodes with an electroactivity loss of 26%. This stability effect, coupled with the high effective surface area and the low impedance profiles, identifies the micro-topographically functionalized PEDOT:PTS coated microelectrodes developed here, as functionalized microelectrodes with potential in neural stimulation and recording performance.

### 2.3. Biological Characterization

Neural interfaces that promote neural integration, with a minimal inflammation response, are persistent challenges within the realms of biomaterials and neural engineering. Even though the cellular response to topography is cell specific, it has been shown that topographical modifications may contribute significantly to addressing the challenges of selective cell adhesion and modulated cell behavior to reduce gliosis at the material–tissue interface.<sup>[11,2]</sup>

The neural response to micropit topographies replicated in PEDOT:PTS coated 1.6 cm<sup>2</sup> Pt electrodes was evaluated using primary ventral mesencephalic (VM) mixed neural cell population in vitro in Figure S5 (Supporting Information).

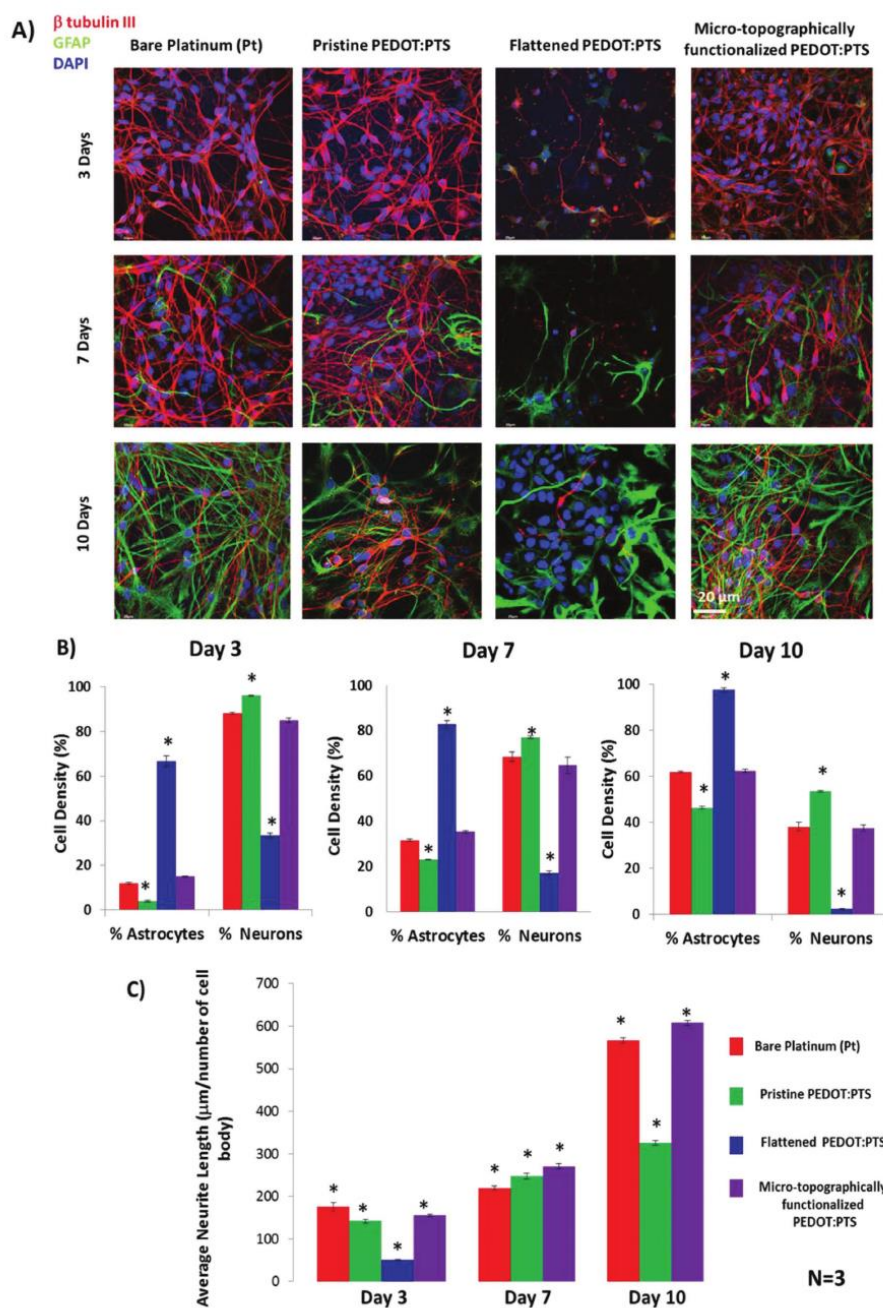
Topographical functionalization to modulate differential cell adhesion and the observation that flat or nonstructured electrodes surfaces favor astrocyte adhesion has been reported previously.<sup>[14,56,113]</sup> A recent study by Seker and co-workers<sup>[56]</sup> demonstrated the efficacy of nano-topographical modification of the electrode surface in reducing focal adhesion formation in astrocytes while maintaining neural integration on np-Au surfaces. Conversely, Qi et al.<sup>[114]</sup> showed that micropatterned

topographies, with dimensions ranging 2–10  $\mu$ m, influence the differentiation of adult neural stem cells (ANSCs) into neurons, and may discourage the differentiation of astrocytes.

Figure 4A shows representative fluorescent micrographs of VM derived mixed cultures of neurons and astrocytes cultured on experimental and control electrodes. All groups were evaluated over a period of three, seven, and ten days in culture. The persistence of neurons and astrocytes on each of the experimental and control groups as a function of time is presented in Figure 4B. The percentage cell density of astrocytes and neurons on each assessed group initially indicated that flattened PEDOT:PTS electrodes induced a significant linear increase of astrocytic presence as a function of time, with a subsequent significant decrease in neuronal presence relative to all experimental and the bare platinum control substrates. By day ten, the flattened PEDOT:PTS coated electrodes exhibited an astrocyte presence of 97.67% and a 2.32% neuron presence. Interestingly, pristine PEDOT:PTS coated electrodes induced a significant decrease in astrocytic presence and a significant increase in neuron cell populations present at each time point relative to all the experimental and control groups. Following ten days in culture, the astrocyte and neuron presence on pristine PEDOT:PTS coated electrodes were 46.39% and 53.60%, respectively. Furthermore, when comparing the neuron and astrocyte cell density populations with control platinum and micro-topographically functionalized PEDOT:PTS coated electrodes, an identical trend with no statistical difference was observed for differential neuron or astrocytes density over time. Following ten days in culture, the astrocyte populations on control platinum and micro-topographically PEDOT:PTS coated electrodes were recorded at 61.97% and 62.46%, respectively, 16% greater than that on pristine PEDOT:PTS coated electrodes.

In conjunction with cell density, as an indicator of cell viability, neurite length on experimental and control substrates was also analyzed (Figure 4C). At day three, a significant decrease in neural length was observed on all experimental groups relative to Pt electrodes on which mean neurite length was 175.08  $\mu$ m  $\pm$  10.55. This trend was lost by day seven and a linear increase in length as a function of electrode surface area was observed. However, neurite length on mechanical flattened control samples could not be quantified due to a significant





reduction in neuron presence, making the application of the stereology method used for the quantification of length invalid.

Further significant differences in neural length were observed by day ten, with significant neurite elongation exhibited in cells cultured on micro-topographically functionalized PEDOT:PTS electrodes ( $607.68 \mu\text{m} \pm 5.53$ ) relative to Pt control ( $566.36 \mu\text{m} \pm 6.35$ ) and pristine PEDOT:PTS coated electrodes ( $325.76 \mu\text{m} \pm 4.66$ ).

These results indicate that pristine PEDOT:PTS coatings do not enhance astrocyte proliferation and adhesion relative to control Pt electrodes and that micropatterning of PEDOT:PTS coatings can be employed to significantly enhance neurite length in vitro. Conversely, mechanically flattened PEDOT:PTS coated electrodes induced overall poor viability/adhesion of the primary mixed VM cell population relative to all other experimental conditions.<sup>[14,113]</sup> That neurons cultured on pristine PEDOT:PTS coated electrodes exhibited a higher frequency but with significantly shorter neural processes relative to Pt electrodes and micro-topographically functionalized PEDOT:PTS coated electrodes may suggest that network development in ventral mesencephalic derived neurons is not entirely supported on nanoroughened, pristine electrodes.<sup>[115,116]</sup> Critically, VM derived glial cells promote neuronal survival and neurite growth by releasing growth factors and providing an ideal biochemical milieu in vitro for neuronal development.<sup>[115]</sup> Thus, although pristine PEDOT:PTS coated electrodes were associated with a significant reduction in astrocyte density and promoted more neural coverage relative to cell population ratios observed on bare platinum and micro-topographically functionalized PEDOT:PTS coated electrodes; this phenomenon did not translate into the development of an extensively interconnected functional neural network. Rather, it may suggest the onset of a proinflammatory response.<sup>[115]</sup> Neurite length was significantly increased on the micro-topographically functionalized PEDOT:PTS coated electrodes by day ten relative to all experimental groups, suggesting that neurons may benefit from the presence of an underlying glia network and a morphological response to micro-topographical features may be manifested in enhanced neurite extension. This observation is supported by previous research into topographical features supporting neural outgrowth through supportive cues.<sup>[84,117–119]</sup> Also, it can be inferred that neurite extension on micro-topographically functionalized PEDOT:PTS coated electrodes may suggest a reduced inflammatory environment from the glial interactions relative to all experimental and control groups.<sup>[115]</sup>

In order to assess the reactivity of astrocytes (the key players in astrogliosis) on fabricated electrodes, the mean cellular area was quantified as a morphological indicator of a reactive astrocyte phenotype again using a primary VM mixed cell culture model. Critically, morphological analysis of astrocyte

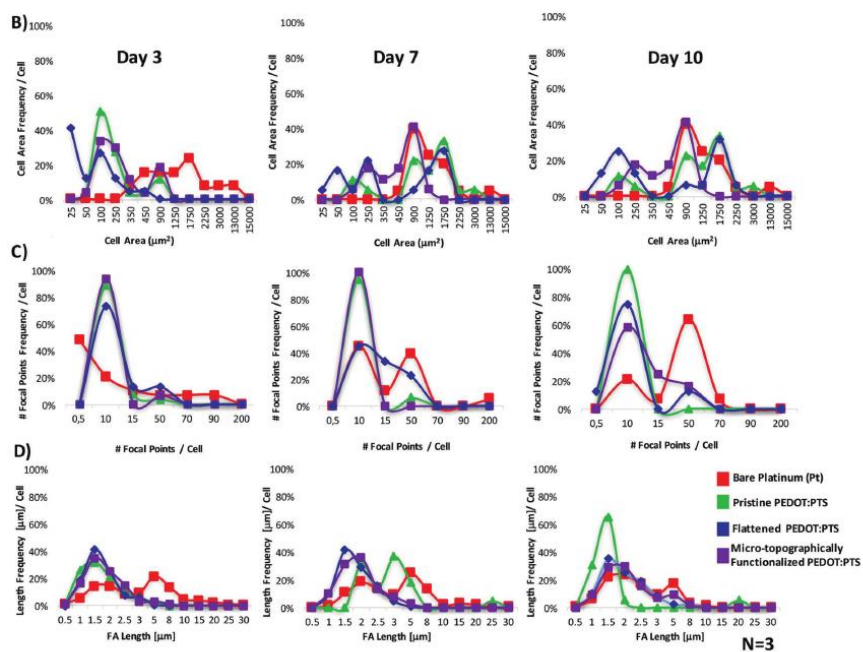
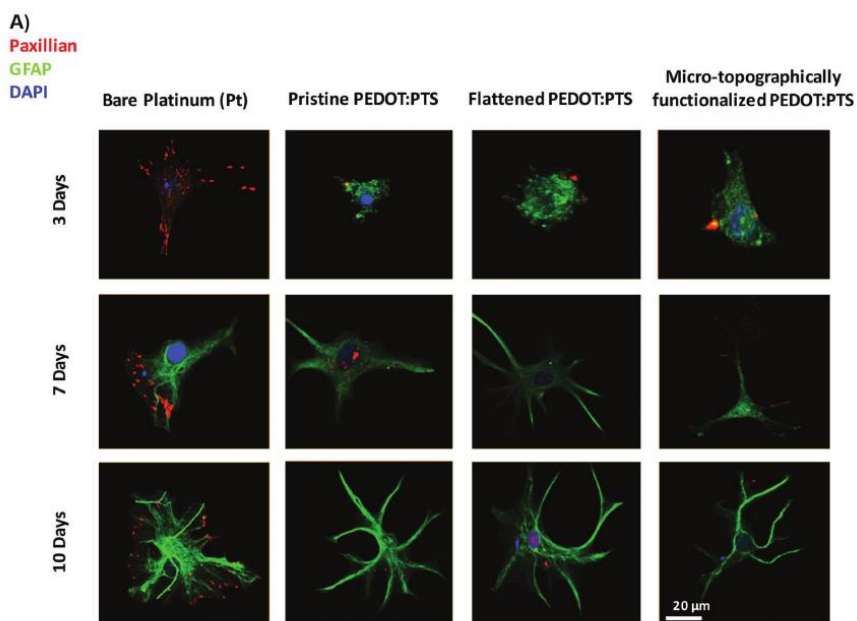
populations has been shown repeatedly to provide helpful insights into resting or activated functional states in astrogliosis, considering astrocytic heterogeneity.<sup>[120,121]</sup> Furthermore, to assess modulated astrocyte morphology and adhesion on experimental electrodes, glial fibrillary acidic protein (GFAP) immunofluorescent labeling was conducted in conjunction with Paxillin labeling, a key focal adhesion protein (Figure 5A). It has been shown in vitro that in 2D cultures neurons will grow on the dorsal surface and extend processes along topographical cues provided by an astrocyte monolayer.<sup>[57]</sup> Consequently, it has been suggested that astrocyte presence on an implanted electrode is critical to support neural integration and neurite outgrowth.<sup>[60]</sup> Rather, it is the reduction of a reactive astrocyte phenotype presence that is a potential functionalization strategy in minimizing astrogliosis in peri-electrode glial scar formation.<sup>[54]</sup>

Representative fluorescent micrographs of isolated astrocytes from the mixed primary VM cell cultures grown on controls Pt and experimental PEDOT:PTS functionalized electrodes were captured over three, seven, and ten days in culture (Figure 5A). Figure 5B represents the distribution of astrocyte cell areas as a function of GFAP staining over time. The distribution of the astrocyte cell area is significantly shifted toward a greater astrocyte cell area on Pt electrodes relative to pristine PEDOT:PTS, flattened PEDOT:PTS, and micro-topographically functionalized PEDOT:PTS coated electrodes. By day ten, the frequency of astrocyte cell areas between the ranges of  $450$  and  $2250 \mu\text{m}^2$  on Pt electrodes was significantly increased. Astrocyte cultured on pristine PEDOT:PTS, flattened PEDOT:PTS, and micro-topographically functionalized PEDOT:PTS coated electrodes, however, exhibited a bimodal distribution of cell area, with significant peaks also observed in the  $50$ – $350 \mu\text{m}^2$  cell area range. Interestingly, micro-topographically functionalized PEDOT:PTS coated electrodes were associated with the lowest astrocyte area distribution when compared to control and experimental substrates at all time points. It was observed by day ten that the 80% of the astrocyte cell areas were confined within the ranges of  $100$  and  $1250 \mu\text{m}^2$ . These findings are particularly important, as it has been shown that the variations in overall astrocytic cell area underlie reactivity implications over time,<sup>[120,122,123]</sup> where enlarged astrocytes areas may translate into moderate and/or severe reactive astrogliosis.<sup>[122]</sup>

Of further interest is the observation that the increased frequency of astrocytes with enlarged cell areas observed on bare platinum, pristine PEDOT:PTS, and flattened coated electrodes is associated with a reduction in neural outgrowth relative to neurons cultured on microfunctionalized PEDOT:PTS electrodes, again pointing to a reactive astrocyte induced disruption of network evolution. This effect was largely accentuated on flattened PEDOT:PTS coated electrodes.

**Figure 4.** Cellular and morphometric analysis of functionalized electrodes. A) Fluorescent images of primary ventral mesencephalic (VM) mixed cell population grown on each of the bare platinum (Pt) and functionalized PEDOT:PTS coated electrodes for three, seven and ten days in culture. Neurons are visualized by anti  $\beta$ -tubulin III, in red, astrocyte cells by anti-GFAP, in green and nuclei are visualized by DAPI, in blue. Bar =  $20 \mu\text{m}$ , objective  $60\times$  magnification. Cell density (%) analysis of astrocytes and neurons presence on each of the electrodes is presented in (B). An overall significant ( $p < 0.05$ ) decrease in viability of neurons and astrocytes density was observed in flattened PEDOT:PTS coated electrodes. Neural length analysis of electrodes presented in (C) showed with significant ( $p < 0.05$ ) longer neurite lengths the neurons grown on micro-topographically functionalized PEDOT:PTS coated electrodes.  $\star = p < 0.05$ .





In order to evaluate perturbation of assessed electrode topography on astrocyte adhesion and to draw parallels between reactive astrocyte phenotype and focal adhesion formation, quantification of mean cellular focal adhesion number and length was carried out (Figure 5C,D). The regulation of focal adhesion formation in adherent cells, such as astrocytes, involves complex recruitment of integrin-dependent signaling pathways mainly mediated by nonreceptor tyrosine kinases, markedly by focal adhesion kinase (FAK).<sup>[124]</sup> Further, it has been shown that mediated signaling through FAK/Paxillin in astrocytes plays an important role in astrocyte cell morphology, where a reduction of tyrosine phosphorylation and paxillin expression is related to the stellation of astrocytes.<sup>[125–127]</sup> However, in pathological situations, astrocytes no longer adopt a stellar appearance but become hypertrophic in morphology, and are associated with increased focal adhesion signaling, so-called reactive astrocytes.<sup>[128–131]</sup> Certainly, cell-adhesion is mainly controlled through cell–substrate interactions, where topographies have been shown to play an essential role.<sup>[50]</sup>

Analysis of the distribution of focal adhesion (FA) frequency and length in astrocytes on bare platinum electrodes indicated that at day three 70% of the astrocytes exhibited ten focal adhesion contacts per astrocyte with lengths ranging between 0.5 and 10  $\mu\text{m}$ . By day ten, a significant increase in astrocytes adhesion was observed with 70% of the astrocytes exhibiting between 15 and 70 focal adhesion points per cell with maintained focal adhesion lengths between the ranges of 0.5 and 8  $\mu\text{m}$  compared to day three. These results suggest a decrease of cell motility owing to the higher number of focal adhesion contacts per cell, but further to the stable lengths achieved,<sup>[52]</sup> results that in light of the augmented astrocytic cell areas observed on these electrodes showed the development of more focal adhesion contacts suggesting the presence of a more reactive astrocyte phenotype. In addition, bare platinum ( $R_a$ : 2 nm), commonly used in neural electrodes, does not allow for the selective control of cell adhesion (Figure 5B), which together with its mechanical rigidity may account for the overall higher reactive astrocyte presence than that of more compliant conducting polymeric coated electrodes.<sup>[132]</sup>

On the other hand, the pristine PEDOT:PTS coated electrodes, the flattened PEDOT:PTS coated electrodes, and the micro-topographically functionalized PEDOT:PTS coated electrodes were associated with similar astrocyte adhesion over time, with overall focal adhesion numbers significantly less than those observed on bare platinum electrodes.

By day ten, more than 80% of the astrocytes on both, pristine PEDOT:PTS and the flattened PEDOT:PTS coated electrodes, presented a mean value of fifteen focal adhesions per cell. Conversely, micro-topographically functionalized PEDOT:PTS coated electrodes induced significant modulation to the distribution

of the number of astrocyte focal adhesion with 38% of the astrocyte population exhibiting an increase in the mean number of focal adhesions per cell of between 15 and 50 focal adhesions per astrocyte. This observation together with the comparatively lower astrocyte areas observed on the micro-topographically functionalized PEDOT:PTS coated electrodes may allude to a differential effect in astrocyte adhesion and a reduction in reactive astrocytes presence as a function of micro-topographical modification. The length of the astrocyte focal adhesion points did not change significantly over time on flattened PEDOT:PTS coated electrodes and on micro-topographically functionalized PEDOT:PTS coated electrodes, with lengths confined between the ranges of 0.5 and 5  $\mu\text{m}$ . By contrast, pristine PEDOT:PTS coated electrodes resulted in shorter astrocyte focal adhesion contact lengths between the ranges of 1 and 1.5  $\mu\text{m}$  by day ten.

It has been shown by our studies in other fields that ordered nanopits topographies are proposed to impair focal adhesion formation by disrupting integrin activation and clustering, an effect enhanced at the microscale length.<sup>[50,51,56,59]</sup> Indeed, experimentally this work has shown that PEDOT:PTS coated electrodes functionalized with a micropit topography have a significant influence on reactive astrocyte adhesion. Furthermore, these findings present opportunities to study reactive astrocyte presence through cytoskeleton-linked proteins signaling mechanisms controlling astrocyte phenotype.

Understanding the glia interactions as key contributors in the glial scar formation is essential,<sup>[54]</sup> and in addition to influencing cytoskeleton-linked proteins, substrate topography has been previously shown to affect cellular function and the synthesis of cytokines and signaling molecules in neural cells.<sup>[133,134]</sup> To elucidate further the roles of topographical functionalization on the neural response in vitro, changes in the expression of proinflammatory cytokines and chemokine factors were assessed via multiplex enzyme-linked immunosorbent assay (ELISA) analysis. Currently, few studies have examined the effect of topographical functionalization on the glial cell functional response in complex mixed cell cultures.<sup>[75]</sup> With this in mind, glial-derived cytokines and chemokine factors, such as interferon- $\gamma$  (IFN- $\gamma$ ), tumor necrosis factor- $\alpha$  (TNF- $\alpha$ ), interleukin-6 (IL-6), interleukin-5 (IL-5), and chemokine factor CXCL-1 (KC/GRO), involved in mediating neuronal–glial interactions and modulation of reactive astrogliosis were selected for analysis.<sup>[135–140]</sup> The release profiles were compared between each of the experimental groups and controls, and with an additional inflammatory control group, VM cells cultured on Thermanox Plastic Coverslips (tissue culture plastic) which received a stimulus of interleukin-1beta (IL-1 $\beta$ ) at a dose of 10 ng mL<sup>-1</sup>. Complementary data for the optimization of the different concentrations of IL-1 $\beta$  as inflammatory stimuli on

**Figure 5.** Morphoadhesion characteristics of astrocyte presence in the functionalized electrodes toward astrocyte reactivity indication. A) Selective fluorescent images of astrocytes from primary ventral mesencephalic (VM) mixed cell population grown on each of the bare platinum (Pt) and functionalized PEDOT:PTS coated electrodes for three, seven, and ten days in culture. Astrocytes are visualized by anti-GFAP, in green, formation of focal adhesion contacts by anti-Paxillin, in red and nuclei are visualized by DAPI, in blue. Bar = 20  $\mu\text{m}$ , objective 60 $\times$  magnification. Frequency distribution in time (three, seven, and ten days) of cytoplasm astrocyte areas ( $\mu\text{m}^2$ ) on bare platinum (Pt) and functionalized PEDOT:PTS coated electrodes is presented in (B). The frequency distribution of astrocyte areas on micro-topographically functionalized PEDOT:PTS coated electrodes showed the lowest frequencies over time. C) The frequency distribution of the astrocyte focal adhesion contact numbers per cell and their corresponding length frequency distribution over time in (D).

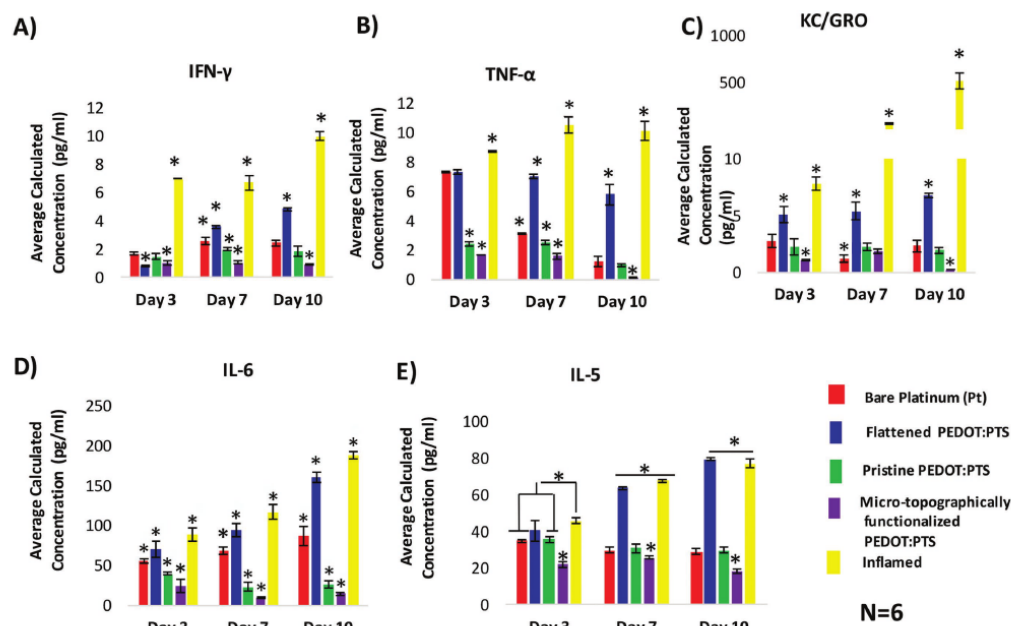


**Figure 6.** Comparative gliosis derived cytokines and chemokine factor profiling for A) interferon- $\gamma$  (IFN- $\gamma$ ), B) tumor necrosis factor- $\alpha$  (TNF- $\alpha$ ), C) chemokine factor CXCL-1 (KC/GRO), D) interleukin-6 (IL-6), E) and interleukin-5 (IL-5). The release expression of each of the signaling molecules is analyzed from primary ventral mesencephalic (VM) mixed cell population supernatants collected at days three, seven, and ten on bare platinum (Pt) and functionalized PEDOT:PTS coated electrodes. An important effect is seen on the micro-topographically functionalized PEDOT:PTS coated electrodes, which presented significantly and consistently low release profiles for each cytokine and chemokine factor analyzed. Results are  $\pm$  STD,  $\star = p < 0.05$ .

VM cells cultures are shown in Figure S6 (Supporting Information) with the analysis of the production of reactive oxygen species (ROS), CellROX, and in Figure S7 (Supporting Information) with the quantification of activated microglia using methods for morphofunctional analysis described in ref. [141], respectively.

The secretion of proinflammatory cytokines and chemokine factors in mixed cell populations cultured on all experimental and control groups is presented in Figure 6. It is interesting to note that even though there is a linear increase in the release profile of IFN- $\gamma$  in mixed cultures exposed to inflamed control conditions and when cultured on flattened PEDOT:PTS coated electrodes over time, Pt electrodes and pristine PEDOT:PTS coated electrodes followed a trend over time that was similar and constant, with no statistical differences noted between the expression profile of IFN- $\gamma$  at day three and day ten, respectively (Figure 6A). Importantly, the lowest release profile of IFN- $\gamma$  was observed with the micro-topographically functionalized PEDOT:PTS coated electrodes, with a maintained overall low and statistically significant release of this cytokine relative to all experimental and control groups by day ten. This cytokine is reportedly a crucial immunological player, as it regulates relevant genes for cell function and cell programming.<sup>[141]</sup> Studies have shown that IFN- $\gamma$  has a unique action on astrocytes, inducing

proinflammatory activities and enhancing astrocyte-immunoreactivity.<sup>[139,142]</sup> In a similar manner, TNF- $\alpha$  cytokine is known to act in synergy with IFN- $\gamma$ ,<sup>[143]</sup> showing a similar release trend on day seven and day ten, respectively, relative to the release profiles of IFN- $\gamma$  on these days (Figure 6B). Over time, a linear decrease in TNF- $\alpha$  release was observed in all groups and controls, except for on the inflamed control group that presented a consistently high release profile of TNF- $\alpha$ . By day ten, a significantly higher release profile of TNF- $\alpha$  was observed in the inflamed control group which was comparable to that observed in VM cells cultured on flattened PEDOT:PTS coated electrodes. Control Pt, pristine PEDOT:PTS, and micro-topographically functionalized PEDOT:PTS groups were associated with a significant reduction in TNF- $\alpha$  synthesis and cells cultured on topographically functionalized PEDOT:PTS coated electrodes produced significantly less TNF- $\alpha$  than Pt control and other PEDOT:PTS experimental groups. These results indicate an activated response from astrocytes and microglia, respectively, with their coordinated involvement in the host response at the material interface.<sup>[139,143]</sup> Furthermore, the micropit topography utilized here also induced a reduced glial cell inflammatory response via chemokine (C-X-C motif) ligand 1 (CXCL-1), also known as KC/GRO (Figure 6C). CXCL-1 is associated with neutrophil recruitment, to a site of inflammation,<sup>[144]</sup> and a study by Rubio and Sanz-Rodríguez<sup>[145]</sup>

showed that astrocytes, as an early cell component of the neuro-immune response, produced CXCL-1 in the chemoattraction of the neutrophils and monocytes in neuroinflammatory diseases. In this work, it was observed that by day ten, in contrast to a relatively high release profile of CXCL-1 from the inflammatory control conditions, an overall significantly lower release response of CXCL-1 was exhibited by VM populations cultured on the micro-topographically PEDOT:PTS functionalized electrodes, a response maintained up to day ten in culture.

In primary mixed cultures, such as in the VM cells used in this research, as a consequence of the orchestrated release of cytokines and growth factors in neuronal–glial interactions,<sup>[139]</sup> there is a synergistic effect that allows them to work as costimulatory molecules to potentiate immune interactions, in this case at the local neuron–glial unit, with a resulting increase of specific cytokines response, such as IL-6.<sup>[138,139,145]</sup>

At day three (Figure 6D), IL-6, which plays a vital role in immune regulation and is produced by astrocytes, microglia, and neurons in injury-inflamed milieu,<sup>[146–150]</sup> showed a significantly potentiated release profile in the inflammatory control group, relative to an observed significant linear decrease in the release profile in VM cells cultured on all control and experimental electrode substrates. On day seven, comparatively significant increases in the release levels of IL-6 were observed on pristine and micro-topographically functionalized PEDOT:PTS electrodes relative to day three on bare platinum electrodes, flattened PEDOT:PTS coated electrodes, and on the inflamed control, with significantly lower levels of IL-6 released VM cells cultured on micro-topographically functionalized PEDOT:PTS electrodes, maintained up to day ten.

Similar trends in the expression levels of IL-5 were also observed (Figure 6E), an important and often overlooked pro-inflammatory cytokine that has been shown to be produced by astrocytes and microglia in vitro.<sup>[138,149]</sup> Further, IL-5 has been shown to induce nerve growth factor secretion by astrocytes.<sup>[151–153]</sup> Again, the released IL-5 concentrations from micro-topographically functionalized PEDOT:PTS coated electrodes showed significant lower release profiles when compared to all groups, controls, and inflamed control, respectively, at all time points.

Cytokines protein interactions adopting a confidence score >0.7 as the threshold to assess associations were performed and are detailed in Figure S8 (Supporting Information). These results suggest that the cytokine expression profiles observed from VM cells cultured on micro-topographically functionalized electrodes support an overall neural–glial interaction at the electrode, associated with minimized reactive gliosis over time.<sup>[154]</sup> Indeed, this work has shown experimentally that the micro-topographically functionalized PEDOT:PTS coated electrodes here developed reduced the cytokine mechanisms of astroglial in vitro. This response was accentuated relative to bare platinum electrodes and pristine PEDOT:PTS coated electrodes, but further stressed when compared to flattened PEDOT:PTS coated electrodes, which resulted in the promotion of a more proinflammatory cytokine release and chemokine factors, reflected in the poor VM cell viability and outgrowth.

To evaluate the neuronal network activity and functionality of the neuronal population interfaced on topographically functionalized electrodes, further studies were conducted with mature

explanted primary rat hippocampal neurons, which unlike embryonic VM populations present functional neuronal network after seven to ten days in culture offering an important advantage to embryonic cells in terms of culture times.<sup>[155]</sup> Rat hippocampal cells were seeded on bare platinum electrodes, pristine PEDOT:PTS, and on the micro-topographically functionalized PEDOT:PTS coated electrodes. Flattened PEDOT:PTS coated electrodes were not further evaluated due to the significant decrease in neuronal presence observed throughout the study.

Rat hippocampal cells successfully adhered and matured in all substrates and were analyzed after eight to ten days in vitro (three series of different cultures each), shown previously to be sufficient time to facilitate functional synaptic network development in vitro with matured explants.<sup>[156–158]</sup>

The formation of active synaptic networks was investigated by simultaneously imaging the intracellular calcium activity of living neurons (ten days in vitro) on representative regions of  $660 \times 660 \mu\text{m}^2$ . Neurons stained with the membrane permeable  $\text{Ca}^{2+}$  dye Oregon Green 488 BAPTA-1 were visualized within the sampled area and  $8 \pm 2$  fluorescent cells were selected (regions of interest, ROIs) in each field ( $n = 25$  fields), as in Figure S9A (Supporting Information). At ten days in vitro, matured neurons are synaptically connected and display spontaneous activity including bursts which manifest as irregular synchronized firing epochs.<sup>[159]</sup> This can be appreciated in Figure S9B (Supporting Information), where two representative traces from ROIs in the same field are shown for each condition. The spontaneous bursting activity was fully blocked by tetrodotoxin (TTX) ( $1 \times 10^{-6}$  M, not shown) application, thus confirming the neuronal nature of the recorded signal.<sup>[159]</sup> The occurrence of spontaneous  $\text{Ca}^{2+}$  episodes in active cells was measured by quantifying the inter-event interval (IEI). IEIs distribution was found to be different in the PEDOT:PTS-interfaced neuronal cultures (pristine and micropatterned electrodes) when compared to those grown onto bare platinum electrodes ( $^{**}p < 0.01$ , box plot in Figure S9C, Supporting Information) suggesting a different coupling of the network with the substrate. However, median IEI values were comparable, being 9 and 10 s for pristine PEDOT:PTS and micro-topographically functionalized PEDOT:PTS, respectively, and 9 s for platinum (Figure S9C, Supporting Information). The tested electrodes demonstrated a good cytocompatibility promoting functional hippocampal neurons development and allowing synaptogenesis and active network formation. In the presence of PEDOT:PTS coatings, neuronal activity appeared to be more organized into regular bursts and it may suggest that these might be related to the generation of a more favorable environment for neuronal activity. In turn, it was evident by the neuronal and astrocyte phenotypes visualized by immunofluorescence image of the specific cytoskeletal component,  $\beta$ -tubulin III, to visualize neurons, and GFAP to visualize astrocytes (Figure S10A, Supporting Information) that a higher neuronal density was present on micro-topographically functionalized PEDOT:PTS coated electrodes. In addition, a decrease in the astrocyte-to-neuron ratio was observed on functionalized electrodes relative to bare platinum or pristine PEDOT:PTS electrodes ( $0.47 \pm 0.16$  vs  $0.73 \pm 0.34$  and  $0.68 \pm 0.26$  for bare platinum and pristine PEDOT:PTS controls



respectively,  $***p < 0.001$  and  $**p < 0.01$ ). These findings indicate that micro-topographically functionalized PEDOT:PTS coated electrodes promote the development of a nonreactive adherent glia network, which promotes neuron–electrode interaction. Therefore, the possibility to exploit micro-topographically engineered PEDOT:PTS electrodes for neural interfacing and astrogliosis modulation is here strengthened.

### 3. Conclusion

The paradigm of neuroelectrode functionalization is the maintenance of electrode functionality and a controlled inflammatory response.<sup>[160,161]</sup> Micropit topographical functionalized PEDOT:PTS coated electrodes were assessed for the first time as a methodology for the design of functionalized neural interface materials with a focus on reduced astrocyte reactive phenotype, enhanced neural integration, and functional capacity.

Topographical functionalized PEDOT:PTS electrodes induced a significant reduction in electrical impedance and an increase in charge storage capacity and effective surface area, while maintaining electrode stability. Furthermore, the role of the micro-topographically modified PEDOT:PTS coated electrodes in reducing the characteristic phenotype associated with astrogliosis in complex primary mixed cell cultures was assessed from the evident morphological changes in cell area, the functional promotion of neural network activity, focal adhesion formation, and the release of proinflammatory cytokines and chemokine factors.

A low temperature imprint-lithography technique developed in this study for the micro-topographically functionalized neuroelectrode interfaces provides a useful benchmark for subsequent studies with neural microelectrodes, and the development of dual functionalization with biological molecules on as-formed conducting polymer coatings. Furthermore, this work could shift the focus on current efforts in the field to attract astrocytes onto the electrode surface, but potentially blocking the negative components found in the glial cell response, *in vitro*.

### 4. Experimental Section

**Fabrication of Microelectrode Arrays:** Ultrashort laser operating at 10 kHz and 1030 nm wavelength with 500 fs pulses duration was used to generate a microelectrode shadow mask in a polyimide film of 0.05 mm thickness. Polyimide samples were placed on a 3D computer controlled stage (Aerotech) which enabled changes in the sample position with micrometer accuracy. The laser was focused on the sample with a 100 mm focal length lens and the scanning system was coupled to the machining stage through combination of different reflectors and mirrors. The laser spot diameter was found to be 25  $\mu\text{m}$  and ablation threshold 0.56  $\text{J cm}^{-2}$ . To avoid the melting of polyimide, a laser fluence of 0.6  $\text{J cm}^{-2}$  just above the threshold and 200 laser scans were used in drawing the electrode circuit design through the polyimide film.

Through-mask sputtering of platinum was achieved with a EMSCOPE SC500 at 25 mA for 20 min. Resulting platinum electrode thickness was measured to be 69.27  $\text{nm} \pm 0.01$  nm and resulted in an electrode size of 287.67  $\mu\text{m} \pm 0.08$   $\mu\text{m}$  in width.

**Imprinting and Die Fabrication:** Micro-topographically functionalized PEDOT:PTS coated electrode were made in a three-step process of

photolithography, nickel die fabrication, and temperature low imprinting process.

**Photolithography:** 100 mm diameter silicon-wafers were first cleaned using the [ozone/distilled (DI) water/dilute-hydrofluoric (HF) acid] cleaning process on a Semitool SAT spray-acid cleaning-tool. The wafers were then coated with photoresist (Fujifilm HiPR6512) and the mask pattern exposed on an Ultratech 1500 stepper, after which the photoresist was developed using Fujifilm OPD5262 developer. A number of different masks were used to give various diameter patterns. The wafers were then dry-etched to the required depth for each pattern using a [SF<sub>6</sub>/C<sub>4</sub>F<sub>8</sub>] plasma on an STS-ASE dry-etch tool. After dry-etching, the photoresist was removed by a combination of O<sub>2</sub> plasma ashing plus Piranha (H<sub>2</sub>SO<sub>4</sub>/H<sub>2</sub>O<sub>2</sub>) wet-strip.

**Nickel Die:** This technique has been described previously.<sup>[51,52]</sup> Briefly, nickel dies were made directly from the patterned resist samples. A thin (50 nm) layer of Ni–V was sputter coated on the samples. That layer acted as an electrode in the subsequent electroplating process. The dies were plated to a thickness of  $\approx 300$  nm. For more information about the procedure, see ref. [162].

**Imprinting Process:** PEDOT:PTS coated electrodes were imprinted by a low temperature imprinting process. Before the imprinting, the processed nickel die master was cut into 1  $\text{cm} \times 1$   $\text{cm}$  pieces, each piece acting as an individual stamp. The polymeric PEDOT:PTS coated electrodes were placed in a desiccator 24 h prior to the imprinting process and then taken one by one to be processed. Using a hydraulic press machine (Carver, Inc), the nickel die stamp was then pressed against the PEDOT:PTS coated electrode, previously placed on pressing paralleled plates, using a compressive force of 1.9 metric tons  $\text{cm}^{-2}$  for 15 min at room temperature.

Flattened controlled nonpatterned PEDOT:PTS coated electrodes were processed by pressing a thick mirror glass stamps against the PEDOT:PTS coated electrode, applying a compressive force of 1.9 metric tons  $\text{cm}^{-2}$  for 15 min at room temperature.

**Physical Characterization—Surface Morphology:** SEM was carried out using a Hitachi S-4700 Cold Field Emission Gun Scanning Electron Microscope (CFE-SEM). The SEM images were taken using an accelerating voltage of 15 kV and spot current of 10  $\mu\text{A}$ . No gold sputtering was used on the conducting PEDOT:PTS coated electrodes.

Scanning electron microscopy for biological samples was carried out using a Hitachi S-4700 CFE-SEM. Cells on experimental electrodes were stabilized in 4% paraformaldehyde with 1% sucrose in 0.1 M piperazine-N,N'-bis(2-ethanesulfonic acid) (PIPES) buffer at pH 7.4 for 5 min. Further, samples were fixed permanently in 2.5% glutaraldehyde for 5 min in PIPES buffer and rinsed three times for 2 min in PIPES buffer. Additional contrasting of the cell was accomplished by staining with 1% osmium tetroxide in PIPES for 1 h at 22 °C and then rinsed in distilled water for 1 min. After this, cells on experimental electrodes were dehydrated through an ethanol/distilled water series (50, 60, 70, 80, 90, 96, and 100%) followed by a hexamethyldisilazane or acetone/ethanol series (25, 50, 75, and 100%). The samples were then left to dry fully and mounted on aluminium stubs, and coated with 10 nm layer of gold (Au).

For surface 3D plots and roughness analysis, AFM was performed as detailed in ref. [7]. All measurements were taken on a Vico Dimension 3100 AFM using TESPA Tips (NanoWorld) (Si < 8 nm tip radius, 42 N  $\text{m}^{-1}$  spring constant, 320 kHz nominal resonance frequency), in tapping mode over an area of 10  $\mu\text{m}^2$  with a 0.5–1 Hz scan rate.

**Physical Characterization—Thickness Measurements:** The thickness of the polymeric PEDOT:PTS coating was measured using a Zygo Newview 100 surface profilometer controlled by MicroPlus software as detailed in ref. [7]. Briefly, a pattern of bright and dark lines–fringes was created as incoming light was split from the limited region between the sample film and the bare platinum electrode. This pattern difference was translated to calculate the height information, resulting in the thickness of the polymeric coatings.

**Chemical Characterization:** X-ray photoelectron spectroscopy (XPS) spectra were acquired on a Kratos AXIS 165 spectrometer XPS system with X-Ray Gun mono Al K $\alpha$  1486.58 eV, 150 W (10 mA, 15 kV), for all



scans with the following parameters: sample temperature in a range of 20–30 °C with a pass energy of 160 eV for survey spectra and 20 eV for narrow regions and steps of 1 eV for survey and 0.05 eV for regions with dwell times of 50 and 100 ms for regions and sweeps for survey of  $\approx 35$ , and for narrow regions of 6–40. The C1s line at 284.8 eV was used as charge reference. Spectra were collected in the normal way to the surface direction with an analysis area of 60  $\mu\text{m}$ . XPS detection limit is estimated to be  $\approx 0.1$  at%. For the data processing, the construction and peak fitting of synthetic peaks in narrow region spectra was done using a Shirley type background and the synthetic peaks were of a mixed Gaussian–Lorentzian type. Relative sensitivity factors used are from CasaXPS library containing Scofield cross-sections.

**Electrochemical Characterization—Preparation of PEDOT:PTS Samples:** The electrodeposition of PEDOT:PTS coatings was conducted under ambient conditions according to methods described previously.<sup>[163]</sup> Briefly, a solution of 0.05 M PEDOT (Sigma-Aldrich, Ireland) and 0.1 M PTS (Sigma-Aldrich, Ireland, 70 000 g mol<sup>-1</sup> MW) was prepared in a 50/50 vol% mixture of acetonitrile and water. The electrolyte solution was placed in an in-house fabricated electrochemical cell, connected to a Princeton Applied Research Potentiostat/Galvanostat model 2273 controlled with Power Suite software. An in-house fabricated platinum microelectrode probe array and a platinum foil (Goodfellow) were used as the working electrode and counter-electrode, respectively. A saturated 3 M KCl Ag/AgCl reference electrode (Bioanalytical Systems) was employed. Galvanostatic electrodeposition was performed and the efficiency of coating, i.e., the amount of polymer deposited on the electrodes, was controlled by the total charge passing during the electrodeposition. When the deposition was finalized, the coated electrodes were soaked in deionized water for 24 h to remove excess of electrolyte and subsequently dried for use. For cell studies, PEDOT:PTS was electrodeposited on electrodes with areas of 1.6 cm<sup>2</sup> to facilitate in vitro manipulations.

**Electrochemical Characterization—Electrochemical Measurements:** Cyclic voltammetry was performed as previously described in ref. [7] using a Princeton Applied Research Potentiostat/Galvanostat model 2273 running with Power Suite software. Measurements were recorded in a custom-made electrochemical cell containing the microelectrode as working electrode, an Ag/AgCl reference electrode (3 M KCl) (Bioanalytical Systems) and a platinum foil counter electrode (Goodfellow) in 1 $\times$  PBS. CVs were run in the potential range from -1.0 to 0.4 V at a scan rate of 0.1 V s<sup>-1</sup>. The CSC was calculated by integrating the area enclosed by the voltammogram.

EIS was performed using a Princeton Applied Research Potentiostat/Galvanostat model 2273 running with Power Suite software with a three-electrode set-up. The measurements were carried out in a frequency range of 0.1 Hz to 100 kHz with an AC sine wave of 40 mV amplitude applied with 0 V DC offset. The results were presented on Bode and Nyquist plots and compared to those of bare platinum microelectrodes and coated gold microelectrodes, to exclude the effect of electrode thickness when compared to PEDOT:PTS coated microelectrodes. The data fitting analysis was performed using EIS Spectrum Analyzer 1.0 software with the application of the Powell algorithm.

Electroactive surface area (ESA) measurements for each microelectrode were done through cyclic voltammetry scans performed in 2.5 mol cm<sup>-3</sup> K<sub>4</sub>[Fe(CN)<sub>6</sub>] 0.1 M KCl solution, in the potential range from -1.0 to 0.4 V at a scan rate of 0.1 V s<sup>-1</sup>. ESA was estimated according to the Randles–Sevcik equation<sup>[164,165]</sup>

$$i_p = 2.69 \times 10^5 AD^{1/2} n^{3/2} \nu^{1/2} C \quad (1)$$

where  $i_p$  is the reduction/oxidation peak current (A),  $n$  is the number of electrons contributing to the redox reaction,  $A$  is the area of the electrode (cm<sup>2</sup>),  $D$  is the diffusion coefficient of Fe(CN)<sub>6</sub><sup>4-</sup> in KCl solution (6.3  $\times 10^{-6}$  cm<sup>2</sup> s<sup>-1</sup>),<sup>[166]</sup>  $C$  is the concentration of the Fe(CN)<sub>6</sub><sup>4-</sup> in the bulk solution (mol cm<sup>-3</sup>), and  $\nu$  is the scan rate (V s<sup>-1</sup>). The measurements were performed in triplicate, the results were expressed as a mean  $\pm$  standard deviation.

The electrochemical stability of microelectrodes was determined as described previously in ref. [8]. Briefly, cyclic voltammetry was performed before and after electrical stability measurements and used to calculate the percentage of loss in charge storage capacity by comparing the CSC of the 1st and 500th cycles. The measurements were performed in triplicate, the results were expressed as a mean  $\pm$  standard deviation.

Force-controlled current–voltage ( $I$ – $V$ ) characteristics were recorded employing C-AFM (in PeakForce Tuna mode, PF Tuna, Bruker). Samples were imaged under ambient conditions with a Bruker Dimension Icon microscope, with a NanoScope IV control unit and PF-TUNA add-on module. One sapphire substrate with gold contact was used to connect samples to form the electric circuit.  $I$ – $V$  curves were recorded at selective positions on the sample surface. C-AFM tips (coated with platinum/iridium) were used as the mobile counter electrode to contact the single-walled carbon nanotubes (SWCNTs) PeakForce-TUNA tips, Bruker. For a schematic of the set-up, see Figure S4 (Supporting Information). The voltage bias was ramped between -500 and 500 mV. The data were then analyzed by NanoScope Analysis (version 1.5, Bruker) and Matlab (version 2016 a).

**Biological Characterization—Cell Culture:** Primary cultures of VM neurons were obtained from the mesencephalon of embryonic Sprague–Dawley rats according to methods previously described by Vallejo-Giraldo et al.<sup>[7]</sup> Briefly, the ventral mesencephalon were dissected from embryonic fourteen-day rat brains and then mechanically dissociated with a pipette until the tissue was dispersed. Cells were grown in a humidified atmosphere of 5% CO<sub>2</sub> at 37 °C and culture in media (Dulbecco's modified Eagle's medium/F12, 33  $\times 10^{-3}$  M D-glucose, 1% L-glutamine, 1% penicillin-streptomycin (PS), 1% fetal calf serum (FCS), supplemented with 2% B27). Controls and experimental groups were cultured for three, seven, and ten days in six well culture plates and sterilized in 70% ethanol for 2 h, and subsequently washed repeatedly with hank's balanced salt solution (HBSS) and/or molecular biology grade water (Sigma). Prior to plating, samples and controls were coated with poly-lysine (Sigma). They were then rinsed three times with molecular biology grade water and left to dry overnight. 50 000 cells cm<sup>-2</sup> were plated on each electrode, and then 3 mL of the culture medium was added to each well and half of the volume was replaced with fresh media every two days for a period of ten days.

For the inflammatory control, primary VM cells were cultured on sterile Thermanox Plastic Coverslips with 13 mm diameter (NUNC/brand products). 50 000 cells cm<sup>-2</sup> were plated on each coverslip, and grown in a humidified atmosphere of 5% CO<sub>2</sub> at 37 °C and culture in media (Dulbecco's modified Eagle's medium/F12, 33  $\times 10^{-3}$  M D-glucose, 1% L-glutamine, 1% PS, 1% FCS, supplemented with 2% B27). 3 mL of the culture medium was added to each well and, after two days in culture, the cells were stimulated with IL-1 $\beta$  (10 ng mL<sup>-1</sup>) prepared in plating media to a final volume of 3 mL and half of the volume was changed every two days for a period of ten days. Data for the optimization of the different concentration of IL-1 $\beta$  as inflammatory stimuli on VM cells cultures are shown in Figure S6 (Supporting Information) with the analysis of the production of ROS, CellROX, and in Figure S7 (Supporting Information) with the quantification of activated microglia using methods for morphofunctional analysis described in ref. [141], respectively.

Dissociated hippocampal neurons were obtained from P1 to P4-old Wistar rats, as previously reported.<sup>[156]</sup> Prior to plating, samples of pristine PEDOT:PTS and micro-topographically functionalized PEDOT:PTS coated electrodes and control bare platinum were sterilized by repeated (3) 10 min-long washes with ethanol followed by 5 min-long washes in molecular biology grade water, both solutions were previously filtered with 0.22  $\mu\text{m}$  cutoff filter (Merck Millipore). Cultured cells were incubated at 37 °C, 5% CO<sub>2</sub> in culture medium composed of Neurobasal-A (Thermo Fischer) containing B27 2% (Gibco) Glutamax 10  $\times 10^{-3}$  M and Gentamycin 0.5  $\times 10^{-6}$  M (Gibco), and used for experiments at eight to ten days in vitro by renewing half of the medium once in this period.

**Ethical Statement (Primary hippocampal cultures):** All experiments were performed in accordance with the EU guidelines (2010/63/UE) and Italian law (decree 26/14) and were approved by the local

authority veterinary service and by our institution (SISSA-ISAS) ethical committee. Every effort was made to minimize animal suffering and to reduce the number of animals used. Animal use was approved by the Italian Ministry of Health, in accordance with the EU Recommendation 2007/526/CE.

**Biological Characterization—Immunofluorescent Labeling:** Indirect double-immunofluorescent labeling was performed to visualize neurons and astrocyte cell populations, as described by Vallejo-Giraldo et al.<sup>[8]</sup> Briefly, VM cells on experimental and control substrates were fixed with 4% paraformaldehyde and 1% of sucrose for 20 min at room temperature at the time point. Once fixed, the samples were washed with PBS and permeabilized with buffered 0.5% Triton X-100 within a buffered isotonic solution (10.3 g sucrose, 0.292 g NaCl, 0.06 g MgCl<sub>2</sub>, 0.476 g 4-(2-hydroxyethyl)-1 piperazineethanesulfonic acid (HEPES) buffer, 0.5 mL Triton X-100, in 100 mL water, pH 7.2) at 4 °C for 5 min. Nonspecific binding sites were blocked with 1% bovine serum albumin (BSA) in PBS at 37 °C for 30 min and subsequently incubated for 2 h with a 1:200 concentration anti-GFAP antibody produced in mouse (Sigma, 1:200) and 1:500 concentration anti-β-Tubulin III antibody produced in rabbit (Sigma, 1:500). Samples were washed three times with 0.05% Tween 20/PBS and then incubated for 1 h in the secondary antibody Alexa Fluor 488 goat anti-Mouse IgG/IgA/IgM (H+L) (molecular probes 1:500) combined with the secondary antibody Alexa Fluor 594 goat anti-Rabbit IgG (H+L) (molecular probes, 1:500). Samples were washed with PBS (5 min × 3) and mounted on microscope cover slides and counterstained with slowfadeR gold antifade reagent with 4',6-diamidino-2-phenylindole (DAPI) for nuclear staining.

Indirect double-immunofluorescent labeling was performed to visualize focal adhesion sites and astrocytes following the fixation and permeabilization processes detailed above. In this case the samples were incubated for 2 h with a 1:200 concentration anti-Paxillin (Rb mAb to Paxillin (Y113) (Life Technologies, 1:200) and with a 1:200 concentration GFAP antibody produced in mouse (Sigma, 1:200). Samples were washed three times with 0.05% Tween 20/PBS and then incubated for 1 h in the secondary antibody Alexa Fluor 488 goat anti-Mouse IgG/IgA/IgM (H+L) (molecular probes 1:500) combined with the secondary antibody Alexa Fluor 594 goat anti-Rabbit IgG (H+L) (molecular probes, 1:100). Samples were washed with PBS (5 min × 3) and mounted on microscope cover slides and counterstained with slowfadeR gold antifade reagent with DAPI for nuclear staining.

Indirect double-immunofluorescent labeling for microglia and astrocytes on inflamed controls was performed using the same methods detailed above. Samples were incubated for 2 h with GFAP antibody produced in mouse (Sigma, 1:200) at a concentration of 1:200 and with anti-rabbit Iba1 (Wako, 1:1000) with a concentration of 1:1000. Samples were washed three times with 0.05% Tween 20/PBS and then incubated for 1 h in the secondary antibody Alexa Fluor 488 goat anti-Mouse IgG/IgA/IgM (H+L) (molecular probes 1:500) combined with the secondary antibody Alexa Fluor 594 goat anti-Rabbit IgG (H+L) (molecular probes, 1:1000). Samples were washed with PBS (5 min × 3) and mounted on microscope cover slides and counterstained with slowfadeR gold antifade reagent with DAPI for nuclear staining.

Hippocampal dissociated cultures were fixed in 4% formaldehyde (prepared from fresh paraformaldehyde) in PBS and permeabilized for 20 min with 0.3% Triton-X-100 (Carlo Erba) in PBS added with 5% FCS (Gibco) and 4% BSA (Sigma-Aldrich) to prevent nonspecific binding of primary antibodies. Samples were subsequently incubated with primary antibodies for 30 min at room temperature and, after being washed with PBS, with secondary antibodies for 45 min. Mounting was performed with antifade medium Vectashield (Vector Laboratories) on 1 mm thick microscope glass slides. Neurons were labeled through anti-β-tubulin III primary antibody (Sigma-Aldrich T2200, 1:300) and visualized with Alexa 594 anti-rabbit in goat as secondary antibody (Invitrogen, 1:500). Astrocytes were stained with mouse anti-GFAP primary antibodies (Sigma-Aldrich G3893, 1:300) and visualized with Alexa 488 anti-mouse in goat as secondary antibody (Invitrogen 1:500). Nuclei were stained with DAPI (Invitrogen, 1:500).

The production of ROS on inflamed controls was visualized using an assay kit, CellROX Green Reagent, for oxidative stress detection ( $2.5 \times 10^{-3}$  M, Thermo Fisher Scientific—C10444). CellROX Green Reagent was diluted in HBSS for a final concentration of  $5 \times 10^{-6}$  M (working solution) that was prepared fresh every time used. During use, this working solution was kept in the dark at 37 °C. After removing cell media, CellROX Green Reagent was added on each sample and incubated at 37 °C for 30 min. After incubation, each sample was fixed and permeabilized using methods described above. 1 h incubation in rhodamine-conjugated phalloidin (Life Technologies, 1:100) prepared in 1% BSA in PBS was followed next for F-actin staining. After being washed with PBS (5 min × 3), samples were mounted with slowfadeR gold antifade reagent with DAPI for nuclear staining and image within 24 h. CellROX Green was visualized using FITC channel.

**Biological Characterization—Microscopy and Image Analysis:** After immunostaining, samples were viewed with an Olympus Fluoview 1000 Confocal Microscope at a fixed scan size of  $1024 \times 1024$  at a ratio 1:1. Cell analysis was performed as described in ref. [8]. At least twenty images at 60× magnification were taken at random from each experimental group and controls. Cell density was analyzed by counting the total number of labeled nuclei corresponding to neurons and astrocytes in an area of  $212 \mu\text{m} \times 212 \mu\text{m}$ . Neurite length was quantified by analyzing nine random fields of view of three different technical replicas from three different samples using established stereological methods.<sup>[69]</sup> The formula used was: neurite length =  $n \times T \times \pi/2$ , where  $n$  is the number of times neurites intersect grid lines and  $T$  = distance between gridlines (taking magnification into account) as described in ref. [167]. Cell area of astrocytes was recorded from the green channel using the threshold function to generate particles that were manually dispersed across the image until good coverage was achieved. The total number of focal adhesion points per cell and their length were quantified by direct scoring with a four pixel-wide line on the FITC channel as previously described in ref. [7] using ImageJ software (National Institutes of Health, USA).

Images of immunolabeled hippocampal dissociated cultures were acquired using a Leica DM6000 Epifluorescence Microscope either at 10× or 20× magnification (dry objectives, and 0.5 NA respectively). Eight fields per culture from three different culture series were collected. In addition, a Nikon C2 confocal microscope was used to acquire higher quality images at 40× magnification (dry objective) to obtain a morphological insight of stained cells. Analysis and images reconstruction were accomplished using NIS-Elements AR (Nikon), Velocity (PerkinElmer), and ImageJ (NIH) software.

**Biological Characterization—Cytokine Inflammation Panel:** The cytokine multiplex assay was performed on primary VM cell mixed population supernatants collected at three, seven, and ten days in culture grown on all experimental groups, controls, and inflamed control. ELISA proinflammatory panel 2 (Rat) (Meso Scale Discovery, UK) cytokine (IL-6, IL-1β, TNF-α, IFN-γ, KC/GRO, IL-4, IL-5, IL-13, IL-10) assays were performed according to the manufacturer's instructions, using six replicas and without adjustments to the recommended standard curve, and sample dilutions. Briefly, 150 μL of blocker H was added on each well of ELISA proinflammatory plate and incubated at room temperature with fast shaking for 1 h. In parallel, in a separate provided plate, an initial 1:2 dilution of samples and culture media were prepared and put under shaking for 15 min. The ELISA proinflammatory plate was then washed three times with at least 150 μL of wash buffer (PBS with 0.05% Tween20) and subsequently, the diluted sample mixed from the additional plate provided was transferred to the ELISA proinflammatory plate with the addition of 25 μL of diluent 40. Incubation at room temperature with shaking for 2 h was then carried out. The ELISA proinflammatory plate was further washed three times with PBS-tween20, and 25 μL of 1× detection antibody solution was added in each well and incubated at room temperature with shaking for 2 h. The ELISA proinflammatory plate was washed three times and further added 150 μL of 2× read buffer T in each well for plate reading using the QuickPlex SQ 120 multiplexing instrument from MSD.

The STRING (Search Tool for the Retrieval of Interacting Genes) database <http://string-db.org> search was performed for known protein interactions adopting a confidence score >0.7 as the threshold to assess associations.

**Calcium Imaging:** Hippocampal dissociated cultures were loaded with cell permeable  $\text{Ca}^{2+}$  dye Oregon Green 488 BAPTA-1 AM (Molecular Probes), 10  $\mu\text{L}$  dimethyl sulfoxide (DMSO) (Sigma-Aldrich) was added to the stock 50  $\mu\text{g}$  of the dye, and cultures were incubated with a final concentration of  $4 \times 10^{-6}$  M for 30 min at 37 °C, 5%  $\text{CO}_2$ , as detailed previously in ref. [7]. Samples were thereafter placed in a recording chamber mounted on an inverted microscope (Nikon Eclipse Ti-U). Cultures were continuously perfused at 5  $\text{mL min}^{-1}$  rate and at room temperature with extracellular solution of composition (mM): 150 NaCl, 4 KCl, 2  $\text{CaCl}_2$ , 1  $\text{MgCl}_2$ , 10 HEPES, 10 glucose (pH adjusted to 7.4 with NaOH, osmolarity 300 mOsm).  $\text{Ca}^{2+}$  dye was excited at 488 nm with a mercury lamp, excitation light was separated from the light emitted from the sample using a 395 nm dichroic mirror and ND filter (1/32). Oregon loaded cultures were observed with a 20 $\times$  objective (0.45 NA PlanFluor) and images were continuously acquired (exposure time 150 ms) using an ORCA-Flash4.0 V2 sCMOS camera (Hamamatsu). The imaging system was controlled by an integrated imaging software (HCLImage Live) and the camera was set to operate on  $2048 \times 2048$  pixels at binning four. After 8 min of spontaneous activity recording,  $1 \times 10^{-6}$  M TTX (a voltage-gated, fast  $\text{Na}^+$  channel blocker, Latoxan) was added to confirm the neuronal nature of the recorded signals. Three fields from each sample (two samples per condition) were recorded and  $8 \pm 2$  cells from each recording were selected by drawing ROIs around cell bodies, as depicted in Figure S9A (Supporting Information). Images were analyzed with both ImageJ software (NIH) and Clampfit software (pClamp suite, 10.4 version, Axon Instruments) in off-line mode.<sup>[168]</sup> The difference between peaks consecutive onset times were computed, to obtain the IEI. Intracellular  $\text{Ca}^{2+}$  transients were expressed as fractional amplitude increase ( $\Delta F/F_0$ , where  $F_0$  is the baseline fluorescence level and  $\Delta F$  is the rise over baseline), the onset time of neuronal activation was determined by detecting those events in the fluorescence signal that exceed at least five times the standard deviation of the noise.

**Statistical Analysis:** All data presented here were confirmed using at least three replicates for each of the test groups and control groups. The results are expressed as the mean of the values  $\pm$  standard error of the mean. One-way ANOVA followed by a Bonferroni test was performed to determine the statistical significance ( $p < 0.05$ ), unless otherwise stated.

## Supporting Information

Supporting Information is available from the Wiley Online Library or from the author.

## Acknowledgements

M.J.P.B. is also an SFI, Starting Investigator SIRG COFUND fellow, grant no. 11/SIRG/B2135. This grant was the principal funder of the research. This publication has also emanated from research supported in part by a research grant from Science Foundation Ireland (SFI) and is cofunded under the European Regional Development Fund under Grant Number 13/RC/2073. The authors would like to thank the following people: Nuala Campbell and Eugenia Pugliese for their help in cell quantification, Dr. Karrina McNamara and Dr. Tofail Syed for their help in XPS analysis. The authors are grateful to the facilities and technical assistance of the NCBES Electron Microscopy unit within the Centre for Microscopy & Imaging at the National University of Ireland Galway, a facility that is funded by NUIG and the Irish Government's Programme for Research in Third Level Institutions, Cycles 4 and 5, National Development Plan 2007–2013 and also to the Genomics & Screening Core at the National

University of Ireland Galway. The authors would like to acknowledge the Tyndall National Institute and the National Access Programme Grant Number NAP428 for preparation of nickel shims emanated from research conducted with the financial support of Science Foundation Ireland under Grant Number [SFI/04/CE/1590a7]. The work performed by N.F. was conducted under the framework of a Marie Skłodowska Curie Incoming Fellowship (EU H2020-MCIF-2015-659454).

## Conflict of Interest

The authors declare no conflict of interest.

## Keywords

astrogliosis, functionalization, inflammation, neural interfaces, topographies

Received: March 4, 2018

Revised: April 17, 2018

Published online: June 3, 2018

- [1] J. Lahr, C. Schwartz, B. Heimbach, A. Aertsen, J. Rickert, T. Ball, *J. Neural Eng.* **2015**, *12*, 043001.
- [2] A. C. Vanleer, J. A. Blanco, J. B. Wagenaar, J. Viventi, D. Contreras, B. Litt, *J. Neural Eng.* **2016**, *13*, 026015.
- [3] P. Fattahi, G. Yang, G. Kim, M. R. Abidian, *Adv. Mater.* **2014**, *26*, 1846.
- [4] D. M. Durand, M. Ghovanloo, E. Krames, *J. Neural Eng.* **2014**, *11*, 020201.
- [5] Z. Zhou, P. Yu, H. M. Geller, C. K. Ober, *Biomacromolecules* **2013**, *14*, 529.
- [6] U. A. Aregueta-Robles, A. J. Woolley, L. A. Poole-Warren, N. H. Lovell, R. A. Green, *Front. Neuroeng.* **2014**, *7*, 15.
- [7] C. Vallejo-Giraldo, N. P. Pampaloni, A. R. Pallipurath, J. O'Connell, P. Mokarian-Tabari, J. D. Holmes, A. Trotier, K. Krukiewicz, G. Orpella-Aceret, E. Pugliese, L. Ballerini, M. Kilcoyne, E. Dowd, L. R. Quinlan, A. Pandit, P. Kavanagh, M. J. P. Biggs, *Adv. Funct. Mater.* **2017**, *28*, 1605035.
- [8] C. Vallejo-Giraldo, E. Pugliese, A. Larranaga, M. A. Fernandez-Yague, J. J. Britton, A. Trotier, G. Tadayyon, A. Kelly, I. Rago, J. R. Sarasua, E. Dowd, L. R. Quinlan, A. Pandit, M. J. P. Biggs, *Nanomedicine* **2016**, *11*, 2547.
- [9] W. F. Agnew, D. B. McCreery, *Neural Prostheses: Fundamental Studies*, Prentice Hall, Englewood Cliffs, NJ **1990**.
- [10] S. F. Cogan, *Annu. Rev. Biomed. Eng.* **2008**, *10*, 275.
- [11] P. J. Rousche, D. S. Pellinen, D. P. Pivin Jr., J. C. Williams, R. J. Vetter, D. R. Kipke, *IEEE Trans. Biomed. Eng.* **2001**, *48*, 361.
- [12] D. Mantione, I. Del Agua, W. Schaafsma, J. Diez-Garcia, B. Castro, H. Sardon, D. Mecerreyes, *Macromol. Biosci.* **2016**, *16*, 1227.
- [13] C. Boehler, T. Stieglitz, M. Asplund, *Biomaterials* **2015**, *67*, 346.
- [14] C. A. R. Chapman, H. Chen, M. Stamou, J. Biener, M. M. Biener, P. J. Lein, E. Seker, *ACS Appl. Mater. Interfaces* **2015**, *7*, 7093.
- [15] M. Asplund, T. Nyberg, O. Inganas, *Polym. Chem.* **2010**, *1*, 1374.
- [16] R. A. Green, S. Baek, L. A. Poole-Warren, P. J. Martens, *Sci. Technol. Adv. Mater.* **2010**, *11*, 014107.
- [17] R. A. Green, N. H. Lovell, G. G. Wallace, L. A. Poole-Warren, *Biomaterials* **2008**, *29*, 3393.
- [18] R. Balint, N. J. Cassidy, S. H. Cartmell, *Acta Biomater.* **2014**, *10*, 2341.
- [19] G. L. Mario Cheong, K. S. Lim, A. Jakubowicz, P. J. Martens, L. A. Poole-Warren, R. A. Green, *Acta Biomater.* **2014**, *10*, 1216.
- [20] C. Vallejo-Giraldo, A. Kelly, M. J. P. Biggs, *Drug Discovery Today* **2014**, *19*, 88.



- [21] Y. Shi, L. Pan, B. Liu, Y. Wang, Y. Cui, Z. Bao, G. Yu, *J. Mater. Chem. A* **2014**, *2*, 6086.
- [22] W. Zhang, F. K. Yang, Z. Pan, J. Zhang, B. Zhao, *Macromol. Rapid Commun.* **2014**, *35*, 350.
- [23] H. Xu, J. M. Holzwarth, Y. Yan, P. Xu, H. Zheng, Y. Yin, S. Li, P. X. Ma, *Biomaterials* **2014**, *35*, 225.
- [24] Z. A. King, C. M. Shaw, S. A. Spanninga, D. C. Martin, *Polymer* **2011**, *52*, 1302.
- [25] D. C. Martin, J. Wu, C. M. Shaw, Z. King, S. A. Spanninga, S. Richardson-Burns, J. Hendricks, J. Yang, *Polym. Rev.* **2010**, *50*, 340.
- [26] V. Castagnola, E. Descamps, A. Lecestre, L. Dahan, J. Rемаud, L. G. Nowak, C. Bergaud, *Biosens. Bioelectron.* **2015**, *67*, 450.
- [27] F. Wu, M. Sun, W. Jiang, K. Zhang, A. Xie, Y. Wang, M. Wang, *J. Mater. Chem. C* **2016**, *4*, 82.
- [28] H. Xiao, M. Zhang, Y. Xiao, J. Che, *Colloids Surf., B* **2015**, *126*, 138.
- [29] J. M. Fonner, L. Forciniti, H. Nguyen, J. D. Byrne, Y. F. Kou, J. Syeda-Nawaz, C. E. Schmidt, *Biomed. Mater.* **2008**, *3*, 034124.
- [30] X. Cui, V. A. Lee, Y. Raphael, J. A. Wiler, J. F. Hetke, D. J. Anderson, D. C. Martin, *J. Biomed. Mater. Res.* **2001**, *56*, 261.
- [31] M. R. Abidian, J. M. Corey, D. R. Kiple, D. C. Martin, *Small* **2010**, *6*, 421.
- [32] M. Wolfs, T. Darmanin, F. Guittard, *Surf. Coat. Technol.* **2014**, *259*, 594.
- [33] M. Culebras, C. Gomez, A. Cantarero, *J. Mater. Chem. A* **2014**, *2*, 10109.
- [34] G. Oyman, C. Geyik, R. Ayranci, M. Ak, D. O. Demirkol, S. Timur, H. Coskunol, *RSC Adv.* **2014**, *4*, 53411.
- [35] Z. Zhu, T. Mankowski, K. Balakrishnan, A. S. Shikoh, F. Touati, M. A. Benammar, M. Mansuripur, C. M. Falco, *ACS Appl. Mater. Interfaces* **2015**, *7*, 16223.
- [36] B. Wei, J. Liu, L. Ouyang, C.-C. Kuo, D. C. Martin, *ACS Appl. Mater. Interfaces* **2015**, *7*, 15388.
- [37] H. Deng, L. Lin, M. Ji, S. Zhang, M. Yang, Q. Fu, *Prog. Polym. Sci.* **2014**, *39*, 627.
- [38] D. Uppalapati, B. J. Boyd, S. Garg, J. Travas-Sejdic, D. Svirskis, *Biomaterials* **2016**, *111*, 149.
- [39] H. Vara, J. E. Collazos-Castro, *ACS Appl. Mater. Interfaces* **2015**, *7*, 27016.
- [40] D. H. Kim, J. A. Wiler, D. J. Anderson, D. R. Kiple, D. C. Martin, *Acta Biomater.* **2010**, *6*, 57.
- [41] M. Asplund, E. Thaning, J. Lundberg, A. C. Sandberg-Nordqvist, B. Kostyszyn, O. Inganäs, H. von Holst, *Biomed. Mater.* **2009**, *4*, 045009.
- [42] P. M. George, A. W. Lyckman, D. A. LaVan, A. Hegde, Y. Leung, R. Avasare, C. Testa, P. M. Alexander, R. Langer, M. Sur, *Biomaterials* **2005**, *26*, 3511.
- [43] T. M. Pearce, J. C. Williams, *Lab Chip* **2007**, *7*, 30.
- [44] M. HajjHassan, V. Chodavarapu, S. Musallam, *Sensors* **2008**, *8*, 6704.
- [45] J. P. Donoghue, *Nat. Neurosci.* **2002**, *5*, 1085.
- [46] N. A. Kotov, J. O. Winter, I. P. Clements, E. Jan, B. P. Timko, S. Campidelli, S. Pathak, A. Mazzatenta, C. M. Lieber, M. Prato, *Adv. Mater.* **2009**, *21*, 3970.
- [47] D. Brüggemann, K. E. Michael, B. Wolfrum, A. Offenhäuser, *Int. J. Nano Biomater.* **2012**, *4*, 108.
- [48] X. Cui, J. F. Hetke, J. A. Wiler, D. J. Anderson, D. C. Martin, *Sens. Actuators, A* **2001**, *93*, 8.
- [49] M. Asplund, T. Nyberg, O. Inganäs, *Polym. Chem.* **2010**, *1*, 1374.
- [50] M. J. P. Biggs, R. G. Richards, M. J. Dalby, *Nanomedicine* **2010**, *6*, 619.
- [51] M. J. P. Biggs, R. G. Richards, N. Gadegaard, R. J. McMurray, S. Affrossman, C. D. Wilkinson, R. O. Oreffo, M. J. Dalby, *J. Biomed. Mater. Res., Part A* **2009**, *91A*, 195.
- [52] M. J. P. Biggs, R. Richards, N. Gadegaard, C. Wilkinson, M. Dalby, *J. Orthop. Res.* **2007**, *25*, 273.
- [53] J. T. Morgan, C. J. Murphy, P. Russell, *Exp. Eye Res.* **2013**, *115*, 1.
- [54] M. V. Sofroniew, *Trends Neurosci.* **2009**, *32*, 638.
- [55] V. S. Polikov, P. A. Tresco, W. M. Reichert, *J. Neurosci. Methods* **2005**, *148*, 1.
- [56] C. A. Chapman, L. Wang, H. Chen, J. Garrison, P. J. Lein, E. Seker, *Adv. Funct. Mater.* **2017**, *27*, 1604631.
- [57] E. S. Ereifej, H. W. Matthew, G. Newaz, A. Mukhopadhyay, G. Auner, I. Salakhutdinov, P. J. VandeVord, *J. Biomed. Mater. Res., Part A* **2013**, *101A*, 1743.
- [58] N. Tawil, P. Wilson, S. Carbonetto, *J. Cell Biol.* **1993**, *120*, 261.
- [59] M. J. P. Biggs, M. J. Dalby, *Proc. Inst. Mech. Eng., Part H* **2010**, *224*, 1441.
- [60] D. A. Turner, D. C. Adamson, *J. Neuropathol. Exp. Neurol.* **2011**, *70*, 167.
- [61] A. M. Turner, N. Dowell, S. W. Turner, L. Kam, M. Isaacson, J. N. Turner, H. G. Craighead, W. Shain, *J. Biomed. Mater. Res.* **2000**, *51*, 430.
- [62] M. Leber, M. Shandhi, A. Hogan, F. Solzbacher, R. Bhandari, S. Negi, *Appl. Surf. Sci.* **2016**, *365*, 180.
- [63] J. Corey, B. Wheeler, G. Brewer, *IEEE Trans. Biomed. Eng.* **1996**, *43*, 944.
- [64] C.-K. Chung, S.-F. Tseng, W.-T. Hsiao, D. Chiang, W.-C. Lin, *J. Laser Micro/Nanoeng.* **2016**, *11*, 395.
- [65] R. Thakar, A. E. Weber, C. A. Morris, L. A. Baker, *Analyst* **2013**, *138*, 5973.
- [66] R. B. Bass, W. W. Clark, J. Z. Zhang, A. W. Lichtenberger, *IEEE Trans. Appl. Supercond.* **2001**, *11*, 92.
- [67] E. Moulin, K. Bittkau, M. Ghosh, G. Bugnon, M. Stuckelberger, M. Meier, F.-J. Haug, J. Hüpkes, C. Ballif, *Sol. Energy Mater. Sol. Cells* **2016**, *145*, 185.
- [68] E. Herth, E. Algré, J. Y. Rauch, J. C. Gerbedoen, N. Defrance, P. Delobelle, *Phys. Status Solidi (a)* **2016**, *213*, 114.
- [69] A. Khaldi, A. Maziz, C. Plesse, C. Soyer, F. Vidal, E. Cattan, *Sens. Actuators, B* **2016**, *229*, 635.
- [70] Z. Li, Y. Chen, X. Zhu, M. Zheng, F. Dong, P. Chen, L. Xu, W. Chu, H. Duan, *Nanotechnology* **2016**, *27*, 365302.
- [71] S. Ma, Y. Xia, Y. Wang, K. Ren, R. Luo, L. Song, X. Chen, J. Chen, Y. Jin, *J. Vac. Sci. Technol., B: Nanotechnol. Microelectron.: Mater. Process., Meas., Phenom.* **2016**, *34*, 052002.
- [72] T. Wulz, B. K. Canfield, L. M. Davis, S. Spanier, E. Lukosi, *Diamond Relat. Mater.* **2017**, *74*, 108.
- [73] L. A. Hof, X. Guo, M. Seo, R. Wüthrich, J. Greener, *Micromachines* **2017**, *8*, 29.
- [74] E. S. Ereifej, M. M.-C. Cheng, G. Mao, P. J. VandeVord, *J. Neurosci. Methods* **2013**, *217*, 17.
- [75] N. Gomez, J. Y. Lee, J. D. Nickels, C. E. Schmidt, *Adv. Funct. Mater.* **2007**, *17*, 1645.
- [76] T. Hoshino, H. Miyazako, A. Nakayama, A. Wagatsuma, K. Mabuchi, *Sens. Actuators, B* **2016**, *236*, 659.
- [77] L. Zhang, S. Ducharme, J. Li, *Appl. Phys. Lett.* **2007**, *91*, 172906.
- [78] Y. Chen, D. A. Ohlberg, X. Li, D. R. Stewart, R. Stanley Williams, J. O. Jeppesen, K. A. Nielsen, J. F. Stoddart, D. L. Olynick, E. Anderson, *Appl. Phys. Lett.* **2003**, *82*, 1610.
- [79] S. Jingfeng, L. Haidong, L. Shumin, T. Li, G. Alexei, D. Stephen, *Nanotechnology* **2016**, *27*, 015302.
- [80] Y. Yang, K. Lee, K. Mielczarek, W. Hu, A. Zakhidov, *Nanotechnology* **2011**, *22*, 485301.
- [81] E. Hourdakis, A. G. Nassiopolou, *IEEE Trans. Electron Dev.* **2016**, *63*, 746.
- [82] J. Kim, K. Wubs, B.-S. Bae, W. S. Kim, *Sci. Technol. Adv. Mater.* **2012**, *13*, 035004.
- [83] A. Ferrari, M. Cecchini, A. Dhawan, S. Micera, I. Tonazzini, R. Stabile, D. Pisignano, F. Beltram, *Nano Lett.* **2011**, *11*, 505.
- [84] D. Franco, F. Milde, M. Klingauf, F. Orsenigo, E. Dejana, D. Poulidakos, M. Cecchini, P. Koumoutsakos, A. Ferrari, V. Kurtcuoglu, *Biomaterials* **2013**, *34*, 1488.

- [85] D. Franco, M. Klingauf, M. Bednarzik, M. Cecchini, V. Kurtcuoglu, J. Gobrecht, D. Poulidakos, A. Ferrari, *Soft Matter* **2011**, *7*, 7313.
- [86] H. Schiff, S. Saxer, S. Park, C. Padeste, U. Piele, J. Gobrecht, *Nanotechnology* **2005**, *16*, S171.
- [87] L. Tan, Y. Kong, S. Pang, A. Yee, *J. Vac. Sci. Technol., B: Microelectron. Nanometer Struct.–Process., Meas., Phenom.* **2004**, *22*, 2486.
- [88] D. Pisignano, L. Persano, M. F. Raganato, P. Visconti, R. Cingolani, G. Barbarella, L. Favaretto, G. Gigli, *Adv. Mater.* **2004**, *16*, 525.
- [89] J. E. Collazos-Castro, G. R. Hernández-Labrado, J. L. Polo, C. García-Rama, *Biomaterials* **2013**, *34*, 3603.
- [90] N. Bhagwat, R. E. Murray, S. I. Shah, K. L. Kiick, D. C. Martin, *Acta Biomater.* **2016**, *41*, 235.
- [91] A. Alves-Sampaio, C. García-Rama, J. E. Collazos-Castro, *Biomaterials* **2016**, *89*, 98.
- [92] D. H. Kim, S. M. Richardson-Burns, J. L. Hendricks, C. Sequera, D. C. Martin, *Adv. Funct. Mater.* **2007**, *17*, 79.
- [93] X. Shuhua, L. Ziyou, Y. Ling, W. Fei, G. Sun, *Mediators Inflammation* **2012**, *2012*, 1.
- [94] A. Struneecka, R. L. Blaylock, O. Struneeck, *J. Appl. Biomed.* **2016**, *14*, 171.
- [95] M. Donoso, A. Méndez-Vilas, J. Bruque, M. González-Martin, *Int. Biodeterior. Biodegrad.* **2007**, *59*, 245.
- [96] K. Krukiewicz, J. K. Zak, *J. Mater. Sci.* **2014**, *49*, 5738.
- [97] K. Krukiewicz, T. Jarosz, J. K. Zak, M. Lapkowski, P. Ruszkowski, T. Bobkiewicz-Kozłowska, B. Bednarczyk-Cwynar, *Acta Biomater.* **2015**, *19*, 158.
- [98] J. Rivnay, P. Leleux, M. Ferro, M. Sessolo, A. Williamson, D. A. Koutsouras, D. Khodagholy, M. Ramuz, X. Strakosas, R. M. Owens, C. Benar, *Sci. Adv.* **2015**, *1*, e1400251.
- [99] K. A. Ludwig, N. B. Langhals, M. D. Joseph, S. M. Richardson-Burns, J. L. Hendricks, D. R. Kipke, *J. Neural Eng.* **2011**, *8*, 014001.
- [100] M. R. Abidian, D. C. Martin, *Biomaterials* **2008**, *29*, 1273.
- [101] M. R. Abidian, K. A. Ludwig, T. C. Marzullo, D. C. Martin, D. R. Kipke, *Adv. Mater.* **2009**, *21*, 3764.
- [102] A. Molina, J. González, E. Laborda, Y. Wang, R. G. Compton, *Phys. Chem. Chem. Phys.* **2011**, *13*, 14694.
- [103] V. Rehacek, I. Hotovy, M. Vojs, F. Mika, *Microsyst. Technol.* **2008**, *14*, 491.
- [104] Z. Lin, K. Ino, H. Shiku, T. Matsue, *Chem. Commun.* **2010**, *46*, 559.
- [105] J. Orozco, C. Fernández-Sánchez, C. Jiménez-Jorquera, *Sensors* **2010**, *10*, 475.
- [106] R. A. Olowu, O. Arotiba, S. N. Mailu, T. T. Waryo, P. Baker, E. Iwuoha, *Sensors* **2010**, *10*, 9872.
- [107] X. Ma, G. Yue, J. Wu, Z. Lan, J.-Y. Lin, *RSC Adv.* **2015**, *5*, 43639.
- [108] W. Wei, Y. Song, L. Wang, S. Zhang, J. Luo, S. Xu, X. Cai, *Microsyst. Nanoeng.* **2015**, *1*, 15002.
- [109] S. Arcot Desai, C.-A. Gutekunst, S. M. Potter, R. E. Gross, *Front. Neuroeng.* **2014**, *7*, 16.
- [110] H. Zhang, J. Shih, J. Zhu, N. A. Kotov, *Nano Lett.* **2012**, *12*, 3391.
- [111] H. S. Mandal, G. L. Knaack, H. Charkhkar, D. G. McHail, J. S. Kaste, T. C. Dumas, N. Peixoto, J. F. Rubinson, J. J. Pancrazio, *Acta Biomater.* **2014**, *10*, 2446.
- [112] M. Nikkha, F. Edalat, S. Manoucheri, A. Khademhosseini, *Biomaterials* **2012**, *33*, 5230.
- [113] F. Cesca, T. Limongi, A. Accardo, A. Rocchi, M. Orlando, V. Shalabaeva, E. Di Fabrizio, F. Benfenati, *RSC Adv.* **2014**, *4*, 45696.
- [114] L. Qi, N. Li, R. Huang, Q. Song, L. Wang, Q. Zhang, R. Su, T. Kong, M. Tang, G. Cheng, *PLoS One* **2013**, *8*, e59022.
- [115] C. Fan, H. Wang, D. Chen, X. Cheng, K. Xiong, X. Luo, Q. Cao, *Neural Regen. Res.* **2014**, *9*, 1770.
- [116] W. Sun, T. Incitti, C. Migliaresi, A. Quattrone, S. Casarosa, A. Motta, *J. Tissue Eng. Regen. Med.* **2015**, *56*, 4846.
- [117] M. B. Runge, M. Dadsetan, J. Baltrusaitis, T. Ruesink, L. Lu, A. J. Windebank, M. J. Yaszemski, *Biomacromolecules* **2010**, *11*, 2845.
- [118] G. Kang, R. B. Borgens, Y. Cho, *Langmuir* **2011**, *27*, 6179.
- [119] X. Shi, Y. Xiao, H. Xiao, G. Harris, T. Wang, J. Che, *Colloids Surf., B* **2016**, *145*, 768.
- [120] M. K. Gottipati, I. Kalinina, E. Bekyarova, R. C. Haddon, V. Pargura, *Nano Lett.* **2012**, *12*, 4742.
- [121] L. Ben Haim, D. H. Rowitch, *Nat. Rev. Neurosci.* **2017**, *18*, 31.
- [122] M. V. Sofroniew, H. V. Vinters, *Acta Neuropathol.* **2010**, *119*, 7.
- [123] N. A. Oberheim, S. A. Goldman, M. Nedergaard, *Astrocytes* **2012**, *814*, 23.
- [124] H. E. Beggs, D. Schahin-Reed, K. Zang, S. Goebbels, K. A. Nave, J. Gorski, K. R. Jones, D. Sretavan, L. F. Reichardt, *Neuroendocrinology* **2003**, *40*, 501.
- [125] G. J. Ramakers, W. H. Moolenaar, *Exp. Cell Res.* **1998**, *245*, 252.
- [126] Y. Koyama, Y. Yoshioka, T. Matsuda, A. Baba, *Glia* **2003**, *43*, 185.
- [127] J. Padmanabhan, D. Clayton, M. L. Shelanski, *J. Neurobiol.* **1999**, *39*, 407.
- [128] S. Paco, M. Hummel, V. Plá, L. Sumoy, F. Aguado, *BMC Genomics* **2016**, *17*, 304.
- [129] D. L. Montgomery, *Vet. Pathol.* **1994**, *31*, 145.
- [130] J. M. Cregg, M. A. DePaul, A. R. Filous, B. T. Lang, A. Tran, *Exp. Neurol.* **2014**, *253*, 197.
- [131] A. D. Gilmour, J. Goding, L. A. Poole-Warren, C. E. Thomson, R. A. Green in *2015 7th Int. IEEE/EMBS Conf. Neural Engineering (NER)*, IEEE, Montpellier, France **2015**, pp. 450–453.
- [132] S. Baek, R. A. Green, L. A. Poole-Warren, *J. Biomed. Mater. Res., Part A* **2014**, *102*, 2743.
- [133] R. Kripparamanan, P. Aswath, A. Zhou, L. Tang, K. T. Nguyen, *J. Nanosci. Nanotechnol.* **2006**, *6*, 1905.
- [134] S. Sonam, S. R. Sathe, E. K. Yim, M. P. Sheetz, C. T. Lim, *Sci. Rep.* **2016**, *6*, 20415.
- [135] G. R. John, S. C. Lee, C. F. Brosnan, *Neuroscientist* **2003**, *9*, 10.
- [136] C. Farina, F. Aloisi, E. Meinel, *Trends Immunol.* **2007**, *28*, 138.
- [137] W. J. Streit, S. D. Hurler, T. S. McGraw, S. L. Semple-Rowland, *J. Neurosci. Res.* **2000**, *61*, 10.
- [138] D. Brück, G. K. Wenning, N. Stefanova, L. Fellner, *Neurobiol. Dis.* **2016**, *85*, 262.
- [139] F. Aloisi, G. Borsellino, A. Caré, U. Testa, P. Gallo, G. Russo, C. Peschle, G. Levi, *Int. J. Dev. Neurosci.* **1995**, *13*, 265.
- [140] C. Lins, R. Borjovic, *Growth Factors* **2001**, *19*, 145.
- [141] S. G. Torres-Platas, S. Comeau, A. Rachalski, G. Dal Bo, C. Cruceanu, G. Turecki, B. Giros, N. Mechawar, *J. Neuroinflammation* **2014**, *11*, 12.
- [142] K. Schroder, P. J. Hertzog, T. Ravasi, D. A. Hume, *J. Leukocyte Biol.* **2004**, *75*, 163.
- [143] D. Miljkovic, M. Momcilovic, I. Stojanovic, S. Stosic-Grujicic, Z. Ramic, M. Mostarica-Stojkovic, *J. Neurosci. Res.* **2007**, *85*, 3598.
- [144] Y. V. N. Cavalcanti, M. C. A. Brelaz, J. K. d. A. L. Neves, J. C. Ferraz, V. R. A. Pereira, *Pulm. Med.* **2012**, *1*, 2012.
- [145] N. Rubio, F. Sanz-Rodriguez, *Virology* **2007**, *358*, 98.
- [146] M. Roy, J.-F. Richard, A. Dumas, L. Vallières, *J. Neuroinflammation* **2012**, *9*, 18.
- [147] M. Ert, A. Quintana, Hidalgo, *Int. J. Biol. Sci.* **2012**, *8*, 1254.
- [148] R. J. Hariri, V. A. Chang, P. S. Barie, R. S. Wang, S. F. Sharif, J. B. Ghajar, *Brain Res.* **1994**, *636*, 139.
- [149] X. Ma, S. L. Reynolds, B. J. Baker, X. Li, E. N. Benveniste, H. Qin, *J. Immunol.* **2010**, *184*, 4898.
- [150] C.-S. Chiang, A. Stalder, A. Samimi, I. Campbell, *Dev. Neurosci.* **1994**, *16*, 212.
- [151] E. Fattori, D. Lazzaro, P. Musiani, A. Modesti, T. Alonzi, G. Ciliberto, *Eur. J. Neurosci.* **1995**, *7*, 2441.
- [152] M. Sawada, A. Suzumura, Y. Itoh, T. Marunouchi, *Neurosci. Lett.* **1993**, *155*, 175.
- [153] H. Awatsuji, Y. Furukawa, M. Hirota, Y. Murakami, S. Nii, S. Furukawa, K. Hayashi, *J. Neurosci. Res.* **1993**, *34*, 539.
- [154] C. Brodie, *FEBS Lett.* **1996**, *394*, 117.
- [155] M. Telias, M. Segal, D. Ben-Yosef, *F1000Research* **2014**, *3*, 196.



- [156] V. Lovat, D. Pantarotto, L. Lagostena, B. Cacciari, M. Grandolfo, M. Righi, G. Spalluto, M. Prato, L. Ballerini, *Nano Lett.* **2005**, *5*, 1107.
- [157] A. Mazzatenta, M. Giugliano, S. Campidelli, L. Gambazzi, L. Businaro, H. Markram, M. Prato, L. Ballerini, *J. Neurosci.* **2007**, *27*, 6931.
- [158] G. Cellot, F. M. Toma, Z. K. Varley, J. Laishram, A. Villari, M. Quintana, S. Cipollone, M. Prato, L. Ballerini, *J. Neurosci.* **2011**, *31*, 12945.
- [159] S. Bosi, R. Rauti, J. Laishram, A. Turco, D. Lonardoni, T. Nieuw, M. Prato, D. Scaini, L. Ballerini, *Sci. Rep.* **2015**, *5*, 9562.
- [160] I. A. Scarisbrick, M. Radulovic, J. E. Burda, N. Larson, S. I. Blaber, C. Giannini, M. Blaber, A. G. Vandell, *Biol. Chem.* **2012**, *393*, 355.
- [161] J. Padmanabhan, T. R. Kyriakides, *Wiley Interdiscip. Rev.: Nanomed. Nanobiotechnol.* **2015**, *7*, 355.
- [162] N. Gadegaard, S. Mosler, N. B. Larsen, *Macromol. Mater. Eng.* **2003**, *288*, 76.
- [163] S. Baek, R. A. Green, L. A. Poole-Warren, *Acta Biomater.* **2014**, *10*, 3048.
- [164] M. Wen, H. Liu, F. Zhang, Y. Zhu, D. Liu, Y. Tian, Q. Wu, *Chem. Commun.* **2009**, 4530.
- [165] A. J. Bard, L. R. Faulkner, J. Leddy, C. G. Zoski, *Electrochemical Methods: Fundamentals and Applications*, Vol. 2, Wiley, New York **1980**.
- [166] N. Stevens, M. Rooney, A. Bond, S. Feldberg, *J. Phys. Chem. A* **2001**, *105*, 9085.
- [167] E. T. Kavanagh, J. P. Loughlin, K. R. Herbert, P. Dockery, A. Samall, K. M. Doyle, A. M. Gorman, *Biochem. Biophys. Res. Commun.* **2006**, *351*, 890.
- [168] R. Rauti, N. Lozano, V. León, D. Scaini, M. Musto, I. Rago, F. P. Ulloa Severino, A. Fabbro, L. Casalis, E. Vázquez, *ACS Nano* **2016**, *10*, 4459.



# Optimization of Organotypic Cultures of Mouse Spleen for Staining and Functional Assays

Francesca Finetti<sup>1</sup>, Nagaja Capitani<sup>1</sup>, Noemi Manganaro<sup>1</sup>, Vanessa Tatangelo<sup>1</sup>, Francesca Libonati<sup>1</sup>, Giulia Panattoni<sup>2</sup>, Ivo Calaresu<sup>2</sup>, Laura Ballerini<sup>2</sup>, Cosima T. Baldari<sup>1\*</sup> and Laura Patrussi<sup>1\*</sup>

<sup>1</sup> Department of Life Sciences, University of Siena, Siena, Italy, <sup>2</sup> International School for Advanced Studies (SISSA/ISAS), Trieste, Italy

## OPEN ACCESS

### Edited by:

Fabrizio Mattei,  
Higher Institute of Health (ISS), Italy

### Reviewed by:

Alessandro Poggi,  
San Martino Hospital (IRCCS), Italy  
Guilan Shi,  
University of South Florida,  
United States

### \*Correspondence:

Cosima T. Baldari  
cosima.baldari@unisi.it  
Laura Patrussi  
patrussi2@unisi.it

### Specialty section:

This article was submitted to  
Cancer Immunity and Immunotherapy,  
a section of the journal  
Frontiers in Immunology

**Received:** 26 November 2019

**Accepted:** 28 February 2020

**Published:** 24 March 2020

### Citation:

Finetti F, Capitani N, Manganaro N, Tatangelo V, Libonati F, Panattoni G, Calaresu I, Ballerini L, Baldari CT and Patrussi L (2020) Optimization of Organotypic Cultures of Mouse Spleen for Staining and Functional Assays. *Front. Immunol.* 11:471. doi: 10.3389/fimmu.2020.00471

By preserving cell viability and three-dimensional localization, organotypic culture stands out among the newest frontiers of cell culture. It has been successfully employed for the study of diseases among which neoplasias, where tumoral cells take advantage of the surrounding stroma to promote their own proliferation and survival. Organotypic culture acquires major importance in the context of the immune system, whose cells cross-talk in a complex and dynamic fashion to elicit productive responses. However, organotypic culture has been as yet poorly developed for and applied to primary and secondary lymphoid organs. Here we describe in detail the development of a protocol suitable for the efficient cutting of mouse spleen, which overcomes technical difficulties related to the peculiar organ texture, and for optimized organotypic culture of spleen slices. Moreover, we used microscopy, immunofluorescence, flow cytometry, and qRT-PCR to demonstrate that the majority of cells residing in spleen slices remain alive and maintain their original location in the organ architecture for several days after cutting. The development of this protocol represents a significant technical improvement in the study of the lymphoid microenvironment in both physiological and pathological conditions involving the immune system.

**Keywords:** organotypic culture, spleen, vibratome, precision-cut, white pulp, red pulp, lymphoma

## INTRODUCTION

Organotypic culture has emerged as a powerful technique which allows the analysis of tissue behavior in a variety of conditions. Initially developed as an alternative to classical 2-D *in vitro* culture of neurons, slices obtained by sectioning the brain region of interest with tissue choppers allowed to maintain neurons alive outside of the body and were found to be suitable for electrophysiological studies (1). Preparation and *in vitro* growth of these slices were progressively optimized to be maintained in culture for several days thanks to the introduction of modern tissue choppers such as vibrating microtomes, that produce thinner and less damaged slices, and tissue support systems, such as agarose, to preserve the 3-D organization of the tissue (1, 2).

Organotypic culture has been extended to several other organs of the neuroendocrine system (1) and, more recently, to tumor-derived tissues (3). Of note, only one report describes the application of this technique to lymphoid tissues of human origin (4), notwithstanding the wealth of information generated over the last decade on the complex interactions that

occur among immune, stromal, and cancer cells (5, 6). Cancer immunotherapies, now applied to a variety of cancers, often result in heterogeneous responses, to which the specific features of the individual tumor microenvironment may contribute (7). Hence, the optimization of organotypic culture of lymphoid organs is critically important to understand the immune cell microenvironment in a variety of tumors.

Efficient preparation of spleen slices faces the challenge posed by the complex structure and texture of this lymphoid organ. The spleen is indeed organized as a “tree” of branching arterial vessels, in which the smaller arterioles end in a venous sinusoidal system. The organ is surrounded by a fibrous capsule of connective tissue, from which the connective trabeculae protrude into the splenic tissue to support vessels (8). Due to this peculiar organ texture, preparation of spleen slices with a chopper is precluded. Spleen is crushed by the blade and slices are not useful for further analyses (unpublished observations).

We developed a new protocol that allowed us to efficiently cut mouse spleens in intact slices and to maintain these alive and responsive for at least 48 h, making them suitable for functional assays. The protocol, that is a modification of protocols developed to obtain precision-cut slices of mouse brain, liver and lung (9–11), is based on the sequential following steps: (1) spleen inclusion into agarose blocks; (2) precision-cut using a vibrating microtome; and (3) 48-h culture of spleen slices. The protocol developed for the preparation of organotypic cultures of mouse spleens has turned out to be a valuable tool to (i) prepare spleen slices with a sufficient degree of tissue integrity; and (ii) maintain this complex tissue in culture for days, in order to be used for functional assays.

## MATERIALS AND EQUIPMENT

### Spleen Harvesting

Scissors, micro-dissecting forceps, 2-ml polypropylene microtubes (Sarstedt), ice box, ice. Culture medium: high glucose Dulbecco Modified Eagle's Medium (DMEM) (Sigma-Aldrich) with 2 U/ml penicillin G (Sigma-Aldrich) and 7.5% bovine calf serum (BCS, Hyclone).

### Precision-Cut of Mouse Spleen

Scissors, curved micro-dissecting forceps, scalpel, small spatula, plastic film, tweezers, agarose, thermometer, microwave, 50 ml beaker, milliQ water, phosphate-buffered saline (PBS), 3.5 ml transfer-pipette (Sarstedt), Compresstome® VF-300-0Z Vibrating Microtome with Specimen tube and Syringe chilling block (Precisionary instruments, Greenville, NC, USA), diagnostic microscope slides (Menzel Glaser-Thermo Scientific), pipettes, pipette tips.

### Culture of Spleen Slices

Laminar airflow chamber, sterile 48-well plates with flat bottom (Sarstedt), cell culture incubator with 5% CO<sub>2</sub>. Culture medium: high glucose Dulbecco Modified Eagle's Medium (DMEM) (Sigma-Aldrich) with 2 U/ml penicillin G (Sigma-Aldrich) and 7.5% BCS (Hyclone).

## METHODS

### Animals

C57BL/6J mice were housed in a pathogen-free and climate-controlled ( $20 \pm 2^\circ\text{C}$ , relative humidity  $55 \pm 10\%$ ) animal facility at the University of Siena. Mice were provided with water and pelleted diet *ad libitum*. All cages are provided with environmental enrichment in the form of nesting material and mouse houses. Procedures and experimentation were carried out in accordance with the 2010/63/EU Directive and approved by the Italian Ministry of Health. Animals were euthanized and spleens were harvested, immediately transferred to ice-cold culture medium (see “Materials” section) and stored on ice.

### Slice Stimulation, RNA Purification, and RT-PCR

RNA extractions were carried out on samples composed of 1, 3, or 5 spleen slices. Samples were homogenized in 1.5 ml microtubes using polypropylene double-ended pestle (Sigma-Aldrich) in 350  $\mu\text{l}$  RLT lysis buffer of the RNeasy Mini Kit (Qiagen) until completely homogenized. RNA was then extracted and retrotranscribed as described (12). RNA amount and quality were assessed using QIAxpress System (Qiagen). Real-time PCR was performed in triplicate on 96-well optical PCR plates (Sarstedt AG, Nümbrecht, Germany) using SSo Fast™ EvaGreen SuperMix (Biorad Laboratories, Hercules, CA) and a CFX96 Real-Time system (Bio-Rad Laboratories, Waltham, MA). Results were processed and analyzed as described (12). Transcript levels were normalized to GAPDH. Spleen slices (3 slices per sample) either freshly cut or cultured for 48 h at  $37^\circ\text{C}$  in culture medium were stimulated with A23187 (Merck, cat. C7522, 500 ng/ml) and phorbol 12-myristate 13-acetate (PMA, Merck, cat. 524400, 100 ng/ml) in culture medium for 6 h at  $37^\circ\text{C}$ , homogenized in 350  $\mu\text{l}$  RLT lysis buffer and RNA was extracted as described above. Primers used for amplification were: mouse CCL19 Forward 5'-3', CAA GAA CAA AGG CAA CAG C; mouse CCL19 Reverse 5'-3', CGG CTT TAT TGG AAG CTC TG; mouse CXCL13 Forward 5'-3', CAT CAT GAG GTG GTG CAA AG; mouse CXCL13 Reverse 5'-3', GGG TCA CAG TGC CAA AGG AAT; mouse GAPDH Forward 5'-3', AAC GAC CCC TTC ATT GAC; mouse GAPDH Reverse 5'-3', TCC ACG ACA TAC TCA GCA C; mouse IL-2 Forward 5'-3', CCC TTG CTA ATC ACT CCT CA; mouse IL-2 Reverse 5'-3', GAA GTG GAG CTT GAA GTG GG; mouse IL-10 Forward 5'-3', CCG GAC AGC ACA CTT CAC AG; mouse IL-10 Reverse 5'-3', TCC ACC ATT TCC CAG ACA AC; mouse IFN- $\gamma$  Forward 5'-3', ACT GGC AAA AGG ATG GTG AC; mouse IFN- $\gamma$  Reverse 5'-3', AAA CTT GGC AAT CTC ATG AAT G.

### Optical and Immunofluorescence Microscopy

Spleen slices were carefully placed on diagnostic microscope slides (Menzel Glaser-Thermo Scientific), left either unlabeled or stained for 8 min with Trypan blue solution 0.4% (Sigma-Aldrich) diluted 1:2 in PBS, washed with PBS until complete removal of the exceeding dye, covered with  $24 \times 60\text{ mm}$  coverslips (VWR) and observed with SZX12 stereo light

microscope (Olympus) and DMRB microscope (Leica microsystems) equipped with Zeiss AxioCam MRC5 digital camera. Images were processed using the AxioVision Rel. 4.6.3. software.

Immunofluorescence microscopy was performed following a modification of the protocol previously described (13). Briefly, spleen slices were transferred with a small spatula to 10-well diagnostic microscope slides (Thermo Scientific), one slice/well, and incubated for 30 min at RT with 30  $\mu$ l fixation buffer (4% paraformaldehyde in PBS) in the dark, washed with PBS and incubated for 30 min at RT with 30  $\mu$ l permeabilization solution (PBS 0.1% BSA plus 0.01% Triton X-100). Slices were then stained with 30  $\mu$ l/well of either unconjugated primary Ab or fluorescently labeled Ab in Hanks' salts at RT in the dark for 2 h, washed with PBS and incubated with 30  $\mu$ l/well of fluorochrome-conjugated secondary antibodies at RT in the dark for 2 h. Slides were washed with Hanks' salts; mounting medium (PBS 90% glycerol) was added and slides covered with 24  $\times$  60 mm coverslips (VWR) and sealed with conventional nail polish. Images were acquired on Zeiss LSM700 confocal microscope using 63 $\times$ , 40 $\times$  and 10 $\times$  objectives. Primary antibodies: FITC Rat anti-mouse CD19 (BD Pharmingen, cat. 553758) 1:30 in Hanks' salts; Alexa Fluor 488 anti-mouse CD3e (eBiosciences, cat. 53-0031-82) 1:30 in Hanks' salts; Rat anti-mouse ER-TR7 (ABD Serotec, cat. MCA2402) 1:50 in Hanks' salts; mouse monoclonal anti-Follicular DC Marker (Santa Cruz, cat. sc-58529, Ki-M9R clone) 1:50 in Hanks' salts. Secondary antibodies: DyLight<sup>®</sup> goat anti-rat 488 (Bethyl, cat. A110-105-D2) and 550 (Bethyl, cat. A110-105-D3) 1:100 in Hanks' salts; Alexa Fluor goat anti-mouse 488 (Thermo-Fisher scientific, cat. A-11001) 1:100 in Hanks' salts; isotype control: FITC Rat IgG2a (BD Pharmingen, cat. 553924).

### Flow Cytometry, Chemotaxis Assays, and Trypan Blue Exclusion

Spleen slices were disaggregated using 70- $\mu$ m Cell strainer filter (BD Falcon<sup>™</sup>) and 1 ml syringe (BioSigma). Cell death was measured by flow cytometry on slice-derived splenocytes by quantifying the % of either Annexin V<sup>+</sup>/Propidium Iodide (PI)<sup>-</sup> or PI<sup>+</sup> cells as described (12). Briefly, 2  $\times$  10<sup>5</sup> cells were resuspended in 200  $\mu$ l PBS and stained with Annexin V FITC (eBiosciences) for 15 min at RT. When required, PI was added to the samples at the final concentration of 10 ng/ml immediately before the flow cytometric analysis using Guava Easy Cyte (Millipore, Billerica, MA) cytometer. Alternatively, cells were stained with Annexin V PE (eBiosciences), fixed (fixation buffer, 4% paraformaldehyde in PBS) and permeabilized (permeabilization solution, PBS 0.1% BSA plus 0.01% Triton X-100), and T lymphocytes, B lymphocytes, follicular dendritic cells (FDC) or reticular fibroblasts were stained with anti-mouse CD3e (eBiosciences) 1:30 in PBS, Rat anti-mouse CD19 (BD Pharmingen) 1:30 in PBS, anti-Follicular DC Marker 1:50 in PBS, and Rat anti-mouse ER-TR7, respectively. Surface CXCR4 and CCR7 were stained with either Rabbit anti-CXCR4 antibody (Abcam, cat. AB124824), 1:50 in PBS, or Rabbit monoclonal anti-CCR7 antibody (Novus Biologicals, cat. NB110-55680, Y59

clone), 1:50 in PBS, and Alexa Fluor goat anti-rabbit 488 secondary antibodies (Thermo-Fisher scientific, cat. A-11002) 1:400 in PBS, in combination with PE Rat anti-mouse CD3e (eBiosciences, cat. 145-2C11, 2C11 clone) 1:30 in PBS or PE Mouse anti-mouse CD22.2 (BD Pharmingen, cat. 553384, Cy34.1 clone) 1:30 in PBS, and analyzed by flow cytometry. Chemotaxis assays were modified from the protocol reported in (14). Briefly, spleen slices were placed on the upper well of Boyden chamber, and allowed to position over the porous membrane of the insert. CXCL12 (Merck, cat. SRP4388, 100 ng/ml) or MIP-3 $\beta$  (Merck, cat. SRP4495, 100 ng/ml) were diluted in culture medium and placed in the lower well of the chamber. Cells were allowed to migrate for 3 h at 37°C, then the migrated cells were recovered from the lower chamber and stained with PE Rat anti-mouse CD3e (eBiosciences) 1:30 in PBS and FITC Rat anti-mouse CD19 (BD Pharmingen) 1:30 in PBS, and analyzed by flow cytometry. Slice-derived splenocytes were stained for 8 min with Trypan blue solution 0.4% (Sigma-Aldrich) diluted 1:2 in PBS and Trypan blue<sup>+</sup> cells were counted using an optical microscope. The percentage of dead cells was assessed by calculating the percentage of Trypan blue<sup>+</sup> cells over the total cell count.

### Statistical Analyses

Mean values, standard deviations and Student's *t*-test were calculated using GraphPad (Prism 7). A level of *p*<0.05 was considered statistically significant.

### Stepwise Procedure for Preparation and *in vitro* Culture of Spleen Slice

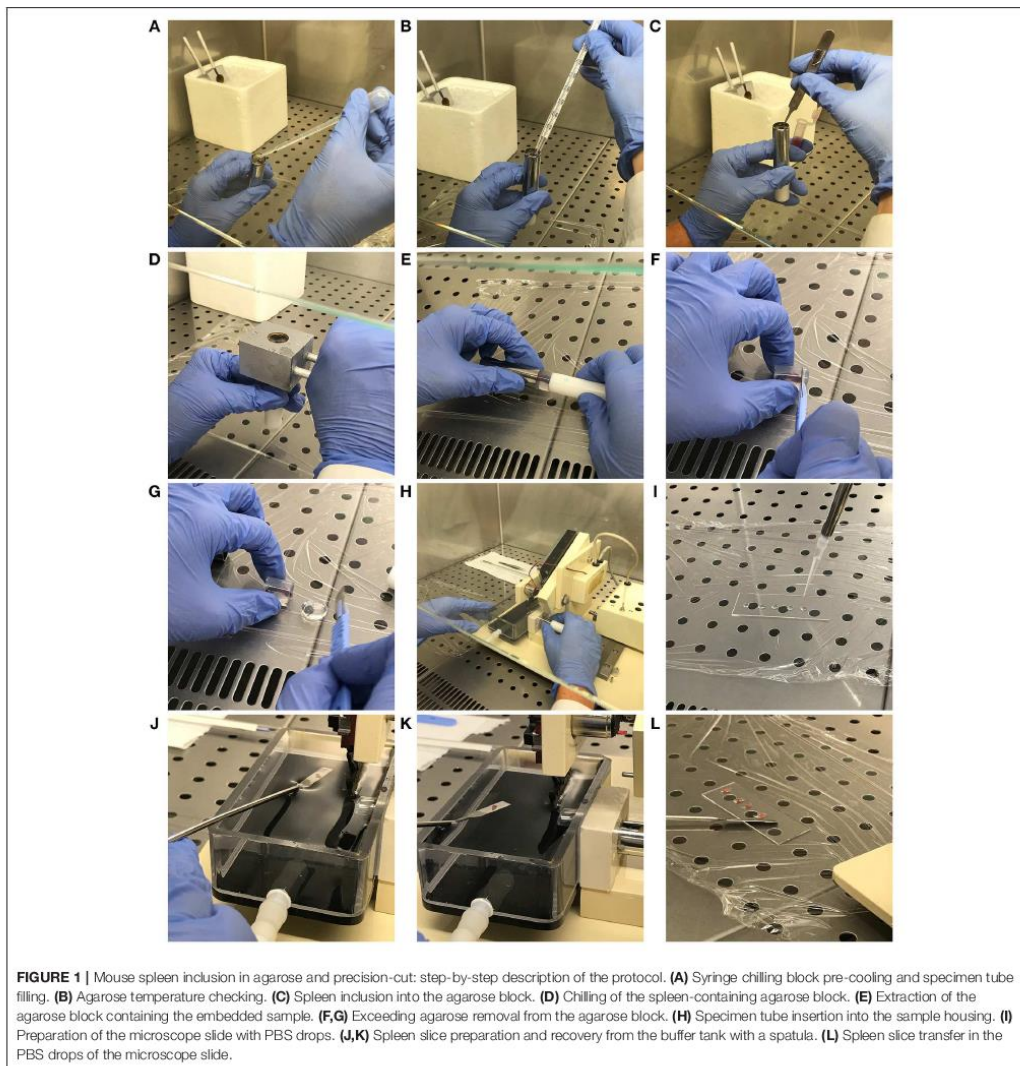
#### Spleen Preparation for Sectioning

- Lay down spleen on clean plastic film using tweezers or curved micro-dissecting forceps;
- Carefully remove fat, fur and debris using scissors and/or scalpel;
- Immediately transfer spleen into ice-cold culture medium until next step.

#### Spleen Inclusion into the Agarose Block

- Set up Compressstome<sup>®</sup> VF-300-0Z Vibrating Microtome (Precisionary Instruments, Greenville, NC, USA) following the manufacturers' instructions;
- Pre-chill syringe chilling block (Precisionary Instruments, Greenville, NC, USA) in ice for at least 10 min;
- Wash diagnostic microscope slides (Thermo Scientific) with MilliQ, then wash with absolute ethanol and allow them to air-dry;
- In a 50 ml beaker prepare 3% agarose solution in MilliQ, melt it by microwave and allow it to cool down to 45°C at room temperature, repeatedly checking the temperature with thermometer and shaking the solution to avoid agarose clumps;
- Open the provided specimen tube (Precisionary Instruments, # VF-SPS-VM-12.5) and fill it with 3–4 ml of 45°C agarose solution (Figure 1A). Check the temperature with thermometer until it reaches 38°C (Figure 1B).





- Carefully pick up the spleen from ice-cold culture medium using tweezers and rapidly insert it vertically into the agarose-containing specimen tube. Pay attention to maintain the spleen in a vertical position during this step (**Figure 1C**).
- Immediately place the pre-chilled syringe chilling block (see step 3.6.2.2) over the specimen tube and leave immobile for at least 2 min (**Figure 1D**). This process accelerates agarose solidification and chills the whole sample.

#### Preparation of Spleen Slices

- Extract the agarose block containing the embedded sample from the specimen tube and place it on clean plastic film (**Figure 1E**). Proceed to remove the portions of agarose which do not contain organ portions with the scalpel, carefully placing the blade perpendicular to the agarose block (**Figures 1E,G**). Place the carved agarose block back in the specimen tube. This step allows the specimen tube containing



agarose-embedded full-length spleen to fit with the Motor Box plunger of the Compressome.

- Insert the specimen tube in the housing and fill the buffer tray with sterile PBS (Figure 1H).
- In order to obtain non-damaged spleen slices, set the cut speed to the minimum and the blade oscillation to the maximum in the instrument control box. Importantly, set the slice thickness to  $\sim 230 \mu\text{m}$ . This is absolutely required to obtain good quality spleen slices. Lower thickness results in profound damage of the spleen structure, while higher thickness does not allow microscope observation and analyses.
- Proceed to spleen slice preparation following the technical instructions provided by the manufacturer.
- While proceeding with tissue cut, place 4–5 drops of PBS in each washed microscope slide with a 200  $\mu\text{l}$  pipette (Figure 1I).
- Recover spleen slices using a spatula (Figures 1J,K) and transfer them in the PBS drops (Figure 1L), carefully removing any trace of agarose.

#### Culture of Spleen Slices

- Transfer slices from the microscope slide to a sterile 48-well plate with flat bottom (Sarstedt) containing 100  $\mu\text{l}$  culture medium in a laminar airflow chamber under sterile conditions (one or more slides per well).
- Maintain in cell culture incubator at 37°C and with 5% CO<sub>2</sub>.
- Check the volume of culture medium every day and be careful not to exceed 100  $\mu\text{l}$  to avoid oxygen deprivation. In case of evaporation, add just the culture medium amount required to cover the slice.

#### Critical Parameters and Trouble Shooting

The efficiency of the whole process primarily depends on step 3.6.2., which describes the building of the agarose block containing the spleen (Figures 1A–D). The temperature of the agarose solution must not exceed 40°C and should ideally be maintained around 38°C to avoid organ damage. Moreover, this temperature allows optimal insertion of the spleen into the agarose, which then quickly polymerizes thereby maintaining the organ in the exact position and vertical orientation where it was placed. This is particularly important since this bean-like organ tends to rotate and lie down over the specimen tube when the agarose solution is too fluid, thereby precluding well-oriented spleen cut.

Non-intact slides, such as slides with breaks in the spleen capsule, must not be used for further analyses since they do not maintain the original organ architecture and they rapidly crinkle. In order to preserve slice integrity, fat and other debris must be removed from the spleen before cut, and air bubble formation in the agarose during the inclusion step must be avoided. Small bubbles are nevertheless quite common since tweezers, sometimes immersed for a few seconds into agarose to maintain the spleen vertical, generate bubbles when extracted from the solidifying agarose.

Although some slices are still included in the polymerized agarose when transferred to the PBS-containing buffer tray,

the majority detach from the agarose disk during cut and float in the PBS, making it extremely hard to retrieve them without inflicting severe damages to the organ structure. We adjusted this step of the protocol using a small spatula to get close to and capture even the smaller PBS-floating slices.

## RESULTS

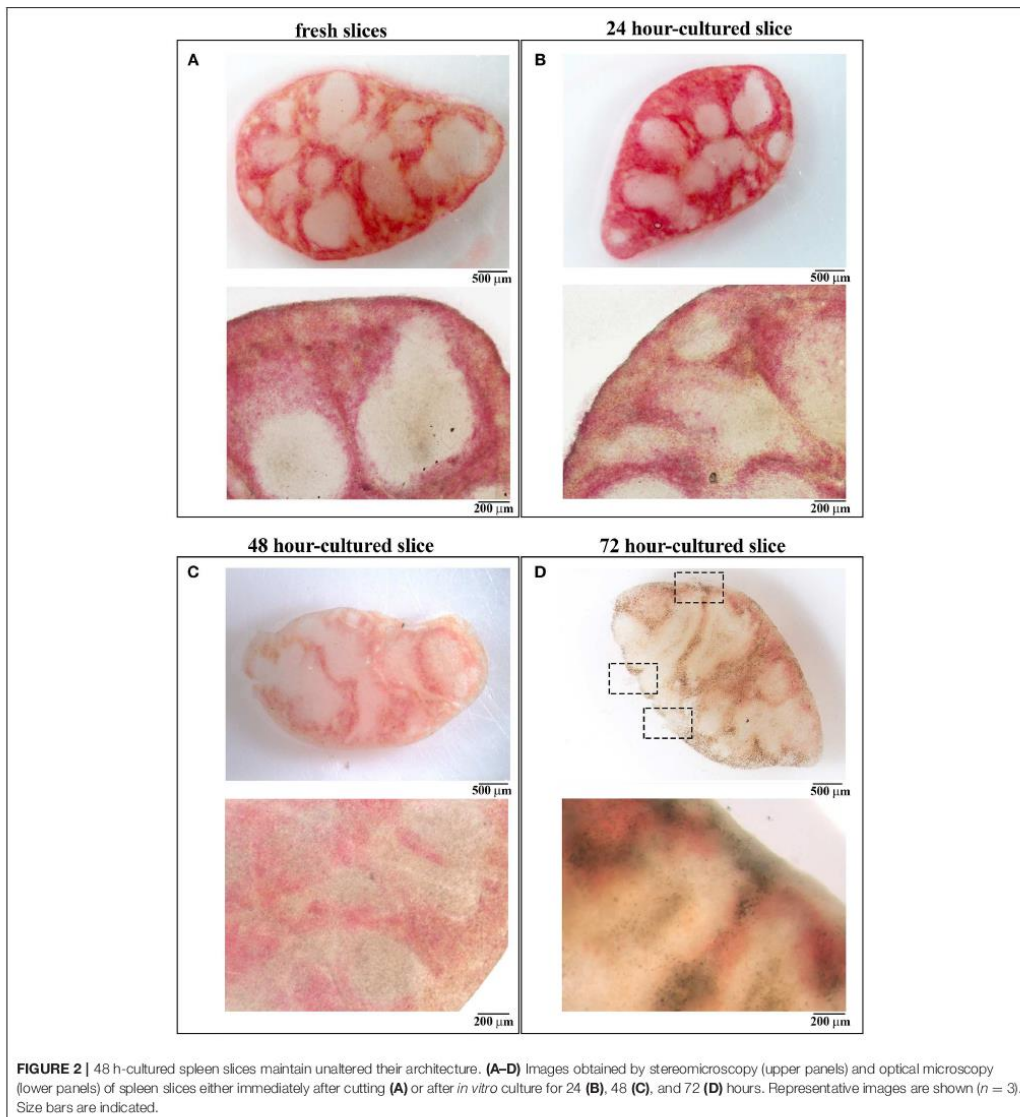
### Spleen Slices Cultured for 48 h *in vitro* Preserve Organ Integrity

Slices obtained applying the protocol described in the “Methods” section were transferred to diagnostic microscope slides and either left unstained or stained with Trypan blue. Optical microscopy was used to evaluate organ architecture. As shown in Figure 2, fresh slices were intact and the splenic structure was unaffected by the cut, with red pulp spacing out wide white pulp areas (Figure 2A).

Slices were cultured for 24, 48, 72, and 96 h in 48-well plates at 37°C with culture medium, one slice per well. To evaluate whether the *in vitro* culturing procedure affects organ architecture, cultured slices were transferred to diagnostic microscope slides and subjected to optical microscopy. As shown in Figure 2, slices cultured for 24 and 48 h were intact and both the splenic structure and the red-white pulp ratio remained almost unchanged when compared to fresh tissues (Figures 2B,C). Beginning from 72 h we observed a high degree of disruption of the slice architecture with wide necrotic zones affecting both the red and the white pulp (Figure 2D) and small ruptures lacerating both the organ texture and the surrounding capsule (see dashed rectangles in Figure 2D), possibly due to extreme slice fragility. We were unable to perform optical microscopy of 96 h-cultured slices, which were extremely damaged during their transfer to the microscope slides (data not shown). Our data suggest that 48 h is the longest time point of *in vitro* culture which maintains unaffected the architecture of spleen slices.

### 48 H-Culture Does Not Significantly Affect Cell Viability of Spleen Slice Cells

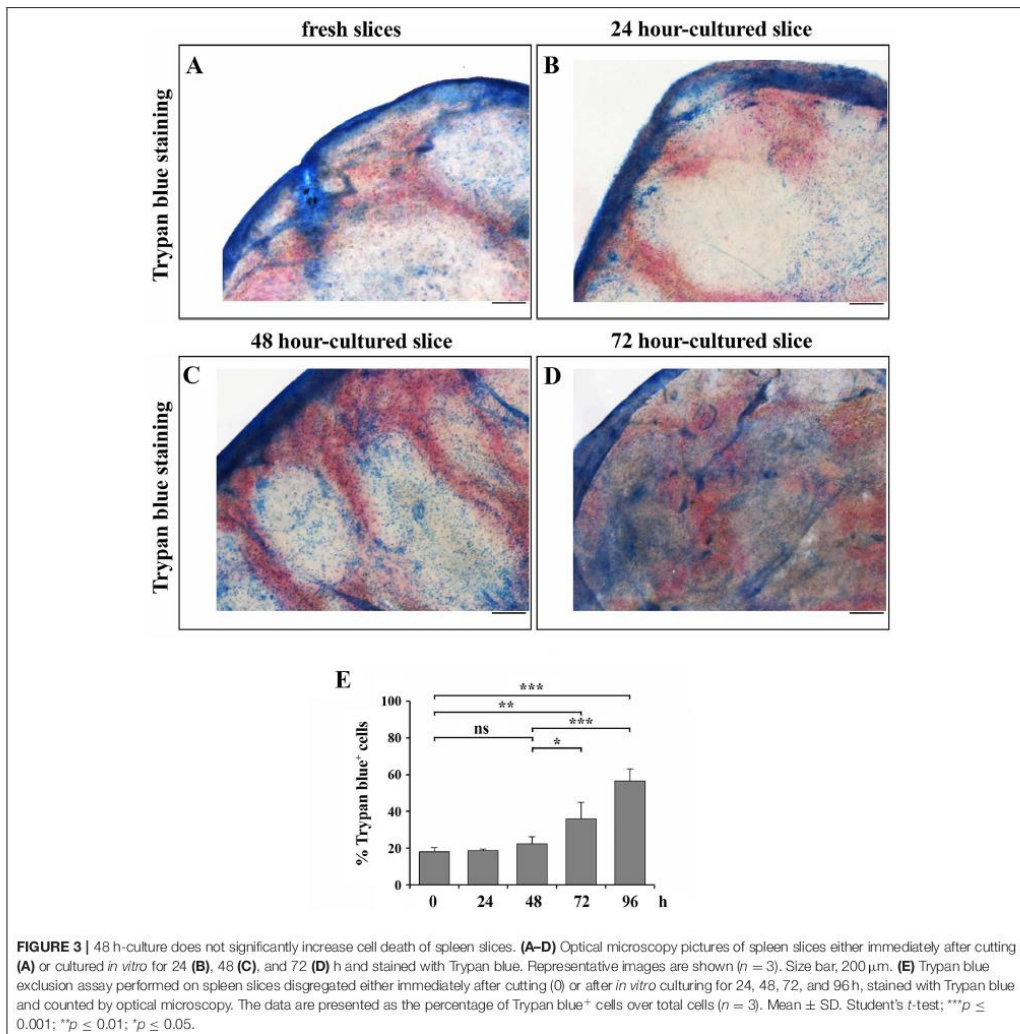
In an attempt to understand whether 48 h-cultured slices also maintain a reasonable degree of cell viability, we analyzed cell death in spleen slices either freshly prepared or cultured for 24, 48, 72, or 96 h at 37°C. Slices were transferred to diagnostic microscope slides, either left unstained, or stained with Trypan blue and then analyzed by optical microscopy. Trypan blue staining of spleen slices showed substantial non-specific staining of the trabecular outer capsule, which occurred independently of the culture time (Figures 3A–D). Trypan blue-positive cells could be observed in both red and white pulp of fresh slices (Figure 3A) and in samples cultured for 24 and 48 h, where staining was not significantly different from staining performed on fresh samples (Figures 3A–C). In contrast, spleen slices cultured for 72 h showed stronger Trypan blue positivity (Figure 3D), which suggests a high degree of cell death. As reported above, we were unable to perform Trypan blue staining



in 96 h-cultured slices, since they broke down during their transfer to the microscope slides.

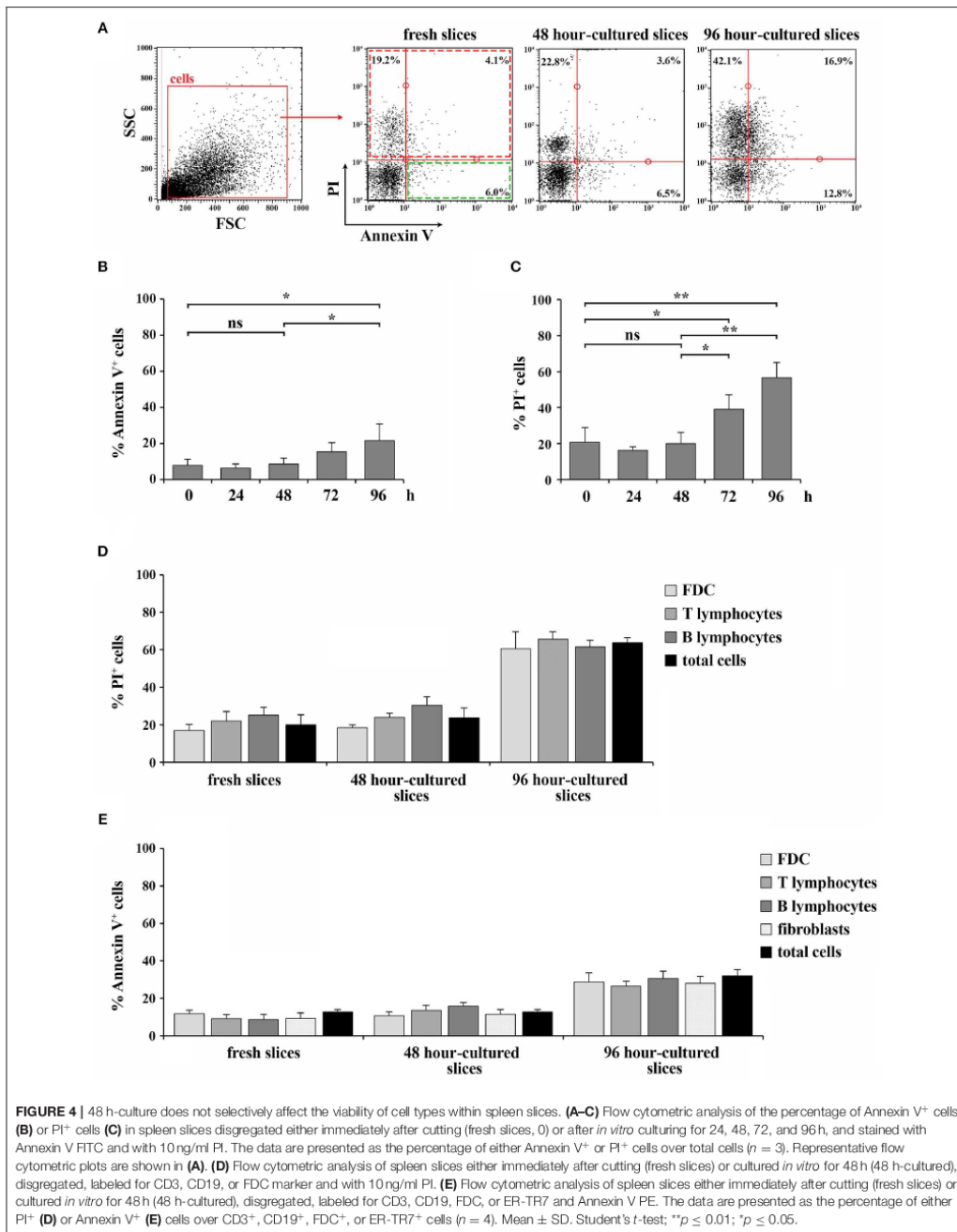
To quantify the extent of cell death, freshly prepared or cultured spleen slices were disaggregated and Trypan blue exclusion assays were performed. In line with the results obtained by optical microscopy, the percentages of Trypan blue<sup>+</sup> cells in

24- and 48 h-cultured slices were comparable to fresh tissues, while longer culture times elicited significantly higher positivity, with a very high percentage of Trypan blue<sup>+</sup> cells in 96 h-cultured slices, indicating a high degree of cell death in slices cultured for over 48 h (Figure 3E). The extent of cell death was also quantified by flow cytometry in spleen slices either

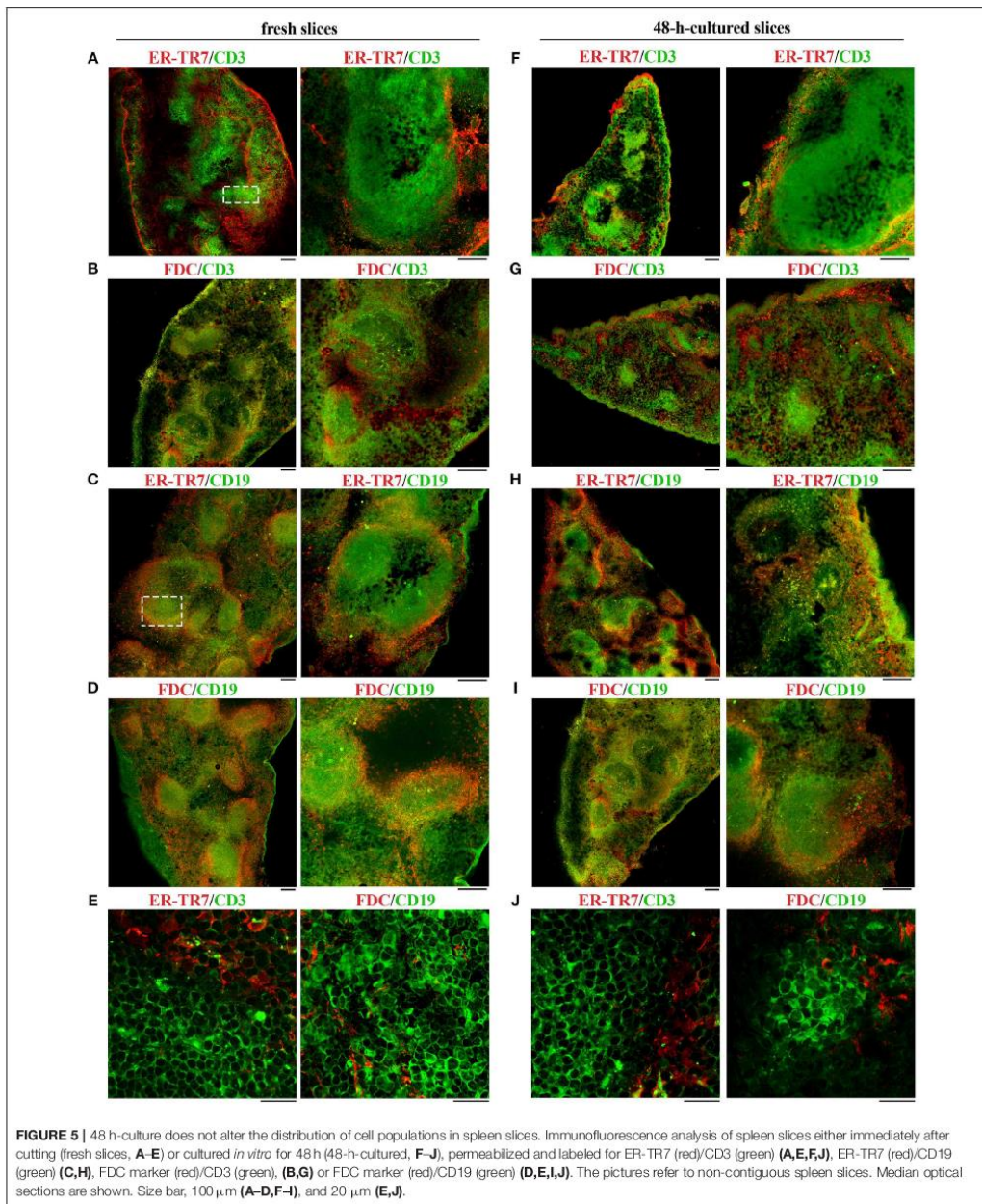


freshly prepared or cultured for 24, 48, 72, or 96 h at 37°C, disaggregated and stained with Annexin V and PI. As shown in **Figure 4**, slices cultured for 24 and 48 h showed percentages of PI<sup>+</sup> dead cells, as well as of Annexin V<sup>+</sup>/PI<sup>-</sup> early apoptotic cells, comparable to freshly cut slices (**Figures 4A–C**). By contrast, the percentage of Annexin V<sup>+</sup>/PI<sup>-</sup> early apoptotic cells and, to a higher extent, of PI<sup>+</sup> dead cells increased in slices cultured at 37°C for longer times (**Figures 4A–C**). These results indicate the beginning of the deterioration process in slices subjected to prolonged *in vitro* culture. To investigate whether the viability

of the different cell types present in the slices was differentially affected during slice culture, we carried out a flow cytometric analysis of spleen slices either freshly prepared or cultured for 48 or 96 h at 37°C, disaggregated and stained with PI in combination with antibodies against CD3, CD19, and FDC, which specifically stain the spleen-resident T cells, B cells and FDCs, respectively. As shown in **Figure 4D**, the deterioration process equally affects all cell types analyzed. Staining of spleen-resident reticular fibroblasts was carried out using an antibody against the specific cytoplasmic marker ER-TR7. This requires









plasma-membrane permeabilization, which prevents labeling of dead cells with PI. To overcome this limitation the relative levels of death in spleen-resident cell populations was also evaluated by staining slice-derived cells with the surface apoptotic marker Annexin V in combination with antibodies against CD3, CD19, FDC, and ER-TR7. As shown in **Figure 4E**, the percentage of Annexin V<sup>+</sup> cells was similar among cell types and did not significantly change compared to total cells. Collectively, our data demonstrate that while 48 h-cultured slices maintain the correct tissue organization and do not display an enhanced degree of cell death compared to freshly cut slices, 72 h-cultured slices appear significantly damaged, indicating that spleen slices can be maintained in culture for no more than 48 h, at least in the culture conditions used.

### Spleen Slices Cultured for 48 h *in vitro* Maintain the Tissue Localization of Cell Populations

The lymphoid tissue that constitutes the white pulp is organized around the arterial vessels in T- and B-cell compartments, whose maintenance is controlled by specific chemokines that attract T and B cells to their respective localization (8, 15). To evaluate the localization of immune cells and to assess the extent of organ texture degeneration in spleen slices subjected to prolonged *in vitro* culturing, cell distribution was assessed by immunofluorescence in spleen slices either immediately after cutting (fresh slices) or cultured for 48 h at 37°C in culture medium (**Figures 5A–J** and **Supplementary Figure 1**). In fresh slices immune cells were mainly distributed in lymphoid compartments, with T cells localized in T cell areas (**Figure 5A**, dashed rectangle), B cells mainly confined to germinal centers (**Figure 5C**, dashed rectangle), with a framework of ER-TR7-secreting reticular fibroblasts and FDC surrounding the marginal zones (**Figures 5A–E**). This structure was maintained almost unchanged in slices cultured for 48 h (**Figures 5F–J**), although we observed a partial decrease in the size (panel G) and/or cellularity (panels G–I) of white pulp areas, which might be accounted for by a partial loss of non-adherent lymphocytes in the culture medium. These results, together with the fact that we were unable to perform the immunofluorescence analysis of 96 h-cultured slices due to their high degree of degeneration, suggest that 48 h-cultured spleen slices are suitable for functional assays.

### RNA Extracted From 48 H-Cultured Spleen Slices Is Suitable for qRT-PCR Analysis

RNA was extracted from homogenates obtained from 1, 3, and 5 spleen slices either immediately after cutting (0 h) or maintained in culture for 48 and 96 h. RNA was quantified and its quality checked using QIAxpress System (Qiagen). As shown in **Figure 6A** and in **Table 1**, the amount of RNA was very low when extracted from 1 slice immediately after cut. Conversely, both the yield and the quality of RNA extracted from 3 and 5 slices were sufficient to allow for retrotranscription (**Figure 6A** and **Table 1**). Similar results were obtained when we analyzed samples cultured for 48 h, where we observed a limited decrease

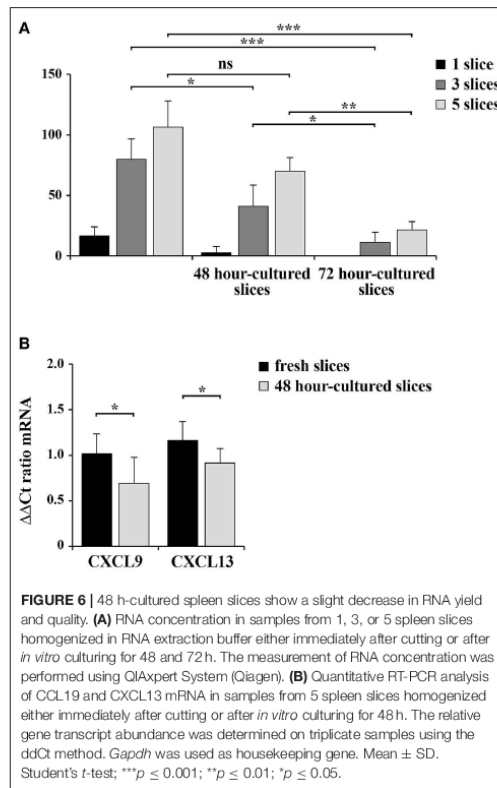


**FIGURE 6** | 48 h-cultured spleen slices show a slight decrease in RNA yield and quality. **(A)** RNA concentration in samples from 1, 3, or 5 spleen slices homogenized in RNA extraction buffer either immediately after cutting or after *in vitro* culturing for 48 and 72 h. The measurement of RNA concentration was performed using QIAxpress System (Qiagen). **(B)** Quantitative RT-PCR analysis of CXCL9 and CXCL13 mRNA in samples from 5 spleen slices homogenized either immediately after cutting or after *in vitro* culturing for 48 h. The relative gene transcript abundance was determined on triplicate samples using the ddCt method. *Gapdh* was used as housekeeping gene. Mean  $\pm$  SD. Student's *t*-test; \*\*\* $p \leq 0.001$ ; \*\* $p \leq 0.01$ ; \* $p \leq 0.05$ .

**TABLE 1** | Yield and quality of RNA isolated from spleen slices (1, 3, or 5 slices/sample) immediately after cutting or cultured for either 48 or 96 h.

Slice number	Culture time (hours)	RNA (ng/ $\mu$ l)	Impurities (A260)	Residue (%)	A260	A260/A280
1	0	11.2	0.43	1.1	0.71	1.83
3	0	83.2	0.00	0.4	2.08	2.06
5	0	121.2	0.01	0.3	4.28	2.08
1	48	N/A	0.11	21.7	0	0
3	48	51.4	0.02	0.9	1.32	2.13
5	48	91.0	0.00	0.5	2.27	2.10
1	96	N/A	0.00	2.6	0.00	0
3	96	11.3	0.01	0.8	0.81	2.17
5	96	32.3	0.02	0.7	0.90	2.11

in both yield and quality of RNA (**Figure 6A** and **Table 1**). As expected, RNA recovery in 96 h-cultured slices was very low (**Figure 6A** and **Table 1**). Based on these results, the quality of

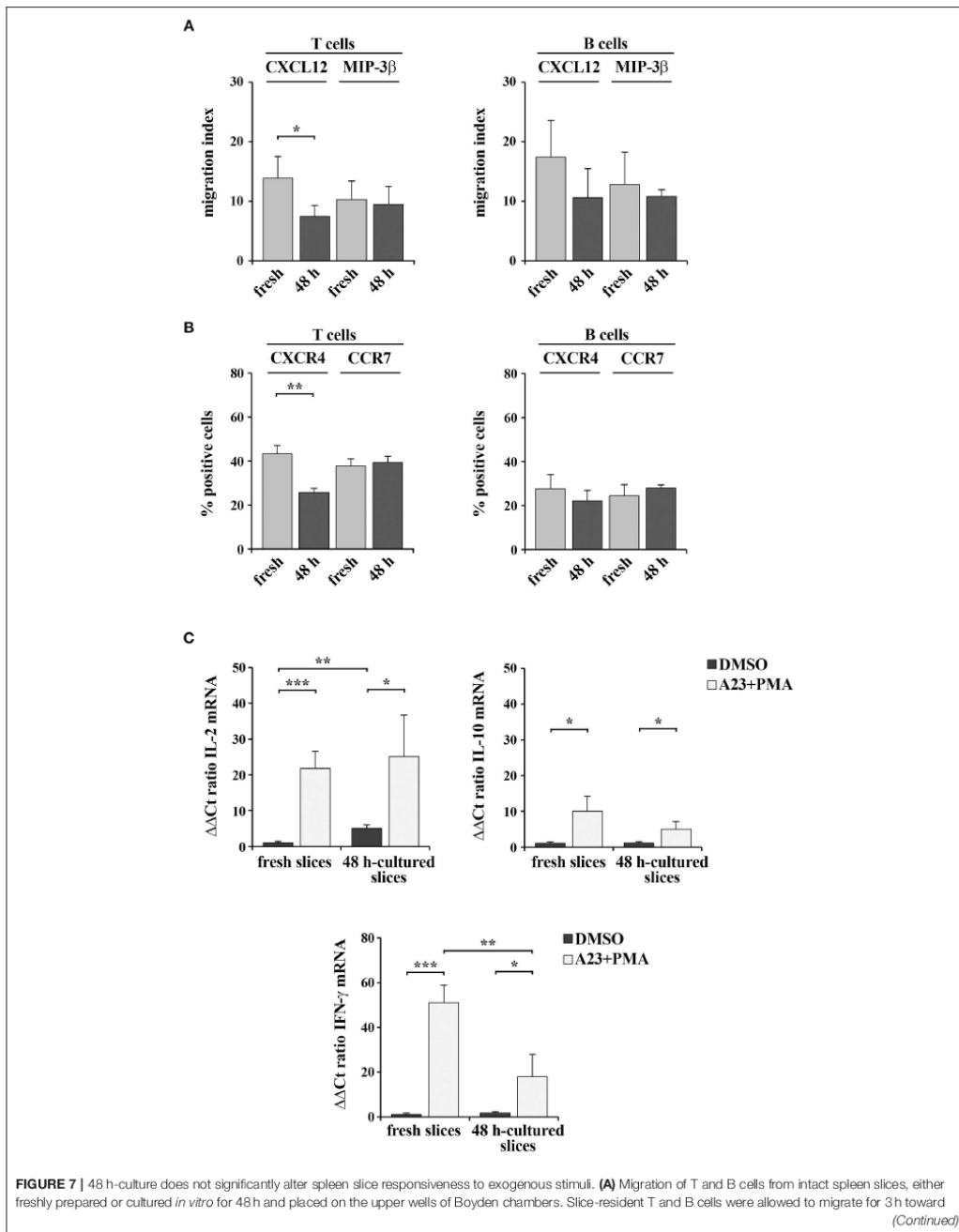


**FIGURE 7** | the lower wells containing 100 ng/ml CXCL12 or MIP3- $\beta$ . Cells recovered from the lower wells were stained with PE anti-CD3 and FITC anti-CD19 antibodies and counted by flow cytometry. The data, obtained on duplicate samples from each spleen slice, are presented as mean migration index (ratio migrated cells in chemokine-treated vs. untreated samples)  $\pm$  SD. **(B)** Flow cytometric analysis of the percentages of CXCR4<sup>+</sup> or CCR7<sup>+</sup> T lymphocytes (stained with anti-CD3 antibodies) and CXCR4<sup>+</sup> or CCR7<sup>+</sup> B lymphocytes (stained with anti-CD22 antibodies) in spleen slices disaggregated either immediately after cutting (fresh) or after *in vitro* culturing for 48 h. The data are presented as the percentage of either CXCR4<sup>+</sup> or CCR7<sup>+</sup> cells over total CD3<sup>+</sup> or CD22<sup>+</sup> cells ( $n = 3$ ). **(C)** Quantitative RT-PCR analysis of IL-2, IL-10, and IFN- $\gamma$  mRNA in samples from 3 spleen slices stimulated for 6 h with 500 ng/ml A23187 (A23) and 100 ng/ml PMA (A23+PMA) or with carrier (DMSO) either immediately after cutting or after *in vitro* culturing for 48 h and then homogenized for RNA extraction. The relative gene transcript abundance was determined on triplicate samples using the ddCt method. *Gapdh* was used as housekeeping gene. Mean  $\pm$  SD. Student's *t* test; \*\* $p \leq 0.001$ ; \* $p \leq 0.01$ ;  $p \leq 0.05$ .

the RNA was assessed by qRT-PCR analysis on RNA obtained from 5 slices either fresh or cultured for 48 h. In order to define the sensitivity of the assay, the transcripts encoding for the chemokines CCL19 (CC-chemokine ligand) and CXCL13 (CXC-chemokine ligand) were selected, due to their very low expression levels in lymphoid tissues under physiologic conditions (16). GAPDH was used as the housekeeping gene. The transcripts for both CCL19 and CXCL13 were easily detectable in fresh slices and were still clearly detectable in slices cultured for 48 h, although slightly decreased (Figure 6B) despite the lower RNA yield of these cultured samples (Figure 6A). Collectively, our data highlight the advantages of the new method described here to obtain live spleen sections which preserve both structure and cell viability and that can be used for functional assays.

### Spleen Slices Cultured for 48 h *in vitro* Are Responsive to Exogenous Stimuli

We assessed whether 48-h *in vitro* culturing preserves the responsiveness of spleen slices to exogenous stimulation. The chemotactic ability of cells within spleen slices either immediately after cutting or cultured for 48 h at 37°C was analyzed by Transwell assays. Intact slices were placed on the upper wells of Boyden chambers and cells were allowed to migrate to the lower wells toward the chemokines CXCL12 or MIP-3 $\beta$ , which bind the respective lymphocyte-specific receptors CXCR4 and CCR7 (17). Migrated T and B cells were then stained with anti-mouse CD3 PE and anti-mouse CD19 FITC antibodies and quantified by flow cytometry. As shown in Figure 7A, chemotaxis of both T and B cells toward MIP-3 $\beta$  (Figure 7A) was barely affected by *in vitro* culturing, as was surface CCR7 (Figure 7B). CXCL12-dependent chemotaxis, although still clearly detectable in 48 h-cultured slices, was slightly decreased (Figure 7A), however this was likely the consequence of a loss of surface CXCR4 rather than a loss of responsiveness (Figure 7B). Hence, cells residing in slices cultured *in vitro* for 48 h maintain their responsiveness to chemotactic stimuli.

Freshly cut and 48 h-cultured spleen slices were also analyzed for their ability to respond to the non-specific mitogenic combination of the Ca<sup>2+</sup> ionophore A23187 and PMA. As a read-out of cell stimulation, we quantified by qRT-PCR the mRNA levels of the cytokines IL-2, IL-10, and IFN- $\gamma$ , which are expressed in lymphocytes and stromal cells following mitogenic stimulation (18, 19). As shown in Figure 7C, both freshly cut slices and slices cultured *in vitro* for 48 h expressed enhanced amounts of the analyzed cytokines following stimulation. Interestingly, while IFN- $\gamma$  expression

was lower in the 48-h *in vitro* cultured slices compared to the freshly cut ones, the expression of both IL-2 and IL-10 was unaffected by *in vitro* culturing (Figure 7C). Collectively, these results demonstrate that spleen slices cultured *in vitro* for 48 h are suitable for functional assays and retain the sensitivity to exogenous stimuli similar to freshly prepared spleen slices.

## DISCUSSION

Here we set up a method that allows for the efficient precision-cut of mouse spleens to obtain non-damaged, live slices for organotypic spleen culture. We furthermore optimized the *in vitro* culture of these slices. We show that spleen slices can be maintained in culture for 48 h without marked loss of organ architecture and with a minimal loss of cell viability, which allows to perform functional assays on slices treated *in vitro*. Moreover, the quality of the RNA isolated from cell homogenates of 48 h-cultured slices is sufficient to allow for the amplification of low-abundance chemokine transcripts.

Organotypic culture technology is routinely used to perform organotypic culture of central nervous system sections (20, 21). However, its application to lymphoid organs has lagged behind. We found only one paper describing this technique on human spleen and lymph node biopsies, where the authors obtain slices not <400  $\mu$ m-thick which survive in culture for up to 1 week (4). The method we propose, which produces 230  $\mu$ m-thick spleen slices or lower, represents a new application of this technique that meets the need to provide an easy-to-handle way to simulate the 3-D context of the immune system where all cellular components are represented in the respective physiological locations. The limited thickness of the slices that we obtain will be useful for treatments *in vitro*, which can easily reach the whole depth of the slices. However, the standard conditions that we apply for the *in vitro* culture of spleen slices do not allow us to maintain tissue slices viable for longer than 48 h, as instead reported by Hoffmann and colleagues for human lymphoid biopsies (4), possibly due to insufficient oxygen perfusion. Organotypic culture often requires dedicated culture media supplemented with specific nutrients or growth factors (22, 23). Optimizing the *in vitro* culture protocol may help prolonging the viability of vibratome-generated, thin spleen slices for longer-term functional assays *in vitro*.

Studying the response of immune cells within their microenvironment has become a central requirement for the development of personalized immunotherapy-based treatments

against cancer (24). It is noteworthy that, among recent technical advances, new miniaturized “organ-on-a-chip” cultures were introduced in an attempt to recapitulate *in vitro* the organ environment by mimicking blood flow through microfluidic systems (25, 26). However, the high costs of this technique preclude its generalized exploitation. By comparison, the organotypic culture represents a cheap, easy-to-handle method to study *in vitro* the interplay among the cellular components of the stromal microenvironment in both physiological and pathological settings and to test the immune cell response to drugs.

## DATA AVAILABILITY STATEMENT

All datasets generated for this study are included in the article/Supplementary Material.

## ETHICS STATEMENT

The animal study was reviewed and approved by the Italian Ministry of Health (197/2015-PR) and OPBA, University of Siena.

## REFERENCES

- Schwerdtfeger LA, Tobet SA. From organotypic culture to body-on-a-chip: a neuroendocrine perspective. *J Neuroendocrinol.* (2019) 31:e12650. doi: 10.1111/jne.12650
- Cyrus Arman A, Sampath AP. Patch clamp recordings from mouse retinal neurons in a dark-adapted slice preparation. *J Vis Exp.* (2010) 12:2107. doi: 10.3791/2107
- Misra S, Moro CF, Del Chiaro M, Pouso S, Sebestyén A, Löhr M, et al. *Ex vivo* organotypic culture system of precision-cut slices of human pancreatic ductal adenocarcinoma. *Sci Rep.* (2019) 9:2133. doi: 10.1038/s41598-019-38603-w
- Hoffmann P, Skibinski G, James K. Organ culture of human lymphoid tissue I. Characteristics of the system. *J Immunol Methods.* (1995) 179:37–49. doi: 10.1016/0022-1759(94)00268-2
- Nagarsheth N, Wicha MS, Zou W. Chemokines in the cancer microenvironment and their relevance in cancer immunotherapy. *Nat Rev Immunol.* (2017) 17:559–72. doi: 10.1038/nri.2017.49
- Lu LC, Chang CJ, Hsu CH. Targeting myeloid-derived suppressor cells in the treatment of hepatocellular carcinoma: current state and future perspectives. *J Hepatocell Carcinoma.* (2019) 6:71–84. doi: 10.2147/jhc.s159693
- Ospov A, Saung MT, Zheng L, Murphy AG. Small molecule immunomodulation: the tumor microenvironment and overcoming immune escape. *J Immunother Cancer.* (2019) 7:224. doi: 10.1186/s40425-019-0667-0
- Mebius RE, Kraal G. Structure and function of the spleen. *Nat Rev Immunol.* (2005) 5:606–16. doi: 10.1038/nri1669
- Mattei G, Cristiani I, Magliaro C, Ahluwalia A. Profile analysis of hepatic porcine and murine brain tissue slices obtained with a vibratome. *PeerJ.* (2015) 3:e932. doi: 10.7717/peerj.932
- Lev-Cohain N, Sapir G, Harris T, Azar A, Gamlil A, Nardi-Schreiber A, et al. Real-time ALT and LDH activities determined in viable precision-cut mouse liver slices using hyperpolarized [1-13C]pyruvate—implications for studies on biopsied liver tissues. *NMR Biomed.* (2019) 32:e4043. doi: 10.1002/nbm.4043
- Rieg AD, Bunting NA, Cranen C, Suleiman S, Spillner JW, Schnöring H, et al. Tyrosine kinase inhibitors relax pulmonary arteries in human and murine precision-cut lung slices. *Respir Res.* (2019) 20:111. doi: 10.1186/s12931-019-1074-2
- Patrussi L, Capitani N, Ulivieri C, Manganaro N, Granai M, Cattaneo F, et al. p66Shc deficiency in the Eμ-TCL1 mouse model of chronic lymphocytic leukemia enhances leukemogenesis by altering the chemokine receptor landscape. *Haematologica.* (2019) 104:2040–52. doi: 10.3324/haematol.2018.209981

## AUTHOR CONTRIBUTIONS

LP, FF, NM, NC, VT, and FL performed the work. LP and CB wrote the manuscript. LB, GP, and IC contributed to set up the spleen slice culture conditions.

## FUNDING

The research leading to these results has received funding from AIRC under IG 2017—ID. 20148 project—P.I. Baldari Cosima.

## ACKNOWLEDGMENTS

The authors wish to thank David Mercati and Sonia Grassini for technical assistance.

## SUPPLEMENTARY MATERIAL

The Supplementary Material for this article can be found online at: <https://www.frontiersin.org/articles/10.3389/fimmu.2020.00471/full#supplementary-material>

- Patrussi L, Capitani N, Martini V, Pizzi M, Trimarco V, Frezzato F, et al. Enhanced chemokine receptor recycling and impaired S1P1 expression promote leukemic cell infiltration of lymph nodes in chronic lymphocytic leukemia. *Cancer Res.* (2015) 75:4153–63. doi: 10.1158/0008-5472.CAN-15-0986
- Patrussi L, Capitani N, Cannizzaro E, Finetti F, Lucherini OM, Pelicci PG, et al. Negative regulation of chemokine receptor signaling and B-cell chemotaxis by p66Shc. *Cell Death Dis.* (2014) 5:e1068. doi: 10.1038/cddis.2014.44
- Schulz O, Hammerschmidt SI, Moschovakis GL, Förster R. Chemokines and chemokine receptors in lymphoid tissue dynamics. *Annu Rev Immunol.* (2016) 34:203–42. doi: 10.1146/annurev-immunol-041015-055649
- Eberlein J, Nguyen TT, Victorino F, Golden-Mason L, Rosen HR, Homann D. Comprehensive assessment of chemokine expression profiles by flow cytometry. *J Clin Invest.* (2010) 120:907–23. doi: 10.1172/JCI40645
- Patrussi L, Capitani N, Baldari CT. Abnormalities in chemokine receptor recycling in chronic lymphocytic leukemia. *Cell Mol Life Sci.* (2019) 76:3249–61. doi: 10.1007/s00018-019-03058-9
- Chopra RK, Holbrook NJ, Powers DC, McCoy MT, Adler WH, Nagel JE. Interleukin 2, interleukin 2 receptor, and interferon- $\gamma$  synthesis and mRNA expression in phorbol myristate acetate and calcium ionophore A23187-stimulated T cells from elderly humans. *Clin Immunol Immunopathol.* (1989) 53:297–308. doi: 10.1016/0090-1229(89)90058-5
- Rachon D, Rimoldi G, Wuttke W. *In vitro* effects of benzophenone-2 and octyl-methoxycinnamate on the production of interferon- $\gamma$  and interleukin-10 by murine splenocytes. *Immunopharmacol Immunotoxicol.* (2006) 28:501–10. doi: 10.1080/08923970600927751
- Pampaloni NP, Rago I, Calaresu I, Cozzarini L, Casalis L, Goldoni A, et al. Transparent carbon nanotubes promote the outgrowth of enthoriondentate projections in lesioned organ slice cultures. *Dev Neurobiol.* (2019). doi: 10.1002/dneu.22711. [Epub ahead of print].
- Musto M, Rauti R, Rodrigues AF, Bonechi E, Ballerini C, Kostarelos K, et al. 3D organotypic spinal cultures: exploring neuron and neuroglia responses upon prolonged exposure to graphene oxide. *Front Syst Neurosci.* (2019) 13:1. doi: 10.3389/fnsys.2019.00001
- Brandenburger M, Wenzel J, Bogdan R, Richardt D, Nguemo F, Reppel M, et al. Organotypic slice culture from human adult ventricular myocardium. *Cardiovasc Res.* (2012) 93:50–9. doi: 10.1093/cvr/cvr259
- Raju ENS, Kuechler J, Behling S, Sridhar S, Hirsland E, Tronnier V, et al. Maintenance of stemlike glioma cells and microglia in an

- organotypic glioma slice model. *Neurosurgery*. (2015) 77:629–43. doi: 10.1227/NEU.0000000000000891
24. Flemming A. Tumour heterogeneity determines immune response. *Nat Rev Immunol*. (2019) 19:662–3. doi: 10.1038/s41577-019-0230-8
25. Sun W, Luo Z, Lee J, Kim HJ, Lee KJ, Tebon P, et al. Organ-on-a-chip for cancer and immune organs modeling. *Adv Healthc Mater*. (2019) 8:e1900754. doi: 10.1002/adhm.201801363
26. Lee SH, Sung JH. Organ-on-a-chip technology for reproducing multiorgan physiology. *Adv Healthc Mater*. (2018) 7:1700419. doi: 10.1002/adhm.201700419

**Conflict of Interest:** The authors declare that the research was conducted in the absence of any commercial or financial relationships that could be construed as a potential conflict of interest.

Copyright © 2020 Finetti, Capitani, Manganaro, Tatangelo, Libonati, Panattoni, Calaresu, Ballerini, Baldari and Patrussi. This is an open-access article distributed under the terms of the Creative Commons Attribution License (CC BY). The use, distribution or reproduction in other forums is permitted, provided the original author(s) and the copyright owner(s) are credited and that the original publication in this journal is cited, in accordance with accepted academic practice. No use, distribution or reproduction is permitted which does not comply with these terms.



## PATENTS INVOLVEMENT

- European Patent Application – No. EP19382889.4 for “**Substrates for Culturing and Stimulating Cells**” with priority date 30/03/2020.
- European Patent Application – No. EP20382637.5 for "**Bidirectional medical devises for monitoring and stimulating neurons**" with priority date 15/07/2020.

## CONCLUSIVE REMARKS

Nanotechnology applications to neuroscience have prompted neurobiology research towards previously unexpected possibilities. If on one hand it provided precious tools to finely dissect cell physiology, mechanics and biophysics, on the other, it permitted an unprecedented level of targeting to neural components [105,198,312,475]. To date, our understanding of CNS cells interaction with the world at the micro and nano scales is supporting the design of clinically oriented neural technologies able to raise not only our knowledge on neurophysiology, but also our capability of approaching to neurological disorders care [196,476,477]. The bibliographic work done in this thesis seeks to recapitulate the reasons of neurobiology's need for nanotechnologies input, the main criteria that implantable materials should meet to interface the CNS and their role in tuning certain physiological or regenerative functions. A mention to available electroceuticals and neural prosthesis is also provided, together with an overview of the future perspectives of this expanding field.

The results I obtained and presented in the previous section contain some encouraging findings, possibly laying the groundwork for further investigations or perhaps prompting towards rational design of neural devices. The consolidated CNTs effect of promoting axonal sprouting and fibers elongation have been challenged in a well characterized model of lesion across the entorhinal-hippocampal complex in organotypic slices. In particular, the main excitatory cortical inputs to the dentate gyrus (the perforant path) were studied by LFP recording and focal electrical stimulation over a transparent carpet of CNTs. The characterization of such connections in intact explants highlighted that CNTs retain the potential for increasing

the synchronization of signals conveyed across this pathway, which might represent a potential tool to investigate seizures formation *in vitro*. Remarkably in severed explants where entorhinal cortex and hippocampal formation were outdistanced at about 0.5 mm, CNTs induced a dramatic fiber sprouting resulting in the functional reconnection and restoration of the excitatory pathways. Indeed, in an additional study we pointed out that CNTs site-selective growth on micropatterns create a favorable environment for neuronal cells which preferentially elongate over CNT stripes. In the same study we also showed that these carbon nanostructures tightly interacting with neuronal membranes are suitable to produce evoked network responses, which just confirms and stresses the potential of this nanomaterial for neuroprosthetics design. Of course, nanometric features offered by CNTs are not the unique way to provide topographical support to neuronal cells [122,140]. In the framework of the ByAxon project I investigated neuronal networks interaction with fakir bed-like nanostructures, namely vertical metallic nanowires (Au-NWs) and polymer composite nanopillars (PS-CNT-NP), as a tool to positively impact neural electrode design. Interestingly, when dissociated hippocampal cells were plated and grown onto selected nanotopographies modulation of neuroglial cells adhesion was observed, with no repercussion on neuronal densities. Such an evidence was encouraging given the drawbacks related to astroglia-mediated electrodes encapsulation upon implantation [168]. Importantly, these observations always associated with sustained synaptic activity (in Ca<sup>2+</sup> live imaging), but also with appropriate cell architecture and absence of cell damage. Both neurons and astroglia isotropically extended their branches over these vertical nanostructures, with the astrocytic component visibly shapeshifting from more flattened to more stellate and branched morphology, likely intending to establish the required physiological interaction with neuronal synapses [478]. In the case of polymeric

nanopillars, patch-clamp recordings in voltage mode were used to address the increased synaptic performance of interfaced neurons, which relied on a synaptogenic effect of the polymeric nanopillars. Finally, both metallic NWs and PS-CNT-NP were used to deliver electrical stimulation and evoke neuronal network activity, ultimately demonstrating their applicability for neural electrode fabrication. In subsequent experiments across the same project I approached other culture models such as transverse and longitudinal spinal cord slices. With these preparations long-term responses of the tissue to artificial materials can be easily addressed by electrophysiological means and immunolabeling. I therefore explored fiber bundles elongation and activity over polymeric micropatterned surfaces (polystyrene and PDMS) using transversal DRG-spinal cord slice cultures, which showed thicker and longer bundles formation compared to control (flat) surfaces. Indeed, if allowed to grow in pairs, spinal slices reconnected over considerable lengths (about 2 mm) by extending their fibers. This seemed to occur in two different fashions with PDMS patterns forming thicker bundles, while PS ones showing more widespread thin fibers elongation. It must be considered that, given the comparable grooves pitch (20  $\mu\text{m}$ ) of the two micropatterned polymers, these first glance observations might be due to the different stiffnesses of the two materials (PS > PDMS), indicating another important feature that needs to be investigated to provide a deeper understanding of neuron-to-nanomaterial interaction [479,480]. To conclude, the most ambitious attempt of this work regarded one of the biggest challenges in neuroscience: highly selective/minimally invasive neural activity recording. Nowadays, such a goal appears as a viable route, which will dramatically impact neurobiology and neurotechnology in the very next future [199,481]. In this context, I explored the possibility to use cutting edge technologies enabling magnetic field sensing at room temperature, for the recording of very small

field variations resulting from neural activity in spinal cord organotypic slices. Despite the irregular reproducibility of the measurements, some recordings provided promising results where spinal network activity (monitored also by  $\text{Ca}^{2+}$  imaging or electrophysiology) was correlated to magnetic signals of neuronal origin, as confirmed by tetrodotoxin application at the end of each experiment. Importantly, in independent experiments I could use these signals to evoke neuronal activity in the premotor region of a spinal cord organotypic slice, by presenting trains of the magnetic waveform to DRG neurons, thereby recruiting sensory pathways and entraining neurons in the ventral horn. These last experiments are sufficient to motivate and encourage the development of magnetic sensor-based neural recording devices with diminished invasiveness.

The overall thematics tackled in this work should be intended as the starting point to the long path required for neural prosthesis formulation, design, engineering and testing. Technological advances and researchers' efforts from the various subfield related to neuroscience will hopefully lead this discipline to a rapid evolution, providing previously unexpected tools to face the most impairing neurological disfunctions.



## BIBLIOGRAPHY

- [1] R. P. Feynman, In *Engineering and Science*; 1960; pp. 22–36.
- [2] D. Kahng, *Electric Field Controlled Semiconductor Device* 1963.
- [3] M. M. Atalla, E. Tannenbaum, E. J. Scheibner, *Bell Syst. Tech. J.* 1959, 38, 749.
- [4] N. Taniguchi, In *Proceedings of the International Conference on Production Engineering*; Tokyo, 1974; pp. 18–23.
- [5] D. Schaming, H. Remita, *Found. Chem.* 2015, 17, 187.
- [6] D. J. Barber, I. C. Freestone, *Archaeometry* 1990, 32, 33.
- [7] C. H. Ian Freestone, Nigel Meeks, Margaret Sax, *Gold Bull.* 2007, 40, 270.
- [8] M. Reibold, P. Paufler, A. A. Levin, W. Kochmann, N. Pätzke, D. C. Meyer, *Nature* 2006, 444, 286.
- [9] M. Reibold, N. Pätzke, A. A. Levin, W. Kochmann, I. P. Shakhverdova, P. Paufler, D. C. Meyer, *Cryst. Res. Technol.* 2009, 44, 1139.
- [10] B. Goodell, X. Xinfeng, Q. Yuhui, G. Daniel, M. Peterson, J. Jellison, J. Nanosci. *Nanotechnol.* 2008, 8, 2472.
- [11] V. Amendola, R. Pilot, M. Frasconi, O. M. Maragò, M. A. Iatì, *J. Phys. Condens. Matter* 2017, 29.
- [12] J. Ueda, M. Samusawa, K. Kumagai, A. Ishida, S. Tanabe, *J. Mater. Sci.* 2014, 49, 3299.
- [13] D. T. Peterson, H. H. Baker, J. D. Verhoeven, *Mater. Charact.* 1990, 24, 355.
- [14] J. Wang, H. L. Duan, Z. P. Huang, B. L. Karihaloo, *Proc. R. Soc. A Math. Phys. Eng. Sci.* 2006, 462, 1355.
- [15] S. Cuenot, C. Frétiigny, S. Demoustier-Champagne, B. Nysten, *Phys. Rev. B - Condens. Matter Mater. Phys.* 2004, 69, 1.
- [16] J. Biener, A. Wittstock, T. F. Baumann, J. Weissmüller, M. Bäumer, A. V. Hamza, *Materials (Basel)*. 2009, 2, 2404.
- [17] M. Che Chon, *J. Struct. Chem.* 2004, 45, S6.
- [18] E. Abbe, *Arch. für Mikroskopische Anat.* 1873, 9, 413.
- [19] B. v. Borries, E. Ruska, *Zeitschrift für Phys.* 1933.
- [20] E. Ruska, *J. Ultrastruct. Mol. Struct. Res.* 1986, 95, 3.
- [21] M. von Ardenne, *Zeitschrift für Phys.* 1938.
- [22] D. McMullan, In *Biological Low-Voltage Scanning Electron Microscopy*; 2008; pp. 1–25.
- [23] G. Binnig, H. Rohrer, *Surf. Sci.* 1983.

- [24] G. Binnig, C. F. Quate, C. Gerber, *Phys. Rev. Lett.* 1986.
- [25] R. D. Piner, J. Zhu, F. Xu, S. Hong, 1999, 283, 661.
- [26] H. Liu, T. J. Webster, *Nanomedicine for implants: A review of studies and necessary experimental tools.* *Biomaterials* 2007.
- [27] S. E. McNeil, *J. Leukoc. Biol.* 2005.
- [28] B. High, A. A. Cole, X. Chen, T. S. Reese, *Electron microscopic tomography reveals discrete transcleft elements at excitatory and inhibitory synapses . Front. Synaptic Neurosci.* 2015, 7, 9.
- [29] T. Ushiki, *Collagen fibers, reticular fibers and elastic fibers. A comprehensive understanding from a morphological viewpoint.* *Arch. Histol. Cytol.* 2002.
- [30] T. Eldsdale, J. Bard, *J. Cell Biol.* 1972.
- [31] F. Gentile, M. Ferrari, P. Decuzzi, *Ann. Biomed. Eng.* 2008.
- [32] A. A. Bogdanov, J. W. Chen, H. W. Kang, R. Weissleder, *Magnetic resonance signal amplification probes. Ernst Schering Res. Found. Workshop* 2005.
- [33] S. V. Vinogradov, E. V. Batrakova, A. V. Kabanov, *Bioconjug. Chem.* 2004.
- [34] P. R. Lockman, M. O. Oyewumi, J. M. Koziara, K. E. Roder, R. J. Mumper, D. D. Allen, *J. Control. Release* 2003.
- [35] S. C. J. Steiniger, J. Kreuter, A. S. Khalansky, I. N. Skidan, A. I. Bobruskin, Z. S. Smirnova, S. E. Severin, R. Uhl, M. Kock, K. D. Geiger, S. E. Gelperina, *Int. J. Cancer* 2004.
- [36] F. Braet, E. Wisse, *Structural and functional aspects of liver sinusoidal endothelial cell fenestrae: a review.* *Comp. Hepatol.* 2002, 1, 1.
- [37] E. Wisse, F. Braet, D. Luo, R. De Zanger, D. Jans, E. Crabbe, A. Vermoesen, *Toxicol. Pathol.* 1996, 24, 100.
- [38] F. Braet, R. de Zanger, M. Baekeland, E. Crabbé, P. van der Smissen, E. Wisse, *Hepatology* 1995.
- [39] M. G. Harisinghani, J. Barentsz, P. F. Hahn, W. M. Deserno, S. Tabatabaei, C. H. Van de Kaa, J. De la Rosette, R. Weissleder, *N. Engl. J. Med.* 2003.
- [40] M. H. Schwenk, *Ferumoxytol: A new intravenous iron preparation for the treatment of iron deficiency anemia in patients with chronic kidney disease.* *Pharmacotherapy* 2010.
- [41] A. S. Thakor, J. V. Jokerst, P. Ghanouni, J. L. Campbell, E. Mittra, S. S. Gambhir, *J. Nucl. Med.* 2016.
- [42] A. C. Anselmo, S. Mitragotri, *Bioeng. Transl. Med.* 2016.
- [43] E. Engel, A. Michiardi, M. Navarro, D. Lacroix, J. A. Planell, *Nanotechnology in regenerative medicine: the materials side.* *Trends Biotechnol.* 2008.
- [44] Y. Ikada, *Challenges in tissue engineering.* *J. R. Soc. Interface* 2006.
- [45] I. Francolini, C. Vuotto, A. Piozzi, G. Donelli, *Antifouling and antimicrobial biomaterials: an overview.* *APMIS* 2017.

- [46] J. L. Harding, M. M. Reynolds, Combating medical device fouling. *Trends Biotechnol.* 2014.
- [47] F. Lotti, F. Ranieri, G. Vadalà, L. Zollo, G. Di Pino, Invasive intraneural interfaces: Foreign body reaction issues. *Front. Neurosci.* 2017.
- [48] E. Mariani, G. Lisignoli, R. M. Borzì, L. Pulsatelli, Biomaterials: Foreign bodies or tuners for the immune response? *Int. J. Mol. Sci.* 2019.
- [49] N. Mansouri, Samira Bagheri, S. Bagheri, *Mater. Sci. Eng. C* 2016, 61, 906.
- [50] V. S. Polikov, P. A. Tresco, W. M. Reichert, *J. Neurosci. Methods* 2005, 148, 1.
- [51] G. Cooper, *Cell A Mol. Approach.* 2000.
- [52] M. Modo, *Front. Neurosci.* 2019, 13, 1.
- [53] D. F. LaRosa, A. H. Rahman, L. A. Turka, *J. Immunol.* 2007.
- [54] N. Akkerman, L. H. K. Defize, *BioEssays* 2017, 39, 1.
- [55] J. Koffler, W. Zhu, X. Qu, O. Platoshyn, J. N. Dulin, J. Brock, L. Graham, P. Lu, J. Sakamoto, M. Marsala, S. Chen, M. H. Tuszynski, *Nat. Med.* 2019, 25, 263.
- [56] M. Pasqua, U. Pereira, A. Messina, C. de Lartigue, P. Vigneron, A. Dubart-Kupperschmitt, C. Legallais, *Tissue Eng. Part A* 2020, ten. TEA.2019.0262.
- [57] C. Legallais, D. Kim, S. M. Mihaila, M. Mihajlovic, M. Figliuzzi, B. Bonandrini, S. Salerno, F. A. Yousef Yengej, M. B. Rookmaaker, N. Sanchez Romero, P. Sainz-Arnal, U. Pereira, M. Pasqua, K. G. F. Gerritsen, M. C. Verhaar, A. Remuzzi, P. M. Baptista, L. De Bartolo, R. Masereeuw, D. Stamatialis, *Bioengineering Organs for Blood Detoxification. Adv. Healthc. Mater.* 2018.
- [58] M. Eiraku, N. Takata, H. Ishibashi, M. Kawada, E. Sakakura, S. Okuda, K. Sekiguchi, T. Adachi, Y. Sasai, *Nature* 2011.
- [59] N. D. Leipzig, M. S. Shoichet, *Biomaterials* 2009, 30, 6867.
- [60] J. Y. Rho, R. B. Ashman, C. H. Turner, *J. Biomech.* 1993, 26, 111.
- [61] S. Choi, H. Lee, R. Ghaffari, T. Hyeon, D. H. Kim, *Adv. Mater.* 2016.
- [62] C. Choi, M. K. Choi, T. Hyeon, D. H. Kim, *Nanomaterial-Based Soft Electronics for Healthcare Applications. ChemNanoMat* 2016.
- [63] L. Zhang, T. J. Webster, *Nanotechnology and nanomaterials: Promises for improved tissue regeneration. Nano Today* 2009.
- [64] S. P. Nukavarapu, S. G. Kumbar, J. L. Brown, N. R. Krogman, A. L. Weikel, M. D. Hindenlang, L. S. Nair, H. R. Allcock, C. T. Laurencin, *Biomacromolecules* 2008.
- [65] J. Kisiday, M. Jin, B. Kurz, H. Hung, C. Semino, S. Zhang, A. J. Grodzinsky, *Proc. Natl. Acad. Sci.* 2002, 99, 9996.
- [66] M. W. Tibbitt, K. S. Anseth, *Hydrogels as extracellular matrix mimics for 3D cell culture. Biotechnol. Bioeng.* 2009.
- [67] E. A. Abou Neel, W. Chrzanowski, V. M. Salih, H. W. Kim, J. C. Knowles, *Tissue engineering in dentistry. J. Dent.* 2014.

- [68] B. L. España-Sánchez, M. E. Cruz-Soto, E. A. Elizalde-Peña, S. Sabasflores-Benítez, A. Roca-Aranda, K. Esquivel-Escalante, G. Luna-Bárceñas, In *Tissue Regeneration*; 2018.
- [69] Z. P. Aguilar, Z. P. Aguilar, *Nanomater. Med. Appl.* 2013, 235.
- [70] P. Senn, M. Roccio, S. Hahnewald, C. Frick, M. Kwiatkowska, M. Ishikawa, P. Bako, H. Li, F. Edin, W. Liu, H. Rask-Andersen, I. Pyykkö, J. Zou, M. Mannerström, H. Keppner, A. Homsey, E. Laux, M. Llera, J. P. Lellouche, S. Ostrovsky, E. Banin, A. Gedanken, N. Perkas, U. Wank, K. H. Wiesmüller, P. Mistrík, H. Benav, C. Garnham, C. Jolly, F. Gander, P. Ulrich, M. Müller, H. Löwenheim, *Otol. Neurotol.* 2017, 38, e224.
- [71] H. Lee, T. K. Choi, Y. B. Lee, H. R. Cho, R. Ghaffari, L. Wang, H. J. Choi, T. D. Chung, N. Lu, T. Hyeon, S. H. Choi, D. H. Kim, *Nat. Nanotechnol.* 2016, 11, 566.
- [72] A. Agarwal, A. Shapero, D. Rodger, M. Humayun, Y. C. Tai, A. Emami, 2018 *IEEE Cust. Integr. Circuits Conf. CICC 2018* 2018, 1.
- [73] N. Lazkani, S. Truitt, N. K. Kawaguchi, A. J. Dewolf, C. A. Van Zant, J. P. Villegas, A. R. Hassel, J. J. Park, C. F. Jones, J. Butler, M. J. A. Rickard, *Proc. Annu. Int. Conf. IEEE Eng. Med. Biol. Soc. EMBS 2019*, 4363.
- [74] T. Pan, J. D. Brown, B. Ziaie, In *Annual International Conference of the IEEE Engineering in Medicine and Biology - Proceedings*; 2006.
- [75] C. Choi, M. K. Choi, S. Liu, M. S. Kim, O. K. Park, C. Im, J. Kim, X. Qin, G. J. Lee, K. W. Cho, M. Kim, E. Joh, J. Lee, D. Son, S. H. Kwon, N. L. Jeon, Y. M. Song, N. Lu, D. H. Kim, *Nat. Commun.* 2017, 8.
- [76] G. Vardi, J. Merrick, *J. Policy Pract. Intellect. Disabil.* 2007, 4, 215.
- [77] J. A. DiMasi, H. G. Grabowski, R. W. Hansen, *J. Health Econ.* 2016, 47, 20.
- [78] M. S. Alavijeh, M. Chishty, M. Z. Qaiser, A. M. Palmer, *NeuroRx* 2005, 2, 554.
- [79] D. Borsook, *Brain* 2012, 135, 320.
- [80] T. Wood, E. Nance, *APL Bioeng.* 2019, 3, 040901.
- [81] H. Acarón Ledesma, X. Li, J. L. Carvalho-de-Souza, W. Wei, F. Bezanilla, B. Tian, An atlas of nano-enabled neural interfaces. *Nat. Nanotechnol.* 2019.
- [82] N. R. Saunders, M. D. Habgood, K. Møllgård, K. M. Dziegielewska, The biological significance of brain barrier mechanisms: Help or hindrance in drug delivery to the central nervous system? *F1000Research* 2016.
- [83] S. Martel, M. Mohammadi, O. Felfoul, Zhao Lu, P. Pouponneau, *Int. J. Rob. Res.* 2009.
- [84] S. Martel, J. B. Mathieu, O. Felfoul, A. Chanu, E. Aboussouan, S. Tamaz, P. Pouponneau, L. Yahia, G. Beaudoin, G. Soulez, M. Mankiewicz, *Appl. Phys. Lett.* 2007.
- [85] J. Hu, S. Huang, L. Zhu, W. Huang, Y. Zhao, K. Jin, Q. Zhuge, *ACS Appl. Mater. Interfaces* 2018, 10, 32988.
- [86] F. Soto, R. Chrostowski, *Front. Bioeng. Biotechnol.* 2018, 6, 1.
- [87] O. A. Carballo-Molina, I. Velasco, *Front. Cell. Neurosci.* 2015, 9, 1.

- [88] N. J. Schaub, C. D. Johnson, B. Cooper, R. J. Gilbert, *J. Neurotrauma* 2016, 33, 1405.
- [89] R. G. Ellis-Behnke, Y. X. Liang, S. W. You, D. K. C. Tay, S. Zhang, K. F. So, G. E. Schneider, *Proc. Natl. Acad. Sci. U. S. A.* 2006, 103, 5054.
- [90] J. Guo, K. K. G. Leung, H. Su, Q. Yuan, L. Wang, T. H. Chu, W. Zhang, J. K. S. Pu, G. K. P. Ng, W. M. Wong, X. Dai, W. Wu, *Nanomedicine Nanotechnology, Biol. Med.* 2009, 5, 345.
- [91] J. Guo, H. Su, Y. Zeng, Y. X. Liang, W. M. Wong, R. G. Ellis-Behnke, K. F. So, W. Wu, *Nanomedicine Nanotechnology, Biol. Med.* 2007, 3, 311.
- [92] X. Zhan, M. Gao, Y. Jiang, W. Zhang, W. M. Wong, Q. Yuan, H. Su, X. Kang, X. Dai, W. Zhang, J. Guo, W. Wu, *Nanomedicine Nanotechnology, Biol. Med.* 2013, 9, 305.
- [93] J. Xie, M. R. MacEwan, A. G. Schwartz, Y. Xia, *Nanoscale* 2010, 2, 35.
- [94] L. Persano, A. Camposeo, C. Tekmen, D. Pisignano, *Macromol. Mater. Eng.* 2013, 298, 504.
- [95] M. P. Prabhakaran, J. Venugopal, C. K. Chan, S. Ramakrishna, *Nanotechnology* 2008.
- [96] H. K. Frost, T. Andersson, S. Johansson, U. Englund-Johansson, P. Ekström, L. B. Dahlin, F. Johansson, *Sci. Rep.* 2018, 8, 1.
- [97] L. N. Novikova, M. K. Kolar, P. J. Kingham, A. Ullrich, S. Oberhoffner, M. Renardy, M. Doser, E. Müller, M. Wiberg, L. N. Novikov, *Acta Biomater.* 2018, 66, 177.
- [98] A. Hurtado, J. M. Cregg, H. B. Wang, D. F. Wendell, M. Oudega, R. J. Gilbert, J. W. McDonald, *Biomaterials* 2011, 32, 6068.
- [99] L. H. Nguyen, M. Gao, J. Lin, W. Wu, J. Wang, S. Y. Chew, *Sci. Rep.* 2017, 7, 1.
- [100] X. Ma, J. Liu, W. Zhu, M. Tang, N. Lawrence, C. Yu, M. Gou, S. Chen, *Adv. Drug Deliv. Rev.* 2018.
- [101] G. D. Mahumane, P. Kumar, L. C. Du Toit, Y. E. Choonara, V. Pillay, 3D scaffolds for brain tissue regeneration: Architectural challenges. *Biomater. Sci.* 2018.
- [102] W. Zhu, X. Ma, M. Gou, D. Mei, K. Zhang, S. Chen, 3D printing of functional biomaterials for tissue engineering. *Curr. Opin. Biotechnol.* 2016.
- [103] R. L. Truby, J. A. Lewis, *Nature* 2016, 540, 371.
- [104] W. Sun, P. Lal, *Comput. Methods Programs Biomed.* 2002, 67, 85.
- [105] N. A. Kotov, J. O. Winter, I. P. Clements, E. Jan, B. P. Timko, S. Campidelli, S. Pathak, A. Mazzatenta, C. M. Lieber, M. Prato, R. V. Bellamkonda, G. A. Silva, N. W. S. Kam, F. Patolsky, L. Ballerini, *Nanomaterials for neural interfaces. Adv. Mater.* 2009.
- [106] A. Fabbro, A. Villari, J. Laishram, D. Scaini, F. M. Toma, A. Turco, M. Prato, L. Ballerini, *ACS Nano* 2012, 6, 2041.
- [107] V. Lovat, D. Pantarotto, L. Lagostena, B. Cacciari, M. Grandolfo, M. Righi, G. Spalluto, M. Prato, L. Ballerini, *Nano Lett.* 2005, 5.



- [108] K. Wang, H. A. Fishman, H. Dai, J. S. Harris, *Nano Lett.* 2006, 6, 2043.
- [109] R. Rauti, N. Lozano, V. León, D. Scaini, M. Musto, I. Rago, F. P. Ulloa Severino, A. Fabbro, L. Casalis, E. Vázquez, K. Kostarelos, M. Prato, L. Ballerini, *ACS Nano* 2016.
- [110] N. P. Pampaloni, D. Scaini, F. Perissinotto, S. Bosi, M. Prato, L. Ballerini, N. Paolo, D. Scaini, F. Perissinotto, S. Bosi, M. Prato, L. Ballerini, *Nanomedicine Nanotechnology, Biol. Med.* 2018, 14, 2521.
- [111] J. G. Hardy, J. Y. Lee, C. E. Schmidt, *Curr. Opin. Biotechnol.* 2013, 24, 847.
- [112] K. A. Ludwig, J. D. Uram, J. Yang, D. C. Martin, D. R. Kipke, *J. Neural Eng.* 2006, 3, 59.
- [113] P. M. George, A. W. Lyckman, D. A. Lavan, A. Hegde, Y. Leung, R. Avasare, C. Testa, P. M. Alexander, R. Langer, M. Sur, *Biomaterials* 2005, 26, 3511.
- [114] D. Khodagholy, T. Doublet, M. Gurfinkel, P. Quilichini, E. Ismailova, P. Leleux, T. Herve, S. Sanaur, C. Bernard, G. G. Malliaras, *Adv. Mater.* 2011, 23, 268.
- [115] S. C. Luo, E. M. Ali, N. C. Tansil, H. H. Yu, S. Gao, E. A. B. Kantchev, J. Y. Ying, *Langmuir* 2008, 24, 8071.
- [116] R. Balint, N. J. Cassidy, S. H. Cartmell, *Conductive polymers: Towards a smart biomaterial for tissue engineering.* *Acta Biomater.* 2014.
- [117] T. J. Rivers, T. W. Hudson, C. E. Schmidt, *Adv. Funct. Mater.* 2002, 12, 33.
- [118] A. C. da Silva, S. I. Córdoba de Torresi, *Front. Mater.* 2019, 6, 1.
- [119] R. G. Harrison, *J. Exp. Zool.* 1910, 9, 787.
- [120] P. Weiss, *J. Exp. Zool.* 1945, 100, 353.
- [121] A. S. G. Curtis, P. Clark, The effects of topographic and mechanical properties of materials on cell behavior. *Crit. Rev. Biocompat.* 1990.
- [122] D. Hoffman-Kim, J. A. Mitchel, R. V. Bellamkonda, *Annu. Rev. Biomed. Eng.* 2010.
- [123] O. Dobrokhotov, M. Samsonov, M. Sokabe, H. Hirata, *Clin. Transl. Med.* 2018, 7, 1.
- [124] M. E. Hatten, C. A. Mason, Mechanisms of glial-guided neuronal migration in vitro and in vivo. *Experientia* 1990.
- [125] J. D. Lathia, B. Patton, D. M. Eckley, T. Magnus, M. R. Mughal, T. Sasaki, M. A. Caldwell, M. S. Rao, M. P. Mattson, C. Ffrench-Constant, *J. Comp. Neurol.* 2007, 505, 630.
- [126] K. L. Mui, C. S. Chen, R. K. Assoian, *J. Cell Sci.* 2016, 129, 1093.
- [127] M. Amano, M. Nakayama, K. Kaibuchi, Rho-kinase/ROCK: A key regulator of the cytoskeleton and cell polarity. *Cytoskeleton* 2010.
- [128] F. Martino, A. R. Perestrelo, V. Vínarský, S. Pagliari, G. Forte, *Front. Physiol.* 2018, 9, 1.
- [129] S. Huvneers, E. H. J. Danen, *J. Cell Sci.* 2009, 122, 1059.
- [130] J. Du, Y. Zu, J. Li, S. Du, Y. Xu, L. Zhang, L. Jiang, Z. Wang, S. Chien, C. Yang, *Sci. Rep.* 2016, 6, 1.
- [131] M. Missler, T. C. Südhof, T. Biederer, *Cold Spring Harb. Perspect. Biol.* 2012, 4.

- [132] D. L. Benson, L. M. Schnapp, L. Shapiro, G. W. Huntley, Making memories stick: Cell-adhesion molecules in synaptic plasticity. *Trends Cell Biol.* 2000.
- [133] J. Arikath, L. F. Reichardt, Cadherins and catenins at synapses: roles in synaptogenesis and synaptic plasticity. *Trends Neurosci.* 2008.
- [134] F. J. Monje, E. J. Kim, D. D. Pollak, M. Cabatic, L. Li, A. Baston, G. Lubec, *NeuroSignals* 2012, 20, 1.
- [135] K. Pozo, L. A. Cingolani, S. Bassani, F. Laurent, M. Passafaro, Y. Goda, *Proc. Natl. Acad. Sci. U. S. A.* 2012.
- [136] M. Nuriya, R. L. Haganir, *J. Neurochem.* 2006.
- [137] L. Saglietti, C. Dequidt, K. Kamieniarz, M. C. Rousset, P. Valnegri, O. Thoumine, F. Beretta, L. Fagni, D. Choquet, C. Sala, M. Sheng, M. Passafaro, *Neuron* 2007.
- [138] C. Zhang, D. Atasoy, D. Araç, X. Yang, M. V. Fucillo, A. J. Robison, J. Ko, A. T. Brunger, T. C. Südhof, *Neuron* 2010.
- [139] K. Baranes, D. Hibsh, S. Cohen, T. Yamin, S. Efroni, A. Sharoni, O. Shefi, *Nano Lett.* 2019, 19, 1451.
- [140] M. Marcus, K. Baranes, M. Park, I. S. Choi, K. Kang, O. Shefi, *Adv. Healthc. Mater.* 2017, 6.
- [141] W. Li, Q. Y. Tang, A. D. Jadhav, A. Narang, W. X. Qian, P. Shi, S. W. Pang, *Sci. Rep.* 2015, 5, 1.
- [142] D. Y. Fozdar, J. Y. Lee, C. E Schmidt, S. Chen, *Int. J. Nanomedicine* 2011.
- [143] R. G. Flemming, C. J. Murphy, G. A. Abrams, S. L. Goodman, P. F. Nealey, *Biomaterials* 1999, 20, 573.
- [144] A. M. Rajnicek, S. Britland, C. D. McCaig, *J. Cell Sci.* 1997.
- [145] J. Seo, J. Kim, S. Joo, J. Y. Choi, K. Kang, W. K. Cho, I. S. Choi, *Small* 2018, 14, 1801763.
- [146] G. Bugnicourt, J. Brocard, A. Nicolas, C. Villard, *Langmuir* 2014.
- [147] L. Micholt, A. Gärtner, D. Prodanov, D. Braeken, C. G. Dotti, C. Bartic, *PLoS One* 2013, 8, e66170.
- [148] A. Kundu, L. Micholt, S. Friedrich, D. R. Rand, C. Bartic, D. Braeken, A. Levchenko, *Lab Chip* 2013, 13, 3070.
- [149] S. Usmani, E. R. Aurand, M. Medelin, A. Fabbro, D. Scaini, J. Laishram, F. B. Rosselli, A. Ansuini, D. Zoccolan, M. Scarselli, M. De Crescenzi, S. Bosi, M. Prato, L. Ballerini, *Sci. Adv.* 2016, 2.
- [150] E. R. Aurand, S. Usmani, M. Medelin, D. Scaini, S. Bosi, F. B. Rosselli, S. Donato, G. Tromba, M. Prato, L. Ballerini, *Adv. Funct. Mater.* 2018.
- [151] N. P. Pampaloni, I. Rago, I. Calaresu, L. Cozzarini, L. Casalis, A. Goldoni, L. Ballerini, D. Scaini, *Dev. Neurobiol.* 2019, 1.
- [152] M. De Volder, S. Park, S. Tawfick, A. J. Hart, *Nat. Commun.* 2014.
- [153] I. Rago, R. Rauti, M. Bevilacqua, I. Calaresu, A. Pozzato, M. Cibinel, M. Dalmiglio, C. Tavagnacco, A. Goldoni, D. Scaini, *Adv. Biosyst.* 2019.

- [154] X. Zhang, S. Prasad, S. Niyogi, A. Morgan, M. Ozkan, C. S. Ozkan, *Sensors Actuators, B Chem.* 2005.
- [155] L. Kam, W. Shain, J. N. Turner, R. Bizios, *Biomaterials* 1999, 20, 2343.
- [156] W. N. Chow, D. G. Simpson, J. W. Bigbee, R. J. Colello, *Neuron Glia Biol.* 2007.
- [157] M. Mattotti, Z. Alvarez, J. A. Ortega, J. A. Planell, E. Engel, S. Alcántara, *Biomaterials* 2012.
- [158] C. A. R. Chapman, H. Chen, M. Stamou, J. Biener, M. M. Biener, P. J. Lein, E. Seker, *ACS Appl. Mater. Interfaces* 2015, 7, 7093.
- [159] C. A. R. Chapman, L. Wang, H. Chen, J. Garrison, P. J. Lein, E. Seker, *Adv. Funct. Mater.* 2017.
- [160] A. E. Hampe, Z. Li, S. Sethi, P. J. Lein, E. Seker, *Nanomaterials* 2018, 8, 1.
- [161] C. Vallejo-Giraldo, K. Krukiewicz, I. Calaresu, J. Zhu, M. Palma, M. Fernandez-Yague, B. McDowell, N. Peixoto, N. Farid, G. O'Connor, L. Ballerini, A. Pandit, M. J. P. Biggs, *Small* 2018, 14, 1800863.
- [162] S. Persheyev, Y. Fan, A. Irving, M. J. Rose, *J. Biomed. Mater. Res. - Part A* 2011.
- [163] L. R. Pires, D. N. Rocha, L. Ambrosio, A. P. Pêgo, *J. R. Soc. Interface* 2015, 12.
- [164] A. Webb, P. Clark, J. Skepper, A. Compston, A. Wood, *J. Cell Sci.* 1995.
- [165] S. M. Wellman, F. Cambi, T. D. Kozai, The role of oligodendrocytes and their progenitors on neural interface technology: A novel perspective on tissue regeneration and repair. *Biomaterials* 2018.
- [166] S. Lee, M. K. Leach, S. A. Redmond, S. Y. C. Chong, S. H. Mellon, S. J. Tuck, Z. Q. Feng, J. M. Corey, J. R. Chan, *Nat. Methods* 2012.
- [167] J. M. Cregg, M. A. DePaul, A. R. Filous, B. T. Lang, A. Tran, J. Silver, *Exp. Neurol.* 2014, 253, 197.
- [168] J. W. Salatino, K. A. Ludwig, T. D. Y. Kozai, E. K. Purcell, *Nat. Biomed. Eng.* 2017, 1, 862.
- [169] J. Moss, T. Ryder, T. Z. Aziz, M. B. Graeber, P. G. Bain, *Brain* 2004.
- [170] A. Verkhatsky, O. A. Krishtal, O. H. Petersen, *Pflugers Arch. Eur. J. Physiol.* 2006, 453, 233.
- [171] L. Galvani, *Bononiensi Sci. Artium Inst. atque Acad. Comment.* 1791.
- [172] C. Matteucci, *Ann Chim Phys* 1842.
- [173] C. Matteucci, P. Savi, P. D. White, *Traité des phénomènes électro-physiologiques des animaux; 1944.*
- [174] L. Nobili, *Ann Chim Phys* 1828.
- [175] J. Bernstein, *Pflüger, Arch. für die Gesamte Physiol. des Menschen und der Thiere* 1868.
- [176] J. Bernstein, 1871.
- [177] R. Caton, *J. Nerv. Ment. Dis.* 1875.
- [178] F. H. Pratt, J. P. Eisenberger, *Am. J. Physiol. Content* 1919.

- [179] G. Ling, R. W. Gerard, *J. Cell. Comp. Physiol.* 1949.
- [180] A. Strickholm, *J. Gen. Physiol.* 1961.
- [181] A. H. Bretag, *J. Gen. Physiol.* 2017.
- [182] J. Zhang, J. Xia, H. Xiong, 2014.
- [183] B. Sakmann, E. Neher, *Annu. Rev. Physiol.* 1984.
- [184] C. L. Li, H. Jasper, *J. Physiol.* 1953.
- [185] A. A. Boulton, G. B. Baker, C. H. Vanderwolf, D. R. Humphrey, E. M. Schmidt, In *Neurophysiological Techniques, II*; 2003.
- [186] A. C. Patil, N. V. Thakor, *Med. Biol. Eng. Comput.* 2016, 54, 23.
- [187] D. H. HUBEL, *Science (80-. )*. 1957, 125, 549.
- [188] J. D. Green, *Nature* 1958.
- [189] E. G. Merrill, A. Ainsworth, *Med. Biol. Eng.* 1972.
- [190] G. E. Loeb, M. J. Bak, E. M. Schmidt, M. Salzman, *IEEE Trans. Biomed. Eng.* 1977.
- [191] H. Suzuki, M. Azuma, *Electroencephalogr. Clin. Neurophysiol.* 1976.
- [192] F. Strumwasser, *Science (80-. )*. 1958.
- [193] S. L. BeMent, K. D. Wise, D. J. Anderson, K. Najafi, K. L. Drake, *IEEE Trans. Biomed. Eng.* 1986.
- [194] K. Najafi, K. D. Wise, *IEEE J. Solid-State Circuits* 1986.
- [195] K. E. Jones, P. K. Campbell, R. A. Normann, *Ann. Biomed. Eng.* 1992.
- [196] R. Chen, A. Canales, P. Anikeeva, *Nat. Rev. Mater.* 2017, 2, 1.
- [197] J. P. Seymour, F. Wu, K. D. Wise, E. Yoon, *Microsystems Nanoeng.* 2017, 3, 1.
- [198] J. A. Frank, M. J. Antonini, P. Anikeeva, *Nat. Biotechnol.* 2019, 37, 1013.
- [199] J. Viventi, D. H. Kim, L. Vigeland, E. S. Frechette, J. A. Blanco, Y. S. Kim, A. E. Avrin, V. R. Tiruvadi, S. W. Hwang, A. C. Vanleer, D. F. Wulsin, K. Davis, C. E. Gelber, L. Palmer, J. Van Der Spiegel, J. Wu, J. Xiao, Y. Huang, D. Contreras, J. A. Rogers, B. Litt, *Nat. Neurosci.* 2011.
- [200] M. A. Escabí, H. L. Read, J. Viventi, D. H. Kim, N. C. Higgins, D. A. Storace, A. S. K. Liu, A. M. Gifford, J. F. Burke, M. Campisi, Y. S. Kim, A. E. Avrin, J. Van der Spiegel, Y. Huang, M. Li, J. Wu, J. A. Rogers, B. Litt, Y. E. Cohen, *J. Neurophysiol.* 2014.
- [201] D. Khodagholy, T. Doublet, P. Quilichini, M. Gurfinkel, P. Leleux, A. Ghestem, E. Ismailova, T. Hervé, S. Sanaur, C. Bernard, G. G. Malliaras, *Nat. Commun.* 2013, 4.
- [202] A. P. Chandrakasan, N. Verma, D. C. Daly, *Annu. Rev. Biomed. Eng.* 2008.
- [203] C. Hassler, T. Boretius, T. Stieglitz, *Polymers for neural implants. J. Polym. Sci. Part B Polym. Phys.* 2011.
- [204] M. S. Malagodi, K. W. Horch, A. A. Schoenberg, *Ann. Biomed. Eng.* 1989.
- [205] T. Lefurge, E. Goodall, K. Horch, L. Stensaas, A. Schoenberg, *Ann. Biomed. Eng.* 1991.

- [206] G. E. Loeb, R. A. Peck, J. Neurosci. Methods 1996.
- [207] K. Yoshida, M. J. Bertram, T. G. H. Cox, R. R. Riso, 377.
- [208] M. Ferguson, D. Sharma, D. Ross, F. Zhao, Adv. Healthc. Mater. 2019, 8, 1.
- [209] C. C. Winterbourn, Toxicol. Lett. 1995, 82–83, 969.
- [210] C. Bennett, F. Mohammed, A. Álvarez-Ciara, M. A. Nguyen, W. D. Dietrich, S. M. Rajguru, W. J. Streit, A. Prasad, Biomaterials 2019, 188, 144.
- [211] L. W. Norton, H. E. Koschwanez, N. A. Wisniewski, B. Klitzman, W. M. Reichert, J. Biomed. Mater. Res. - Part A 2007.
- [212] J. Selvakumaran, J. L. Keddie, D. J. Ewins, M. P. Hughes, J. Mater. Sci. Mater. Med. 2008, 19, 143.
- [213] C. Im, J. M. Seo, Biomed. Eng. Lett. 2016, 6, 104.
- [214] C. T. McKee, J. A. Last, P. Russell, C. J. Murphy, Tissue Eng. - Part B Rev. 2011, 17, 155.
- [215] J. C. Barrese, N. Rao, K. Paroo, C. Triebwasser, C. Vargas-Irwin, L. Franquemont, J. P. Donoghue, J. Neural Eng. 2013.
- [216] M. Jorfi, J. L. Skousen, C. Weder, J. R. Capadona, J. Neural Eng. 2015, 12.
- [217] H. J. Kim, D. N. Heo, Y. J. Lee, S. J. Lee, J. Y. Kang, S. H. Lee, I. K. Kwon, S. H. Do, Sci. Rep. 2017.
- [218] G. L. Knaack, D. G. McHail, G. Borda, B. Koo, N. Peixoto, S. F. Cogan, T. C. Dumas, J. J. Pancrazio, Front. Neurosci. 2016, 10, 1.
- [219] C. A. Diaz-Botia, L. E. Luna, R. M. Neely, M. Chamanzar, C. Carraro, J. M. Carmena, P. N. Sabes, R. Maboudian, M. M. Maharbiz, J. Neural Eng. 2017, 14, 056006.
- [220] F. Deku, Y. Cohen, A. Joshi-Imre, A. Kanneganti, T. J. Gardner, S. F. Cogan, J. Neural Eng. 2018.
- [221] M. S. Lord, M. Foss, F. Besenbacher, Nano Today 2010, 5, 66.
- [222] V. B. Damodaran, S. N. Murthy, Biomater. Res. 2016.
- [223] T. M. Gwon, C. Kim, S. Shin, J. H. Park, J. H. Kim, S. J. Kim, Biomed. Eng. Lett. 2016, 6, 148.
- [224] T. D. Yoshida Kozai, N. B. Langhals, P. R. Patel, X. Deng, H. Zhang, K. L. Smith, J. Lahann, N. A. Kotov, D. R. Kipke, Nat. Mater. 2012, 11, 1065.
- [225] A. Blau, A. Murr, S. Wolff, E. Sernagor, P. Medini, G. Iurilli, C. Ziegler, F. Benfenati, Biomaterials 2011, 32, 1778.
- [226] C. Yao, Q. Li, J. Guo, F. Yan, I. M. Hsing, Adv. Healthc. Mater. 2015.
- [227] N. Lago, A. Cester, Appl. Sci. 2017, 7.
- [228] N. A. Staples, J. A. Goding, A. D. Gilmour, K. Y. Aristovich, P. Byrnes-Preston, D. S. Holder, J. W. Morley, N. H. Lovell, D. J. Chew, R. A. Green, Front. Neurosci. 2018.



- [229] Y. Liu, J. Liu, S. Chen, T. Lei, Y. Kim, S. Niu, H. Wang, X. Wang, A. M. Foudeh, J. B. H. Tok, Z. Bao, *Nat. Biomed. Eng.* 2019.
- [230] J. Liu, T. M. Fu, Z. Cheng, G. Hong, T. Zhou, L. Jin, M. Duvvuri, Z. Jiang, P. Kruskal, C. Xie, Z. Suo, Y. Fang, C. M. Lieber, *Nat. Nanotechnol.* 2015, 10, 629.
- [231] T. Zhou, G. Hong, T. M. Fu, X. Yang, T. G. Schuhmann, R. D. Viveros, C. M. Lieber, *Proc. Natl. Acad. Sci. U. S. A.* 2017, 114, 5894.
- [232] G. Hong, X. Yang, T. Zhou, C. M. Lieber, *Curr. Opin. Neurobiol.* 2018, 50, 33.
- [233] F. Barbieri, V. Trauchessec, L. Caruso, J. Trejo-Rosillo, B. Telenczuk, E. Paul, T. Bal, A. Destexhe, C. Fermon, M. Pannetier-Lecoeur, G. Ouanounou, *Sci. Rep.* 2016, 6, 1.
- [234] L. Caruso, T. Wunderle, C. M. Lewis, J. Valadeiro, V. Trauchessec, J. Trejo Rosillo, J. P. Amaral, J. Ni, P. Jendritzka, C. Fermon, S. Cardoso, P. P. Freitas, P. Fries, M. Pannetier-Lecoeur, *Neuron* 2017, 95, 1283.
- [235] P. P. Sharma, G. Gervasoni, E. Albisetti, F. D'Ercoli, M. Monticelli, D. Moretti, N. Forte, A. Rocchi, G. Ferrari, P. Baldelli, M. Sampietro, F. Benfenati, R. Bertacco, D. Petti, *AIP Adv.* 2017, 7.
- [236] M. Ward, E. L. Schofield, *Therapy* 2010, 7, 321.
- [237] In *Cerebrospinal Fluid in Neurologic Disorders*; Deisenhammer, F.; Teunissen, C. E.; Tumani, H., Eds.; *Handbook of Clinical Neurology*; Elsevier, 2018; Vol. 146, pp. v–vi.
- [238] L. Huang, J. Hu, S. Huang, B. Wang, F. Siaw-Debrah, M. Nyanzu, Y. Zhang, Q. Zhuge, *Prog. Neurobiol.* 2017, 157, 29.
- [239] S. Jacobson, E. M. Marcus, S. Pugsley, In *Neuroanatomy for the Neuroscientist*; Jacobson, S.; Marcus, E. M.; Pugsley, S., Eds.; Springer International Publishing: Cham, 2018; pp. 269–295.
- [240] D. Tomalik-Scharte, A. Lazar, U. Fuhr, J. Kirchheiner, The clinical role of genetic polymorphisms in drug-metabolizing enzymes. *Pharmacogenomics J.* 2008.
- [241] S. Ahmed, Z. Zhou, J. Zhou, S. Q. Chen, *Pharmacogenomics of Drug Metabolizing Enzymes and Transporters: Relevance to Precision Medicine. Genomics, Proteomics Bioinforma.* 2016.
- [242] G. Tsoucalas, M. Karamanou, M. Lymperi, V. Gennimata, G. Androutsos, 2014, 65.
- [243] S. A. P. Haddad, R. P. M. Houben, W. A. Serdijin, *IEEE Eng. Med. Biol. Mag.* 2006, 25, 38.
- [244] R. V. Shannon, *Curr. Opin. Neurol.* 2012, 25, 61.
- [245] Y. H. L. Luo, L. da Cruz, The Argus® II Retinal Prosthesis System. *Prog. Retin. Eye Res.* 2016.
- [246] B. Cochener, G. Boutillier, M. Lamard, C. Auberger-Zagnoli, *J. Refract. Surg.* 2018.
- [247] R. F. Dallapiazza, P. De Vloo, A. Fomenko, D. J. Lee, C. Hamani, R. P. Munhoz, M. Hodaie, A. M. Lozano, A. Fasano, S. K. Kalia, In *Parkinson's Disease: Pathogenesis and Clinical Aspects*; Stoker, T. B.; Greenland, J. C., Eds.; Codon Publications: Brisbane (AU), 2018; pp. 145–160.
- [248] A. M. Lozano, N. Lipsman, H. Bergman, P. Brown, S. Chabardes, J. W. Chang, K. Matthews,

- C. C. McIntyre, T. E. Schlaepfer, M. Schulder, Y. Temel, J. Volkmann, J. K. Krauss, *Nat. Rev. Neurol.* 2019, 15, 148.
- [249] R. van den Brand, J. B. Mignardot, J. von Zitzewitz, C. Le Goff, N. Fumeaux, F. Wagner, M. Capogrosso, E. Martin Moraud, S. Micera, B. Schurch, A. Curt, S. Carda, J. Bloch, G. Courtine, *Ann. Phys. Rehabil. Med.* 2015, 58, 232.
- [250] M. L. Gill, P. J. Grahn, J. S. Calvert, M. B. Linde, I. A. Lavrov, J. A. Strommen, L. A. Beck, D. G. Sayenko, M. G. Van Straaten, D. I. Drubach, D. D. Veith, A. R. Thoreson, C. Lopez, Y. P. Gerasimenko, V. R. Edgerton, K. H. Lee, K. D. Zhao, *Nat. Med.* 2018, 24, 1677.
- [251] I. Lavrov, C. J. Dy, A. J. Fong, Y. Gerasimenko, G. Courtine, H. Zhong, R. R. Roy, V. R. Edgerton, *J. Neurosci.* 2008.
- [252] M. Capogrosso, T. Milekovic, D. Borton, F. Wagner, E. M. Moraud, J. B. Mignardot, N. Buse, J. Gandar, Q. Barraud, D. Xing, E. Rey, S. Duis, Y. Jianzhong, W. K. D. Ko, Q. Li, P. Detemple, T. Denison, S. Micera, E. Bezard, J. Bloch, G. Courtine, *Nature* 2016, 539, 284.
- [253] P. Verrills, C. Sinclair, A. Barnard, *J. Pain Res.* 2016, 9, 481.
- [254] R. Vallejo, K. Bradley, L. Kapural, *Spine (Phila. Pa. 1976)*. 2017, 42, S53.
- [255] K. Famm, B. Litt, K. J. Tracey, E. S. Boyden, M. Slaoui, M. Famm, Kristoffer;Litt, Brian; Tracey, Kevin J.; Boyden, Edward S.; Slaoui, *Nature* 2013, 5.
- [256] S. Reardon, *Nature* 2014, 511, 18.
- [257] C. M. Noller, Y. A. Levine, T. M. Urakov, J. P. Aronson, M. S. Nash, *Front. Neurosci.* 2019, 13, 1.
- [258] S. C. Schachter, C. B. Saper, *Epilepsia* 1998.
- [259] C. Heck, S. L. Helmers, C. M. DeGiorgio, *Neurology* 2002.
- [260] Q. Gao, G. Luan, *Neuropsychiatry (London)*. 2017.
- [261] L. V. Borovikova, S. Ivanova, M. Zhang, H. Yang, G. I. Botchkina, L. R. Watkins, H. Wang, N. Abumrad, J. W. Eaton, K. J. Tracey, *Nature* 2000.
- [262] H. Wang, M. Yu, M. Ochani, C. A. Amella, M. Tanovic, S. Susarla, J. H. Li, H. Wang, H. Yang, L. Ulloa, Y. Al-Abed, C. J. Czura, K. J. Tracey, *Nature* 2003, 421, 384.
- [263] V. A. Pavlov, H. Wang, C. J. Czura, S. G. Friedman, K. J. Tracey, *The Cholinergic Anti-inflammatory Pathway: A Missing Link in Neuroimmunomodulation. Mol. Med.* 2003, 9, 125–134.
- [264] F. A. Koopman, S. S. Chavan, S. Miljko, S. Grazio, S. Sokolovic, P. R. Schuurman, A. D. Mehta, Y. A. Levine, M. Faltys, R. Zitnik, K. J. Tracey, P. P. Tak, *Proc. Natl. Acad. Sci. U. S. A.* 2016, 113, 8284.
- [265] A. Kanashiro, F. Sônego, R. G. Ferreira, F. V. S. Castanheira, C. A. Leite, V. F. Borges, D. C. Nascimento, D. F. Cólón, J. C. Alves-Filho, L. Ulloa, F. Q. Cunha, *Therapeutic potential and limitations of cholinergic anti-inflammatory pathway in sepsis. Pharmacol. Res.* 2017.

- [266] S. C. Payne, J. B. Furness, M. J. Stebbing, *Nat. Rev. Gastroenterol. Hepatol.* 2019, 16, 89.
- [267] M. Guyot, T. Simon, F. Ceppo, C. Panzolini, A. Guyon, J. Lavergne, E. Murriss, D. Daoudlarian, R. Brusini, H. Zarif, S. Abélanet, S. Hugues-Ascery, J. L. Divoux, S. J. Lewis, A. Sridhar, N. Glaichenhaus, P. Blancou, *Nat. Biotechnol.* 2019, 37, 1446.
- [268] S. C. Lumsden, A. N. Clarkson, Y. O. Cakmak, *Front. Neurosci.* 2020, 14.
- [269] H. U. Lee, A. Blasiak, D. R. Agrawal, D. T. B. Loong, N. V. Thakor, A. H. All, J. S. Ho, I. H. Yang, *PLoS One* 2017.
- [270] A. N. Koppes, A. M. Seggio, D. M. Thompson, In *Journal of Neural Engineering*; 2011.
- [271] C. Chen, X. Bai, Y. Ding, I. S. Lee, Electrical stimulation as a novel tool for regulating cell behavior in tissue engineering. *Biomater. Res.* 2019.
- [272] K. B. Mirza, C. T. Golden, K. Nikolic, C. Toumazou, *Front. Neurosci.* 2019, 13, 1.
- [273] C. M. Goss, *Yale J. Biol. Med.* 1937.
- [274] R. Yuste, From the neuron doctrine to neural networks. *Nat. Rev. Neurosci.* 2015.
- [275] R. G. Harrison, *Proc. Soc. Exp. Biol. Med.* 1907.
- [276] A. Carrel, *J. Exp. Med.* 1912.
- [277] L. J. Millet, M. U. Gillette, *Yale J. Biol. Med.* 2012, 85, 501.
- [278] G. A. Banker, W. M. Cowan, *Brain Res.* 1977, 126, 397.
- [279] J. Ray, D. A. Peterson, M. Schinstine, F. H. Gage, *Proc. Natl. Acad. Sci. U. S. A.* 1993, 90, 3602.
- [280] C. Albuquerque, D. J. Joseph, P. Choudhury, A. B. MacDermott, *Cold Spring Harb. Protoc.* 2009, 2009.
- [281] S. Kaech, G. Banker, *Nat. Protoc.* 2006, 1, 2406.
- [282] G. M. J. Beaudoin, S. H. Lee, D. Singh, Y. Yuan, Y. G. Ng, L. F. Reichardt, J. Arikath, *Nat. Protoc.* 2012, 7, 1741.
- [283] B. A. Reynolds, S. Weiss, *Science (80-. )*. 1992.
- [284] L. Conti, S. M. Pollard, T. Gorba, E. Reitano, M. Toselli, G. Biella, Y. Sun, S. Sanzone, Q. L. Ying, E. Cattaneo, A. Smith, *PLoS Biol.* 2005, 3, 1594.
- [285] S. M. Pollard, L. Conti, Y. Sun, D. Goffredo, A. Smith, *Cereb. Cortex* 2006, 16.
- [286] N. S. Roy, T. Nakano, H. M. Keyoung, M. Windrem, W. K. Rashbaum, M. L. Alonso, J. Kang, W. Peng, M. K. Carpenter, J. Lin, M. Nedergaard, S. A. Goldman, *Nat. Biotechnol.* 2004, 22, 297.
- [287] C. Lorenz, P. Lesimple, R. Bukowiecki, A. Zink, G. Inak, B. Mlody, M. Singh, M. Semtner, N. Mah, K. Auré, M. Leong, O. Zabiegalov, E. M. Lyras, V. Pfiffer, B. Fauler, J. Eichhorst, B. Wiesner, N. Huebner, J. Priller, T. Mielke, D. Meierhofer, Z. Izsvák, J. C. Meier, F. Bouillaud, J. Adjaye, M. Schuelke, E. E. Wanker, A. Lombès, A. Prigione, *Cell Stem Cell* 2017.

- [288] I. Kelava, M. A. Lancaster, Stem Cell Models of Human Brain Development. Cell Stem Cell 2016.
- [289] G. Liang, Y. Zhang, Genetic and epigenetic variations in iPSCs: Potential causes and implications for application. Cell Stem Cell 2013.
- [290] R. J. Lund, E. Närvä, R. Lahesmaa, Genetic and epigenetic stability of human pluripotent stem cells. Nat. Rev. Genet. 2012.
- [291] P. Charlesworth, E. Cotterill, A. Morton, S. G. N. Grant, S. J. Eglén, Neural Dev. 2015, 10, 1.
- [292] Y. Penn, M. Segal, E. Moses, Proc. Natl. Acad. Sci. U. S. A. 2016.
- [293] B. Stevens, S. Porta, L. L. Haak, V. Gallo, R. D. Fields, Neuron 2002.
- [294] M. P. Mattson, S. B. Kater, Brain Res. 1989, 490, 110.
- [295] G. Q. Bi, M. M. Poo, J. Neurosci. 1998, 18, 10464.
- [296] A. N. Van Den Pol, K. Obrietan, A. B. Belousov, Y. Yang, H. C. Heller, J. Comp. Neurol. 1998, 399, 541.
- [297] Y. C. Lin, Z. H. Huang, I. S. Jan, C. C. Yeh, H. J. Wu, Y. C. Chou, Y. C. Chang, J. Neurosci. Res. 2002, 67, 484.
- [298] J. Yang, L. L. Thio, D. B. Clifford, C. F. Zorumski, Dev. Brain Res. 1993, 71, 19.
- [299] D. A. Wagenaar, J. Pine, S. M. Potter, J. Neurosci. Methods 2004, 138, 27.
- [300] A. El Hady, G. Afshar, K. Bröking, O. M. Schlüter, T. Geisel, W. Stühmer, F. Wolf, Front. Neural Circuits 2013.
- [301] S. Stern, A. Agudelo-Toro, A. Rotem, E. Moses, A. Neef, PLoS One 2015, 10.
- [302] L. Wan, S. Zhang, R. Xia, W. Ding, J. Neurosci. Res. 2010, 88, 2578.
- [303] T. Gordon, Electrical Stimulation to Enhance Axon Regeneration After Peripheral Nerve Injuries in Animal Models and Humans. Neurotherapeutics 2016.
- [304] T. Ishibashi, K. A. Dakin, B. Stevens, P. R. Lee, S. V. Kozlov, C. L. Stewart, R. D. Fields, Neuron 2006.
- [305] C. L. Paíno, C. Fernandez-Valle, M. L. Bates, M. B. Bunge, J. Neurocytol. 1994, 23, 433.
- [306] A. G. Rabchevsky, W. J. Streit, J. Neurosci. Res. 1997, 47, 34.
- [307] D. L. Hynds, N. Rangappa, J. Ter Beest, D. M. Snow, A. G. Rabchevsky, Glia 2004, 46, 218.
- [308] M. Manzati, T. Sorbo, M. Giugliano, L. Ballerini, Mol. Brain 2020, 13, 1.
- [309] N. Gresa-Arribas, C. Viéitez, G. Dentesano, J. Serratosa, J. Saura, C. Solà, PLoS One 2012, 7.
- [310] N. Goshi, R. K. Morgan, P. J. Lein, E. Seker, J. Neuroinflammation 2020, 17, 1.
- [311] M. V. Accardi, M. K. Pugsley, R. Forster, E. Troncy, H. Huang, S. Authier, J. Pharmacol. Toxicol. Methods 2016, 81, 47.

- [312] N. P. Pampaloni, M. Giugliano, D. Scaini, L. Ballerini, R. Rauti, *Front. Neurosci.* 2019, 12, 953.
- [313] SCENIHR (Scientific Committee on Emerging and Newly Identified Health Risks), The appropriateness of existing methodologies to assess the potential risks associated with engineered and adventitious products of nanotechnologies; 2006.
- [314] A. Mazzatenta, M. Giugliano, S. Campidelli, L. Gambazzi, L. Businaro, H. Markram, M. Prato, L. Ballerini, *J. Neurosci.* 2007, 27, 6931.
- [315] G. Cellot, E. Cilia, S. Cipollone, V. Rancic, A. Sucapane, S. Giordani, L. Gambazzi, H. Markram, M. Grandolfo, D. Scaini, F. Gelain, L. Casalis, M. Prato, M. Giugliano, L. Ballerini, *Nat. Nanotechnol.* 2009.
- [316] G. Cellot, F. M. Toma, Z. Kasap Varley, J. Laishram, A. Villari, M. Quintana, S. Cipollone, M. Prato, L. Ballerini, *J. Neurosci.* 2011, 31, 12945.
- [317] N. P. Pampaloni, M. Lottner, M. Giugliano, A. Matruglio, F. D'Amico, M. Prato, J. A. Garrido, L. Ballerini, D. Scaini, *Nat. Nanotechnol.* 2018, 13, 755.
- [318] N. Secomandi, A. Franceschi Biagioni, K. Kostarelos, G. Cellot, L. Ballerini, *Nanomedicine Nanotechnology, Biol. Med.* 2020, 26, 102174.
- [319] H. Charkhkar, G. L. Knaack, H. S. Mandal, E. W. Keefer, J. J. Pancrazio, 2014 36th Annu. Int. Conf. IEEE Eng. Med. Biol. Soc. EMBC 2014 2014, 469.
- [320] Y. H. Kim, G. H. Kim, A. Y. Kim, Y. H. Han, M. A. Chung, S. D. Jung, *J. Neural Eng.* 2015, 12.
- [321] D. W. Jeong, G. H. Kim, N. Y. Kim, Z. Lee, S. D. Jung, J. O. Lee, *RSC Adv.* 2017, 7, 3273.
- [322] A. Domínguez-bajo, B. L. Rodilla, A. Arché-núñez, E. López-dolado, M. T. González, 2020, 2000117, 1.
- [323] P. Fromherz, A. Offenhäusser, T. Vetter, J. Weis, *Science (80-. )*. 1991.
- [324] S. Ronchi, M. Fiscella, C. Marchetti, V. Viswam, J. Müller, U. Frey, A. Hierlemann, *Front. Neurosci.* 2019, 13.
- [325] Y. Zhao, S. S. You, A. Zhang, J. H. Lee, J. Huang, C. M. Lieber, *Nat. Nanotechnol.* 2019.
- [326] P. Fromherz, *Solid. State. Electron.* 2008, 52, 1364.
- [327] J. Cheng, L. Wu, X. W. Du, Q. H. Jin, J. L. Zhao, Y. Sen Xu, *J. Microelectromechanical Syst.* 2014, 23, 1311.
- [328] Y. Li, K. A. Kilian, *Adv. Healthc. Mater.* 2015.
- [329] K. Duval, H. Grover, L. H. Han, Y. Mou, A. F. Pegoraro, J. Fredberg, Z. Chen, *Modeling physiological events in 2D vs. 3D cell culture. Physiology* 2017.
- [330] S. G. K.J. Jensen, *Compr Physiol* 2013, 29, 997.
- [331] T. Ast, V. K. Mootha, *Nat. Metab.* 2019, 1, 858.



- [332] L. Lossi, A. Merighi, *Front. Vet. Sci.* 2018, 5, 1.
- [333] C. Humpel, *Neuroscience* 2015.
- [334] A. A. Maximow, *Tissue-cultures of young mammalian embryos*; 1925.
- [335] M. B. Bornstein, M. R. Murray, *J. Biophys. Biochem. Cytol.* 1958, 4, 499.
- [336] E. R. Peterson, S. M. Crain, M. R. Murray, *Zeitschrift für Zellforsch. und Mikroskopische Anat.* 1965.
- [337] S. M. Crain, *Int. Rev. Neurobiol.* 1966, 1.
- [338] B. Hoffer, Å. Seiger, T. Ljungberg, L. Olson, *Brain Res.* 1974.
- [339] B. H. Gähwiler, *J. Neurosci. Methods* 1981, 4, 329.
- [340] L. Stoppini, P. A. Buchs, D. Muller, *J. Neurosci. Methods* 1991.
- [341] J. Marksteiner, C. Humpel, *Mol. Psychiatry* 2008, 13, 939.
- [342] S. Cho, A. Wood, M. Bowlby, *Curr. Neuropharmacol.* 2007, 5, 19.
- [343] S. Pandamooz, M. S. Saied, M. Nabiuni, L. Dargahi, M. Pourghasem, *Folia Biol. (Czech Republic)* 2016, 62, 263.
- [344] D. M. Magalhães, N. Pereira, D. M. Rombo, C. Beltrão-Cavacas, A. M. Sebastião, C. A. Valente, *J. Neuroinflammation* 2018.
- [345] C. L. Croft, H. S. Futch, B. D. Moore, T. E. Golde, *Mol. Neurodegener.* 2019, 14, 1.
- [346] B. Hutter-Schmid, K. M. Kniewallner, C. Humpel, *Front. Cell Dev. Biol.* 2015, 3, 1.
- [347] J. L. Dupont, E. Fourcaudot, H. Beekenkamp, B. Poulain, J. L. Bossu, *Cerebellum* 2006.
- [348] S. C. Eun, Y. L. So, J. Y. Park, S. G. Hong, D. R. Pan, *J. Vet. Sci.* 2007.
- [349] J. Rohrbacher, N. Ichinohe, S. T. Kitai, *Neuroscience* 2000.
- [350] B. H. Gähwiler, F. Hefti, *Neuroscience* 1984, 13, 681.
- [351] D. Li, P. M. Field, U. Starega, Y. Li, G. Raisman, *Neuroscience* 1993, 52, 799.
- [352] P. L. Woodhams, D. J. Atkinson, *Exp. Neurol.* 1996, 140, 68.
- [353] U. F. Braschler, A. Iannone, C. Spenger, J. Streit, H. R. Lüscher, *J. Neurosci. Methods* 1989.
- [354] P. Branchereau, J. Chapron, P. Meyrand, *J. Neurosci.* 2002.
- [355] D. Avossa, M. D. Rosato-Siri, F. Mazarrol, L. Ballerini, *Neuroscience* 2003.
- [356] E. Cherubini, J. L. Gaiarsa, Y. Ben-Ari, *Trends Neurosci.* 1991.
- [357] D. G. Amaral, M. P. Witter, *Neuroscience* 1989.
- [358] R. S. Sloviter, T. Lomo, *Updating the lamellar hypothesis of hippocampal organization.* *Front. Neural Circuits* 2012.
- [359] G. Xiong, H. Metheny, B. N. Johnson, A. S. Cohen, *Front. Neuroanat.* 2017.

- [360] C. Spenger, U. F. Braschler, J. Streit, H.-R. Luscher, *Eur. J. Neurosci.* 1991, 3, 1037.
- [361] J. Streit, C. Spenger, H.-R. Luscher, *Eur. J. Neurosci.* 1991, 3, 1054.
- [362] J. Gerardo-Nava, D. Hodde, I. Katona, A. Bozkurt, T. Grehl, H. W. M. Steinbusch, J. Weis, G. A. Brook, *Biomaterials* 2014, 35, 4288.
- [363] A. Chvátal, A. Pastor, M. Mauch, E. Syková, H. Kettenmann, *Eur. J. Neurosci.* 1995.
- [364] J. W. Dani, A. Chernjavsky, S. J. Smith, 1992, 8, 429.
- [365] T. Sasaki, T. Ishikawa, R. Abe, R. Nakayama, A. Asada, N. Matsuki, Y. Ikegaya, *J. Physiol.* 2014, 592, 2771.
- [366] N. P. Hailer, J. D. Järhult, R. Nitsch, *Glia* 1996, 18, 319.
- [367] A. di Penta, B. Moreno, S. Reix, B. Fernandez-Diez, M. Villanueva, O. Errea, N. Escala, K. Vandenbroeck, J. X. Comella, P. Villoslada, *PLoS One* 2013, 8.
- [368] V. Giacco, G. Panattoni, M. Medelin, E. Bonechi, A. Aldinucci, C. Ballerini, L. Ballerini, *J. Neuroinflammation* 2019, 16, 1.
- [369] M. Haber, S. Vautrin, E. J. Fry, K. K. Murai, *Glia* 2009, 57, 1000.
- [370] R. A. Hill, J. Medved, K. D. Patel, A. Nishiyama, *J. Vis. Exp.* 2014, e51835.
- [371] M. Pohland, R. Glumm, F. Wiekhorst, J. Kiwit, J. Glumm, *Int. J. Nanomedicine* 2017.
- [372] A. P. Weightman, S. I. Jenkins, D. M. Chari, *Nano Res.* 2016.
- [373] M. Machado-Pereira, T. Santos, L. Ferreira, L. Bernardino, R. Ferreira, *Mediators Inflamm.* 2017.
- [374] M. Medelin, V. Giacco, A. Aldinucci, G. Castronovo, E. Bonechi, A. Sibilla, M. Tanturli, M. Torcia, L. Ballerini, F. Cozzolino, C. Ballerini, *Mol. Brain* 2018, 11, 1.
- [375] M. Musto, R. Rauti, A. F. Rodrigues, E. Bonechi, C. Ballerini, K. Kostarelos, L. Ballerini, *Front. Syst. Neurosci.* 2019, 13, 1.
- [376] Z. Yu, T. E. McKnight, M. N. Ericson, A. V. Melechko, M. L. Simpson, B. Morrison, *Nano Lett.* 2007.
- [377] P. Thiébaud, N. F. De Rooij, M. Koudelka-Hep, L. Stoppini, *IEEE Trans. Biomed. Eng.* 1997.
- [378] L. Stoppini, S. Dupont, P. Corrèges, J. Neurosci. *Methods* 1997.
- [379] U. Egert, B. Schlosshauer, S. Fennrich, W. Nisch, M. Fejtl, T. Knott, T. Müller, H. Hämmerle, *Brain Res. Protoc.* 1998.
- [380] B. Besl, P. Fromherz, *Eur. J. Neurosci.* 2002.
- [381] W. Gong, J. Sencar, D. J. Bakkum, D. Jäckel, M. E. J. Obien, M. Radivojevic, A. R. Hierlemann, *Front. Neurosci.* 2016.
- [382] J. H. Breasted, *The Edwin Smith Surgical Papyrus, Volume 1: Hieroglyphic Transliteration, Translation, and Commentary.*; 1930.
- [383] S. G. Marketos, P. K. Skiadas, *Spine (Phila. Pa. 1976).* 1999.

- [384] S. Naderi, U. Türe, T. G. Pait, *Neurosurg. Focus* 2004, 16, 20.
- [385] E. Flatau, *Atlas of the Human Brain: And the Course of the Nerve-fibres*; S. Karger, 1894.
- [386] B. Rexed, *J. Comp. Neurol.* 1952, 96, 415.
- [387] B. Rexed, *J. Comp. Neurol.* 1954, 100, 297.
- [388] M. E. Scheibel, A. B. Scheibel, *Brain Res.* 1966.
- [389] M. E. Scheibel, A. B. Scheibel, *Brain Res.* 1968.
- [390] S. Hochman, *Curr. Biol.* 2007, 17, 950.
- [391] S. Jacobson, E. M. Marcus, S. Pugsley, In *Neuroanatomy for the Neuroscientist*; 2018.
- [392] G. Sengul, C. Watson, *Ascending and Descending Pathways in the Spinal Cord*; Fourth Edi.; Elsevier Inc., 2015.
- [393] A. C. Conta, D. J. Stelzner, *The Propriospinal System*; Elsevier Ltd, 2009.
- [394] G. Sengul, *Spinal Cord Cyto- and Chemoarchitecture*; Fourth Edi.; Elsevier Inc., 2015; Vol. 1.
- [395] G. Sengul, *Primary Afferent Projections to the Spinal Cord*; Fourth Edi.; Elsevier Inc., 2015.
- [396] A. Nogradi, *Transplantation of Neural Tissue into the Spinal Cord*; Neuroscience Intelligence Unit; Springer US: Boston, MA, 2006.
- [397] N. Stifani, *Front. Cell. Neurosci.* 2014, 8, 1.
- [398] P. J. Osseward, S. L. Pfaff, *Curr. Opin. Neurobiol.* 2019, 56, 175.
- [399] WHO, ISCoS, *International Perspectives on Spinal Cord Injury*; Malta, 2013.
- [400] A. S. C. I. Association, *ASIA*, Chicago 1982.
- [401] R. Betz, F. Biering-Sørensen, S. P. Burns, W. Donovan, D. E. Graves, J. Guest, L. Jones, S. Kirshblum, A. Krassioukov, M. J. Mulcahey, M. Schmidt Read, G. M. Rodriguez, R. Rupp, C. Schuld, K. Tansey, K. Walden, *Spinal Cord* 2019, 57, 815.
- [402] R. P. Bunge, W. R. Puckett, J. L. Becerra, A. Marcillo, R. M. Quencer, *Adv. Neurol.* 1993.
- [403] C. E. Hulsebosch, *Adv. Physiol. Educ.* 2002, 26, 238.
- [404] J. W. Rowland, G. W. J. Hawryluk, B. Kwon, M. G. Fehlings, *Neurosurg. Focus* 2008, 25, 1.
- [405] C. H. Tator, *Neurosurgery* 1998, 42, 696.
- [406] S. Liu, Y. Li, H. M. C. Choi, C. Sarkar, E. Y. Koh, J. Wu, M. M. Lipinski, *Cell Death Dis.* 2018.
- [407] M. S. Beattie, G. E. Hermann, R. C. Rogers, J. C. Bresnahan, *Prog. Brain Res.* 2002.
- [408] M. C. Tsai, C. P. Wei, D. Y. Lee, Y. T. Tseng, M. D. Tsai, Y. L. Shih, Y. H. Lee, S. F. Chang, S. J. Leu, *Surg. Neurol.* 2008.
- [409] J. Lier, B. Ondruschka, I. Bechmann, J. Dreßler, *Int. J. Legal Med.* 2020.
- [410] M. Arundine, M. Tymianski, *Cell. Mol. Life Sci.* 2004, 61, 657.

- [411] F. A. X. Schanne, A. B. Kane, E. E. Young, J. L. Farber, *Science* (80-. ). 1979.
- [412] P. G. Sullivan, S. Krishnamurthy, S. P. Patel, J. D. Pandya, A. G. Rabchevsky, *J. Neurotrauma* 2007, 24, 991.
- [413] A. I. Faden, R. P. Simon, *Ann. Neurol.* 1988.
- [414] J. J. Lemasters, T. P. Theruvath, Z. Zhong, A. L. Nieminen, Mitochondrial calcium and the permeability transition in cell death. *Biochim. Biophys. Acta - Bioenerg.* 2009.
- [415] E. Park, A. A. Velumian, M. G. Fehlings, The role of excitotoxicity in secondary mechanisms of spinal cord injury: A review with an emphasis on the implications for white matter degeneration. *J. Neurotrauma* 2004.
- [416] A. G. Rabchevsky, F. M. Michael, S. P. Patel, *Exp. Neurol.* 2020, 330, 113332.
- [417] X. Zhou, X. J. He, Y. Ren, Function of microglia and macrophages in secondary damage after spinal cord injury. *Neural Regen. Res.* 2014.
- [418] M. S. Beattie, A. A. Farooqui, J. C. Bresnahan, Review of current evidence for apoptosis after spinal cord injury. *J. Neurotrauma* 2000.
- [419] A. Buss, K. Pech, D. Merkler, B. A. Kakulas, D. Martin, J. Schoenen, J. Noth, M. E. Schwab, G. A. Brook, *Brain* 2005.
- [420] J. W. Fawcett, R. A. Asher, *Brain Res. Bull.* 1999, 49, 377.
- [421] T. Hagg, M. Oudega, *J. Neurotrauma* 2006, 23, 264.
- [422] J. H. Bruce, M. D. Norenberg, S. Kraydieh, W. Puckett, A. Marcillo, D. Dietrich, *J. Neurotrauma* 2000.
- [423] C. Soderblom, X. Luo, E. Blumenthal, E. Bray, K. Lyapichev, J. Ramos, V. Krishnan, C. Lai-Hsu, K. K. Park, P. Tsoufas, J. K. Lee, *J. Neurosci.* 2013.
- [424] A. Biyani, W. S. Ei Masry, *Paraplegia* 1994.
- [425] M. E. Schwab, D. Bartholdi, *Physiol. Rev.* 1996, 76, 319.
- [426] C. E. Hill, M. S. Beattie, J. C. Bresnahan, *Exp. Neurol.* 2001, 171, 153.
- [427] S. Quraishie, L. H. Forbes, M. R. Andrews, *Neural Plast.* 2018, 2018.
- [428] C. T. Liverman, B. M. Altevogt, J. E. Joy, R. T. Johnson, *Spinal Cord Injury: Progress, Promise, and Priorities*; 2005.
- [429] G. W. J. Hawryluk, J. Rowland, B. K. Kwon, M. G. Fehlings, *Neurosurg. Focus* 2008.
- [430] C. Moritz, *Nat. Neurosci.* 2018, 21, 1647.
- [431] T. H. Hutson, S. Di Giovanni, *Nat. Rev. Neurol.* 2019, 15, 732.
- [432] S. Thuret, L. D. F. Moon, F. H. Gage, *Nat. Rev. Neurosci.* 2006, 7, 628.
- [433] T. Liu, J. D. Houle, J. Xu, B. P. Chan, S. Y. Chew, *Tissue Eng. - Part A* 2012, 18, 1057.
- [434] S. Usmani, A. Franceschi Biagioni, M. Medelin, D. Scaini, R. Casani, E. R. Aurand, D. Padro, A. Egimendia, P. Ramos Cabrer, M.

- Scarselli, M. De Crescenzi, M. Prato, L. Ballerini, Proc. Natl. Acad. Sci. 2020, 117, 25212.
- [435] X. M. Xu, V. Guénard, N. Kleitman, P. Aebischer, M. B. Bunge, Exp. Neurol. 1995, 134, 261.
- [436] X. M. Xu, V. Guénard, N. Kleitman, M. B. Bunge, J. Comp. Neurol. 1995, 351, 145.
- [437] J. D. Guest, A. Rao, L. Olson, M. B. Bunge, R. P. Bunge, Exp. Neurol. 1997, 148, 502.
- [438] A. Chen, X. M. Xu, N. Kleitman, M. B. Bunge, Exp. Neurol. 1996, 138, 261.
- [439] S. Liu, T. Schackel, N. Weidner, R. Puttagunta, Front. Cell. Neurosci. 2018, 11.
- [440] D. Cigognini, A. Satta, B. Colleoni, D. Silva, M. Donegà, S. Antonini, F. Gelain, PLoS One 2011, 6.
- [441] L. T. A. Hong, Y. M. Kim, H. H. Park, D. H. Hwang, Y. Cui, E. M. Lee, S. Yahn, J. K. Lee, S. C. Song, B. G. Kim, Nat. Commun. 2017, 8, 1.
- [442] Z. Nazemi, M. S. Nourbakhsh, S. Kiani, Y. Heydari, M. K. Ashtiani, H. Daemi, H. Baharvand, J. Control. Release 2020, 321, 145.
- [443] Z. Gong, D. Lei, C. Wang, C. Yu, K. Xia, J. Shu, L. Ying, J. Du, J. Wang, X. Huang, L. Ni, C. Wang, J. Lin, F. Li, Z. You, C. Liang, ACS Biomater. Sci. Eng. 2020.
- [444] J. L. Collinger, S. Foldes, T. M. Bruns, B. Wodlinger, R. Gaunt, D. J. Weber, J. Spinal Cord Med. 2013, 36, 258.
- [445] S. Luo, H. Xu, Y. Zuo, X. Liu, A. H. All, NeuroMolecular Med. 2020.
- [446] J. B. Zimmermann, A. Jackson, Front. Neurosci. 2014, 8, 1.
- [447] W. D. Memberg, K. H. Polasek, R. L. Hart, A. M. Bryden, K. L. Kilgore, G. A. Nemunaitis, H. A. Hoyen, M. W. Keith, R. F. Kirsch, Arch. Phys. Med. Rehabil. 2014, 95.
- [448] E. Rejc, C. Angeli, S. Harkema, PLoS One 2015, 10, 1.
- [449] E. Rejc, C. A. Angeli, D. Atkinson, S. J. Harkema, Sci. Rep. 2017, 7, 1.
- [450] G. Taccola, D. Sayenko, P. Gad, Y. Gerasimenko, V. R. Edgerton, Prog. Neurobiol. 2018, 160, 64.
- [451] E. Formento, K. Minassian, F. Wagner, J. B. Mignardot, C. G. Le Goff-Mignardot, A. Rowald, J. Bloch, S. Micera, M. Capogrosso, G. Courtine, Nat. Neurosci. 2018, 21, 1728.
- [452] S. Hamid, R. Hayek, Eur. Spine J. 2008, 17, 1256.
- [453] S. E. Mondello, M. R. Kasten, P. J. Horner, C. T. Moritz, Front. Neurosci. 2014, 8, 1.
- [454] G. Courtine, B. Song, R. R. Roy, H. Zhong, J. E. Herrmann, Y. Ao, J. Qi, V. R. Edgerton, M. V. Sofroniew, Nat. Med. 2008, 14, 69.
- [455] R. Van Den Brand, J. Heutschi, Q. Barraud, J. DiGiovanna, K. Bartholdi, M. Huerlimann, L. Friedli, I. Vollenweider, E. M. Moraud, S. Duis, N. Dominici, S. Micera, P. Musienko, G. Courtine, Science (80-. ). 2012.
- [456] I. R. Mineev, P. Musienko, A. Hirsch, Q. Barraud, N. Wenger, E. M. Moraud, J. Gandar, M. Capogrosso, T. Milekovic, L. Asboth, R. F. Torres, N. Vachicouras, Q. Liu, N. Pavlova, S. Duis, A.



- Larmagnac, J. Vörös, S. Micera, Z. Suo, G. Courtine, S. P. Lacour, *Science* (80-. ). 2015.
- [457] P. J. Grahn, G. W. Mallory, B. Michael Berry, J. T. Hachmann, D. A. Lobel, J. Luis Lujan, *Front. Neurosci.* 2014, 8, 1.
- [458] E. M. Moraud, J. Von Zitzewitz, J. Miehlsbradt, S. Wurth, E. Formento, J. DiGiovanna, M. Capogrosso, G. Courtine, S. Micera, *Sci. Rep.* 2018, 8, 1.
- [459] M. Capogrosso, N. Wenger, S. Raspopovic, P. Musienko, J. Beauparlant, L. B. Luciani, G. Courtine, S. Micera, *J. Neurosci.* 2013, 33, 19326.
- [460] W. Wang, J. L. Collinger, A. D. Degenhart, E. C. Tyler-Kabara, A. B. Schwartz, D. W. Moran, D. J. Weber, B. Wodlinger, R. K. Vinjamuri, R. C. Ashmore, J. W. Kelly, M. L. Boninger, *PLoS One* 2013, 8, 1.
- [461] N. J. Hill, T. N. Lal, M. Schröder, T. Hinterberger, B. Wilhelm, F. Nijboer, U. Mochty, G. Widman, C. Elger, B. Schölkopf, A. Kübler, N. Birbaumer, In *IEEE Transactions on Neural Systems and Rehabilitation Engineering*; 2006.
- [462] D. J. Weber, R. B. Stein, D. G. Everaert, A. Prochazka, *J. Neural Eng.* 2007, 4.
- [463] T. M. Bruns, J. B. Wagenaar, M. J. Bauman, R. A. Gaunt, D. J. Weber, *J. Neural Eng.* 2013, 10.
- [464] B. J. Holinski, D. G. Everaert, V. K. Mushahwar, R. B. Stein, *J. Neural Eng.* 2013, 10, 056008.
- [465] N. Wenger, E. M. Moraud, S. Raspopovic, M. Bonizzato, J. DiGiovanna, P. Musienko, M. Morari, S. Micera, G. Courtine, *Sci. Transl. Med.* 2014, 6.
- [466] B. Barra, K. Zhuang, S. Conti, G. Schiavone, S. Lacour, J. Bloch, G. Courtine, M. Capogrosso, In *Proceedings of the 41st Annual International Conference of the IEEE Engineering in Medicine and Biology Society (EMBC)*; 2019.
- [467] P. Kibleur, S. R. Tata, N. Greiner, S. Conti, B. Barra, K. Zhuang, M. Kaeser, A. Ijspeert, M. Capogrosso, *IEEE Trans. Neural Syst. Rehabil. Eng.* 2020, 28, 1668.
- [468] B. M. London, L. R. Jordan, C. R. Jackson, L. E. Miller, *IEEE Trans. Neural Syst. Rehabil. Eng.* 2008, 16, 32.
- [469] J. E. O'Doherty, M. A. Lebedev, P. J. Ifft, K. Z. Zhuang, S. Shokur, H. Bleuler, M. A. L. Nicolelis, *Nature* 2011, 479, 228.
- [470] J. A. Berg, J. F. Dammann, F. V. Tenore, G. A. Tabot, J. L. Boback, L. R. Manfredi, M. L. Peterson, K. D. Katyal, M. S. Johannes, A. Makhlin, R. Wilcox, R. K. Franklin, R. J. Vogelstein, N. G. Hatsopoulos, S. J. Bensmaia, *IEEE Trans. Neural Syst. Rehabil. Eng.* 2013, 21, 500.
- [471] G. Cellot, P. Lagonegro, G. Tarabella, D. Scaini, F. Fabbri, S. Iannotta, M. Prato, G. Salviati, L. Ballerini, *Front. Neurosci.* 2016, 9, 1.
- [472] B. Bonnici, J. P. Kapfhammer, *Eur. J. Neurosci.* 2008, 27, 2483.
- [473] M. Abu-Rub, S. McMahon, D. I. Zeugolis, A. Windebank, A. Pandit, *Drug Discov. Today* 2010, 15, 436.
- [474] J. Sypecka, S. Koniusz, M. Kawalec, A. Sarnowska, *Stem Cells Int.* 2015.

- [475] D. Scaini, L. Ballerini, *Curr. Opin. Neurobiol.* 2018, 50, 50.
- [476] M. Srikanth, J. A. Kessler, *Nat. Rev. Neurol.* 2012, 8, 307.
- [477] G. Hong, C. M. Lieber, *Nat. Rev. Neurosci.* 2019, 20, 330.
- [478] J. Schiweck, B. J. Eickholt, K. Murk, *Front. Cell. Neurosci.* 2018, 12, 1.
- [479] J. M. Stukel, R. K. Willits, *Tissue Eng. - Part B Rev.* 2016, 22, 173.
- [480] M. Chighizola, T. Dini, C. Lenardi, P. Milani, A. Podestà, C. Schulte, *Biophys. Rev.* 2019, 11, 701.
- [481] D. Khodagholy, J. N. Gelinias, T. Thesen, W. Doyle, O. Devinsky, G. G. Malliaras, G. Buzsáki, *Nat. Neurosci.* 2015, 18, 310.